Winter sea ice characteristics in the central Arctic from thermal infrared imaging

Dissertation submitted by

Linda Thielke

in fulfillment of the requirements
for the degree of

Doctor of Natural Sciences (Dr. rer. nat.)

to

Faculty 1
Physics and Electrical Engineering
University of Bremen

Submission: 13 April 2023
Colloquium: 21 June 2023

Universität Bremen

1. Reviewer: Dr. Gunnar Spreen
Institute of Environmental Physics
University of Bremen

2. Reviewer: Prof. Dr. Monika Rhein
Institute of Environmental Physics
University of Bremen

This dissertation was written in the working group 'Remote Sensing of Polar Regions' of the Institute of Environmental Physics, University of Bremen.

Abstract

This dissertation is based on helicopter-borne thermal infrared (TIR) imaging performed during the MOSAiC expedition in the central Arctic in winter. The aim is to increase the understanding of processes influencing the Arctic heat budget. TIR imaging benefits from the large temperature differences between the colder thick sea ice and the warmer leads of open water or covered with thin ice. Between October 2019 and April 2020, 35 helicopter flights were used for investigation on the local (5–10 km) and regional scale (20–40 km). From several thousands of images, surface temperature maps at 1 m resolution were created for each flight. This thesis focuses on (i) melt pond pre-conditioning based on warm temperature anomalies, (ii) lead classification resulting in area fraction, width distribution, and orientations down to the spatial scale of meters, and (iii) the relevance of the satellite sub-footprint scale variability of surface temperatures for the heat exchange.

Melt ponds are a crucial part of the summer heat budget as they lower the surface albedo and contribute to the positive ice-albedo feedback. The comparison of winter temperature and summer images from the same ice revealed the presence of warm anomalies of 0.3–2.5 K at the melt pond locations of the subsequent summer. This pre-conditioning enabled a correct seasonal prediction of 41% of the melt ponds.

Leads are relevant for the winter heat budget as they allow for an increased heat transfer from the warmer ocean to the colder atmosphere. The determined lead area fraction is 1.2% on average and up to 4% on 24 December 2019, with stronger variability on the local than on the regional scale. The power law distribution of lead width has a negative exponent of 2.63 that is valid to a width of 3 m. Consequently, there is an exponentially larger number of narrow than wider leads.

The numerous small-scale leads are not resolved in operationally used satellite products. Due to the lack of sub-footprint scale variability the sensible heat flux derived from these products is underestimated. The decrease of the average sensible heat flux of up to $0.69\,\mathrm{W\,m^{-2}}$ between the 1 m and re-gridded 1 km resolution helicopter data has a linear relation with the lead area fraction. A comparison between the overlapping helicopter and satellite surface temperatures of MODIS showed no alignment in spatial variability. The thesis' findings provide results to improve satellite retrievals and model parameterizations.

Zusammenfassung

Diese Dissertation nutzt Hubschrauber basierte Infrarot-Thermografie Bilder, die während der MOSAiC Expedition in der zentralen Arktis aufgenommen wurden. Das Ziel ist, das Verständnis für Prozesse zu erhöhen, die das arktischen Wärmebudget beeinflussen. Diese Methode nutzt die großen Temperaturunterschiede zwischen dem kalten, dicken Meereis und den wärmeren Meereisrinnen mit offener Wasseroberfläche oder bedeckt mit dünnem Eis. Zwischen Oktober 2019 und April 2020 wurden die Daten von 35 Hubschrauberflüge auf lokaler (5–10 km) und regionaler (20-40 km) Ebene untersucht. Aus mehreren tausend Bildern wurden Oberflächentemperaturkarten mit einer Auflösung von 1 m für jeden Hubschrauberflug erstellt. Der Fokus dieser Arbeit liegt auf (i) den Vorbedingungen von Schmelztümpeln aufgrund warmer Temperaturanomalien, (ii) der Klassifizierung von Meereisrinnen für die Bestimmung des Flächenanteils, der Breitenverteilung und der Ausrichtung von Meereisrinnen bis zu einer räumlichen Skala von Metern und (iii) der Relevanz der Variabilität innerhalb eines Satelliten-Fußabdrucks von Satellitendaten für den Wärmeaustausch.

Schmelztümpel sind im Sommer ein entscheidender Teil des Wärmehaushalts, da sie die Oberflächenalbedo verringern und zur verstärkenden Eis-Albedo-Rückkopplung beitragen. Der Vergleich von Wintertemperaturen und Sommerbildern desselben Eises zeigt das Vorhandensein von warmen Anomalien zwischen 0.3 und 2.5 K an der Stelle der Schmelztümpel im darauffolgenden Sommer. Das Verständnis der Vorbedingung ermöglicht eine korrekte saisonale Vorhersage von 41% der Schmelztümpel.

Meereisrinnen sind für den Wärmehaushalt im Winter relevant, da sie einen erhöhten Wärmeaustausch von wärmerem Ozean zu kälterer Atmosphäre ermöglichen. Der Flächenanteil von Meereisrinnen ist im Durchschnitt 1.2% und maximal 4% am 24. Dezember 2019. Für den Flächenanteil gibt es eine stärkere Variabilität auf lokaler als auf regionaler Ebene. Die Verteilung der Rinnenbreite folgt einem Potenzgesetz mit einem negativen Exponenten von 2.63 und gilt bis zu einer Breite von 3 m. Daher gibt es eine exponentiell größere Anzahl von schmalen Meereisrinnen im Gegensatz zu breiteren Meereisrinnen.

Die zahlreichen kleinräumigen Rinnen sind in operationell genutzten Satellitenprodukten nicht direkt repräsentiert. Durch die fehlende Variabilität innerhalb eines Satelliten-Fußabdrucks wird der aus diesen Produkten abgeleitete sensible Wärmefluss unterschätzt.

Die Abnahme des sensiblen Wärmeflusses zwischen den Helikopterdaten mit einer Auflösung von 1 m und den grober aufgelösten 1 km Daten hat eine lineare Beziehung mit dem Flächenanteil der Rinnen. Ein Vergleich zwischen den sich überlappenden Helikopter- und Satelliten-Eisoberflächentemperaturen von MODIS zeigt keine Übereinstimmung in der räumlichen Variabilität. Die Ergebnisse der Dissertation können dazu beitragen Parameterisierungen für Satellitenprodukte und Modelle zu verbessern.

Acronyms

CO	Central Observatory
DITB	drop-in-the-bucket
EM	electromagnetic
IR	infrared
FYI	first-year ice
MPF	melt pond fraction
MOSAiC	Multidisciplinary drifting Observatory for the Study of Arctic Climate
MODIS	Moderate Resolution Imaging Spectroradiometer
MYI	multi-year ice
NSIDC	National Snow and Ice Data Center
RGB	Optical orthomosaic
RISE	Responsible Science Initiative
RL	refrozen leads
SAR	Synthetic Aperture Radar
SHEBA	Surface Heat Budget of the Arctic Ocean
SYI	second-year ice
TIR	thermal infrared
TC	topography controlled
WMO	World Meteorological Organization
YI	young ice

Contents

Chapter 1

Introduction

This chapter is divided into four sections. In Section 1.1, this thesis is motivated by looking at the big picture of Arctic sea ice research with a focus on the changing sea ice (Subsection 1.1.1) and the importance of the Arctic heat budget (Subsection 1.1.2). Also, the MOSAiC expedition (Subsection 1.1.3), the relevance of different Arctic observation methods (Subsection 1.1.4), and the potential of thermal infrared (TIR) imaging (Subsection 1.1.5) are described. Following, the aims of this thesis, including four research questions (Section 1.2), the thesis structure (Section 1.3), and the publications of this thesis (Section 1.4) are presented.

1.1 Motivation

I have the greatest respect for the pioneers of Arctic research who did valuable work on which the researcher build on today. As one example of many, I would like to name Fridtjof Nansen, who had an exceptional understanding and courage to make a challenging expedition. He was analyzing the sea ice drift and using the Transpolar Drift for his Arctic expedition 1893–1896 to reach the North Pole.

The Arctic Ocean is a deep basin with a depth of up to a few kilometers, covered by an comparable very thin layer of sea ice that is critical for the Arctic climate system. Seeing the present Arctic with my own eyes made me concerned about the future changes. My curiosity about the state and processes of the Arctic sea ice motivated me to conduct the research presented in this thesis.

The Arctic climate is a complex and fascinating but also fragile system. The Arctic sea ice, i.e., the thinning and shrinking of its extent, has changed faster in recent decades than in the past (Meredith et al., 2019). These changes are expected to continue towards a seasonally ice-free Arctic around the mid-century, as shown in future simulations (Notz and Community, 2020). The vanishing sea ice in the Arctic Ocean is expected to have various effects, including an increased availability of shipping routes and resources (e.g.,

Deser et al., 2010). The ongoing changes also have an impact on the people who live in the Arctic region and, therefore, are heavily influenced by the changing Arctic climate (e.g., Deser et al., 2010).

The Arctic climate system can be imagined as a puzzle with many puzzle pieces. Each study adds one puzzle piece to make the overall picture clearer, better understandable, and may even reveal new connections. This thesis presents the application of helciopter-borne TIR imaging for a new understanding of sea ice characteristics during winter in the central Arctic and adds a few new puzzle pieces. Before diving into the new results, this section describes the big picture of the Arctic climate system, i.e., the puzzle pieces which are already put together, to set the scene for the new results presented in this work.

Studying the winter properties of sea ice is especially important during the current changing climate, which is emphasized in the Arctic (Subsection 1.1.1). The accelerated warming of the high northern regions is called Arctic Amplification (Serreze et al., 2009). While sea ice has manifold interactions with the ocean beneath and the atmosphere above, the focus of this thesis is on the surface temperature, i.e., the interface between the sea ice or snow and the atmosphere as well as its relevance for the Arctic heat budget (Subsection 1.1.2). To investigate the detailed processes of Arctic sea ice, observations are crucial. They are performed with satellite remote sensing, airborne campaigns, or in-situ measurements (Subsection 1.1.4). Airborne and in-situ observational methods were performed during the year-long Multidisciplinary drifting Observatory for the Study of Arctic Climate (MOSAiC) expedition in the Arctic Ocean (Subsection 1.1.3) and build a valuable interdisciplinary year-long dataset. The primary dataset of the thesis are surface temperature maps, based on helicopter-borne TIR imaging, which has a high potential to investigate the small-scale variety (order of meters) of sea ice properties (Subsection 1.1.5).

1.1.1 The changing Arctic sea ice

Changes in sea ice can have significant impact on the Arctic climate, including changes in temperature, oceanic and atmospheric circulation, and ecosystem dynamics, as well as potential feedbacks to the global climate. The study by Rantanen et al. (2022) showed that the near-surface air temperature in the Arctic is increasing up to four times faster than in the rest of the Earth. This Arctic Amplification makes the changing climate even more emerging in the future Arctic. The amplified warming goes along with the retreat of sea ice, which is potentially seasonally disappearing in the Arctic, while it is, as written above, a crucial component of the puzzle.

This thesis focuses on the sea ice component in the Arctic climate system. The ocean, atmosphere, and sea ice have interconnections and feedback processes that make the Arctic climate a complex system (e.g., Previdi et al., 2021; Wendisch et al., 2023). Sea ice plays a

vital role in the global climate system by reflecting sunlight during summer and regulating heat and moisture exchange between the ocean and the atmosphere. It also provides a habitat for a variety of marine animals, including seals, polar bears, and some species of birds (Laidre and Regehr, 2017). Thus, there are implications for the ecosystem (see below).

Looking at the sea ice extent as the most known indicator of the sea ice state, there is a decline within the last decades (Figure 1.1). Holland et al. (2006) found that there is a potential for a rapid sea ice retreat during the Arctic summer, which might be influenced by increased ocean heat transport into the Arctic. Additionally, the warming during Arctic winter is at least four times stronger than during summer (Bintanja and Van Der Linden, 2013). There is a faster decline of winter sea ice during recent years (2000 onwards) compared to the years 1979–1999 (Stroeve and Notz, 2018). Since the sea ice is thinning, there is an even stronger signal in the sea ice volume combining the decrease of extent and thickness.

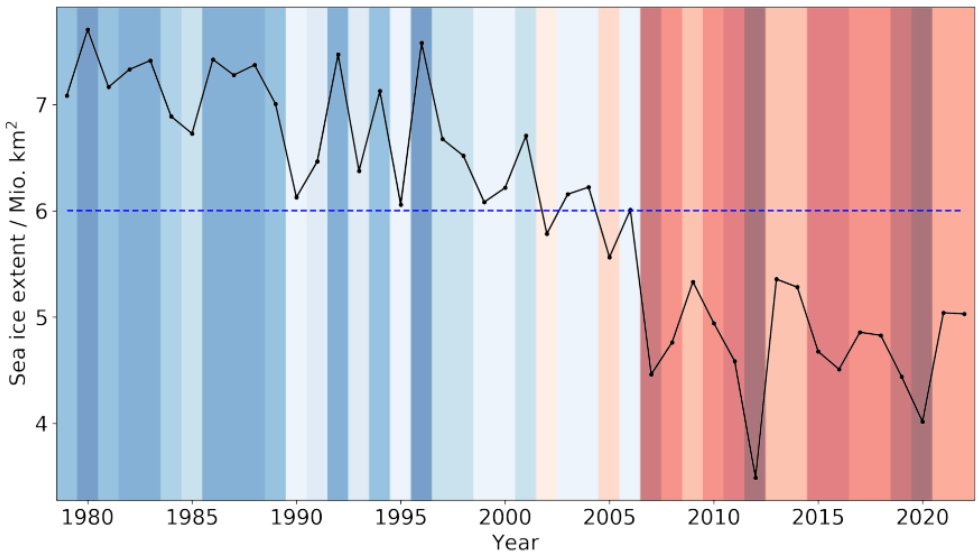

Figure 1.1: Arctic sea ice extent in September between 1979 and 2022[1]. The blue dashed line shows the average for the full time series. The divergent colors represent the positive (blue) or negative (red) difference to the mean for each year. Please note that the scale on the y-axis does not start at zero. The visualisation of the colors is inspired by the initiative *ShowYourStripes* (https://showyourstripes.info/s/globe).

Also, the age distribution of sea ice is changing towards younger ice (Stroeve et al., 2012). Sumata et al. (2023) found that with the transition in 2007 the Arctic sea ice has

[1]Sea ice concentration data from 1979 to 2022 were obtained from https://www.meereisportal.de (grant: REKLIM-2013-04).

a thinner and uniform ice state and the thinning of sea ice is a result of the reduction of its residence time. The proportion of the multi-year ice (MYI) (Subsection 2.2.1) is decreasing while the remaining first-year ice (FYI) has different sea ice properties. The ice properties influence the processes in, under, and above the sea ice. The younger and thinner ice is more sensitive, especially to atmospheric effects like the ice-albedo feedback (Perovich et al., 2011; Serreze et al., 2009) or the wind forcing (Spreen et al., 2011), which can cause a higher variability in the sea ice extent (Stroeve et al., 2012). Also, the thinner ice pack becomes more mobile with an increased drift speed (Kwok et al., 2013) and more vulnerable to ice dynamics which results in leads with open water or thin ice (e.g., Shokr and Sinha, 2015). However, based on TIR satellite data, Willmes and Heinemann (2016) and Willmes et al. (2023) found no trend in the lead fraction for the period 2002–2021.

Resulting from the smaller sea ice ice extent, the larger open water area allows more heat absorption during summer through solar radiation (Stroeve et al., 2014). The smaller sea ice cover at the end of the melt season (01 October 2019) and the advanced sea ice cover six months later on 01 April 2020 are shown in Figure 1.2 as it represents the Arctic sea ice conditions during the MOSAiC expedition from which the here presented data are (Subsection 1.1.3). While the melting season in the central Arctic is only 2.5 months long, there is a lengthening of the melt season of 4 to 5 days per decade (Stroeve et al., 2012, 2014). Simulating the future evolution of sea ice reveals an accelerated decrease of the September sea ice extent (Stroeve et al., 2012). Thus, there is a need for a better process understanding which can be incorporated into climate models. Predicting the future Arctic climate has relevance for stakeholders and is a key aspect of policies for the Arctic region (Pörtner et al., 2022).

The Arctic winter

Observing the Central Arctic during winter can be challenging due to continuous darkness and harsh conditions. Nevertheless, as presented in this thesis, the MOSAiC expedition (Subsection 1.1.3) successfully conducted winter observations. An example is discussed for a location in the central Arctic that corresponds to the location of the MOSAiC expedition on 21 January 2020, the day for the case study in Chapter 4. ERA5 data of a fixed location are used to exclude the spatial drift and provide a complete time series for the MOSAiC expedition. Detailed meteorological information for the MOSAiC drift can be found in Rinke et al. (2021). The Arctic experiences significant seasonal differences between summer and winter, owing to the transition between polar night and polar day (Figure 1.3). Despite these differences, the seasons are strongly interconnected, with winter ice growth shaping the sea ice basis for summer melt and summer melt setting the starting conditions for winter sea ice growth, with crucial transitions in spring and autumn. The transition between polar night and day causes large differences in air and

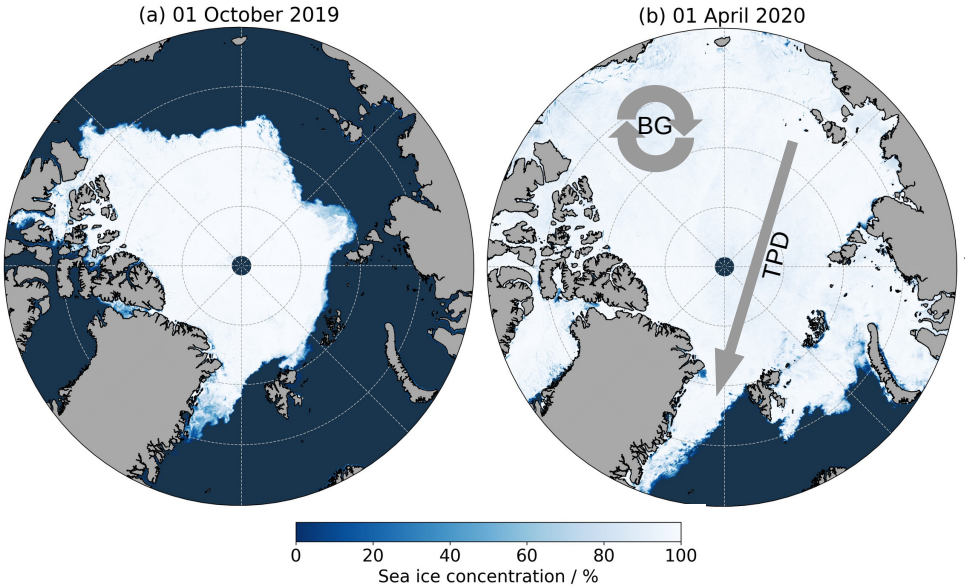

Figure 1.2: Arctic sea ice concentration at one 1 km resolution from the merged sea ice concentration product[2](Ludwig et al., 2019). The sea ice cover for the two days: (a) 01 October 2019, and (b) 01 April 2020 as examplary dates for low and high sea ice extent during the MOSAiC expedition. In (b) the typical flow pattern Transpolar drift (TPD) and Beaufort Gyre (BG) is displayed.

skin temperature with more than 20 K (for the running mean) (Figure 1.3 (a)). The skin temperature during mid-winter and summer is slightly lower due to the longwave radiative cooling (winter) and the limitation at the melting point of the ice (summer). The radiative cooling is represented by the negative net longwave radiation, which is most prominent during winter (Figure 1.3 (b)). The net shortwave radiation is zero during winter but the dominating component during summer. Processes dependent on solar radiation, such as photosynthesis or surface melt, are much reduced during to winter. Also, the latent heat flux is close to zero during winter because of the lack of humidity. The sensible heat flux has the largest magnitude during winter due to the strong temperature contrasts between the atmosphere and the ocean; going from the warmer ocean to the colder atmosphere (here negative upward flux). Winter is the period for Arctic sea ice growth, driven by the heat loss from the warmer ocean to the colder atmosphere (Subsection 2.2.4). The growing sea ice and its snow cover act as a blanket for the Arctic Ocean, significantly dampening heat exchange.

[2]We thank the Institute of Environmental Physics, University of Bremen for the provision of the merged Moderate Resolution Imaging Spectroradiometer (MODIS)-AMSR2 sea-ice concentration data at https://data.seaice.uni-bremen.de/modis_amsr2 (last access 06 April 2023).

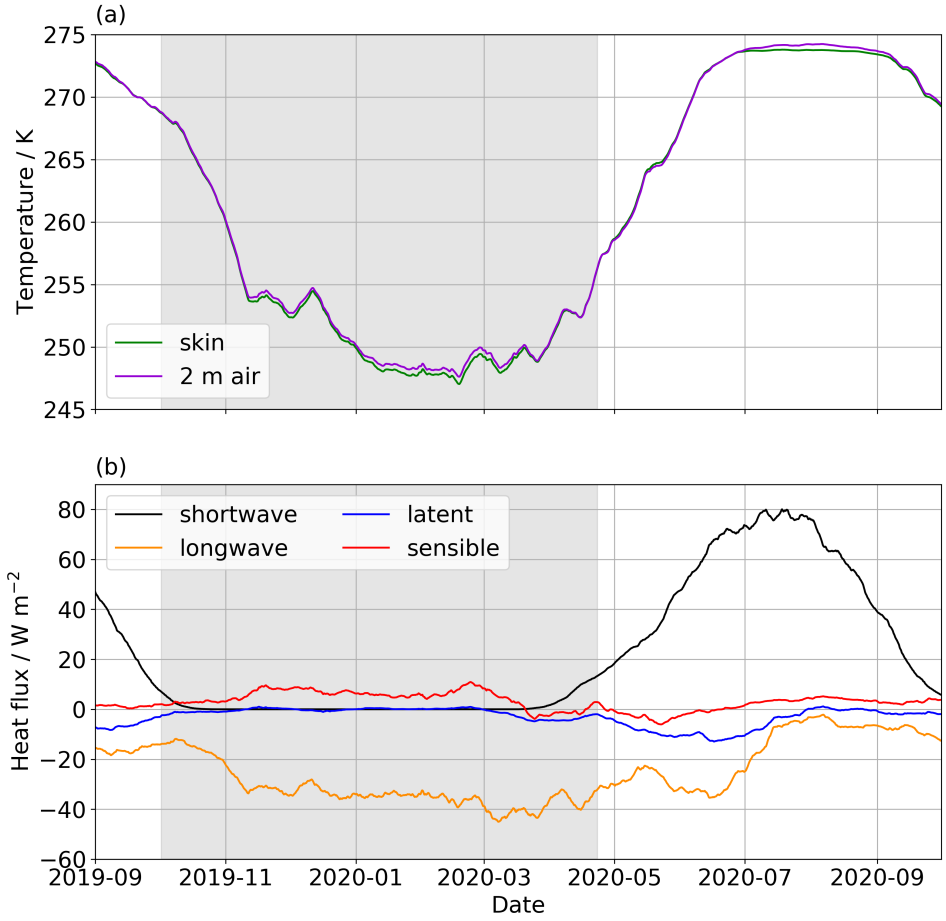

Figure 1.3: Seasonal evolution of Arctic (a) 1 m air and skin temperature and (b) heat flux components: net shortwave, net longwave, latent, sensible (here downward fluxes are considered positive). The 30 days running mean is shown to exclude the daily variations. The data are at the location of RV *Polarstern* during a MOSAiC helicopter flight on 21 January 2020 (96.12087°N; 87.48890°E); used in Chapter 4. The shaded area indicates the period of the presented helicopter flight. The data are taken from ERA5[3](Hersbach et al., 2023).

The role of the ocean and the atmosphere

This Subsection highlights selected aspects, first for the ocean and then for the atmosphere, because of their interconnection to Arctic sea ice processes. Sea ice floats in the Arctic Ocean and has an interface with the Arctic atmosphere at the snow or sea ice surface. During winter, the sea ice creates a layer on the ocean surface with an insulating effect. Then the sea ice melts in the summer, exposing the ocean surface to the atmosphere and causing the ocean to warm up, which is emphasized by the retreat of the sea ice cover.

[3]The ERA5 hourly data was downloaded from the Copernicus Climate Change Service (C3S) (2023).

The connection between oceanic, sea ice, and atmospheric processes in the Arctic climate is complex and interdependent. Key processes connecting these components are the heat, moisture, and momentum exchange.

The Arctic Ocean is up to 4500 m deep and mostly surrounded by land. Water enters the Arctic Ocean primarily through Fram Strait and Barents Sea (Atlantic water transported by the Atlantic Meridional Overturning Circulation, AMOC), and through Bering Strait (Pacific water) (Rudels, 2009). The incoming water gets colder and denser (Rudels, 2009), which drives the ocean circulation. The fresher and colder outflow happens through the Canadian Arctic Archipelago and Fram Strait (Rudels, 2009), while the outflow also exports sea ice out of the Arctic Ocean towards lower latitudes (Rampal et al., 2009; Spreen et al., 2011) where it eventually melts. The sea ice and the surface waters within the Arctic Ocean move along two main flow patterns: the Beaufort Gyre and the Transpolar Drift Stream, illustrated in Figure 1.2 (b) (Rudels, 2009; Timmermans and Marshall, 2020). The Beaufort Gyre follows the prevailing anticyclonic (clockwise) wind pattern while there is a persistent polar High.

The exchange of heat, moisture, and momentum is constrained to the upper 50–100 m of the Arctic Ocean (Rudels et al., 1994) due to a strong vertical stratification. Through sea ice or melt water, there is fresher water on top of the saltier water. In the Arctic, there is an increase in salinity by brine rejection in the freezing process of sea water. The resulting halocline insulates between the deeper and warmer Atlantic water (400–700 m according to Rudels (2009)) and the surface (Korhonen et al., 2013). In the European Basin of the Arctic Ocean, the influence of Atlantic waters is becoming more pronounced (e.g., Ingvaldsen et al., 2021), a phenomenon known as Atlantification that is related to the changing climate. As one effect of the Atlantification the sea ice in the Barents Sea is retreating to the north, leading to increased vertical mixing of the upper ocean (Polyakov et al., 2017). Polyakov et al. (2020) describes a weakening of the halocline and a positive feedback process: less sea ice cover allows for increased mixing that weakens the stratification of the upper ocean and enables more heat release. The increasing heat fluxes from the Atlantic heat below the halocline to the surface has potential to melt sea ice (Timmermans and Marshall, 2020). The additional heat can be also transferred to the atmosphere (Steele et al., 2008).

An increasing freshwater input in the recent years, related to global warming, comes from precipitation, river runoff, and melt impacts ocean processes by increasing stratification (e.g., Haine et al., 2015; Timmermans and Marshall, 2020), which can hinder the vertical exchange of gases, moisture, and heat (e.g., Stroeve and Notz, 2018). Concerning these processes, Timmermans and Marshall (2020) discuss the potential of the two different processes: on the one hand, more mixing by momentum input from wind in the

new open water areas; on the other hand, stratification strengthening through freshwater input from the melt. Moreover, anthropogenic emissions have led to more carbon dioxid from the atmosphere being dissolved in the ocean, causing acidification that affects marine chemistry and ecosystems (Terhaar et al., 2020; Kwiatkowski et al., 2020).

The atmospheric anthropogenic carbon dioxide causes warming, resulting in an increased air temperature. In the lowest layer of the atmosphere, there is a strong coupling between air temperature and surface temperature (Vihma and Pirazzini, 2005), connecting the atmospheric changes to the sea ice or snow surface. Warmer air temperatures can cause a transition from snow to liquid precipitation. Also, there is a moistening in the Arctic across all seasons (e.g., Wendisch et al., 2023) since warmer air can hold more humidity. The increased humidity leads to an increase in cloudiness (Wang and Key, 2003; Vavrus, 2004). However, the understanding of clouds remains challenging in a coupled Arctic climate system (e.g., Wendisch et al., 2023). They are important for the radiation transfer by trapping the outgoing longwave radiation (winter and summer) or shielding the incoming shortwave radiation (summer) (Maykut and Untersteiner, 1971; Perovich et al., 1999) and, therefore, alter the sea ice growth or melt (Maykut and Untersteiner, 1971; Curry and Ebert, 1990).

Also, there is a trend of increasing number of cyclones which alter the sea ice (e.g., Valkonen et al., 2021). The cyclones coming into the Arctic, mostly connected with warmer temperatures, precipitation, and high winds, alter the sea ice conditions by, e.g., changing the surface properties with consequences for satellite retrievals. During the MOSAiC expedition, two events, among others, were investigated: a warming event in April 2020 (Rückert et al., 2023) and a rain on snow event in September 2020 (Stroeve et al., 2022). Both events influenced the satellite retrieval by altering the snow and sea ice properties.

Implications for the ecosystem

Focussing on the Arctic ecosystem, thinner ice and a higher fraction of open water favors an increased primary production (Arrigo and van Dijken, 2015) and early phytoplankton blooms due to more light input (Assmy et al., 2017), that can cause again more absorption of the solar radiation (Goosse et al., 2018) leading to a warmer upper ocean. The warmer ocean expanding to the north allows for the migration of new fish species. With the Atlantification, not only the northward transport of heat but also the transport of nutrients and planktonic organisms is amplified (Oziel et al., 2020). It favors the transition to more temperate Arctic ecosystems creating a biological driver for the movement of southern species (Oziel et al., 2020). Those ecosystem components, which are specialized for the Arctic conditions, have challenges adapting to the rapid changes. Additionally, the acidification of the ocean is challenging marine organisms (Terhaar et al., 2020). Fur-

ther, the reduction of the resolved oxygen is observed, which is harmful to marine species (Kwiatkowski et al., 2020).

Effect on the mid-latitudes

Writing this thesis in Germany, I am curious in how much the changes in the Arctic influence the mid-latitudes. Due to the amplified warming of the Arctic, the temperature contrast between the mid-latitudes and the Arctic, i.e., the meridional gradient is decreasing. Following, the jet stream could weaken (detailed summary of the processes in Cohen et al. (2020)). Vihma (2014) states that there is a potential for a connection between the decline of the sea ice and cold winters in the mid-latitudes. Still, current studies could only find weak relations (Blackport et al., 2019; Cohen et al., 2020) and could not find a connection to the reduction of sea ice (Blackport et al., 2019). Observations suggest a link between the Arctic Amplification and more persistent weather patterns in the mid-latitudes (Francis and Vavrus, 2012), while models rarely replicate this pattern (Blackport et al., 2019; Cohen et al., 2020).

1.1.2 The importance of the Arctic heat budget

"The surplus heat needed to explain the loss of Arctic sea ice during the past few decades is on the order of 1 W m^{-2}. Observing, attributing, and predicting such a small amount of energy remain daunting problems."
Kwok and Untersteiner, 2011, Physics Today

The flux difference of $1\,\mathrm{W\,m^{-2}}$ is comparable to a thinning of sea ice by about $0.1\,\mathrm{m\,yr^{-1}}$ (Kwok and Untersteiner, 2011). Kwok and Untersteiner (2011) name challenges, like the accuracy of the measurements which do not meet the order of magnitude of $1\,\mathrm{W\,m^2}$ or missing information about processes like lateral melt of sea ice. Their results show that the ice thickness can be strongly altered by small changes in the heat content. Besides the described atmospheric warming, the heat input from the ocean might be changed due to the Atlantification and a different mixing by more wind energy input or more freshwater availability (Subsection 1.1.1). Already in Subsection 1.1.1, it is described that there is more heat absorption in the upper ocean for a shrinking sea ice extent. Furthermore, the thinner ice and smaller sea ice area reduce the Arctic sea ice's role as a blanket for the Arctic Ocean (less insulation). Thus, stronger interaction occur between the ocean, the ice and snow, and the atmosphere (Hansen et al., 2005), as well as the increase of the heat fluxes. Projections from the Community Earth System Model version 1 Large Ensemble (CESM1-LE) show future increasing ocean heat flux towards the atmosphere caused by reducing ice thickness and snow depth (Landrum and Holland, 2022). This has several implications, like a more unstable atmospheric boundary layer in fall and early winter.

Further, the sea ice loss could add a radiative forcing from solar radiation, that can be estimated based on satellite data (Pistone et al., 2019). The set of the vertical heat fluxes for winter and summer are displayed in Figure 1.4. The shortwave radiation is only relevant during summer, and the longwave radiation can be influenced by clouds. Moreover, the turbulent sensible and latent heat flux transports heat at the snow-atmosphere interface (ocean-atmosphere if no sea ice and snow is present). The conductive heat flux describes the heat transfer through the snow and ice pack. The ocean fluxes influence the processes at the ice-ocean interface, e.g., ice growth. Details and background information about the physical process determining the Arctic heat budget, particularly the various heat fluxes, are presented in Subsection 2.2.4.

The expedition Surface Heat Budget of the Arctic Ocean (SHEBA) was conducted in 1997/1998 to gain a better knowledge of the Arctic heat budget, which resulted in novel findings that were also essential for modeling purposess (Uttal et al., 2002). According to Cao et al. (2019), there is still a need for more investigations due to insufficient understanding of the sea ice heat budget. Here, the MOSAiC expedition (Subsection 1.1.3) can add data and knowledge from more recent measurements providing a large suite of interdisciplinary observations. Collaborations such as the winter heat budget group (Section A.3) use a large set of observations for heat budget calculations. The heat budget is sensitive to changes in various parameters, such as sea ice extent (Cao et al., 2019). Thus, the context of the single observations is critical. Another essential factor in accurately representing the heat budget is the snow cover, which has complex and heterogeneous properties, e.g., snow depth and thermal conductivity (e.g., Huwald et al., 2005; Shokr and Sinha, 2015). The generally high spatial variability of snow and ice makes it difficult to create a representative dataset for model simulations (Huwald et al., 2005). Climate and weather prediction models rely on a good representation of the heat budget of sea ice (Lüpkes et al., 2008).

The role of leads

As the sea ice is thinning, it becomes more sensitive to ice dynamics. Following, more leads could be created. Especially in the winter season, leads are fundamental for the heat exchange between the ocean and the atmosphere (Alam and Curry, 1995). However, Willmes et al. (2023) did not see an increase in the lead frequencies for 2002-2021, only a high inter-annual variability. Over leads, surface temperatures can be up to 40 K warmer (e.g., Lüpkes et al., 2008; Marcq and Weiss, 2012) and cause an increase in sensible heat flux of up to 2 magnitudes (Maykut, 1978). The scheme in Figure 1.5 illustrates the heat exchange for lead areas (open water or thin ice) in contrast to the snow-covered thick ice. The resulting heat flux is largest in winter when no clouds are present, and the temperature contrast between snow/ice and open water is largest (Lüpkes et al., 2008). In this thesis

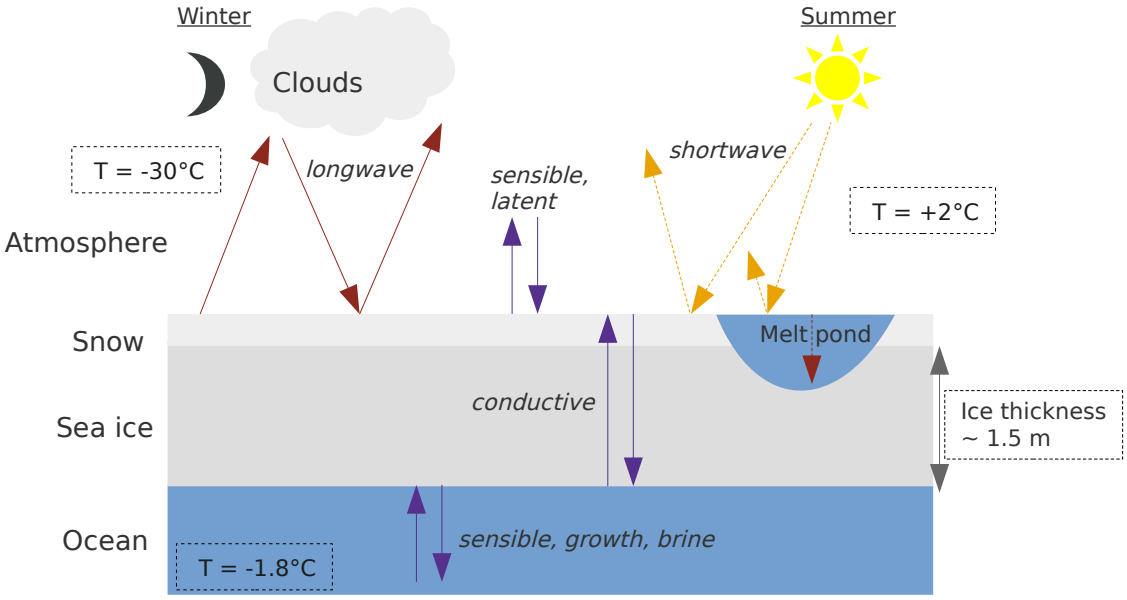

Figure 1.4: Simplified scheme of the vertical heat fluxes for snow-covered sea ice, discriminated for winter (left) and summer (right). During winter there is a much lower air temperature than summer and compared to the ocean temperature. Typical values, also for the ice thickness, and names of the fluxes are displayed in the Figure.

helicopter-borne data are used, which are mostly recorded during clear-sky conditions. Only a small fraction of leads (1%) can strongly influence the heat flux of the given area and alter the stability of the lower atmosphere (Maykut, 1978). Lüpkes et al. (2008) shows that the reduction of 1% in ice concentration (increase in lead fraction) can cause an atmospheric temperature signal of 3.5 K which illustrates the strong sensitivity to the lead fraction, an important parameter that is discussed in Chapter 5. However, observations of leads are difficult to perform in the field because, e.g., no instruments can be directly placed on the lead. Due to the strong ocean heat loss in winter, leads are important areas of fast ice growth (Maykut, 1982). Small leads are important because narrow leads have a stronger temperature gradient which can cause more enhanced exchange over smaller width (Alam and Curry, 1995; Marcq and Weiss, 2012). Interestingly, a model study by Li et al. (2020) shows that leads do not necessarily result in more humidity in the lower atmosphere. They found that leads are quickly covered with thin ice, particularly in winter. This allows the exchange of sensible heat but hampers the moisture transport. Due to the heat exchange, the preferably stable boundary layer becomes more turbulent.

1.1.3 The MOSAiC expedition

This thesis is based on data from the MOSAiC expedition (https://mosaic-expedition.org/). The MOSAiC expedition was the largest Arctic expedition, that took place from

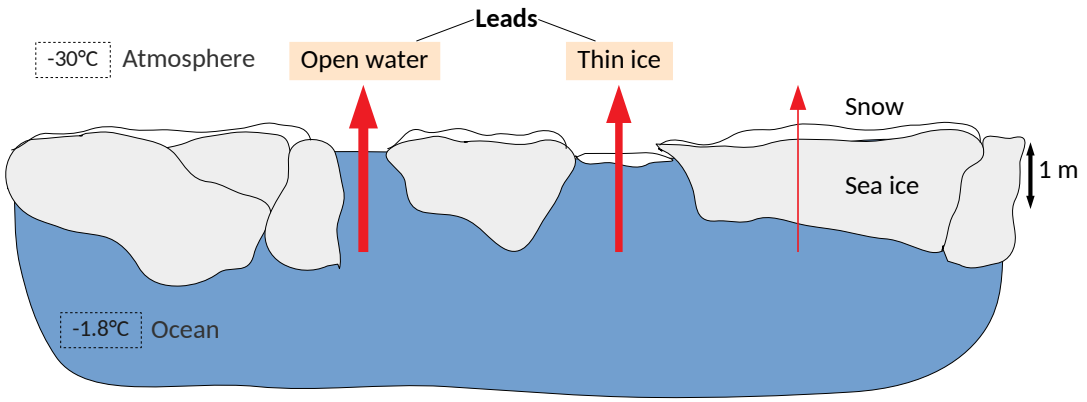

Figure 1.5: Scheme illustrating the increased heat exchange (red arrows) through leads (open water or thin ice) compared to snow-covered thick ice. This winter case has a heat transfer from the much warmer ocean to the colder atmosphere.

September 2019 to October 2020. This expedition was motivated by the Fram Expedition led by Fridtjof Nansen from 1893 to 1896 along the Transpolar Drift. The international expedition with a team of over 600 scientists included a year-long interdisciplinary measurement program studying physical, chemical, and biological processes (Nicolaus et al., 2022; Rabe et al., 2022; Shupe et al., 2022). The main goal of MOSAiC is to study the Arctic climate system and its interactions with the Earth's atmosphere, oceans, and biosphere, focusing on the role of sea ice. A Central Observatory (CO), an ice floe as the main measurement site for this expedition, was located within a few kilometers of RV *Polarstern*, which was frozen in the sea ice and served as the central reference point. Within the CO there was a high amount and density of various measurement sites for many different parameter. In addition, a network of buoys and measurement stations was installed a few tens of kilometers away from RV *Polarstern* to monitor sea ice conditions, among other Arctic components. The drift of RV *Polarstern* started in the Northern Laptev Sea and continued through the Central Arctic towards the Fram Strait. The expedition was performed in five phases, called legs. For the last part of the expedition (leg 5) a new CO had to be set up in the Central Arctic because the previous floe was broken apart.

The vast data collection is a basis for scientific research for many more years, representing the "New Arctic" in a changing climate. The expedition generated a wealth of data and insights that will be used to improve models of the Arctic climate and, in the long term, to inform policy decisions related to the region. From the close collaborations in the field and from the collaborations afterward, many cross-cutting science projects evolved. One example is the winter heat budget group that involves many members from different disciplines, described in the Appendix, Section A.3.

The results of this thesis focus on the winter months (October 2019 to April 2020, leg 1–3). I participated in the fifth leg of the expedition (August–October 2020) by supporting mainly the on-ice remote sensing measurements (contributions listed in the Appendix, Section A.1). From my work during the expedition, I had contributions to other scientific studies (listed in the Appendix, Section A.2).

1.1.4 Observing Arctic sea ice

In this work, helicopter-borne surface temperatures at 1 m resolution are analyzed. However, the high spatial resolution of 1 m has a limited spatial extent restricted to a few kilometers. For the operational daily pan-Arctic observations, among others, TIR satellite-based applications are used but limited to the spatial resolution of 1 km. Thus, more detailed measurements are essential for a better process understanding and validation of the satellite products, which can be used to investigate the Arctic-wide scale on a daily basis. With high-resolution observations small-scale features can be studied because small-scale leads that are very efficient in heat exchange (Marcq and Weiss, 2012), or small changes in sea ice concentration that can cause a significant increase in the air temperature (Lüpkes et al., 2008).

The central Arctic, where this thesis' measurements are located, is remote and difficult to access. Thus, in-situ observations are rare, particularly during winter, and satellites are the common observation tool for Arctic sea ice. Besides the presented TIR applications, several other methods like visual imaging or microwave remote sensing are applied. TIR is very valuable in the polar night due to large temperature contrast, while visual observations can be only used when light is available. However, TIR and visual methods are affected by clouds. Microwave remote sensing can observe the surface through clouds and is independent of daylight but have a comparable low spatial resolution (except for Synthetic Aperture Radar (SAR)). Satellite-based observations can provide, depending on the method, information about various parameters at different horizontal resolutions. There are, e.g., sea ice concentration from AMSR (Advanced Microwave Scanning Radiometer) (6.25 km res.) (Spreen et al., 2008), thin ice thickness from SMOS (Soil Moisture and Ocean Salinity) (Huntemann et al., 2014) (40 km res.), ice classification from Synthetic Aperture Radar (SAR) (3.5 m res.) (Kortum et al., 2022), melt pond fraction from Sentinel-2 (10 m res.) (Niehaus et al., 2023), or lead fraction from MODIS (1 km res.) (Willmes and Heinemann, 2016). There are advances by combining different remote sensing methods, e.g., creating 1 km resolution sea ice concentration by merging TIR and passive microwave data (Ludwig et al., 2020). Satellite-based observations are often used as model input as they provide near-real-time observations and cover the evolution over a longer period (Kwok and Untersteiner, 2011). Thus, a good quality of the retrieved physical parameter is crucial. On the intermediate scale, airborne measurements can bridge

between the in-situ and satellite-based observations, for example, Operation IceBridge (Studinger et al., 2010) or the here included helicopter-borne program during MOSAiC.

In-situ observations require a lot of resources and effort to collect datasets and measurements at a specific location, are limited in time but are essential for the detailed process understanding. Examples are the AIDJEX (Arctic Ice Dynamics Joint Experiment) (Bjornert, 1975), the LeadEx (Lead Experiment) (LeadEx Group, 1993), SHEBA (Uttal et al., 2002), and the recent MOSAiC expedition (Subsection 1.1.3). Since there are only occasional in-situ observations, other observing methods are required. Also, the local measurements might not be representative for the large extent of the Arctic sea ice (Maykut, 1982; Zakhvatkina et al., 2019). Moreover, the interpretation of spatially restricted measurements is challenging because of the complexity of the processes (Maykut, 1982).

On the one hand, in-situ observations are important for the process understanding of the remote observations (airborne or space-borne). On the other hand, the remote observations have an added value to put in-situ observations into context. All in all, different types of measurements on varying scales are required to analyze various processes. This is needed for a better representation of the processes in climate models.

1.1.5 Potential of thermal infrared images

TIR imaging is a technique that uses a specific type of camera, measuring the thermal radiation emitted by objects. These cameras are sensitive to TIR spectrum with wavelenght around 10 μm.

TIR imaging is used in a variety of applications, including scientific observations of the thermal signatures of the Earth's surface, such as vegetation, animals, and humans (especially in low light conditions), industrial inspection, and security in the event of, e.g., overheating. In the here presented measurement setup, TIR imaging was performed from a helicopter, capturing the sea ice surface.

This work is based on the composite of the TIR images, i.e., georeferenced surface temperature maps of full helicopter flights (Chapter 3). In this part, I highlight single TIR images, which consist of detailed information on the sea ice surface and have large potential for further studies concerning the spatial variability of surface temperatures. These examples motivate selected cases to show the potential of the images, but do not present specific results. My collection of the eight images are presented in Figure 1.6, recorded between 19 November 2019 and 23 April 2020. In the images, the blue colors indicate relatively low temperatures (thick ice with snow cover), and the red colors are relatively high temperatures, primarily represented in leads. Please note the different

spatial scales (dependent on angle and altitude of the camera), and different temperature ranges, chosen to have the most details visible.

The images (a) and (f) show local cold spots, which could be snow accumulation causing higher insulation. For image (f), on 28 January 2020 the cold spots are quite distinct. On 19 November 2019 (image (a)), the structures are a bit blurry and have warmer temperatures on one specific site. This could be due to snow drift from the storm event that occurred in the days preceding the image acquisition. At the obstacles for potential snow accumulation, the wind could have blown away at one side and created warmer surface temperature due to the missing insulation from the snow. Also, the more elongated cold features in the middle of the images are caused by snow drift. A similar but less distinct snow drift can be seen in image (f). At this time, there was a calm weather period and, therefore, not much snow transportation.

For image (b), I would like to keep the focus on the lower horizontal lead, which includes some colder blurry structures. The surface temperatures are well below the freezing point. Thus, the lead is already frozen. Due to still ongoing ice dynamics, ice rafting of the thin ice might caused this temperature structure. This means that ice is sliding on top of the other ice, creating colder surface temperatures by thickening the ice cover or having colder air between the thin ice.

Sea ice in the Arctic Ocean moves due to wind and ocean forces and can break into several pieces. Image (c), taken on 25 December 2019, nicely illustrates what small-scale sea ice fractures on a 500 m scale can look like. The cracks in the sea ice have different orientations and separate ice pieces of different sizes. This can be relevant for ice rheology.

In image (d), also taken on 25 December 2019, I would like to draw attention to the surface temperature pattern in the lead, which is already over-frozen due to the surface temperature well below the seawater freezing point. Unlike in image (b), the temperature anomalies are more aligned and warmer instead of colder. Based on the shape, there have probably been waves while freezing and conserving the wave pattern.

Leads are often highlighted in this Subsection as they are favorable for TIR imaging because of their large surface temperature contrast to the pack ice. In image (e) on 07 January 2020, the homogeneity in the upper part and the heterogeneity in the lower part illustrate how much the surface temperature structures can differ wihtin one lead. The vertically oriented lead has a width of up to 150 m with a uniform surface temperature at the top, indicating homogeneous ice growth. In the lower part, many ice floes of thicker ice (colder temperatures as in the surrounding of the lead) float in different sizes, introducing a high spatial variability of the surface temperature. Hence, single leads are not simple to interpret.

Image (g) includes colder linear structures, also over a refrozen lead. On 21 March 2020, at the MOSAiC site, the sun was already above the horizon. Thus, these linear colder structures could be a shadowing effect resulting in lower surface temperature in the shadowed regions. Also, because these features are long and thin this could represent single peaks in the ice surface topography. The length of the potential shadow is reasonable because the sun stands very low at this time of the year. This means also low solar intensity, which makes it unclear if the solar heating is already strong enough to increase the surface temperature so there is a shadowing effect.

The last image (h), recorded on 23 April 2020, shows stronger temperature effects from the solar radiation. For several elongated features, potentially ridges, there are lower temperatures throughout one side and warmer temperature along the other side. At this time of the year, the sun is already higher in the sky and thus does not cast such long shadows. Also, this is only valid for features at a specific orientation probably corresponding to the sun orientation. Further, the lead consists of a large variety of surface temperatures; the larger homogeneous light orange part is probably already covered with snow, while the warmer part is still breaking up or covered by very thin ice. Lastly, this image holds another interesting feature - the circular pattern roughly at the point (250,250) around an obstacle. The surface temperatures probably reflect wind-driven snow drift around this obstacle, which causes small temperature differences at the surface.

For several cases, the surface temperature seems to reflect the surface topography, influenced by different snow depth and ice thickness and therefore also alters the surface temperature. The comparison between the helicopter-borne surface topography and surface temperature is encouraged for future work as both observations were operated in parallel in the helicopter. Consequently, a joint analysis of both helicopter-borne observations is a valuable addition, as done in Chapter 4. Additionally to the presented images, three more single images and their features are discussed in Chapter 3.

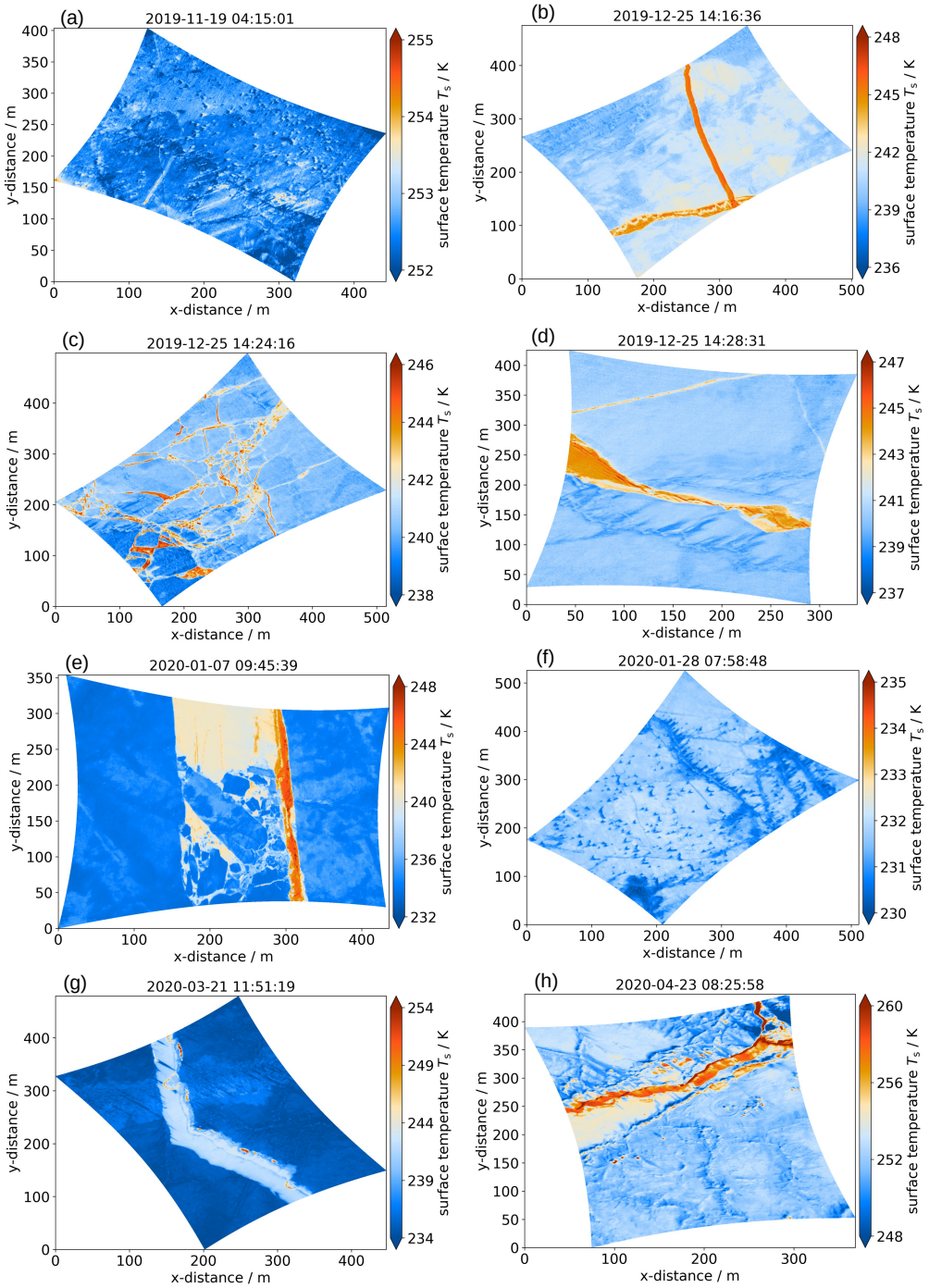

Figure 1.6: Selection of eight single TIR images showing cases of different small-scale features. The images are sorted chronologically with (a) 19 November 2019, (b,c,d) 25 December 2019, (e) 07 January 2020, (f) 28 January 2020, (g) 21 March 2020, (h) 23 April 2020. Please note that all images have different spatial scales (dependent on camera angle and altitude) and different ranges of temperatures associated with the colormap to make the features best visible.

1.2 Aims of the thesis

This thesis, "Winter sea ice characteristics in the central Arctic from thermal infrared imaging", strives to present findings based on high-resolution helicopter-borne data collected during the MOSAiC expedition in 2019 and 2020 (Subsection 1.1.3). This work focuses on a derived product: georeferenced surface temperature maps created from thousands of images taken during helicopter flights (presented in Chapter 3). For the first time, TIR imaging is used to this large extent to investigate small-scale properties of Arctic sea ice. Here, the small-scale is defined as surface characteristics in the order of a few meters, captured by surface temperature maps that have a horizontal resolution of 1 m.

The TIR imaging method has a considerable added value for winter observation since optical images are unavailable during polar night in the Arctic winter. The unique setup of the MOSAiC expedition, observing the same sea ice from autumn until summer, makes it possible to combine TIR observations in winter and visual imaging in summer to connect the sea ice conditions of both seasons (presented in Chapter 4). The low air temperatures during Arctic winter determine the surface temperature of snow and ice pack and cause a strong temperature contrast to the relatively warm ocean, which is kept at the freezing point of salty sea water (-1.8°C). The temperature differences allow a clear separation between leads (linear cracks in the sea ice) and the thicker sea ice, mostly covered with snow. Leads are formed by ice dynamics and covered by open water or thin ice. The data provide a novel dataset for the winter season on small spatial scales. Following, the lead properties are investigated and compared to previous studies (presented in Chapter 5). The knowledge on the smallest scales helps the understanding of the role of sub-footprint scale variability of operationally used TIR satellites. The aim is to compare the sensible heat flux (calculated from the surface temperature maps) and its spatial variability on the scale of a satellite footprint (1 km, results presented in Chapter 6).

Consequently, this thesis is based on four research questions:

R1 What is the potential of thermal infrared (TIR) imaging for the spatial analysis of sea ice during winter? [Chapter 3]

R2 To which extent do winter surface temperatures reveal information about the characteristics of melt ponds? [Chapter 4]

R3 What are the geometrical properties of leads on horizontal scales of meters? [Chapter 5]

R4 Do satellite surface temperatures sufficiently represent the sub-footprint scale variability of the sensible heat exchange? [Chapter 6]

1.3 Thesis structure

The structure of this thesis is displayed in Figure 1.7. In Chapter 2, the theoretical background for the content of this thesis is presented, focusing on the radiative transfer in the TIR spectral range as well as sea ice physics with a focus on the Arctic heat budget. This is followed by a description of the data and methods used in this thesis (Chapter 3) providing surface temperature maps as the key dataset of this thesis. Chapter 4 presents a case study of a comparison between a winter surface temperature map and a summer visual map, which explains the preconditioning of melt ponds in winter. The small-scale leads are analyzed in the subsequent Chapter 5 based on the surface temperature variability for the whole MOSAiC winter 2019/2020. This motivates the investigation of the sub-footprint scale variability of TIR satellite surface temperatures based on the high-resolution helicopter-borne surface temperatures presented in Chapter 6. In the final Chapter 7, I present the key findings by answering the research questions (R1–R4). The thesis is closed with a short summary an outlook of the future possibilities building on the findings of this thesis.

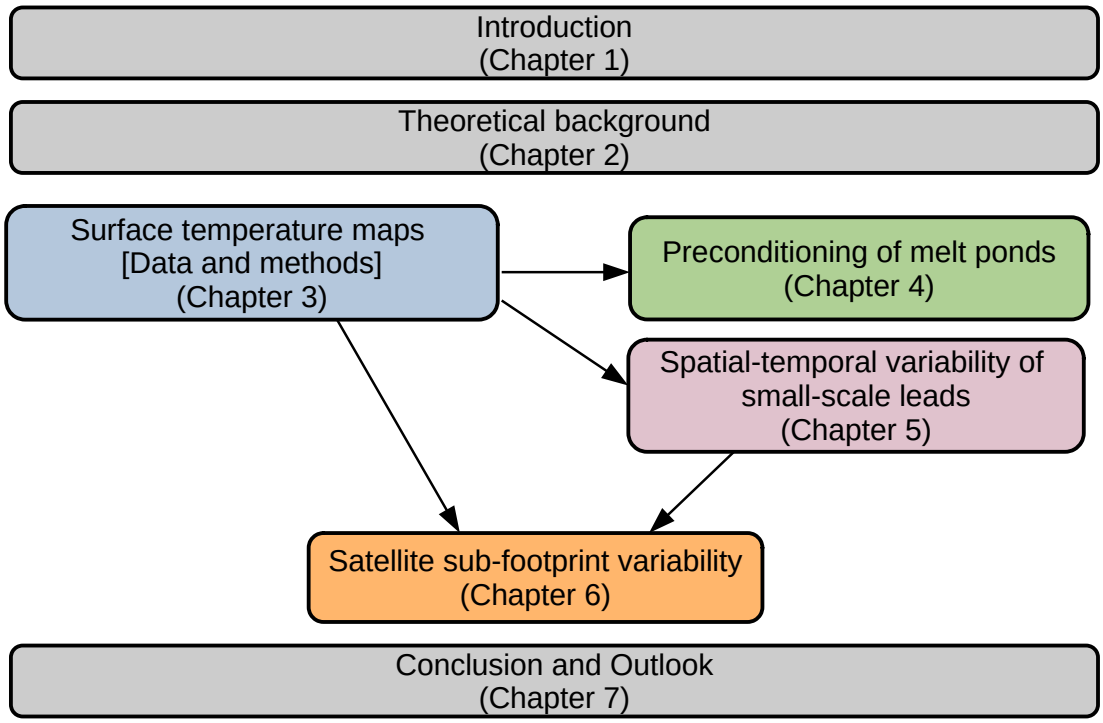

Figure 1.7: Scheme of this thesis' structure. Introduction, Theoretical background, as well as Conclusion and Outlook (gray) provide overarching information. Chapter 3 includes the description of data and methods which provides the dataset for the Chapters 4, 5, and 6. Chapter 5 also contributes to Chapter 6.

1.4 Publications in the thesis

This section lists the publications that are included in this thesis. Chapter 3 is based on publication (P1) presenting the data, methods, and technical validation. This publication resulted in the surface temperature data publication (D1) (images, maps in 1 m and 5 m resolution). The publication (P2) is a case study about melt pond preconditioning and is included in Chapter 4. Furthermore, small-scale leads are investigated in Chapter 5, which is based on publication (P3). The publication (P3) includes the data publication (D2). Contributions to other manuscripts and data publications can be found in Section A.1 and Section A.2.

Peer-reviewed publications[4]

(P1) **Thielke, L.**, M. Huntemann, S. Hendricks, A. Jutila, R. Ricker, G. Spreen (2022). Sea ice surface temperatures from helicopter-borne thermal infrared imaging during the MOSAiC expedition. *Scientific Data*, 9(1), 364. https://doi.org/10.1038/s41597-022-01461-9 [Chapter 3]

(P2) **Thielke, L.**, N. Fuchs, G. Spreen, B. Tremblay, G. Birnbaum, M. Huntemann, N. Hutter, P. Itkin, A. Jutila, M. A. Webster (2023). Preconditioning of summer melt ponds from winter sea ice surface temperature. *Geophysical Research Letters*, 50, e2022GL101493. https://doi.org/10.1029/2022GL101493 [Chapter 4]

(P3) **Thielke, L.**, G. Spreen, M. Huntemann, D. Murashkin (2023, in review for Elementa Sci. Anth.). Spatio-temporal variability of small-scale leads based on helicopter winter sea ice surface temperatures [Preprint]. *EarthArXiv*. https://doi.org/10.31223/X5R07W [Chapter 5]

Data publications

(D1) **Thielke, L.**, M. Huntemann, S. Hendricks, A. Jutila, R. Ricker, G. Spreen (2022). Helicopter-borne thermal infrared sea ice surface temperatures during the MOSAiC expedition, version 2 [Dataset]. *PANGAEA*, https://doi.org/10.1594/PANGAEA.941017

(D2) **Thielke, L.**, M. Huntemann; G. Spreen (2022): Lead classification maps from helicopter-borne surface temperatures during the MOSAiC expedition [Dataset]. *PANGAEA*, https://doi.org/10.1594/PANGAEA.951569

[4]**Remark.** Chapters 3 and 4 are peer-reviewed published papers, and Chapter 5 is currently under review in a peer-reviewed journal. Chapter 3, 4, 5, and 6 were compiled with contributions from the mentioned co-authors, and are based on the manuscripts, which leads to minor variations in style, language, tenses, symbols, and abbreviations throughout the thesis. Summaries of my contributions are given at the beginning of each of these chapters.

Chapter 2

Theoretical background

In this chapter, I concisely summarize the theory on which this thesis is based. In the first part (Section 2.1), the principles of remote sensing are explained, including thermal radiation, the definition of emissivity, and the atmospheric influence affecting thermal radiation. In the second part (Section 2.2), the sea ice physics are presented with a focus on ice types and thickness, two sea ice focus features of this thesis: leads and melt ponds, and the heat fluxes across sea ice.

This section aims to provide an overview of the relevant sea ice processes, which helps the understanding of this thesis. Data and methods concerning the helicopter-borne TIR imaging and the resulting surface temperature maps as the key data set of this thesis are given in Chapter 3. More detailed theoretical background is part of the specific topics (Chapters 3–6). Subsection 2.1.1 is based on Lubin and Massom (2006); otherwise the main source for this chapter is Shokr and Sinha (2015). Other references are indicated in the text. The notations in this chapter are for a few cases adjusted from the sources.

2.1 Remote sensing

The focus of this thesis is on data from airborne remote sensing. Remote sensing, airborne and space-borne, is a crucial part of polar observations (Subsection 1.1.4). For the Earth system observations, electromagnetic (EM) radiation is measured while it is reflected or emitted by the given surface or atmospheric layer. There are two types of detection methods: passive and active. For the passive measurement methods, the reflected and emitted radiation is detected. Active measurement principles send out EM radiation and detect the backscattered or reflected signal from the given surface (Lubin and Massom, 2006). The aim is to translate the observations into physical information about the target. Radiation characteristics of sea ice, snow, and open water are caused by different physical properties (temperature, salinity, reflectivity, surface roughness, and more). The surface properties can be differentiated by the remote sensing methods (Shokr and Sinha, 2015).

2.1.1 Thermal radiation

Radio waves, microwaves, infrared radiation, visible light, ultraviolet radiation, X-rays, and gamma rays are all examples of EM radiation. The greenhouse effect, where the Earth absorbs solar radiation and re-emits some of it as thermal infrared (TIR) radiation, is important because this is responsible for the temperature of the Earth's surface and atmosphere. EM radiation is also responsible for producing ozone in the Earth's atmosphere, protecting life on Earth from harmful ultraviolet radiation. From the remote sensing perspective, different instruments and techniques are used to measure and analyze EM radiation for studying the Earth's land surfaces, oceans, and atmosphere.

All materials emit EM radiation. The radiation intensity depends on temperature and wavelength. For remote sensing, the relevant spectral range of the EM spectrum ranges from visible blue (0.4–0.5 μm) to microwave (0.001–1 m). This thesis focuses on the TIR radiation from 7.5–14 μm.

In the following, the radiation theory is explained. For simplicity, an idealized material is assumed which is a blackbody that absorbs all radiation and emits with perfect efficiency. For a blackbody, the specific intensity of the radiation is described by Planck's Law, shown as the equation of wavenumber ν ($1/\lambda$) (Equation 2.1) and wavelength λ (Equation 2.2):

$$B_\nu(T) = \frac{2hc^{-2}\nu^3}{\exp(\frac{h\nu}{kT}) - 1}, \quad \text{and} \tag{2.1}$$

$$B_\lambda(T) = \frac{2hc^2\lambda^{-5}}{\exp(\frac{hc}{\lambda kT}) - 1}. \tag{2.2}$$

The equations depend on the temperature T, Planck's constant h, the speed of light c, and the Boltzmann's constant k.

For a given wavelength λ, there is a corresponding maximum in thermally emitted intensity (derived from the differentiated Planck's law), called Wien's displacement law Equation 2.3. It explains that the maximum intensity shifts depending on the wavelength, while the maximum is located at shorter wavelengths with increasing temperature (Figure 2.1):

$$\lambda_m T = 2,987.9\,\mu\text{m}\,\text{K}. \tag{2.3}$$

The Earth has its maximum emission at 10 μm with a temperature of about 300 K. The sun's maximum is in the visible range with a temperature of about 6000 K (Shokr and Sinha, 2015).

The total flux emitted by a blackbody is determined by the integration of the Planck's law over all wavenumbers, known as Stefan-Boltzmann law:

$$\pi B(T) = \pi \int_0^\infty B_\nu(T)\ \mathrm{d}\nu = \sigma T^4 \tag{2.4}$$

with the Stefan-Boltzmann constant σ.

In the microwave range and for temperatures on Earth, it is valid that $hc/\lambda kT << 1$. Thus, the Planck's law (Equation 2.2) reduces to the Rayleigh-Jeans approximation for the specific intensity of the radiation:

$$B_\lambda(T) = \frac{2ckT}{\lambda^4}. \tag{2.5}$$

Therefore, the intensity is proportional to the temperature. In the TIR region, the Rayleigh-Jeans approximation does not apply. Therefore, the Planck's law must be inverted or integrated with a finite bandwidth to retrieve the temperature. For the application of TIR imaging, it is assumed that the Planck's law was already considered for the recording of the brightness temperature (explanation in Chapter 3) and, thus, there is a linearity of the temperature for our data ($T_\mathrm{b} = \varepsilon T$, see Subsection 2.1.2).

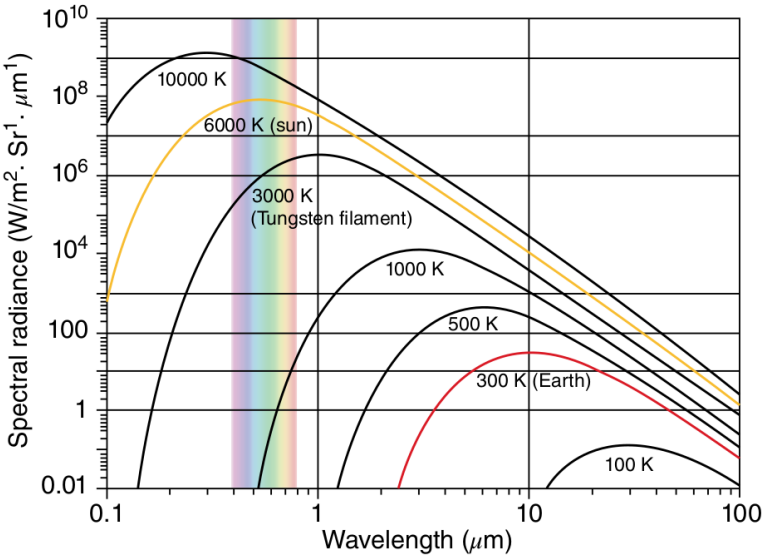

Figure 2.1: Blackbody radiation according to the Planck's law in dependence of the wavelength (visible spectral range with background colors), shown for different temperatures. The Earth at 300 K is highlighted in red. [Taken from Shokr and Sinha (2015), Figure 7.19 therein. I am thankful to the American Geophysical Union and John Wiley & Sons, Inc. for granting me permission to use this figure.]

2.1.2 Emissivity

Emissivity is a measure of an object's ability to emit thermal radiation. After the radiation is absorbed, the material emits radiation to stay in a thermal equilibrium. The emissivity value is defined as the ratio of the thermal radiation emitted by an object to the thermal radiation emitted by a blackbody at the same temperature. An object's emissivity ε

depends on its surface material and temperature and can range from 0 to 1 (0=perfectly non-emissive material; 1=perfect emission/blackbody). Generally, ice and water have very high (close to 1) and nearly equal emissivities, while snow has a slightly lower emissivity than ice. The absorption for snow and ice in the TIR range is very strong. This is why there is a small penetration depth (sub-millimeter), and the surface below a thin snow or ice layer is not affecting the thermal radiation. The emission ε in the TIR and microwave region is described with the parameter brightness temperature T_b. The brightness temperature T_b describes the temperature a blackbody would have to emit the same radiation as the observed greybody:

$$\varepsilon = \frac{R_\mathrm{G}}{R_\mathrm{B}} = \frac{\sigma T_\mathrm{b}^4}{\sigma T^4} = \left[\frac{T_\mathrm{b}}{T}\right]^4, \tag{2.6}$$

with the emitted radiation of a given body R_G and blackbody R_B, the brightness temperature T_b and the physical temperature T.

Following, the brightness temperature T_b defines as:

$$T_\mathrm{b} = \varepsilon^{\frac{1}{4}} T. \tag{2.7}$$

For the TIR spectral range, the emission is proportional to the physical temperature (to the power of four). The brightness temperature in the TIR region is less sensitive to changes in emissivity and more sensitive to the physical temperature (compared to the microwave region). With dependence on T^4, small changes in the temperature result in substantial changes of the radiated energy.

For snow and ice, the emissivity values depend on the surface type and incidence angle, shown with in-situ and model data from Hori et al. (2013). The here presented surface temperature data include information about the incidence angle, but the surface type classification of each pixel is difficult (except for leads, see Chapter 5). Thus, there is no discrimination of the emissivity value applied in this thesis. Figure 2.2 illustrates the emissivity variation with surface type and incidence angle over the spectral range of 8–13μm. The surface is distinguished between fine, medium, and coarse snow as well as between sun crust and smooth bare ice. With a focus on winter sea ice data, medium granular snow (Figure 2.2 b) and smooth bare ice (Figure 2.2 e) are described because they are typical sea ice surface types during winter. The smooth bare ice applies to refreezing leads while most of the winter sea ice surface is covered with snow. As the temperatures are very low and ice is forming very fast during winter, open water is rarely observed. Within the spectral range from 8 to 13 μm there are much lower emissivity values reached for smooth bare ice (note the different axis ranges). The emissivity has a maximum value between 10 and 11 μm, where the Earth's TIR radiation peaks. At the peak, the emissivity is close to 1. It decreases to about 0.985 for medium granular snow and 0.95 for smooth bare ice at 13 μm. For typical incidence angle of the here presented helicopter-borne

observations are between 0° and 45° and have similar emissivity values. Only for larger incidence angles at 75° the emissivity strongly decreases.

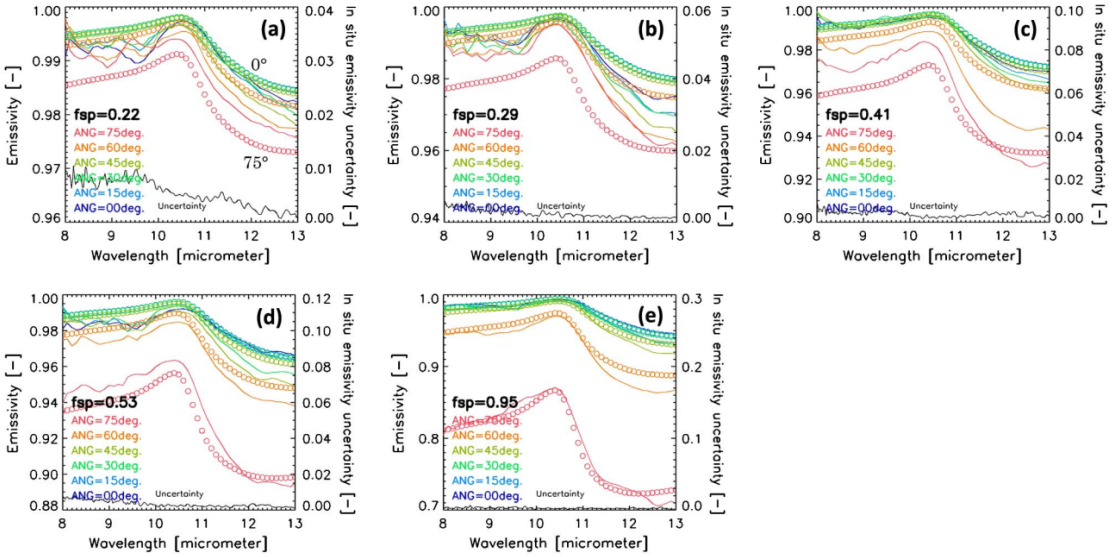

Figure 2.2: Comparison between the simulated spectral directional emissivity (circle symbols) with in-situ measured ones (solid lines) for (a) fine dendrite snow, (b) medium granular snow, (c) coarse grained snow, (d) sun crust, and (e) smooth bare ice, shown for six incidence angles (ANG) of 0, 15, 30, 45, 60, and 75°. The weighting parameters f_{sp} were determined so that the RMSE of the simulated spectra for all incidence angles is at a minimum. Shown as a thin solid line around the bottom of each figure is the uncertainty of the in-situ measured emissivity due to the instrument self-emission from Hori et al. (2006). [Reprinted with permission from Hori et al. (2013) (Figure 10 therein) © The Optical Society.]

2.1.3 Atmospheric influence

Remote sensing methods that observe the surface must consider the atmospheric influence on the retrieved signal because the multiple complex interactions with the atmosphere can alter the signal. While aerosols mostly affect shortwave radiation, longwave radiation (including TIR) is mostly influenced by cloud particles. One further factor is the gas composition of the atmosphere, influencing the TIR region through mainly water vapor and carbon dioxide (Lubin and Massom, 2006). Thus, remote sensing applications have to use atmospheric windows (specific spectral ranges) where the transmission of the signal is high (Figure 2.3). Due to the sensitivity to the atmospheric composition, TIR applications have difficulties determining cloud-free areas, particularly for thin clouds and fog.

The received radiance $L(T_\mathrm{b})$ is determined by the combination of the signal from the surface and from the atmosphere:

$$L(T_\mathrm{b}) = \varepsilon L_\mathrm{sfc}(T_\mathrm{s})\tau + L_\mathrm{atm} + (1-\varepsilon)TL_\mathrm{atm} \tag{2.8}$$

with atmospheric transmittance τ, radiance emitted from the radiating surface layer L_sfc, radiance emitted by the atmosphere L_atm, surface temperature T_s, and surface emissivity ε.

During winter, for a cold atmosphere under clear sky conditions, the contribution by the atmosphere can be negligibly small (neglected for the here used helicopter-borne data, Chapter 3). TIR satellite remote sensing retrieval of surface temperature can account for the atmospheric influence using the split window technique, i.e., combining two channels (11 μm and 12 μm) as 12 μm is more sensitive to water vapor.

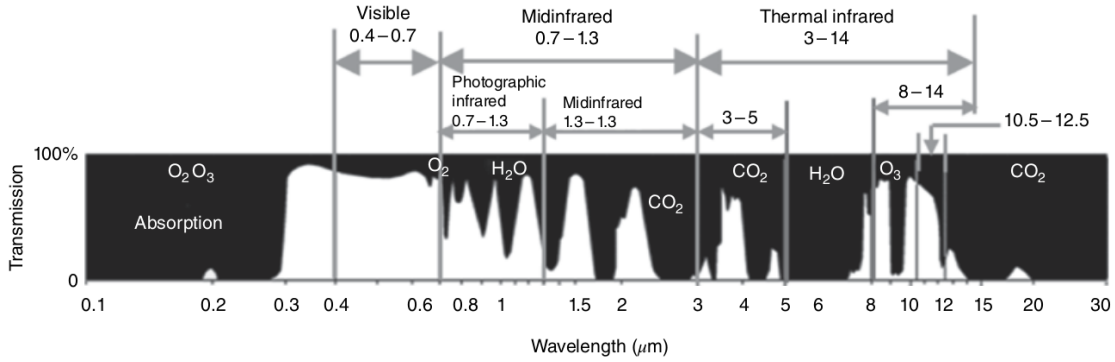

Figure 2.3: Transmission of the atmosphere influenced by different atmospheric gases in the spectral range from 0.1 to 30 μm. [Taken from Shokr and Sinha (2015), Figure 7.36 therein. I am thankful to the American Geophysical Union and John Wiley & Sons, Inc. for granting me permission to use this figure.]]

2.2 Sea ice physics

As mentioned in Chapter 1, the Arctic sea ice extent is a common parameter to describe the state of the sea ice. The Arctic sea ice extent is defined by the area where the ice concentration is 15% or more, according to the definition of the National Snow and Ice Data Center (NSIDC). The sea ice concentration can be described as the areal fraction of sea ice in a given area (Lubin and Massom, 2006). It is essential to correctly determine the ice concentration because an open water fraction of only 1% in winter would have the same ice production as the 99% aerial coverage of thicker ice (Maykut, 1982).

Different processes concerning dynamics and thermodynamics determine the sea ice state and its changes. The dynamics and thermodynamics of sea ice refer to the physical processes governing the movement, deformation, formation, or melting of sea ice. Dynamics are defined by the conversion laws of ice momentum and mass, as well as ice redistribution and rheology (Lubin and Massom, 2006). Sea ice dynamics describe the ice movement that can alter the sea ice structures by creating pressure ridges through convergence or openings in the ice (leads) through divergence. The thermodynamics are defined by the heat exchange of sea ice with the atmosphere and the ocean. Additional heat during summer causes the melt and thinning of the ice, while during winter, the ice formation and ice growth are driven by the heat transfer from the ocean to the cold atmosphere. Overall, the dynamics and thermodynamics of sea ice are complex and multifaceted, influenced by a range of physical processes and environmental factors. As motivated in Chapter 1, this thesis aims to add to a better understanding of the Arctic heat budget and, therefore, focuses on thermodynamics (Subsection 2.2.4).

2.2.1 Ice type and thickness

Due to the big differences in heat exchange over thin ice (or open water) and thick ice (Subsection 1.1.2 and Subsection 2.2.4), it is crucial to classify the sea ice conditions and its types. The sea ice is spatially variable with different ice thicknesses (Maykut, 1982). Continuous observations are important because the ice pack changes constantly due to dynamic and thermodynamic processes creating a complex ice pack on different time scales with up to several days (Maykut, 1982).

The area of open water in the central Arctic during winter is usually about 1% while the fraction of young ice (YI) is higher at around 10% (Maykut, 1978; Thorndike et al., 1975). Especially the thin ice areas are very efficient in heat exchange, and, therefore, contributing to ice growth and salt rejection (Maykut, 1982). Due to their influence on the heat budget, it is helpful to define further thin ice classes, which can be divided into new ice, dark nilas (<0.5 cm), light nilas (0.5–10 cm), gray YI (10-15 cm), and gray-white YI (15-30 cm).

For thicker ice there are three predominant types of sea ice (according to World Meteorological Organization (WMO) definition), FYI, second-year ice (SYI) (sea ice that has survived one summer), and MYI (sea ice that has survived at least two summer). SYI and MYI (perennial) have different physical properties than FYI (seasonal). The perennial ice is less saline, has a different topography (e.g., depressions from drained melt ponds), and thicker ice. The criteria for ice classification are ice thickness (also related to age), ice form (e.g., pancake), ice concentration, and properties of the ice surface (e.g., surface roughness). The ice thickness (in winter) determines ice growth, turbulent heat

fluxes, and brine rejection. These processes are about two magnitudes lower for perennial ice compared to thin ice (Maykut, 1982). This thesis focus on data from the MOSAiC expedition (Subsection 1.1.3). The mean ice thickness during MOSAiC showed a strong seasonal cycle from 1.1 m to 2.5 m from fall 2019 to early summer 2020 with a dynamic contribution of about 0.4 m (von Albedyll et al., 2022b).

2.2.2 Focus feature: Lead

Sea ice leads are a complex and multifaceted aspect of the polar regions, with impacts on the ecosystems, climate, and economic activities of these regions In this work, also small cracks are considered as leads (WMO lead definition for width >50 m). Drifting sea ice experiences complex motions on different scales. The forces are determined by wind stress (primary), ocean current stress (secondary), internal ice resistance, Coriolis force, sea surface tilt, and tidal force. Leads open due to the divergence of the ice field. The opening or closing of a lead can happen on timescales of days. The lead width varies from a meter to a few kilometers, and the lead length can be up to tens of kilometers.

Winter leads have strong turbulent heat fluxes (sensible, latent), and the freezing of the open water happens very fast due to very low atmospheric temperatures (Maykut, 1978, 1982). Thus, leads are areas of large ice production relevant for the sea ice mass balance and brine rejection (Maykut, 1982) that influences the upper ocean stability. On the one hand, leads can increase cloud formation due to additional humidity from open water areas. On the other hand, thin-ice covered leads can lead to the reduction of clouds according to the study of Li et al. (2020). A thin ice cover prevents the humidity from reaching the atmosphere but allows for more turbulence in the lower atmosphere due to an increased sensible heat flux (Li et al., 2020). Additionally, thinner ice is more likely to be affected by deformation.

The TIR observation in winter is a suitable tool for lead classification due to the large temperature contrast of leads compared to the surrounding thicker ice (Subsection 1.1.2). Statistical properties, like intersection angle or width, are important for the representation of lead in models. Regional and global models are limited in spatial resolution and have to parameterize physical processes. It is known that the distribution of lead width follows a power law (e.g., Muchow et al., 2021). The power law relation is also known from other phenomena in nature, e.g., earthquakes (Ross et al., 2019).

2.2.3 Focus feature: Melt pond

Melt ponds are pools of meltwater that form on the surface of sea ice during the Arctic summer months. They are a common feature of the Arctic sea ice and are created when the surface of the sea ice absorbs solar radiation, causing it to melt. The initial melt is

linked to the spatial variation of snow (Petrich et al., 2012) (source of freshwater), while a thick snow cover delays the ice decay. As the meltwater flows across the surface of the ice, it can accumulate in low-lying areas, forming ponds (Eicken et al., 2004; Polashenski et al., 2012). Therefore, melt ponds form in depressions of the ice surface and change the heat conduction from the surface to the ocean. Distinct depressions can be found more likely on deformed ice, while ponds on level ice often expand widely.

The surface melt is determined by the air temperature and absorbed solar radiation, and is crucial for the Arctic summer heat budget (e.g., Nicolaus et al., 2012) Melt ponds are darker in color than the surrounding sea ice and, therefore, have a lower albedo and absorb more sunlight than the ice (Equation 2.10). The color of the melt pond depends on their depth and the thickness of the underlying ice. The presence of darker melt ponds on the sea ice cover causes it to absorb more solar radiation, leading to more melting and an increase the melt pond coverage (e.g, Curry et al., 1995; Light et al., 2022). This process is called ice-albedo feedback loop. As the ice is porous and has vertical channels, the meltwater can drain later in the season to the ocean, also reducing the salinity in the sea ice. It is possible that melt ponds melt through the full ice column and connect with the ocean, which allows the mixing of the freshwater in the pond and the salty sea water. During autumn, when the air temperatures are below the freezing point the melt pond freeze from top to bottom and potentially re-appear in the subsequent melt season.

2.2.4 Heat fluxes across sea ice

The sea ice surface temperature, key parameter of this thesis, describes the interface between the atmosphere and snow or ice, and is strongly relevant for the sea ice heat budget (Subsection 1.1.2). The heat exchange controls the sea ice mass balance, a key aspect of the Arctic state (Lubin and Massom, 2006). There are four main thermal processes for sea ice: heat exchange between air and ice, between ice and ocean, heat conduction through the ice, and latent heat (phase changes) causing ice growth or melt. Heat exchange between sea ice and the atmosphere occurs through conduction, convection, and radiation, and between sea ice and the ocean through conduction and convection.

During winter, the heat is transferred from the warmer ocean water to the colder sea ice through conduction at the interface between the two. Additionally, the movement of warmer water beneath the sea ice can cause convective heat exchange as the warmer water rises and mixes with the colder water near the surface. Overall, the heat exchange processes between sea ice and its surroundings play a key role in regulating the temperature of the sea ice and the surrounding environment, as well as in shaping the physical properties and behavior of the sea ice. Nevertheless, the ocean flux is small and not included in this work because the focus is on the snow/ice-atmosphere interface. Also, lateral fluxes are neglected.

The sum of the vertical heat fluxes defines the one-dimensional heat budget (Equation 2.9):

$$F_\mathrm{r} - F_\mathrm{l}^\mathrm{up} - F_\mathrm{l}^\mathrm{dn} + F_\mathrm{s} + F_\mathrm{e} + F_\mathrm{c} = 0, \tag{2.9}$$

with absorbed solar radiation F_r (Equation 2.10), upwelling and downwelling longwave radiation F_l^up (Equation 2.11) and F_l^dn(Equation 2.12) (radiation of the surface and the atmosphere), as well as sensible, latent, and conductive heat fluxes F_s (Equation 2.13), F_e (Equation 2.14), F_c (Equation 2.15).

The different heat fluxes of the budget are defined in the following. The atmospheric variables are taken for a specific reference height, often at 2 m or 10 m above the surface.

- The shortwave radiation is defined as:

$$F_\mathrm{r} = (1-\alpha)F_\mathrm{sw} - i_0(1-\alpha)F_\mathrm{sw}, \tag{2.10}$$

  with surface albedo α, incoming shortwave radiation F_sw, and transmittance i_0 (T_λ for thermal radiation). The second term is the transmitted radiation flux. The shortwave radiation is zero for our winter data because there is no sunlight in the Arctic.

- The upwelling and downwelling longwave radiation are the dominating terms during winter and are defined as:

$$F_\mathrm{l}^{up} = \varepsilon_\mathrm{i}\sigma T_\mathrm{s}^4 \tag{2.11}$$

  and

$$F_\mathrm{l}^\mathrm{dn} = \varepsilon_\mathrm{a}\sigma T_\mathrm{a}^4, \tag{2.12}$$

  with the Stefan-Boltzmann constant σ, emissivity of snow or ice ε_i, emissivity of the atmosphere ε_a (function of cloud cover), surface temperature T_s, and air temperature T_a.

- The turbulent fluxes of sensible and latent heat are defined as:

$$F_\mathrm{s} = \rho_\mathrm{a} c_\mathrm{p} C_\mathrm{s} u (T_\mathrm{a} - T_\mathrm{s}) \tag{2.13}$$

  and

$$F_\mathrm{e} = \rho_\mathrm{a} L C_\mathrm{e} u (f e_\mathrm{sa} - e_\mathrm{s0}), \tag{2.14}$$

  with air density ρ_a, specific heat of air c_p, latent heat of vaporization L, bulk transfer coefficients for heat and evaporation C_s and C_e, saturation vapor pressure at the surface and in the reference height e_s0 and e_sa, the relative humidity f, and wind

speed u. The bulk transfer coefficients for heat C_s and moisture C_e are differentiated between thin ice (0.003) and thick ice (0.00175). The latent heat flux is negligible small during winter due to the low availability of humidity.

- The conductive heat flux is defined as:

$$F_c = \frac{k_i k_s (T_f - T_s)}{k_i h_s + k_s h_i}, \tag{2.15}$$

with thermal conductivity of sea ice k_i (dependent on T_s and salinity) and snow k_s (0.31 $Wm^{-1}K^{-1}$), snow depth h_s, ice thickness h_i, and the freezing temperature of seawater T_f (dependent on the salinity). The freezing point of sea water is at -1.8°C for a salinity of 35‰.

The thermal conductivity is higher for ice than for water and decreases with increasing salinity. A typical value for the ice thermal conductivity k_i is 2.1 $Wm^{-1}K^{-1}$. The snow conditions are determined by snow fall, mostly in spring and fall, as well as the re-distribution by winds and property changes due to metamorphism. The snow on top of sea ice reduces ice growth during winter due to its small snow thermal conductivity k_s. For snow conditions, there is high variability between 0.03–0.80 $Wm^{-1}K^{-1}$ (lower for drier snow). Following, the heat flux strongly depends on snow depth (Maykut, 1978).

The surface temperature (of sea ice or snow) is a fundamental parameter in the Arctic heat budget as many fluxes are explicit functions of the surface temperature T_s (Lubin and Massom, 2006). The surface determines several heat budget components, i.e., longwave radiation, sensible heat exchange between ice/snow and atmosphere, as well as the conductive flux through the ice pack and snow layer (Lubin and Massom, 2006). Due to the high spatial variability of the different parameters, it is challenging to infer the regional heat fluxes from single measurements, while models (e.g., ice thickness distribution of Thorndike et al. (1975)) and remote sensing observation (e.g., helicopter-borne imaging) can add valuable knowledge (Maykut, 1982).

Thermodynamic thin ice thickness

The heat balance can be used to estimate ice thickness up to 50 cm from surface temperature (e.g., recorded with TIR imaging). For thicker ice (above 1 m thickness), the heat flux is not sensitive to thickness changes anymore (Maykut, 1978). Hence, the ice thickness distribution below 1 m thickness is important for the sea ice heat budget (Maykut, 1978; Shokr and Sinha, 2015).

The heat balance can be used to calculate the relationship between ice thickness and surface temperature. Figure 2.4 shows the relationship between surface temperature and

ice thickness on 16 January 2020 as an example time step from the time series along the MOSAiC drift. The results are calculated with the thermodynamic model SNOWPACK (Wever et al., 2020) (simulations were performed by Dr. Philip Rostosky). The model is forced with atmospheric data from ERA5 along the location of the MOSAiC drift track. New ice growth is initialized at each time step with an initial ice thickness of 1 cm (started in October 2019). Following, a nearly continuous suite of ice thicknesses is calculated. The surface temperature strongly depends on the thin ice thickness, which allows a definite ice thickness determination. For ice above 30 cm thickness, the relation is no longer explicit due to changes in air temperature, wind speed, or snow fall which alter the forcing and the surface temperature at a given time.

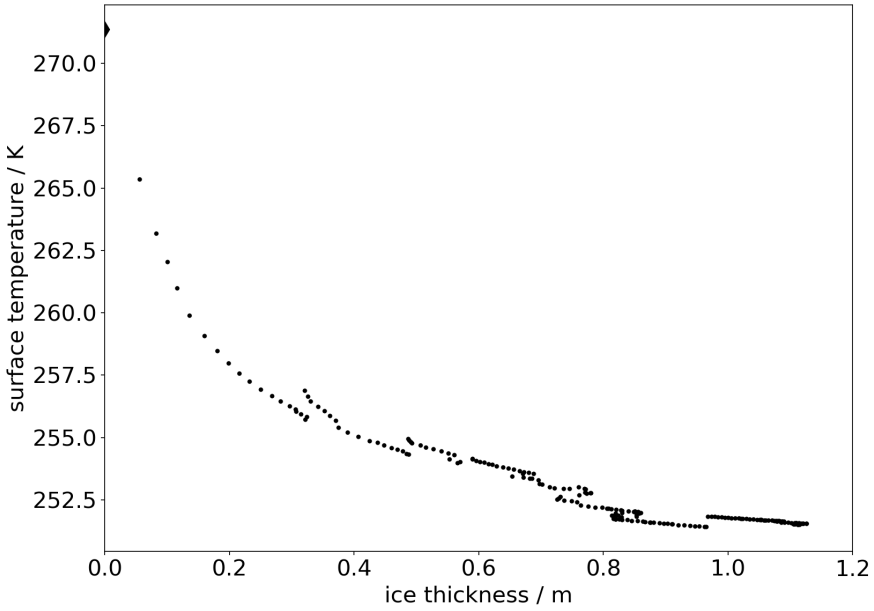

Figure 2.4: Ice thickness (limited to 1.2 m) versus surface temperature from the SNOWPACK simulation on 16 January 2020 with atmospheric forcing from ERA5 for the MOSAiC drift track.

Chapter 3

Helicopter-borne thermal infrared imaging

This chapter is based on the following publication:

Thielke, L., M. Huntemann, S. Hendricks, A. Jutila, R. Ricker, G. Spreen (2022). Sea ice surface temperatures from helicopter-borne thermal infrared imaging during the MOSAiC expedition. *Scientific Data*, 9(1), 364. https://doi.org/10.1038/s41597-022-01461-9

Relevance

In this chapter, we address the first research question R1: *What is the potential of thermal infrared (TIR) imaging for the spatial analysis of sea ice during winter?*

TIR imaging of sea ice performed during the MOSAiC expedition had never been implemented before to this extent, considering the lack of winter observations in the Arctic. The full winter season was covered with 35 helicopter flights between October 2019 and April 2020. We present detailed information on the data and methods. The result are accessible and easy-to-handle surface temperature maps. This advanced data product provides the basis to perform analysis of sea ice features beyond the scale of a single image, as in Chapter 4, Chapter 5, and Chapter 6. The spatial context is valuable for the analysis in combination with other measurements.

Contributions

I contributed to the development of the methods and processed the data. I wrote the first draft of the manuscript.

Abstract

The sea ice surface temperature is important to understand the Arctic winter heat budget. We conducted 35 helicopter flights with an infrared camera in winter 2019/2020 during the Multidisciplinary Drifting Observatory for the Study of Arctic Climate (MOSAiC) expedition. The flights were performed from a local, 5 to 10 km scale up to a regional, 20 to 40 km scale. The infrared camera recorded thermal infrared (TIR) brightness temperatures, which we converted to surface temperatures. More than 150000 images from all flights can be investigated individually. As an advanced data product, we created surface temperature maps for every flight with a 1 m resolution. We corrected image gradients, applied an ice drift correction, georeferenced all pixels, and corrected the surface temperature by its natural temporal drift, which results in time-fixed surface temperature maps for a consistent analysis of one flight. The temporal and spatial variability of sea ice characteristics is an important contribution to an increased understanding of the Arctic heat budget and, in particular, for the validation of satellite products.

3.1 Background and Summary

The measurement program was part of the Multidisciplinary Drifting Observatory for the Study of Arctic Climate (MOSAiC) expedition (https://mosaic-expedition.org), which took place in the Arctic from October 2019 to October 2020 and was divided into five legs (Shupe et al., 2020). RV *Polarstern* (Alfred-Wegener-Institut Helmholtz-Zentrum für Polar- und Meeresforschung, 2017) was drifting attached to an ice floe along the transpolar drift from about 85°N north of the Laptev Sea towards Fram Strait between Svalbard and Greenland (Shupe et al., 2020; Krumpen et al., 2021). To study the Arctic climate, a research camp, called CO, was installed on a second-year ice (SYI) floe that survived the summer and originated from the Laptev Sea (Krumpen et al., 2020). The ice of the MOSAiC floe was very rotten and porous from the summer melt at the beginning of the drift. The level ice areas were characterized by a high fraction (>60%) of refrozen melt ponds, which had physical properties more similar to first-year ice (FYI). FYI was developing in the surroundings of the floe (later reaching about 30% fraction) and in cracks frequently cutting through the CO throughout the drift. Additional measurements were performed on the surrounding sea ice within a Distributed Network (DN) of autonomous measurement platforms and from the air by helicopters and drones.

From October 2019 to April 2020, we performed 35 helicopter flights with an infrared (IR) camera on the Airbus Helicopter MBB-BK 117 C-1 over Arctic sea ice. All flights covered a similar sea ice area in the near vicinity of the drifting RV *Polarstern*. The IR camera took more than 150000 images in total with 640x48s0 brightness temperature values, which we converted to surface temperatures. All images of each flight are combined in one surface temperature map for every flight with a high spatial resolution of 1 m. The maps allow an investigation of spatial and temporal variability on a seasonal time scale based on the series of flights throughout the whole winter season. Measurements of the thermal radiation can be performed without daylight. Thus, TIR observations are valuable source of data in the polar night during the Arctic winter. Detecting the thermal radiation is an appropriate tool because there are large temperature differences between open water or thin ice and snow-covered thick ice and helps to detect different surface characteristics which are, e.g., leads (cracks in the sea ice) as warm anomalies. Examples for the application of TIR observations are lead detection (Willmes and Heinemann, 2015), sea ice concentration retrieval (Ludwig et al., 2020), thin ice thickness estimation(Adams et al., 2012), and surface heat flux estimates (Qu et al., 2019).

Especially for the central Arctic, in-situ data rarely exist for the winter season. Therefore, operational observations are provided only by satellites. Here, our helicopter-borne, high spatial resolution data can resolve surface temperatures on a satellite sub-footprint scale which can help to improve the satellite retrievals. A high spatial resolution of 1 m

is crucial since small-scale features like narrow cracks in the ice can release a significant amount of heat from the ocean to the atmosphere for the usual winter case when the atmosphere is colder than the water (Maykut, 1978). This becomes especially important in a warming Arctic (Dai et al., 2019) while the sea ice is getting thinner, moves faster, and therefore breaks up more easily (Kwok, 2018; Spreen et al., 2011; Meredith et al., 2019; Stroeve et al., 2012). These small-scale cracks are not directly represented in thermal satellite data. Satellites are the main source for Arctic sea ice observation but have a spatial resolution of about 1 km in the thermal infrared (TIR) region. For example, Willmes and Heinemann (2016) developed pan-Arctic lead maps with a resolution of down to 1 km from data of the Moderate Resolution Imaging Spectroradiometer (MODIS). As they point out, the current uncertainties in satellite retrievals are, among other things, caused by missing validation datasets. Satellite-derived parameters are crucial for the evaluation of the larger regional and Arctic-wide climate context of the MOSAiC measurements like, e.g., the sea ice concentration, thickness, lead fraction, and ice drift time series along the MOSAiC drift track (Krumpen et al., 2021).

As examples, we present and discuss three images and two maps from the IR camera observations to show the potential of the data. Beforehand, we explain the uncertainties and corrections, which have to be considered for the use of the data. We provide a detailed description of the processing method for the images, the mapping, and the approach to have a time-fixed surface temperature. We discuss the surface temperature distribution and the two-dimensional image- and map-based analysis for the investigation of the spatial distribution of specific features. Lastly, we give suggestions about possible applications for the IR images and maps.

3.2 Methods

The processing of the temperature images resulted in two types of datasets. First, the processed images are provided for every flight including the corrections applied here. Based on the corrected images, gridded data are provided as temperature maps which result from the whole set of images in one flight as an advanced dataset. The processing steps are displayed in Figure 3.1. A list of flights and variables are described and, if necessary, updated in our data manual (Thielke et al., 2022a).

3.2.1 Camera details

The images were recorded with the Infrared VarioCAM HD head 680 from InfraTec (SENSOR, 2021b) which was positioned in a helicopter with the nadir downwards view towards the sea ice surface (Figure 3.2). All essential technical details about the IR camera are highlighted in this paragraph and listed in Table 3.1. The broadband TIR imaging was

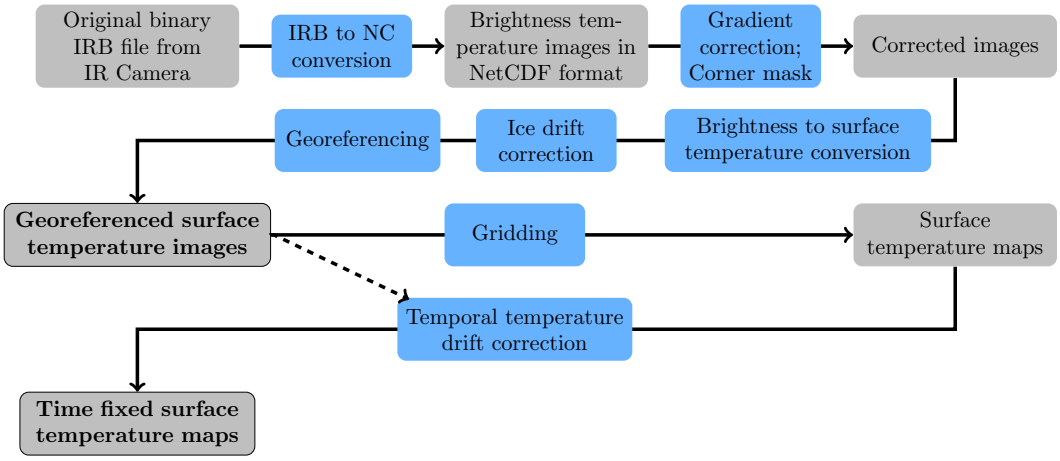

Figure 3.1: The flow chart is presenting the processing steps from the raw data of the IR camera to the time-fixed surface temperature map as part of the finished product (NC = NetCDF). The grey boxes indicate the data status and the grey, black-framed boxes with the bold font indicate the published data products. The blue boxes show the performed processing steps according to the methods explained in this study. The dashed arrow shows the input of the single images, which is used for finding the best fit of the temporal temperature drift correction.

performed in the TIR region of the electromagnetic spectrum from 7.5 to 14 μm, which includes the Earth's radiation peak at 10 μm (Shokr and Sinha, 2015, page 293). The accuracy for the measured brightness temperature is 1 K and its precision is 0.02 K. To distinguish features on the ground within one image the precision is more important than the accuracy. The calibration of the device was done down to the target temperature of -8°C with a measured deviation of 0.6 K. It has to be considered that the measurements had mainly been performed at lower temperatures. The minimum temperature by the manufacturer is -40°C while we could measure even lower temperatures of the sky. During the measurement we reached the limit a few times, but did not exceed the limit extensively. Therefore the accuracy could slightly change for colder temperatures but this is neglected in this study. A sufficient overlap of the images is guaranteed by an acquisition rate of 1 Hz. The raw data were measured at an even higher frequency of 4 Hz, but down-sampled here to 1 Hz. During the recording, every 15 to 60 seconds a non-uniformity compensation (NUC) ensured that there was a minimized camera-internal drift in the temperature. The focus was adjusted after reaching the final flight altitude and stayed fixed for the whole flight. We assume to have the same focus for all flights because all measurements were performed at the similar flight altitude. More information about the device *ir_variocam_02* and its actions during the expedition are stored in the Alfred-Wegener-Institut (AWI) Sensor platform (https://sensor.awi.de/) (SENSOR, 2021b).

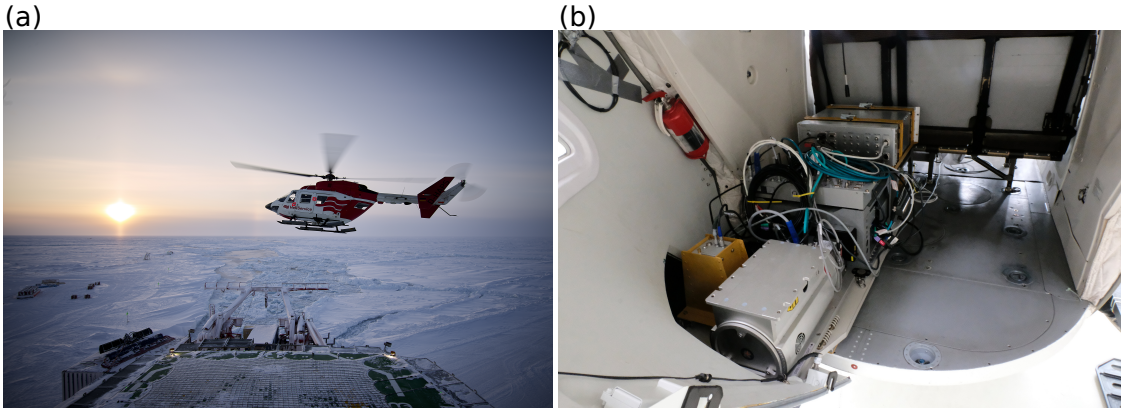

Figure 3.2: The images illustrate the measurement setup during the expedition. (a) The photo shows a helicopter flying close to RV *Polarstern* which is surrounded by sea ice (Credits: Alfred-Wegener-Institut/Michel Gutsche, CC-BY 4.0). (b) This photo shows the setup of the instruments in the cargo compartment of the helicopter. The IR camera is installed in the yellow box looking through a cutout (not visible) nadir downward towards the surface (Credits: Alfred-Wegener-Institut/Stefan Hendricks).

Detector type	Uncooled microbolometer-FPA, Pitch 25 μm
Detector format	(640 x 480) Pixel
Spectral range	(7.5 ... 14) μm
Temperature range	(-40 ... 1200) °C
Thermal resolution	up to 0.02 K
Accuracy	1% for < 0°C
Field of view	(56.1 x 43.6)°
Focal length	15 mm
Focus	Manual

Table 3.1: Technical details for the TIR camera VarioCAM HD head 680 GW from InfraTec GmbH Infrarotsensorik und Messtechnik.

3.2.2 Helicopter-borne survey flights

The 35 flights were conducted during the first three legs of the expedition between 02 October 2019 and 23 April 2020 at an altitude of around 300 m and with a duration of about 90 minutes. The general objective of this measurement program was to have weekly flights. The frequency of flights varied because it depended on the weather conditions, was adapted to cover interesting events in the sea ice area, and some flights had to be aborted due to bad weather. There was a higher flight frequency in the earlier part of the drift, but a lower frequency in the latter part. This resulted in a larger geographic distance between the flights due to a faster ice drift during that period (Figure 3.3); mind that the local ice surface did not necessarily change faster because of that, because the MOSAiC was drifting with the ice. Nine flights are not included in this dataset yet because they

require additional processing, e.g., the IR camera has missing GPS data. They include seven flights from the wintertime and two flights during the last leg in September 2020 which were mainly conducted over thin ice areas at the ice margins and not cover the MOSAiC floe. Their data will be published at a later stage.

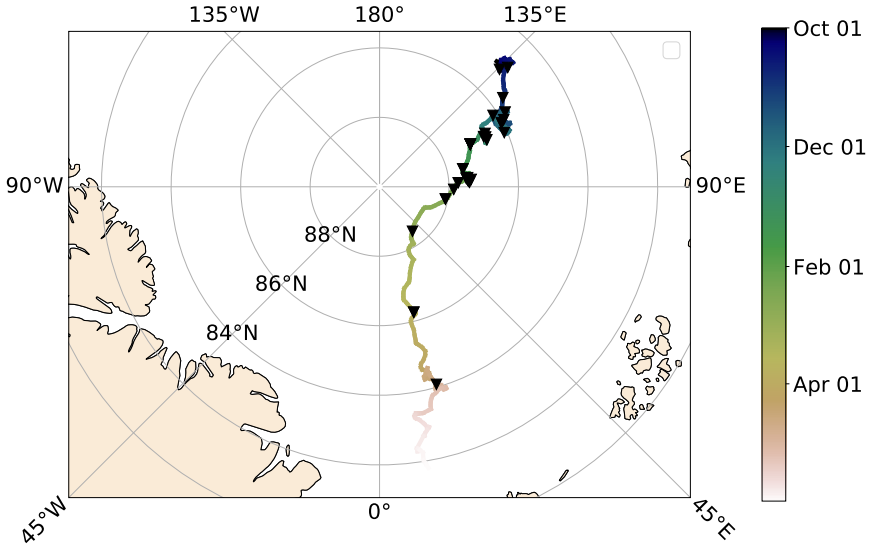

Figure 3.3: The map presents the locations of the measurements included in this study. The location of helicopter flights are marked with black triangles along the MOSAiC drift track from the northern Laptev Sea towards the Fram Strait with color-coded time.

There are four different flight types in our measurement program that cover (i) the Central Observatory (CO), (ii) the three nodes of large sensor sites (L-Sites) (L1, L2, L3) in the Distributed Network (DN), (iii) single L-Site (grids), or (iv) a specific event, e.g., a lead opening. The CO flights (i) observed the local ice conditions of the MOSAiC ice floe in high spatial detail (Figure 3.4 (a)) and L-Site flights (ii) allowed an investigation of the ice conditions on a regional scale. The regional L-Site flights (ii) were flown in a triangle pattern covering the three L-Sites, located in the corners of the flight pattern (Figure 3.4 (b)). On 08 January 2020 the different L-Sites were overflown separately in the same patterns as the CO surveys, i.e. single L-Site grids (iii). The main weekly time series consists of the CO flights (i) and L-Site flights (ii).

3.2.3 Sea ice surface temperature

In the TIR range, the measured brightness temperature is close to the actual surface temperature. As a first approximation, the surface temperature T_s was calculated from the

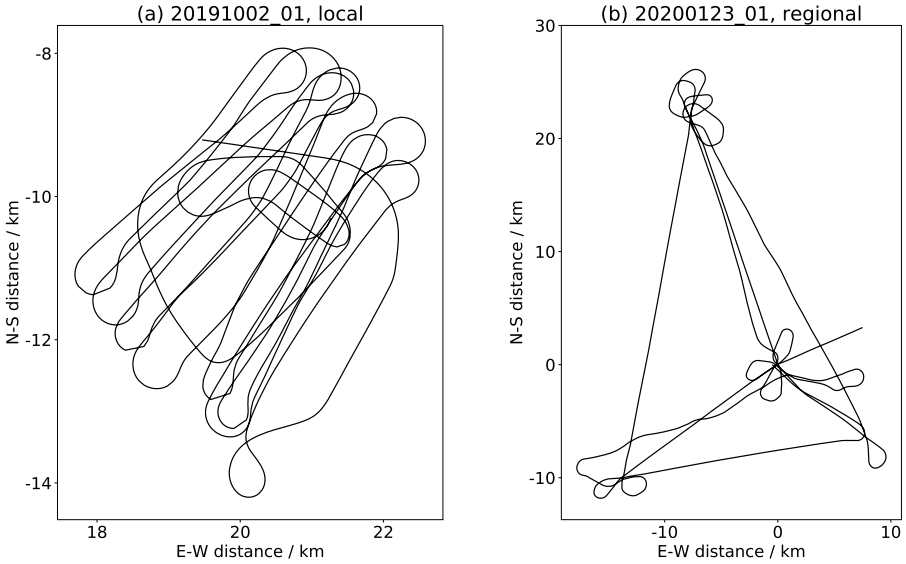

Figure 3.4: To get an idea about the coverage of surface for different flight patterns, we display the flight tracks for (a) local CO flight 20191002_01 and (b) regional L-Site flight 20200123_01. The axes show the distance in meter. The center point (0,0) is the location of RV *Polarstern*. For the flight 20191002_01 in (a) (0,0) is outside the map because RV *Polarstern* was not located at the MOSAiC ice floe yet.

up-welling brightness temperature $T_{\mathrm{b,up}}$, measured with the IR Camera, and the emissivity e (Shokr and Sinha, 2015, page 294) with

$$T_{\mathrm{s}} = \frac{T_{\mathrm{b,up}}}{e}. \tag{3.1}$$

For emissivities close to one, as in our case, the measured brightness temperature can be approximated to change linearly with the physical temperature. The Plank law is already considered during the recording of the brightness temperature. The influence of the down-welling brightness temperature was neglected for simplicity. The emissivity e is assumed to be a constant value of 0.996 for all incidence angles and surface types following Høyer et al. (2017). Here the downwelling contribution with (1-e) T_{s} would be 1 K at 250 K surface temperature which is the same range as the accuracy of the measured temperature. We used this emissivity, because the instrument of the Høyer et al. (2017) study, i.e., a Cambell Scientific IR120 radiometer, has with 8 to 14 μm a very similar spectral range to our instrument. However, the spectral weight function might differ. An emissivity of 0.97 was used for other infrared observations, e.g., by the NSIDC during Operation IceBridge flights with a KT19 thermometer with a spectral response from 9.6 to 11.5 μm. The lower emissivity value of 0.97 would lead to overestimated surface temperatures compared to our used value of 0.996. The accuracy of the surface temperature is determined by the accuracy of the brightness temperature (1 K, see Camera details) as well as of the accuracy

of the emissivity. The additional uncertainty by the emissivity can be influenced by the incidence angle or change of surface type (Hori et al., 2013).

In future studies, the aim is to apply a more detailed theory to retrieve a higher accuracy of the surface temperature T_s. Additionally, it has to be considered that the penetration depth for TIR radiation is very small of a few μm, which allows an influence by atmospheric parameters, like the air temperature, wind speed, or cloud cover (Shokr and Sinha, 2015, page 294).

3.2.4 Image correction

Corner mask

In all flights, warm temperature anomalies were found in one corner. The IR camera looked through an open cutout in the helicopter bottom structure. The higher values were probably caused by a shielding effect from the structure of the helicopter, which slightly influenced the temperature recording in the respective corner. To remove false high temperatures in the respective corner, a corner mask is provided for every flight and can be applied to each image. We generally recommend to exclude the corner areas of the images in any case due to distortions in the higher incidence angle regime.

Radial image gradient

In every image, a radial gradient of the recorded temperature occurs. This gradient is likely caused by an artificial effect of the camera. We corrected it by an empirical radial gradient which is calculated by averaging images of a flight and applied for every flight independently. For this, only images with an average temperature below the 25th percentile of all images are considered to exclude warm features like leads which could influence the resulting gradient. The gradient is relative to the center temperature, which is assumed to be the truth. This lens effect correction was applied to all datasets and the correction array is included in the image-based dataset for every flight so that the original, uncorrected images can be reproduced if needed. In Figure 3.5, a case example from the flight on 02 October 2019 illustrates the correction of an image by the gradient. The original image (Figure 3.5 (a)) shows colder outer parts of the image. With the reference value in the center of the image, the image was corrected by a specific factor (Figure 3.5 (b)) resulting in a corrected image without a radial gradient (Figure 3.5 (c)).

3.2.5 Mapping

After processing the image data, we produced flight maps by combining all images in one grid. The gridded dataset consists of temperature values with assigned coordinates (longitude and latitude) as well as relative coordinates to *Polarstern* for co-location with

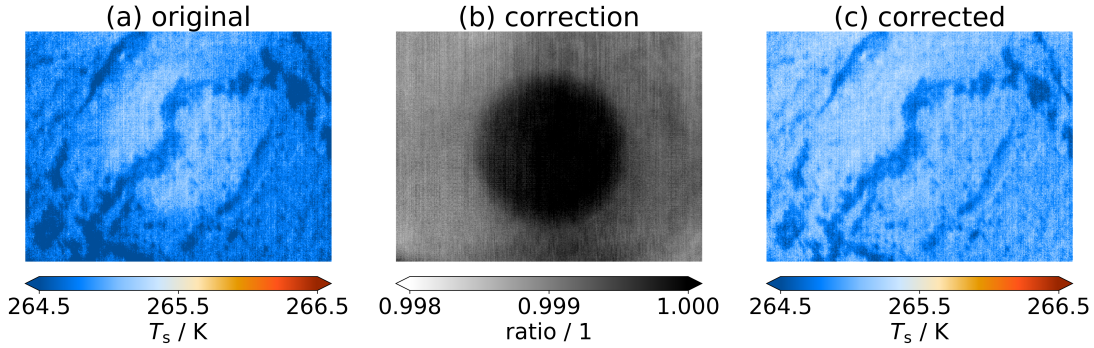

Figure 3.5: The image gradient correction of the surface temperature T_s is presented with an example image of the flight 20191002_01 with (a) the original image of surface temperature in K, (b) the correction array and (c) the corrected image of surface temperature in K.

other measurements. This mapping was done in three steps, which are described in more detail in the following and which is illustrated in Figure 3.6. First, the ice drift correction was performed to correct the coordinates to the target time which is the middle of the flight. Second, all image pixels had to be georeferenced under consideration of the helicopter position and rotation. Third and last, all pixels were assigned to the closest grid cell in the equidistant grid.

Some images were discarded if they were outside the main flight pattern, not yet at the main flight altitude level of around 300 m, or not usable due to the internal calibration (NUC). Here one image per NUC had to be discarded. As a benefit of excluding the discarded images, the maps are more compact in terms of data coverage of the covered area and better suited for the statistical and visual interpretation of the spatial variability in the defined area. In the following part, we explain the detailed methods for the image mapping.

Ice drift correction

Assuming the average ice drift of 8.52 km per day according to Krumpen et al. (2021), the sea ice drifted about 500 m during a 90-minute flight. Thus, a piece of ice at a specific location at the beginning of the flight was at another location later during the flight. Therefore, we corrected the coordinates of every image based on the drift of RV *Polarstern* to be in the coordinate system of the target time in the middle of each flight. The position and heading data (Rex, 2020; Haas, 2020; Kanzow, 2020) of RV *Polarstern*, which was achored directly to the ice floe, were recorded with the high-performance inertial navigation system (INS) Motion Sensor Hydrins 1 (SENSOR, 2021c). For the ice drift correction, we use linear interpolated data of 10-minutes interval *Polarstern* positions to correct each image accordingly with the assumption of homogeneous ice movement across

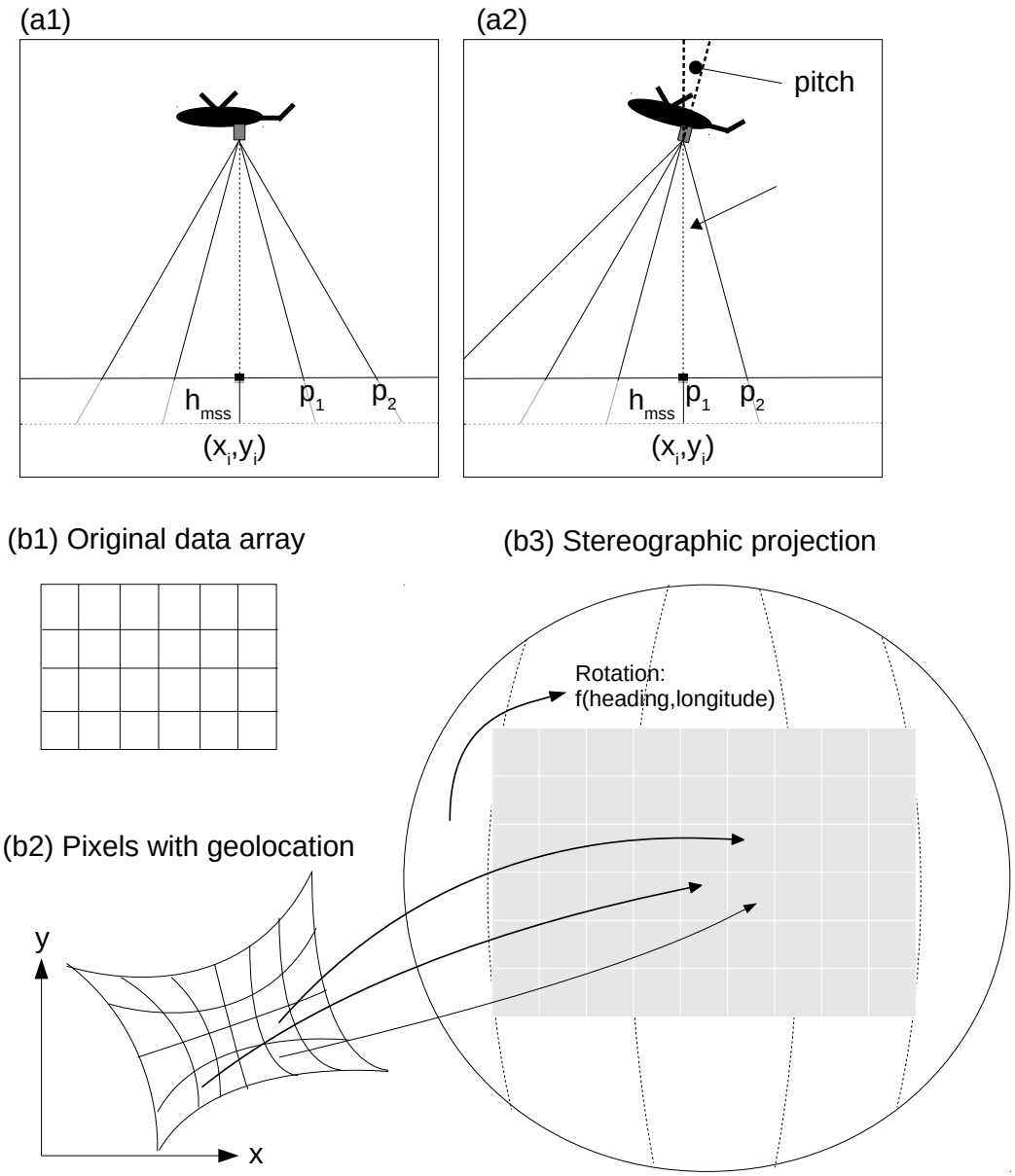

Figure 3.6: The schematic illustrates the different parts of the mapping method applied to the images. We calculate the positions on the ground based on the helicopter position (a1) which change with the helicopter position and rotation (a2). We also consider the reduction of the ellipsoid height from the GPS by the mean sea surface height h_{mss} because it changes the actual position of the pixel on the plane. The pixel locations are determined based on the reference point (x_i,y_i) at the known nadir location. In the next step, the projection method starts with the data array from the image (b1), which is further processed to the georeferenced images with x,y coordinates (b2). Finally, the pixels of the image are assigned to an equidistant grid with a stereographic projection (b3).

the entire flight area. We took the GPS position at the target time as the reference point for the stereographic projection which is used for the final gridded temperature maps.

RV *Polarstern* is always in the center of the stereographic projection and for the rotated relative coordinates RV *Polarstern*'s heading is defining the positive y-axis and the starboard direction is the positive x-axis. By this, relative distances of the flight data are kept comparable between all flights. The resulting map contains the locations of the observed sea ice surface at the target time. This was used to calculate a relative coordinate system with distances towards the reference point at RV *Polarstern*.

Georeferencing

Based on the corrected image location and the stereographic projection, every pixel is geolocated. All projections are done with the WGS84 ellipsoid. The geolocation of each pixel is determined based on a pinhole camera model and a transformation from the camera to the plane (Barber et al., 2006). While the pitch angle was generally low during the flight, the roll angle was increased during turns and discarded in cases of a high angle with more than 40 degrees to avoid large distortions in the projection. Values from images with a high roll angle were discarded if data with a roll of less than 20 degrees were available. In general, we would recommend using the data of high roll angle with caution because large distortion can cause uncertainties in the geolocation. We correct the ellipsoid height, measured by the helicopter GNSS, by the mean sea surface height by Andersen and Knudsen (2009). Additionally, we perform a distortion correction for the images to reach a more accurate pixel position. We use the positioning data which were recorded with an embedded GNSS inertial system Applanix AP 60-AIR (SENSOR, 2021a) which was installed in the helicopter next to the IR camera (Figure 3.2).

For an increased accuracy in the geolocation, we performed an optimization for the following six input parameters:

- Time (time offset between IR Camera and GNSS)
- Three components of a fixed camera rotation with respect to the helicopter (roll, pitch, heading)
- Internal camera parameters (effective focal length, radial distortion coefficient)

The optimization procedure consists of different steps. At first, common features between different images were determined using a consecutive execution of edge detection, pattern matching, homograhic fitting and cleaning using a RANSAC (RANdom SAmple Consensus (Fischler and Bolles, 1981)) based method. The euclidean distance between the same feature in pairs of two different images in the final coordinate system is subject to minimization. Since the feature detection, despite initial outlier correction, were not perfect,

even for a good matching parameter, a high bias in the sum or mean of the determined distances. Therefore, we used a loss function employing the 70th percentile of the distances of ground projected point matches in one images pair and then another 70th percentile of these values from all used images as loss. This parameter was then minimized using an adaptive differential evolution optimizer (Feldt, 2021).

For our processing we determined two different sets of correction parameters because there was change of the camera setup at the start of Leg 2. The parameter are listed with the order (time offset, roll offset, pitch offset, heading offset, effective focal length, radial distortion coefficient):

- For Leg 1 (until 20191206_01):
  (0.49762,0.458456,0.134936,88.3343,604.362,-0.407934)
- For Leg 2 and 3 (20191224_01 onwards):
  (0.510041,0.349084,-0.279992,90.2153,604.107,-0.420221)

For the respective leg the optimization was done for one specific flight, i. e., 20191002_01 for Leg 1 and 20191224_01 for Leg 2. Since there was the same camera on all three legs, the focal length and radial distortion parameter should not change. As a result, determined by the optimization, these parameters ended up very close. For all flights, we use these optimized parameters. Additionally, we manually determined a time offset for each flight because the IR camera is recording the time only with the full second. But for a flight speed of around 45 m/s, a time difference of 0.5 s can already cause a significant position shift of the images. As expected, we have mostly a time correction below 1 s. In cases of a higher time shift, probably the required initial time synchronisation was not performed. The time offset for every flight is included in the image NetCDF file while the time variable contains the final (corrected) time used.

In addition, the following modifications had to be done during the processing:

- Until 20191130_01: rotation of image by 180°(camera was rotated in the helicopter)
- Excluding images in the middle of the flight 20191105_01 because of missing position data
- Correct heading by the difference of the actual longitude and the central longitude of the projection
- Change of sign of pitch angle

Gridding

After having a georeference for all pixels in every image, we assigned the pixels of all images to an equidistant grid of 1 m. The original images have a higher resolution of approximately 0.5 m at nadir. However, 1 m guarantees full coverage of all grid points for the final map, even under a higher incidence angle. After the ice drift correction, the pixel coordinates of all images are assigned to a grid cell of the stereographic grid map referenced to the target time (Figure 3.6). In case several values fit in one grid cell, the value closest to the target time was taken and the overlap discarded. In addition to the gridded surface temperature, we included the longitude, latitude, time, roll, and pitch, measured by the Applanix AP 60-AIR (SENSOR, 2021a), as gridded data as well. This set of parameters contains all necessary information for the interpretation of the physical parameters. We also included relative coordinates which are comparable for the whole dataset period. They have one constant reference point at RV *Polarstern* whereas the longitude and latitude coordinates were changing constantly with the drift. The rotated relative coordinates have always the same orientation,also with RV *Polarstern* as reference (see Ice drift correction). The 5 m resolution are the block average of the 1 m resolution data.

Uncertainties of the geolocation

Uncertainties in the mapping can be caused by the ice drift correction which is well-defined for the area of the CO, close to RV *Polarstern*, but can differ for outer areas. The surrounding sea ice could have drifted differently than the CO during the flight, which cannot be considered because there are no data available. However, this effect is small for the duration of one flight. Three to five Automatic Identification System (AIS) base-stations were installed in the CO, which could have served as an alternative to provide the ice drift correction. However, compared to the ship GNSS and INS system the AIS stations showed jitter of tens of meters, i.e., noise in the GPS position with time which could lead to a temporal variability of the signal and therefore some inconsistencies. Therefore we decided to use the RV *Polarstern* position data. The only disadvantage of that would occur if RV *Polarstern* would move relative to the CO during a helicopter flight, which did not happen for our flights here mentioned. The uncertainty of the ship's navigation system Hydrins is 0.01 deg for the heading and 0.03 m for the position (SENSOR, 2021c) which is neglectable for our 1 m resolution data.

Additionally, there are uncertainties caused by the installation of the instruments in the helicopter. The IR camera and the INS were deployed at different positions on the instruments plate in the helicopter, both with independent spring dampers (Figure 3.2), which could respond differently to vibrations of the helicopter. This would result in small angular noise, which was neglected. The uncertainty from the positional difference is small

and is mostly overcome with the optimization which provides us with the optimal input parameter for the given setup. The pixel distance at the surface is dependent on the flight altitude which we corrected by the mean sea surface height (Figure 3.6 (a1)), but did not consider the changes due to tides, currents, or atmospheric pressure loading. In addition, IR camera images were projected to a plane at the distance of the helicopter to the mean sea surface height, which is probably lower than the sea ice surface. But, compared to the difference to the actual surface height, we consider this error negligible. The outer areas of the images (100 pixels in y-direction, the small axis of the image) were cut off to reduce the effect of perspective and corresponding lowering of the resolution in the mapped data. Even with this cut of the data, coverage along flight direction is sufficient since the overlap is large. There might be a small time-drift in the IR camera time (<2 s/day, i.e., about 0.1 s per flight), which can reduce the matching of the position data and the image. Based on the results of the georeferencing and gridding, we estimate the error of geolocation to a maximum of 10 m. For the L-Sites flights with large distances to RV *Polarstern* a larger shift is possible due to, e.g., inhomogeneous ice drift. Since the flights were performed quite far north it has to be considered that the INS data quality was degraded due to the close proximity to the earth rotational axes (Paturel et al., 2015). Further quantification of the actual pixel-wise uncertainty in geolocation can not be performed with the methods available to us. Small shifts in the geolocation can cause issues in the matching of the same features from different images, but this does not change the statistics of the surface temperatures. Further quantification of geolocation uncertainty requires co-location with other point measurements on the floe which was not performed for this dataset.

3.2.6 Temperature-drift correction

During most flights, the temperature changes with time. This becomes clearly visible when different swathes in one flight are crossing. As an example, two neighboring images from different times within a flight have a temperature difference of 2.6 K for the local flights 20191105_01 or 20191230_01 and even 3.95 K for the regional flight 20191230_01. That is physically reasonable because changes in atmospheric parameters like cloud cover, wind speed, or air temperature can alter the surface temperature within the flight duration of about 90 minutes. A further investigation of the reasoning for this temperature drift will be performed in another study. However, this temporal temperature change would make it challenging or not possible to analyze the temperature maps of a whole flight coherently. Thus, we derived the time-fixed surface temperature by a temporal correction of the temperature change. This makes surface features in the data more easily interpretable because the temporal temperature changes do not have to be taken into account. For this, we corrected the surface temperatures of a whole flight by relative differences to the target time in the middle of the flight. The fixed surface temperature $T_{\mathrm{s,fixed}}$ was corrected based on the fit function f_i of the 10th percentile as lowest surface temperature T_{s} values for

each image (Equation 3.2). The 10th percentile was chosen because it represents the fairly constant background temperature of cold snow-covered thick ice and is not influenced by varying warmer features like cracks in the sea ice.

The temporal temperature change was corrected by a fit function with the target time t_0 and the actual time of the pixel t (Equation 3.2):

$$T_{\mathrm{s,fixed}} = T_{\mathrm{s}} - (f_i(t) - f_i(t_0)), \tag{3.2}$$

whereas f_i represents the fit function. Since there are different temporal behaviour for the flights, there are four fit types applied on every flight which are tested for all flights: 1) linear, 2) quadratic, 3) third-degree polynomial, and 4) exponential (Equation 3.3 to Equation 3.6):

$$f_{\mathrm{lin}}(t) = \mathrm{a}_1 \cdot t + \mathrm{c}\,, \tag{3.3}$$

$$f_{\mathrm{quad}}(t) = \mathrm{a}_2 \cdot t^2 + \mathrm{a}_1 \cdot t + \mathrm{c}\,, \tag{3.4}$$

$$f_{\mathrm{poly}}(t) = \mathrm{a}_3 \cdot t^3 + \mathrm{a}_2 \cdot t^2 + \mathrm{a}_1 \cdot t + \mathrm{c}\,, \tag{3.5}$$

$$f_{\mathrm{exp}}(t) = \mathrm{a} \cdot \exp(-\mathrm{b} \cdot (t - t_0)) + \mathrm{c}. \tag{3.6}$$

The best fit type was selected by the smallest Chi-squared statistic. The selected, flight-specific fit type and parameters are listed in Table 3.2. The fit parameters a_1, a_2, a_3, a, b, and c are fixed for each flight. The time t is given in seconds since day start. For the exponential fit, the initial guess was: (a=0, b=0.0001, c=200). Some flights needed a slightly different initial guess with (a=-0.1,b=0.0001,c=200) or (a=0,b=-0.0001,c=200) because otherwise no solution could be found. The fit was performed to data only in the vicinity of the center of the CO, i.e. the position of RV *Polarstern* with 1 km extent in every direction and 100 measurement points from the start and end of the flight to cover the whole period. Often the flight starts and ends close to RV *Polarstern* anyway. As an exception, the mean longitude and latitude were used as the center point for the first CO and the three L-Site grids because during the flight RV *Polarstern* was not overflown. This restriction ensures that mostly the same sea ice surfaces of the CO are considered for the fit. That is especially important for the regional flights where a larger area and therefore a larger variability of surface temperatures is included. The temperature range for every flight (Table 3.2) is an indicator of the magnitude of temperature change in the respective flight. Here we considered the range between start and endpoint as an estimation of the homogeneity of the respective flight.

3.3 Data Records

All data of the IR camera, including the images, the maps, and the plots of the maps, are published in PANGAEA with open access (Thielke et al., 2022d). Specific information about the data, like the list of processed and unprocessed flights as well as definitions of variables and their dimensions can be found in our data manual (Thielke et al., 2022a), which will be updated if changes occur. The data were converted from the raw, binary format IRB to a NetCDF4 file format. There are two types of datasets with one that contains the image-based data and the other that contains processed maps with 1 m and 5 m horizontal resolution. The 5 m grid is added for smaller file size and easier data handling but is otherwise identical to the 1 m dataset. Each dataset type contains one NetCDF file for each flight. For the single images dataset all images of one flight are combined in one NetCDF file with the single images aligned along the third dimension (time). All files include the stereographic projection parameters used for the mapping.

The flights have two identifications that can be used: (i) the Flight-ID, including the date of the flight, and (ii) the Device Operation, a unique ID, which was created during the MOSAiC expedition. The main variable is the surface temperature complemented by additional data necessary to process and interpret the data. All the position data of the helicopter are required to reference each pixel to the correct geolocation. The position data are published with the temperature data from the IR Camera but recorded with the embedded GNSS inertial system Applanix (SENSOR, 2021a) which was installed in the helicopter as well. The position data of RV *Polarstern* (Rex, 2020; Haas, 2020; Kanzow, 2020) from the device Hydrins 1 are used in a temporal resolution of 10 minutes, but were interpolated to 1 second for the ice drift correction. Also the 10 min weather data from *Polarstern* are used (Schmithüsen et al., 2021a,c,b). Both, position and weather data, were downloaded from the AWI data platform (https://dship.awi.de). The mean sea surface height data is based on Andersen and Knudsen (2009) and taken from https://ftp.space.dtu.dk/pub/DTU21/1_MIN/. The processing steps of the data are summarized in Figure 3.1.

3.4 Technical validation

This section presents the technical validation of the surface temperature data concerning temperature structures in the images, high resolution map and the temperature distributions, artefacts in the maps, as well as the atmospheric conditions during the helicopter flights.

Flight ID	Fit type	a1	a2	a3	c	a	b	T_{start} / K	T_{end} / K	T_{range} / K
20191002_01	linear	-0.000072	-	-	266.302890	-	-	264.74	264.58	-0.16
20191020_01	exponential	-	-	-	258.045648	-4.302381e+00	1.501635e-03	253.74	258.00	4.26
20191029_01	linear	0.000054	-	-	255.915111	-	-	256.40	256.57	0.17
20191105_01	polynomial	-0.409536	1.584149e-05	-2.044194e-10	3774.198780	-	-	245.71	241.73	-3.98
20191112_01	exponential	-	-	-	248.708455	-4.325600e-03	-1.497353e-03	248.70	246.61	-2.09
20191112_02	linear	-0.000245	-	-	256.629279	-	-	247.42	246.94	-0.49
20191119_01	polynomial	-0.598430	3.687198e-05	-7.537312e-10	3475.193411	-	-	252.54	255.19	2.65
20191130_01	exponential	-	-	-	233.891970	1.797889e+00	2.399643e-03	235.69	233.89	-1.80
20191206_01	exponential	-	-	-	239.973808	-6.599342e-01	1.239892e-02	239.31	239.97	0.66
20191224_01	exponential	-	-	-	239.124792	-2.166376e-01	-3.849560e-04	238.91	236.91	-1.99
20191225_01	linear	-0.000383	-	-	259.256967	-	-	239.58	237.66	-1.92
20191228_01	linear	-0.000114	-	-	235.795076	-	-	232.89	232.39	-0.50
20191230_01	exponential	-	-	-	237.346076	4.226815e+00	2.073296e-03	241.57	237.35	-4.23
20200107_01	exponential	-	-	-	234.376458	8.064973e-07	-2.406496e-03	234.38	234.79	0.41
20200107_02	linear	0.000234	-	-	223.698382	-	-	234.05	235.34	1.29
20200108_01	exponential	-	-	-	3938.795777	-3.699968e+03	4.535519e-08	238.83	239.20	0.38
20200108_03	linear	0.000770	-	-	213.448575	-	-	240.43	242.26	1.83
20200108_04	polynomial	6.814246	-1.428722e-04	9.981858e-10	-108058.120312	-	-	240.30	238.96	-1.34
20200116_01	exponential	-	-	-	240.280738	2.140605e+00	7.520096e-04	242.42	240.36	-2.06
20200116_02	exponential	-	-	-	240.638773	-1.312025e+00	5.731116e-04	239.33	240.58	1.25
20200121_01	exponential	-	-	-	233.777378	2.341788e+00	2.278946e-03	236.12	233.78	-2.34
20200123_01	exponential	-	-	-	233.528294	3.893223e-01	2.898193e-03	233.92	233.53	-0.39
20200123_02	linear	0.000039	-	-	231.193934	-	-	233.08	233.20	0.12
20200125_01	quadratic	-0.001041	3.797253e-09	-	274.179663	-	-	234.41	233.27	-1.14
20200128_01	polynomial	-0.060552	2.275804e-06	-2.846043e-11	766.664327	-	-	230.98	230.40	-0.58
20200202_01	quadratic	-0.001395	1.891434e-08	-	254.646072	-	-	231.93	231.36	-0.57
20200204_01	quadratic	-0.010815	1.760454e-07	-	402.498456	-	-	239.63	237.34	-2.29
20200209_01	linear	-0.001180	-	-	286.716503	-	-	239.57	233.12	-6.45
20200212_01	polynomial	-0.013750	3.870068e-07	-3.623340e-12	394.977441	-	-	232.53	232.48	-0.04
20200217_01	polynomial	-2.414028	9.524740e-05	-1.252518e-09	20624.648178	-	-	233.12	232.82	-0.31
20200217_02	exponential	-	-	-	232.575541	-7.909334e-01	1.417581e-03	231.78	232.58	0.79
20200227_01	quadratic	-0.004935	5.481852e-08	-	343.906063	-	-	233.00	232.92	-0.08
20200321_01	quadratic	-0.000908	1.255406e-08	-	250.002788	-	-	234.13	233.57	-0.56
20200321_02	linear	-0.000634	-	-	261.227104	-	-	237.33	234.14	-3.19
20200423_01	exponential	-	-	-	248.087844	2.106613e+00	-9.915066e-05	250.19	252.07	1.88

Table 3.2: Temporal temperature correction: Fit parameters of surface temperature T_s according to Equation 3.3, 3.4, 3.5, and 3.6 for every flight. For each flight the best fit type (linear, quadratic, polynomial, or exponential) is selected. The start and end temperature (T_{start} and T_{end}) as well as the resulting temperature range T_{range} indicate the trend and the amount of temperature change within a specific flight.

3.4.1 Temperature structures in images

Single images have a lot of information and illustrate the potential of the data. Here we present three example images from 05 November 2019, 25 January 2020, and 23 April 2020. Please mind that the three cases have different temperature ranges.

Figure 3.7 (a) illustrates the thermal signature due to human influence. RV *Polarstern* is visible in the image due to the warm structures of the ship. A warmer area on the starboard side of the ship was the logistics area and appears because some snow was compressed or removed and therefore the heat conductivity increased. Even single tracks can be identified because they are warmer than the surroundings which can be explained with the same principle of heat conduction. Other features in the bottom half of the image are linear and cold structures, which indicate the deformation of the ice, i.e., ridges. We can also identify blurry, cold spots that could be caused by snowdrift. Thus, topographical features can be investigated from this two-dimensional temperature variation.

In Figure 3.7 (b), a lead with internal surface temperature variability is present. The warmer temperatures in the middle of the image are caused by a newly opened lead, which is covered by thin ice, whereas the surrounding thick ice is substantially colder. There is a temperature change orthogonal to the lead edges with warmer temperatures on the left-hand side and colder on the right-hand side. The temperature difference can be explained by different thin ice thicknesses which could be caused by ice movement and associated rafting due to wind forces. Wind pressure can cause compressed and therefore colder ice whereas reduced ice thickness leads to higher temperatures.

For Figure 3.7 (c) most of the surface is thick, snow-covered ice, which is characterized by colder temperatures. The warm linear structure, i.e., a lead, reaches from the lower left to the upper middle part. Next to the lead, there is a slightly warmer line and in the lower left a high variability of warm and cold surface temperatures. The corresponding RGB image, taken at the same time, illustrates the visual appearance of the same surface (Figure 3.7 (d)). We selected this particular case because sufficient daylight was available for the RGB images, whereas during the polar night it was too dark to see the surface in the visible range. The white area corresponds with the cold, snow-covered sea ice, whereas the warm crack has the dark ocean color. The comparison illustrates that the surface of leads is affected predominantly by the warmer ocean compared to the colder atmosphere. Also, the thin line next to the lead can be identified in the visible range. The high variability in the lower left part is caused by broken-up ice, i.e., small floes, which result in partly missing insulation from consolidated snow-covered ice.

3.4.2 High resolution temperature maps

Combining the images to a map provides the opportunity to analyze the spatial characteristics and variability of the surface temperature for a larger area. The gridded temperature

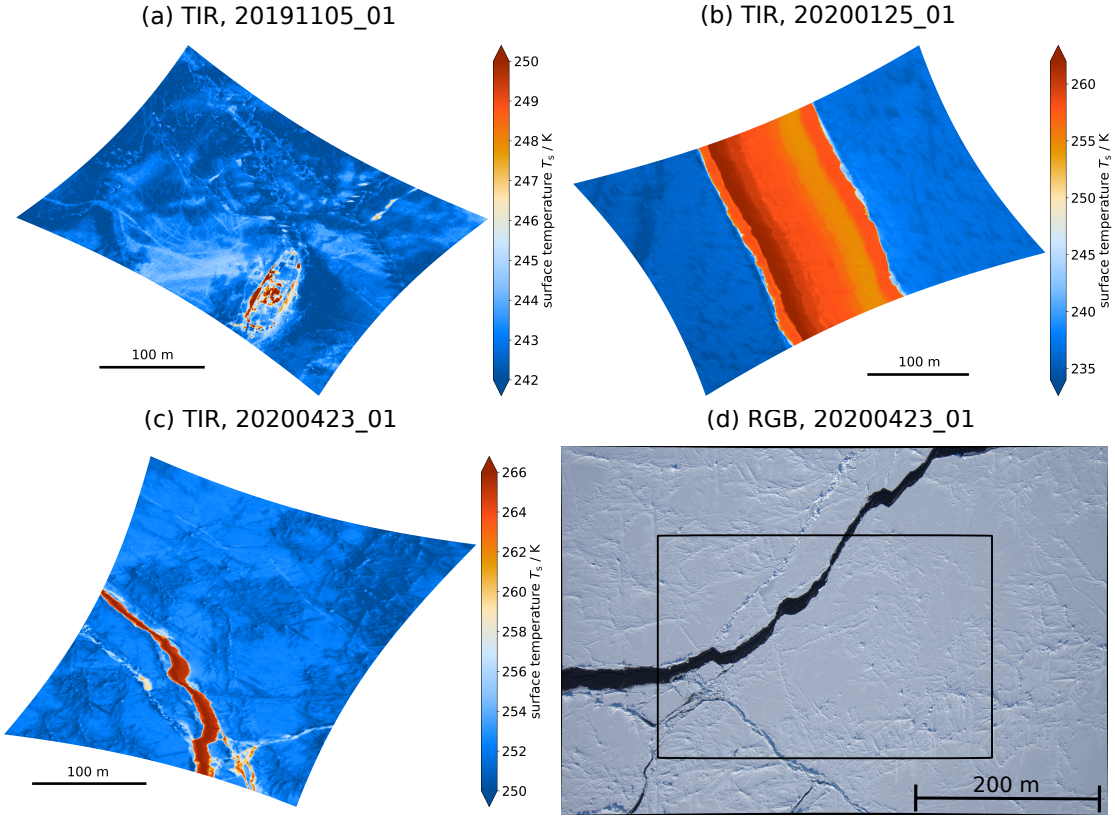

Figure 3.7: The images show example images recorded with the IR camera. Please note that all TIR images have a different temperature range and are oriented with North to the top and East to the right. (a) Surface temperature image from the flight 20191105_01 at 07:22:14 UTC. The warm structures show RV *Polarstern* in the lower part. Next to the ship, the human influence is visible by slightly warmer surface temperatures in the logistics area and the tracks going away from the ship. Topographic features stand out from a more homogeneous area in the upper part of the image. (b) Surface temperature image from the flight 20200125_01 at 12:49:11 UTC. The warm middle part is a crack in the ice with different warm temperature regimes (reddish) indicating different thin ice thicknesses. The outer sides are colder (bluish) because of thick ice which is covered by snow. (c) Surface temperature image from the flight 20200423_01 at 07:45:47 UTC. The area is dominated by cold temperatures due to thick, snow-covered, and partly deformed ice. A warm crack is reaching from the lower part to the middle left part. In the lower right part of the image, smaller cracks are visible. (d) The RGB image form 23 April 2020 is taken at the same time as the TIR image (c) and shows the surface characteristics in the visible range. The black rectangle define the area covered by the TIR image (c). The thick, snow-covered sea ice surface appears white while the crack is dark due to the ocean color. (Credits for the RGB image: Alfred-Wegener-Institut/Gerit Birnbaum).

data are corrected for ice drift as well as for the temporal temperature change as explained above and named as time-fixed surface temperature.

Figure 3.8 (a) shows a map of the time-fixed surface temperature for the local flight on 02 October 2019 and shows the initial MOSAiC ice floe and its surroundings. This flight covered the area of and around the CO which was not installed yet. In the center, very low temperatures can be associated with thicker ice which survived the summer and was the main area for the CO. The surroundings have higher temperatures which represents thinner ice. The central thicker ice area is framed by warm thin structures from the north-east and south-west. These are cracks in the ice with a surface of open water or thin ice.

The time-fixed surface temperatures for the regional flight on 23 January 2020 appear cold and rather homogeneous (Figure 3.8 (b)). This is plausible because the air temperature was very cold for a longer period. Consequently, the ice thickness increased and the MOSAiC ice floe consolidated with the surrounding ice. For this triangle flight pattern, the maps are more difficult to interpret because the area is larger with a smaller coverage of surface temperature data. Nevertheless, warmer linear structures, i.e. leads, are present in this flight, for example, at the northernmost L-Site as well as between the two southern L-Sites.

The temperature distributions of the two flights have different characteristic (Figure 3.8 (c) and (d)). The flights have a different temperature regime and a different range (1st to 99th percentile). The local flight on 02 October 2019 reaches from 264.42 K to 268.77 K, resulting in a range of 4.35 K, whereas the regional flight on 23 January 2020 has a wider range from 233.56 K to 252.51 K, resulting in a range of 18.96 K. Local minima discriminate different ice classes or surface types.

The local flight (Figure 3.8 (c)) has two peaks in the colder part and one at the warmer end of the temperature distribution. These peaks in the distribution reflect the sea ice properties described above. The warmest peak at 268.6 K represents the cracks in the ice covered by open water or thin ice. The coldest peak at 265.0 K is caused by the thick ice of the future CO in the center of the map whereas the middle peak at 265.8 K is related to the slightly thinner ice in the surroundings.

The regional flight (Figure 3.8 (d)) has mainly very low surface temperatures and therefore the global maximum in the coldest part of the distribution at 234.2 K. Aligned with the two-dimensional appearance in the map, the ice conditions on 23 January 2020 were dominated by thicker ice. Still, there is a variation in the warmer part of surface temperature distribution, associated with thin ice, which is separated from the lowest temperatures by the minimum at around 247.5 K. This thin ice cover can still appear under very cold conditions because it started to grow later in cracks of the ice that were opened due to ice dynamics. The several local minima in the warmer part of the distribution

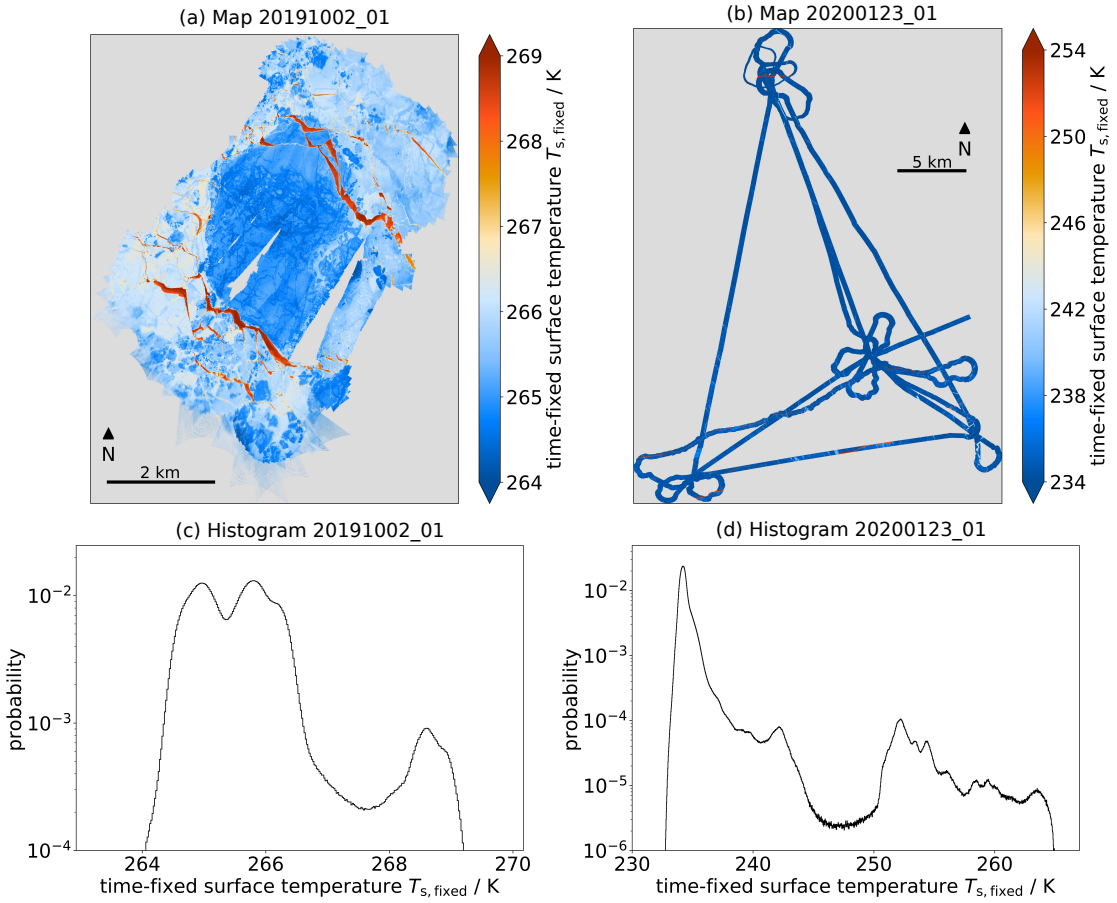

Figure 3.8: The combination of maps (a,b) and histograms (c,d) contains the surface temperature information of the advanced data product. Please note the different temperature ranges for the two flights. (a) The time-fixed surface temperature map of the local CO flight 20191002_01 is dominated by cold temperatures (bluish) in the middle part where there is thicker ice surrounded by thinner ice (warmer, light blue). Warm linear structures (reddish) are cracks in the ice, created by ice dynamics, with a surface cover of open water or thin ice. (b) The time-fixed surface temperature map of the regional L-Site flight 20200123_01 consists of mainly cold temperatures (bluish) representing thick, consolidated ice broken by a few cracks (reddish) in the southernmost east-west line and the northernmost L-Site. The black diamond indicates the position of RV *Polarstern* whereas for 20191002_01 RV *Polarstern* was not at the floe yet. The logarithmic probability of the time-fixed surface temperature for the gridded data for (c) local CO flight 20191002_01 and (d) regional L-Site flight 20200123_01. With the logarithmic scale, the small probabilities towards the higher temperatures are better distinguishable. The main maxima in the respective cold range indicate the main ice classes.

indicate that there are several distinct thin ice classes. These are likely associated with lead opening events at different lag times before the overflight, i.e. the length of the ice growth period is different for the different temperature classes. Another option is rafting of thin ice in leads.

3.4.3 Artefacts in the maps

As already discussed in the methodology there are some uncertainties with the data, which influences the outcome of our processing, i.e, the maps. In Figure 3.9, we present possible artefacts the user should be aware of. Within the surface temperature maps temperature jumps can exist (Figure 3.9 (a)). There are two possible reasons. 1) The regular internal calibration adjusts the temperature to compensate for a temperature drift and thus can cause an abrupt shift. 2) (shown here) The temporal drift which could not be fully corrected results in a temperature shift along the intersection of two swaths with a given time difference. The geolocation uncertainty (Figure 3.9 (b)) can cause shifts between two overlying tracks which results in a discontinuity of the sea ice structures. Figure 3.9 (c) shows the influence of high incidence angles. Large incidence angles (i.e., roll) during a turn have larger distortions and can have slight shifts in geolocation. From this, blurry structures can be caused and therefore we recommend using temperature values with incidence angles (roll) smaller than 20 degrees. But for statistical interpretation, the high incidence areas can be used as additional data. For a low temperature contrast scene, vertical lines can be visible. These vertical lines come from the images and are a known issues of the measurement technology of microbolometers as in Alhussein and Haider (2016).

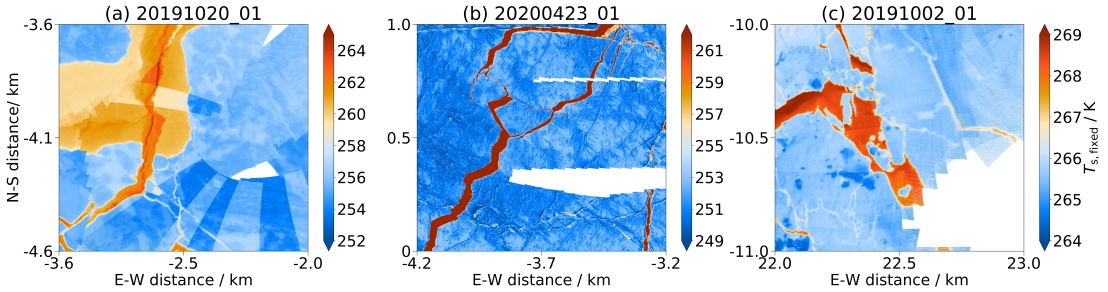

Figure 3.9: Three examples of artefacts from three different flights which can occur in the maps of the time-fixed surface temperature $T_{s,fixed}$. All examples show a 1 km by 1 km part of the 1 m resolution map. In panel (a) temperature jumps from flight 20191020_01 are shown. They occur because images from different times are taken while the surface temperature has a temporal drift during the flight. In panel (b) a geolocation offset between different swaths of flight 20200423_01 is illustrated, probably caused by irregular ice drift in between the recording. Panel (c) shows blurry structures in a area with high incidence angles during the flight 20191002_01.

3.4.4 Atmospheric conditions

As described above, the surface temperature is influenced by the atmosphere. Here we provide the basic meteorological information for all flights. There is no sufficient data for a quantitative analysis. The atmospheric data lack the spatial information which we would need to cover our flight area, especially for the spatially variable cloud coverage. The atmospheric parameters from RV *Polarstern* are presented with start/end conditions in Figure 3.10 and the cloud conditions from the flight weather reports (Deutscher Wetterdienst (German Weather Service), 2021) are listed in Table 3.3. This helps to better assess the potential atmospheric effect on the surface temperature. The flights were performed only during calm conditions which reduce the atmospheric influence to a minimum. The atmospheric parameters measured at *Polarstern* are mostly stable within one flight while they only change from flight to flight (Figure 3.10).

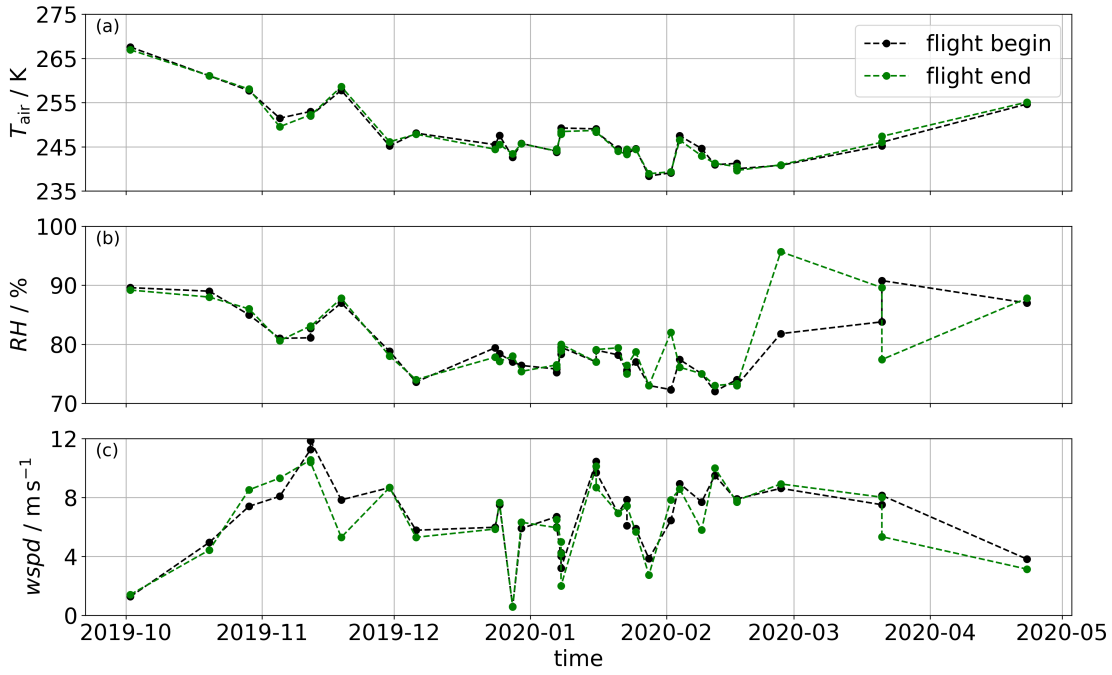

Figure 3.10: The meteorological conditions at *Polarstern* (Schmithüsen et al., 2021a,c,b) at the beginning (black) and end (green) of all flights for the parameter (a) air temperature T_{air}, (b) relative humidity RH, and (c) wind speed $wspd$. Additional cloud information are listed in Table 3.3.

The air temperature (Figure 3.10 (a)) was stable within each flight with changes of at most 2 K. The relative humidity changes (Figure 3.10 (b)) for the flights on 27 February 2020 and 21 March 2020 and thus can influence the measured surface temperature due to changes in emissivity within the atmospheric pathway. Figure 3.10 (c) shows that the wind speed varies the most within the flights in October/November and on 21 March 2020. The

given cloud conditions are expected to have a minor influence except for potential local fog patches or sea fog over leads. The reported clouds are considerably higher than the flight altitude. Nevertheless, a change in cloud cover could change the incoming longwave radiation and therefore the surface temperature.

Usage Notes

All data are provided in a NetCDF and do not need specific software to be read.

Images

The image-based data include time, positioning of the device, and georeferenced coordinates for each pixel which allows gridding of all images without repeating the georeferencing. Thereby the overlap of the images can be used differently than done here or other methods could be applied for the gridding. Based on the temperature arrays and the position and rotation data of the helicopter, the georeferencing can be reproduced.

Maps

The map-based data are provided with longitude/latitude coordinates as well as the relative coordinates, which are distances relative to the position of RV *Polarstern*. The rotated relative coordinates provide a consistent coordinate system for all flights. This allows co-locating measurements for different times during the expedition while the longitude and latitude are changing due to the ice drift. For co-location with measurements without direct relation to the expedition, longitude and latitude can be used. For the analysis of the time series of gridded data, the RV *Polarstern*-centered coordinate system based on a stereographic projection with constant relative distances is recommended. Within the range of 5 to 40 km, the distortion is assumed to be negligible.

Flight ID	Cloud coverage	Cloud type	Lower cloud level / ft	Low clouds/mist/fog
20191002_01	BKN/OVC	ST/SC	800-1300	possible
20191020_01	SCT/BKN	SC	2000-3000	possible
20191029_01	BKN/OVC	SC	3000-4000	possible
20191105_01	SCT/BKN	SC/AS	3000-4500	occasional
20191112_01	SCT/BKN	SC/AS	3000-4000	occasional
20191112_02	SCT/BKN	SC/AS	3000-4000	occasional
20191119_01	SCT/BKN	CI/CS	>10000	occasional
20191130_01	-	-	-	occasional
20191206_01	FEW/SCT	AC/CI	>10000	occasional
20191224_01	-	-	-	occasional
20191225_01	SCT	SC	2000	occasional
20191228_01	SCT/BKN	SC/AC	2500-4500	possible
20191230_01	BKN	SC/AC	4000-5000	possible
20200107_01	SCT/BKN (isolated)	SC	1500-3000	possible
20200107_02	SCT/BKN (isolated)	SC	1500-3000	possible
20200108_01	SCT/BKN (isolated)	SC	4000	possible
20200108_03	SCT/BKN (isolated)	SC	4000	possible
20200108_04	FEW/SCT (isolated)	SC	3500-6000	possible
20200116_01	SCT/BKN	ST/SC	400-1000	occasional
20200116_02	SCT/BKN	ST/SC	400-1000	occasional
20200121_01	SCT/BKN (isolated)	SC	2500-3500	possible
20200123_01	FEW/SCT	ST	200-400	possible
20200123_02	FEW/SCT	ST	200-400	possible
20200125_01	FEW/SCT	ST	300	possible
20200128_01	SCT/BKN (isolated)	ST	300-600	possible
20200202_01	SCT/BKN (isolated)	ST	200-600	possible
20200204_01	SCT/BKN (isolated)	ST	200-600	possible
20200209_01	SCT/BKN	AS	>6000	possible
20200212_01	SCT/BKN (isolated)	ST	500	possible
20200217_01	SCT/BKN (isolated)	ST/SC	500-1000	possible
20200217_02	SCT/BKN (isolated)	ST/SC	500-1000	possible
20200227_01	SCT/BKN (isolated)	ST	500	possible
20200321_01	SCT/BKN (isolated)	ST	1000	possible
20200321_02	SCT/BKN (isolated)	ST	1000	possible
20200423_01	FEW/SCT (isolated)	AC	8000	possible

Table 3.3: Cloud conditions during the helicopter flights based on the flight report by the DWD (Deutscher Wetterdienst (German Weather Service), 2021). Please note, that high cirrus are not included if low clouds are present, because the low clouds have a significant higher influence on the surface temperature. The used abbreviations for cloud type are: AC=Altocumulus, AS=Altostratus, CI=Cirrus, CU=Cumulus, SC=Stratocumulus, ST=Stratus; and for cloud coverage: FEW=Few (1/8-2/8), SCT=Scattered (3/8-4/8), BKN=Broken (5/8-7/8), OVC=Overcast (8/8).

Application examples

Further ideas for the application of the surface temperature could be the use of temperature distributions of the sea ice surface to derive other surface properties, like ice types. Two-dimensional temperature patterns can be used to determine topographic features, which is difficult based on the one-dimensional temperature distribution due to the small temperature differences. Besides the statistical analysis, digital image processing methods could be applied to the image data. Generally, there is a lot of potential for analysis and comparison, in particular, in the context of the broad spectrum of measurements during the MOSAiC expedition (Nicolaus et al., 2022; Shupe et al., 2022; Rabe et al., 2022). The variety of measurements taken during the expedition should motivate to compare find-

ings among different variables to gain an improved understanding of connected processes between ocean, ice, air as well as biochemical components of the Arctic.

Based on the data presented here, further investigations of the thermal properties of sea ice will be performed and compared to other measurements taken at the same time and/or within the same area to gain a better process understanding of the Arctic climate system with the focus on the snow/ice-air interface. While the dataset presented here is suitable for most applications, there is still room for improvement for specific cases, mainly in terms of accuracy for the surface temperature values and the geolocation. All presented data are available under open access. New approaches for the data are encouraged and discussions with the authors of this paper are welcome.

Code availability

The data processing and analysis were performed with Python 3. The code responsible for processing and analyzing the maps and the images is published under open access (Thielke and Huntemann, 2022). The used colormap for the temperature is individually defined and provided as well. It is suited to visualize temperature structures for Arctic winter conditions. In case of specific requests, please contact the corresponding author directly.

Acknowledgements

This work was supported by the German Ministry for Education and Research (BMBF) as part of the International Multidisciplinary drifting Observatory for the Study of the Arctic Climate (grant MOSAiC20192020), and IceSense (grants 03F0866B and 03F0866A). We acknowledge the support by the Deutsche Forschungsgemeinschaft (DFG) through the International Research Training Group IRTG 1904 ArcTrain (grant 221211316), and the MOSAiCmicrowaveRS project (grant 420499875). We thank all persons involved in the expedition of the Research Vessel *Polarstern* during MOSAiC in 2019-2020 (AWI_PS122_00), and especially, HeliService and their pilots (Nixdorf et al., 2021). Without them the helicopter survey flights and the collection of this dataset would not have been possible. We thank Alexander Mchedlishvili for proof reading the manuscript. We thank the DWD for providing us the flight weather reports of Leg 1, 2, and 3 (Deutscher Wetterdienst (German Weather Service), 2021).

Chapter 4

Preconditioning of melt ponds

This chapter is based on the following publication:

Thielke, L., N. Fuchs, G. Spreen, B. Tremblay, G. Birnbaum, M. Huntemann, N. Hutter, P. Itkin, A. Jutila, M. A. Webster (2023). Preconditioning of summer melt ponds from winter sea ice surface temperature. *Geophysical Research Letters*, 50, e2022GL101493. https://doi.org/10.1029/2022GL101493

Relevance

In this chapter, we address the second research question R2: *To which extent do winter surface temperatures reveal information about the characteristics of melt ponds?*

Melt ponds are a crucial part of the Arctic summer heat budget because they lower the surface albedo of sea ice and, thus, contribute to the ice-albedo feedback. The MOSAiC expedition provided a unique opportunity for high-resolution helicopter-borne observations of the same ice in winter and summer. The surface temperature maps at 1 m resolution, presented in Chapter 3, have the ability to resolve warm anomalies which align with the geometries of summer melt ponds. From this, the conditions in winter, before the actual appearance of the leads, can be investigated.

Contributions

I contributed to the conceptualization of this study, data curation, methodology, and formal analysis. I performed the investigation and wrote the first draft of the manuscript.

Abstract

Comparing helicopter-borne surface temperature maps in winter and optical orthomosaics in summer from the year-long Multidisciplinary drifting Observatory for the Study of Arctic Climate (MOSAiC) expedition, we find a strong geometric correlation between warm anomalies in winter and melt pond location the following summer. Warm anomalies are associated with thinner snow and ice, i.e., surface depression and refrozen leads, that allow for water accumulation during melt. Warm surface temperature anomalies in January were 0.3 K to 2.5 K warmer on sea ice that later formed melt ponds. A one-dimensional steady-state thermodynamic model shows that the observed surface temperature differences are in line with the observed ice thickness and snow depth. We demonstrate the potential of seasonal prediction of summer melt pond location and coverage from winter surface temperature observations. A threshold-based classification achieves a correct classification for 41% of the melt ponds.

Plain Language Summary

We compare winter surface temperatures from an infrared camera with summer photographs of sea ice with melt ponds. The datasets were recorded from a helicopter during the Multidisciplinary drifting Observatory for the Study of Arctic Climate (MOSAiC) expedition. Melt ponds form on sea ice in summer when the snow melts and water accumulates in the lower locations on the ice floes. Melt ponds are very important for the Arctic energy budget because they strongly change the sea ice brightness and thus the amount of solar energy absorbed by the ice. We find surface characteristics with similar size and location between warmer areas in winter and the location of melt ponds in summer. For a better process understanding, we calculate the surface temperature with a simple model and find that the warm temperature anomalies are due to thinner ice and snow. Stronger warm temperature anomalies appear in new cracks in the ice which are covered with newly formed, thin ice. With a temperature-based classification, we are able to estimate the summer melt pond fraction.

4.1 Introduction

Melt ponds on Arctic sea ice are an important component of the summer energy budget (e.g., Nicolaus et al., 2012). Melt water collects at the ice surface during summer melt in topographic lows. Melt ponds contribute to the ice–albedo feedback by lowering the surface albedo (e.g., Curry et al., 1995; Light et al., 2022). For autumn, Anhaus et al. (2021) showed that melt ponds influence light transmission. The preconditioning of melt ponds can be partly explained by ice topography (e.g., Flocco et al., 2015; Polashenski et al., 2012), predominately for deformed second-year ice (SYI), or snow dunes and snow accumulations (Petrich et al., 2012; Polashenski et al., 2012), mainly on level first-year ice (FYI). Additional factors for melt pond preconditioning are ice permeability and pond hydrology (Eicken et al., 2002, 2004). There are distinct differences between melt ponds on level or deformed ice. The melt pond location and size are controlled by the topography of deformed ice while on level ice melt ponds can cover large areas (Webster et al., 2022). The ice topography, induced by ridges or leads, are either remnant from the previous seasons' dynamic events or can be newly created due to ice dynamics and/or snow accumulation (Polashenski et al., 2012). Also, refrozen melt ponds can have a lower ice surface elevation and ice thickness compared to the surroundings. There are still large uncertainties in models to predict melt pond evolution, especially their parameterization of size, depth, and effect on light transmission (Light et al., 2008; Flocco et al., 2012; Webster et al., 2022).

In the following, we document how anomalies in the winter sea ice surface temperature are connected with melt pond coverage the following summer; opening the door for the use of high-resolution infrared satellite data for seasonal prediction of melt pond fraction (MPF). Higher resolution thermal infrared (TIR) satellites, like Landsat 8, focus to date only on the lower latitudes. We use high-resolution, helicopter-borne surface temperature maps from the Arctic in winter to identify areas of warmer surface temperatures compared to the surroundings (warm anomalies). We strive to gain more knowledge on the preconditioning effects of such anomalies for the next summer's MPF. Surface temperatures in winter are sensitive to the ice and especially snow thickness, which both insulate the surface from the warmer ocean.

Specifically, we present a case study from the observations of the MOSAiC expedition from September 2019 to October 2020 (Nicolaus et al., 2022; Shupe et al., 2022; Rabe et al., 2022). RV *Polarstern* (Alfred-Wegener-Institut Helmholtz-Zentrum für Polar- und Meeresforschung, 2017) drifted with the sea ice from the northern Laptev Sea towards the Fram Strait. This study combines helicopter-borne TIR imaging with optical orthomosaics and topography data from an airborne laser scanner (ALS), snow and ice thickness measurements from ground-based transects, as well as atmospheric measurements of temperature, wind speed, and longwave radiation.

We approximate the location and area of summer melt ponds using the preceding winter's sea ice surface temperature data. Based on the comparison of the helicopter-borne maps, we find warm surface ice temperature anomalies in winter at the location of the next summer's melt ponds. We use a simple one-dimensional thermodynamic model to identify the drivers of the warm anomalies. To conclude, we discuss the potential, limitations, and implications of these novel findings to use them for the improvement of modelling and new ideas for high-resolution satellite remote sensing.

4.2 Data and Methods

We investigate the same sea ice area several months apart and perform a one-to-one comparison between summer and winter. The main datasets are recorded with helicopter-borne imaging: TIR for the polar night (Thielke et al., 2022e) and optically during the polar day. The rich additional MOSAiC datasets are ideally suited to constrain the physical conditions during the seasons.

4.2.1 Study area

The study area (1.3 km × 1.3 km) consists of level FYI as well as deformed SYI that survived the previous summer melt (Krumpen et al., 2020). The remnant of the MOSAiC floe observed in summer during leg 4, was during winter (legs 1 and 2) in the deformed ice area at the edge of the main sampling sites (about 1.5 km distance from RV *Polarstern*). The area of the MOSAiC floe in summer is marked by the red polygon in Figure 4.1.

4.2.2 Optical orthomosaic in summer

We use the optical orthomosaic from 30 June 2020 as the ground truth for the MPF on the MOSAiC floe during summer. The orthomosaic, a composite of aerial RGB images, clearly illustrates the melt ponds as darker grayish-blueish areas in contrast to white ice and the almost black open water around the floe. These optical differences are used in a supervised classification algorithm developed for aerial images of sea ice to semantically divide the orthomosaic into surface type class objects. To reduce the impact of noise on pixel level, the minimum size of the resulting *snow/ice*, *pond*, *submerged ice*, and *open water* objects is limited to 100 pixels at a pixel area of 0.25 m^2 (Fuchs, 2023). The estimated error is below ±2% for the derived MPF.

4.2.3 Aerial surface temperatures in winter

The surface temperature maps are based on helicopter-borne TIR imaging, performed with the VarioCam HD head 680 camera with a brightness temperature precision of 0.02 K and accuracy of 1 K (Thielke et al., 2022e). We use gridded surface temperatures at 1 m

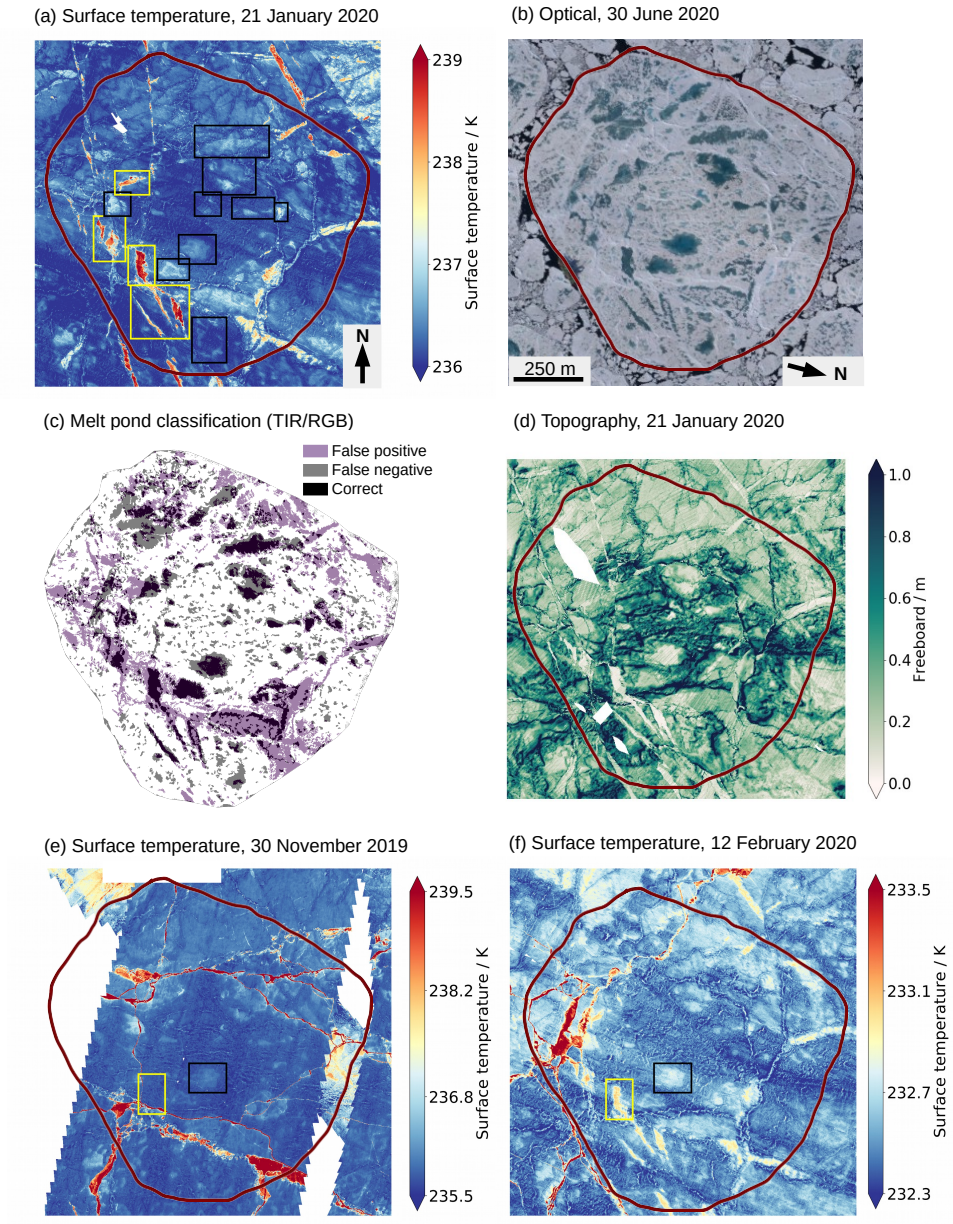

Figure 4.1: (a) Surface temperature map (TIR) on 21 January 2020 with the boxes indicating the warm anomalies. Yellow boxes are refrozen leads (RL) and black boxes are topography controlled (TC). (b) Optical orthomosaic (RGB) from 30 June 2020 showing the melt ponds as grayish-blueish colors. (c) Overlay of melt pond classification based on a surface temperature threshold on 21 January 2020 and based on RGB classification on 30 June 2020 with fractions of 26% and 22%, respectively. [Purple: only classified by TIR (false positive); Gray: only classified by RGB (false negative); Black: classified in both data (correct).] (d) Freeboard map showing snow surface topography on 21 January 2020. Surface temperatures on (e) 30 November 2019 and (f) 12 February 2020 (note that the colorbar is different for better visibility). The two boxes are indicating the RL and TC cases highlighted in the study. The outline of the summer ice floe as a red polygon for reference.

horizontal resolution. We focus on data from 21 January 2020 that contained numerous distinct thermal features. For comparison, we show the warm anomalies in the flight on 30 November 2019 and 12 February 2020 (Figure 4.1 e,f). The temperature anomalies which originate from leads only appeared after end of December 2019 and their temperature signal decreased with time. The topography-driven temperature anomalies vary in the same range of temperature difference in between 30 November 2019 and 12 February 2020. Additional information about the aerial surface temperatures, within the context of the study area, is provided in the Supplement (Section 4.6).

4.2.4 Definition of warm anomalies

There are two approaches used to define the warm anomalies on the temperature map of 21 January 2020. The first method is more specific to each of the 13 identified cases (boxes in Figure 4.1 a), which is more applicable to the meter scale, while the other is a temperature threshold for identifying warm patches across the 1.5 km floe to perform a melt pond classification.

1) Based on the "ground truth" of the summer optical orthomosaic, we manually defined 13 warm anomalies in the surface temperature map from 21 January 2020. In each box, we analyze two manually selected temperature cross-sections covering both the warm anomaly and the surroundings (Figure 4.2). We further manually classify the cross-sections in an "anomaly" and "surrounding" part. The temperatures of the two classes are averaged while the transitions between the two are not analyzed. From that, the surface temperature difference $\Delta T_{\mathrm{s,obs}}$ between the two classes is calculated. For the precise definition of the melt pond location, we need a manual classification because the larger scale spatial variability is in the same range as the temperature difference of the warm anomalies.

2) To retrieve the MPF of the whole study area we apply one fixed temperature threshold of 236.35 K to the aerial surface temperature to classify it in melt ponds and ice. The threshold is manually selected by tuning for the most reasonable outcome of the temperature classification compared to the optical ground truth. From this, we can investigate the performance of the winter melt pond classification based on surface temperatures. The classification is very sensitive to the threshold. Varying the temperature threshold between 236.0 K and 236.7 K results in a large spread of the classified area ranging from 90% to 10%. Thus, a precise selection of the threshold is crucial. Due to the additional dependence on meteorological conditions, a single generalized threshold is not applicable, but an individual situation-specific tuning could be used. We compare the temperature classification to the classified orthomosaic in terms of location and fraction. Both maps are manually superimposed to achieve the best overlap (Figure 4.1 c).

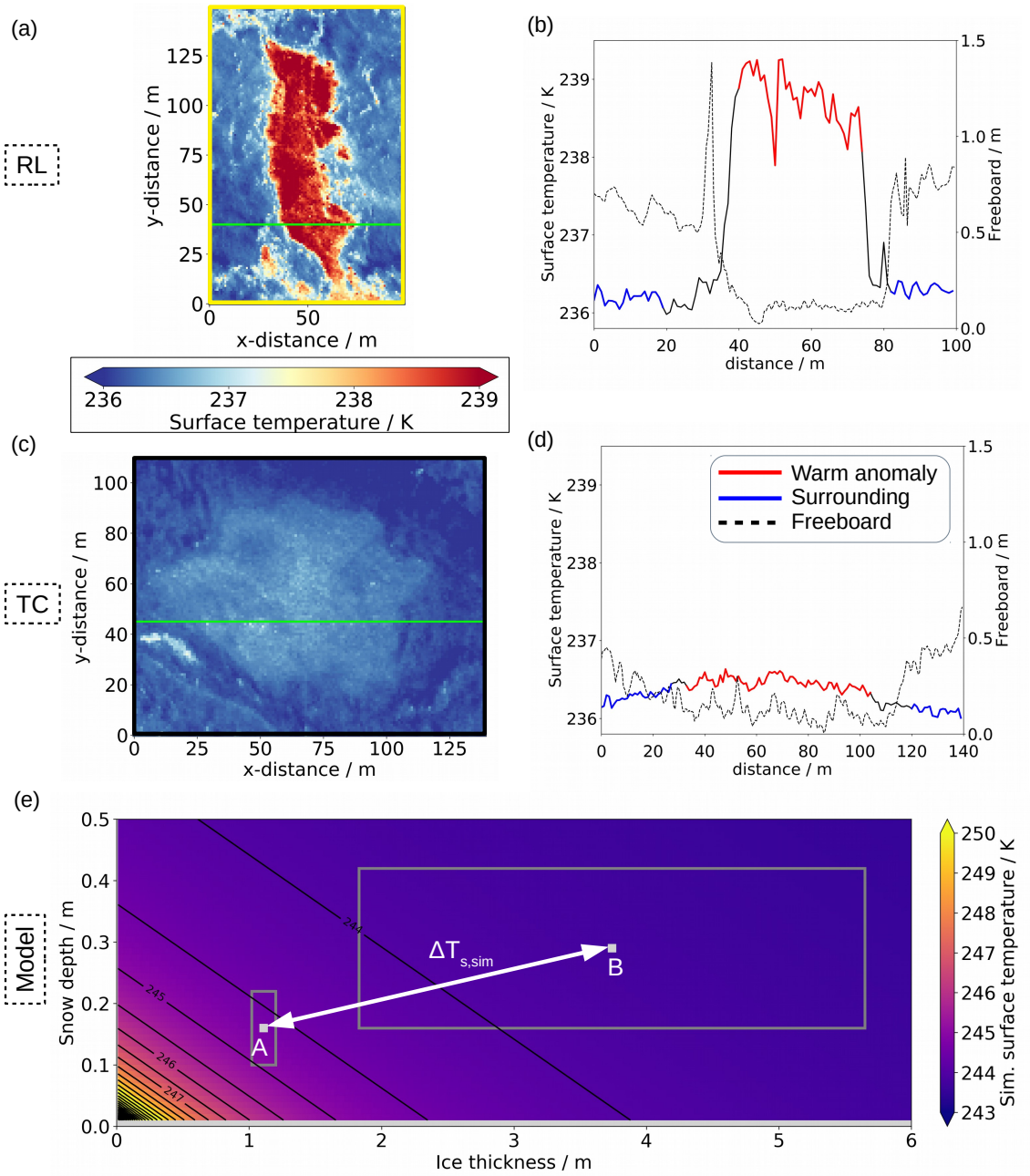

Figure 4.2: (a,b) Case example for RL (Box 3). (c,d) Case example for TC (Box 5). (a,c) Surface temperature map of the box with a cross-section (green line). (b,d) Surface temperature along the cross-section with the classification of the warm anomaly (red) and the surroundings (blue) and freeboard of the same cross-section (black, dashed). (e) Simulated surface temperature (colored) for ice thickness versus snow depth on 21 January 2020. The black contour lines show the surface temperature step size of 0.5 K. Point "A": typical for the level ice in the warm anomalies; point "B": typical for deformed ice in the surroundings. The boxes are defined based on the mean and standard deviation of the snow and ice thickness.

4.2.5 Surface topography

The snow surface topography is retrieved from the ALS, which was operated in the helicopter, parallel to the TIR camera. We use snow freeboard to evaluate the topography of the areas of the warm anomalies and their surroundings as an additional variable for the winter conditions. We consider the relative freeboard due to a possible mean deviation of the ALS derived freeboard data.

4.2.6 Snow and ice conditions

To evaluate the snow and ice conditions, we use measurements along a transect (called "Northern Loop"), which were taken over deformed ice close to our study data. The transect is long enough (about 1.4 km) and covers different ice regimes to represent well the spatial variability of snow depth and ice thickness. More information about the transect location can be found in Figure 2 of Nicolaus et al. (2022). We discriminate between level and deformed ice based on the roughness determined from the 50 m running mean and standard deviation of the ice thickness, same as in Itkin et al. (2023). The level ice thickness is capped at 2 m (assumed thermodynamical growth limit). We use the standard deviation as classification of level ice (<0.2 m) and of deformed ice (>0.6 m). The values of snow and ice thickness measured at the specific transect days (transects were performed monthly to bi-weekly) are fitted polynomially and retrieved for 21 January 2020.

4.2.7 Thermodynamic sea ice model

We implement a one-dimensional steady-state thermodynamic sea ice model to investigate the sensitivity of the surface temperature to changes in snow and ice thickness as well as atmospheric parameters, i.e., 2 m air temperature, 10 m wind speed, and downwelling longwave radiation.

The surface heat budget is defined as (Shokr and Sinha, 2015):

$$F_{\mathrm{LW,down}} - F_{\mathrm{LW,up}} + F_{\mathrm{cond}} - F_{\mathrm{sens}} = 0, \tag{4.1}$$

where $F_{\mathrm{LW,down}}$ and $F_{\mathrm{LW,up}}$ are the downwelling and upwelling longwave radiation, F_{cond} the conductive heat flux, and F_{sens} the sensible heat flux. Fluxes towards the surface are considered positive. Shortwave radiation is not relevant during winter and the latent heat flux is negligibly small. With the one-dimensional model, we do not consider lateral heat fluxes which we assume to be negligible.

Linearizing $F_{\mathrm{LW,up}}$ using Taylor expansion, the simulated surface temperature $T_{\mathrm{s,sim}}$ is:

$$T_{\mathrm{s,sim}} = \frac{F_{\mathrm{LW,down}} - a + T_{\mathrm{w}}\, d + c\, u\, T_{\mathrm{a}}}{b + c\, u + d}, \quad \text{where} \quad d = \left(\frac{h_{\mathrm{i}}}{k_{\mathrm{i}}} + \frac{h_{\mathrm{s}}}{k_{\mathrm{s}}}\right)^{-1}. \tag{4.2}$$

T_w is the sea water temperature at freezing point, c is the combined sensible transfer coefficient, u the wind speed, h_i is the ice thickness, h_s is the snow depth, k_i and k_s are the thermal conductivity of ice and snow respectively, a and b are the coefficients of linearization.

The model is forced with atmospheric data from the meteorological tower on the floe and longwave radiation from a radiation station, both at the recording time of the surface temperatures. The snow and ice thicknesses of level and deformed ice are taken from the transect data. There can be absolute differences in surface temperature between our observations of TIR surface temperatures and the simulated physical temperature. However, this does not impact relative differences across the floe, which are most important here. The full model descriptions and input parameters can be found in the Supplement (Table 4.6).

4.3 Results

In this section the results of this study are presented. This comprises the definition of the warm anomaly types, the description of the local temperature differences, the comparison of observations and thermodynamic model output, and the temperature-based melt pond classification.

4.3.1 Warm anomaly types

Comparing the melt ponds from the optical orthomosaic (Figure 4.1 b) with warm anomalies of the surface temperature map in winter (Figure 4.1 a), we find clear similarities in location and shape. Although we did not have any visual appearance of melt ponds in winter and spring, we detected winter temperature anomalies, that became melt ponds in the subsequent summer (boxes in Figure 4.1 a; numbers in the Supplement Figure 4.3).

Based on the observed temperature contrasts and their physical explanation, we define and manually select two types of these warm anomalies:

a) refrozen leads (RL): newly formed, thin ice in between thicker ice, showing strong positive temperature anomalies.

b) topography controlled (TC): level ice surrounded by deformed ice, showing weak positive temperature anomalies.

The refrozen leads can be identified easily by their elongated shape and higher surface temperatures due to thinner ice formed after a recent dynamic event. They have a lower surface elevation than the surroundings and potentially collect more snow, which favors melt water collection in summer.

Besides the correlation with the optical orthomosiac, we find the same for areas of low elevation in the topography map from the ALS (Figure 4.1 d). Thus, warm anomalies have thinner ice and snow compared to the surroundings of deformed ice with increased freeboard and surface roughness (also shown in Figure 4.2 b,d). Based on this topography data, we can determine TC anomalies although they show a comparatively small temperature difference. Many of the TC anomalies already have the shape of melt ponds and thus potentially were melt ponds already the summer before.

4.3.2 Local temperature differences

We show the results from the manual classification in each box (Supplement Table 4.2). The surface temperature differences of the two warm anomaly types on 21 January vary between 0.3 K and 2.5 K. We find a connection between the temperature difference and the type of anomalies. For the RL (four anomalies), we have a higher temperature difference of 1.7 K–2.5 K (median=2.0 K, std=0.33 K), while the TC anomalies (nine anomalies) have a temperature difference of 0.3 K–0.7 K (median=0.4 K, std=0.17 K).

For simplicity, we focus on one case of each type, RL and TC, because they have a well-distinguishable temperature anomaly. In Figure 4.2, we show the temperature maps for one RL-case ($\Delta T_{\mathrm{obs}} = 2.5\,\mathrm{K}$) and one TC-case ($\Delta T_{\mathrm{obs}} = 0.3\,\mathrm{K}$) as well as the aligned cross-sections of temperature and freeboard. The cross-sections are classified into warm anomaly (red) and surroundings (blue). The freeboard change is inversely proportional to the temperature change (Figure 4.2 b,d). This is consistent with our expectations that the freeboard decreases while the temperature increases, and vice versa. Looking at all helicopter TIR data, we see that RL only appear after the end of December and then the surface temperature difference decreases due to ice growth and potential snow accumulation from 11.8 K to 0.5 K. For TC there is no trend with time while it varies at 0.2 K–1.3 K. The different stages of the warm anomalies on 30 November 2019 and 12 February 2020 are displayed in Figure 4.1 e and f. Temperature differences of all 13 warm anomalies on 21 January 2020 and in two cases for all 10 helicopter flights between November and February are listed in the Supplement (Table 4.1 and Table 4.2).

4.3.3 Comparison of observations and thermodynamic model

We compare the warm anomalies from the TIR observation on 21 January 2020 with simulated surface temperature differences, calculated with a steady state one-dimensional thermodynamic model (Subsection 4.2.7) to understand better what is causing the warm winter anomalies. The lower temperature contrast of TC anomalies must be investigated in more detail while for the RL cases it is clear that the newly formed, thinner ice causes the larger temperature differences. Thus, we focus on the TC anomalies on 21 January 2020.

Snow depth and ice thickness from the transect data represent the spatial variability of the study area and show a snow depth of 0.16 m ± 0.06 m for level (A) and 0.29 m ± 0.13 m for deformed ice (B) (Figure 4.2 e). The ice thickness is 1.11 m ± 0.09 m for level ice (A) and 3.74 m ± 1.91 m for deformed ice (B). Based on these representative average values, we implement two regimes of snow depth and ice thickness in our thermodynamic model. The simulated mean temperature difference $\Delta T_{\mathrm{s,sim}}$ between the warm anomaly (level) and surroundings (deformed) is 0.88 K with a spread of 0.09 K–1.47 K (Figure 4.2 e) while 0.30 K–0.70 K is observed (Subsection 4.3.2).

Thus, the thermodynamic model slightly overestimates the temperature anomaly. The simulated temperature difference using the same snow depth for level and deformed ice (0.23 m) would be 0.59 K. Therefore, the effect of variable snow depth accounts for 0.29 K of the 0.88 K in our simulation. But this snow depth variability is quite uncertain based on our limited amount of measurements. On the short spatial and temporal range, the atmospheric conditions are considered constant and do not cause additional variability.

4.3.4 Temperature-based melt pond classification

The threshold-based TIR classification is able to approximate the next summer MPF of an ice floe. With a temperature threshold of 236.35 K, applied to the surface temperature map on 21 January 2020, we derive a MPF of 26% (Figure 4.1 c). This is slightly higher than the fraction of 22% for the optical classification on 30 June 2020. With the ponds expanding after the first drainage event in mid-July, however, the optical observations also show a higher fraction of 24% on 22 July 2020. Thus, we are able to partly replicate the summer melt pond classification, already six months in advance. This is a first step towards a seasonal prediction of melt ponds.

The shortcomings are the uncertainties on level FYI as well as that we are missing smaller melt ponds (melt pond size distribution follows a power law (Popović et al., 2018; Huang et al., 2016)). Also the high spatial variability of the surface temperature influences the classification which is sensitive to small changes in the threshold. The temperature classification performed correctly for 41% of the optical classified ponds (Figure 4.2 c). The remaining 59% are not classified although in summer melt ponds are present (false negative). In relation to the whole surface area of the floe, the fraction of false positive (17% of the floe) and false negative (13% of the floe) are in the same order of magnitude. Therefore, the overall MPF is similar for the TIR and optical classification, which can be a coincidence. However, as 41% of the summer melt ponds are correctly identified in the winter TIR data, that number is the approximate performance of the winter to summer melt pond prediction.

4.4 Discussion

Studies about melt pond properties (Huang et al., 2016) and photogrammetry of the sea ice topography (Divine et al., 2016) using optical data are limited to the summer season. Helicopter-borne ALS data, available in summer and winter, were also used to explore the role of surface roughness for melt pond presence (Webster et al., 2022). The topography, measured by the ALS, is included to a large extent in the surface temperatures while the surface temperatures contain additionally thermodynamic surface information. Thus, there is high potential to further fuse these two datasets. With high-resolution winter surface temperatures, we add an additional data source for a better understanding of melt pond precursors outside the summer season. We show for the first time that melt pond locations can be already seen in winter temperature anomalies due to the thermodynamic properties of snow and sea ice.

We find areas of refrozen leads or level ice with thinner snow at the location of the surface temperature anomalies and deformed ice in the surroundings. This is reasonable because areas of low elevation tend to turn into melt ponds (Polashenski et al., 2012). The ice topography and snow variability align with the findings of Scott and Feltham (2010) and Holland et al. (2012). Two modes, corresponding to level and deformed ice as found in the transect ice thickness (1.11 m and 3.74 m), are also visible in the ice thickness transect performed on 07 January 2020 over parts of the study area (Supplement Figure 4.4). When we zoom into the study area, these modes are represented also by the ALS freeboard. We can identify modes for each of the anomalies which are below the surroundings (Supplement Figure 4.5). This strengthens our assumptions for the two ice thickness regimes in the thermodynamic model. Previous studies stated that snow plays an important role for melt pond formation (Scott and Feltham, 2010; Petrich et al., 2012). In our study, we can confirm the importance of snow: the snow depth is linked to the ice topography, i.e., thinner snow is present over level ice and causes warm temperature anomalies (Itkin et al., 2023). During the MOSAiC expedition there was thin snow compared to the climatology which makes the anomalies more emphasized due to less insulation by the snow (Itkin et al., 2023).

The presence of some TC melt ponds coincides with the locations of re-frozen melt ponds from the previous summer. Itkin et al. (2023) shows presence of re-frozen melt ponds in the southern part of the Central Observatory (CO) in October. The size of the warm anomalies over the southern and other parts of CO suggests that the re-frozen melt ponds were wide spread. The re-appearance of melt ponds at the previous season's location was already mentioned before in the context of the Surface Heat Budget of the Arctic Ocean (SHEBA) expedition (Eicken et al., 2001). In one case (Box 4), we find a warmer circle around a colder middle part, which could indicate a bottom-up melt pond

from last summer. The trough of the previous melt pond could serve as the melt water collection location and seed the appearance of a melt pond in the next season.

To simulate the surface temperature, we assumed a commonly used value of snow thermal conductivity (k_s=0.30 W m^{-1} K^{-1}, Bitz and Lipscomb (1999)). The model results are sensitive to the thermal conductivity potentially leading to overestimated results. The investigation of the thermal conductivity is an important but large topic itself and out of the scope of this study.

The threshold-based temperature melt pond classification proves its potential in this case study. The threshold must be adapted to different environmental conditions before it can be used further, e.g., in models. The absolute surface temperature and its anomaly are affected by atmospheric parameters, such as air temperature and wind speed. Thus a statistical analysis of the surface temperature distribution could be used to find the best threshold. The comparison to the optical classification shows that a single threshold has still some problems to classify melt pond locations correctly. 41% of the summer locations are correctly predicted and thus the majority was not. This shows the limit of our prediction: while 41% is still a useful prediction we cannot expect to identify all summer melt ponds already in winter. However, our comparison does not take sea ice dynamics as well as snow accumulation and redistribution between winter and summer into account. Melt ponds can expand more easily on level ice, which presumably leads to the rather poor performance of our classification on level ice. As stated in the introduction, there are other factors we do not consider, like ice permeability and pond hydrology of different ice types, which will help to develop further constraints for the classification. Thus some of the mismatches might be due to that and can partly explain the good match of the classified overall MPF of 26% in winter and 22% (maximum 24%) in summer.

Regarding the timing of the compared datasets: We compare our winter surface temperature to an advanced melt pond extent (30 June), before the drainage of the melt ponds happened. The mid-winter surface temperatures (21 January) have a large contrast due to very low air temperature and the warmer ocean. We presume that the winter temperature anomalies align best when surface depressions are filled with melt water.

Melt pond schemes in regional and climate models could benefit from our findings: melt ponds should be tracked in models throughout the whole year and not only in summer. This increases the potential for melt pond prediction. So far the ice and snow topography is not represented sufficiently in General Circulation Models (e.g., Flocco et al., 2012). But in this study, we show how important the ice topography and roughness are for melt pond formation, already in winter. Nevertheless, the models have a much coarser spatial resolution and are potentially pan-Arctic. Thus, our results would need to be adapted for larger scales.

Until now, refrozen leads were not considered as an indicator of melt ponds. The refrozen leads can add potential areas for next summer's melt pond formation. Here, we can show that a proper representation of lead formation and ice dynamics is necessary to improve the melt pond prediction. Thus, the area of refrozen leads explains a part of the MPF of the following summer. While sea ice is becoming thinner, it becomes more dynamic, and more leads can form. Thus, there is potential for an increased area of melt ponds in the future, which can alter the albedo of sea ice.

Further, TIR remote sensing data can help to support our findings. Satellites instead of helicopter surveys would be an ideal tool to cover larger areas. However, so far, higher resolution TIR satellite remote sensing is performed only in lower latitudes, while we show their potential benefits for the whole Arctic. Nevertheless, their current spatial resolution of about 100 m is still not sufficient to resolve the warm anomalies, which are usually smaller. This study should motivate to implement high-resolution TIR satellite-based observations, like the upcoming Copernicus Land Surface Temperature Monitoring mission with 30 m resolution (Koetz et al., 2018), to resolve small-scale physical processes on a wider scale and extend their coverage to polar regions. In addition, our applied methods have to be further developed to have a more automatic application to a variety of datasets.

4.5 Conclusion

We show that warm surface temperature anomalies over sea ice in winter can be co-located with melt ponds of the following summer. We define two different types of warm anomalies: refrozen leads and topography controlled melt ponds. The warm anomalies of the topography controlled melt ponds are characterized by level ice compared to the deformed surroundings, which means thinner snow and ice for the warm anomalies. With a thermodynamic model, we are able to replicate (with a slight ΔT overestimation) the observed surface temperature difference based on observed snow and ice thickness difference and atmospheric parameters. Thus, we can fully attribute the warm anomaly to the ice and snow cover (and not, e.g., wind-driven effects), which eventually also affects later pond formation. Based on a simple threshold-based classification, we are able to use high-resolution surface temperature in winter as a seasonal prediction tool for the summer MPF. The winter prediction of the observed summer MPF agrees within their uncertainty and 41% of the summer melt pond locations are identified correctly.

As Scott and Feltham (2010) and Landy et al. (2014) point out, there is a need for a better understanding of physical processes influencing melt pond formation and evolution which is driven by meteorological events, ice dynamics, and thermodynamics. The relationships between winter ice surface temperature and melt pond development found

here can serve the development of improved melt pond parameterizations in regional and climate models. They should track refrozen lead locations throughout the winter and take pond formation in refrozen leads into account to simulate a more realistic melt pond distribution. As shown in this study, there is a large potential for high-resolution TIR data to study small-scale properties of sea ice, either from airborne platforms like here or hopefully in future satellite missions.

Data and software availability

Datasets:

- Optical orthomosaics: https://doi.org/10.1594/PANGAEA.949167 (Fuchs and Birnbaum, 2022)
- Surface temperature maps: https://doi.org/10.1594/PANGAEA.940846 (Thielke et al., 2022b)
- Freeboard map: https://doi.pangaea.de/10.1594/PANGAEA.951010 (Hutter et al., 2022) [dataset in review]
- Atmospheric parameter: https://doi.org/10.18739/A2VM42Z5F (Cox et al., 2021) [updated version used]
- Radiation: https://doi.org/10.1594/PANGAEA.952359 (Pirazzini et al., 2022)
- Transect ice thickness: https://doi.org/10.1594/PANGAEA.943666 (Hendricks et al., 2022)
- Transect snow depth: https://doi.org/10.1594/PANGAEA.937781 (Itkin et al., 2021)

Software:

- Optical image classification: https://doi.org/10.5281/zenodo.7548469 (Fuchs, 2023)

Acknowledgments

This work was supported by the German Ministry for Education and Research (BMBF) as part of the International Multidisciplinary drifting Observatory for the Study of the Arctic Climate (grant MOSAiC20192020), NiceLABpro (grant 03F0867A), and IceSense (grants 03F0866B and 03F0866A). We acknowledge the support by the Deutsche Forschungsgemeinschaft (DFG) through the International Research Training Group IRTG 1904 ArcTrain (grant 221211316), and the MOSAiCmicrowaveRS project (grant 420499875). PI was supported by Research Council of Norway (SIDRiFT, grant 287871). MAW conducted

this work under the National Aeronautics and Space Administrations New Investigator Program in Earth Science (80NSSC20K0658) and the National Science Foundation Project (2138786). NH was partially funded by the Cooperative Institute for Climate, Ocean, & Ecosystem Studies (CIOCES) under NOAA Cooperative Agreement NA20OAR4320271, Contribution No 2022-1245. We thank all persons involved in the expedition of the Research Vessel *Polarstern* during MOSAiC in 2019-2020 (AWI_PS122_00), and especially, HeliService and their pilots (Nixdorf et al., 2021). We also thank for the discussion and support around this project: Philipp Anhaus, Larysa Istomina, Felix Linhardt, Niklas Neckel, and Marcel Nicolaus. We thank the reviewers for the very constructive feedback which helped to improve the manuscript.

4.6 Supplement

Warm temperature anomalies

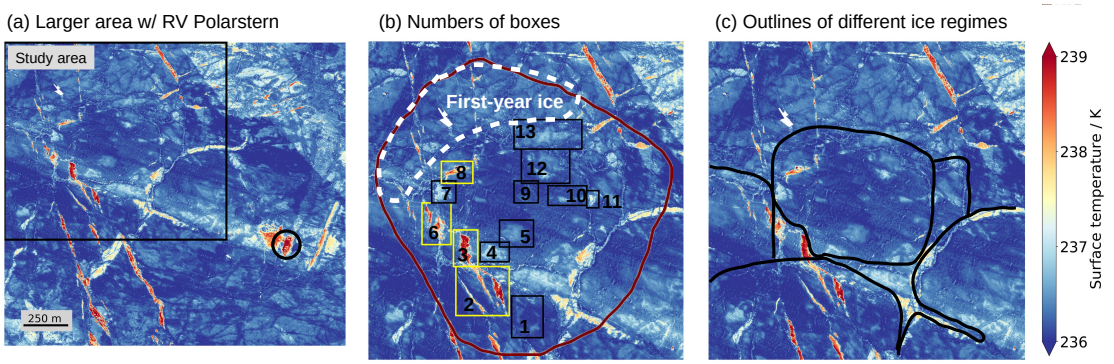

Figure 4.3: Surface temperature maps on 21 January 2020 with (a) a larger area selection with the study area (black box) in context to RV *Polarstern* (black circle), (b) the same as Figure 1 (a), but with the numbers of the boxes to have the possibility to refer to the single boxes. The white dashed line shows the area which is FYI while the rest of the floe area is SYI. (c) shows the outline of different ice regimes in the study area.

Table 4.1: Box properties: warm anomaly type, temperature difference $\Delta T_{\mathrm{s,obs}}$, box size, shape description, and additional comments. The types are i) refrozen leads (RL) or ii) topography controlled (TC).

Box No.	Type	$\Delta T_{\mathrm{s,obs}}$ / K	Box size (x*y) / m	Shape	Comment
1	TC	0.3	130*170	oval	several parts
2	RL	2.0	220*200	elongated	three parts
3	RL	2.5	100*150	elongated	-
4	TC	0.4	120*80	oval	Warmer outer circle
5	TC	0.3	140*110	oval	scattered
6	RL	2.0	120*170	elongated	-
7	TC	0.7	180*90	oval	-
8	RL	1.7	130*90	elongated	-
9	TC	0.5	100*90	oval	scattered
10	TC	0.4	160*80	oval	scattered
11	TC	0.7	50*70	oval	-
12	TC	0.6	200*140	oval	two parts
13	TC	0.3	280*120	oval	-

Table 4.2: Temperature difference (Warm anomaly - Surroundings) at the ten helicopter survey dates between 30 November 2019 and 12 February 2020 for the warm anomalies in the RL-case (refrozen lead, Box 3) and TC-case (topography controlled, Box 5). The refrozen lead only appears after 28 December 2020 because of ice dynamics.

Date	RL-case $\Delta T_{\mathrm{s,obs}}$/K	TC-case $\Delta T_{\mathrm{s,obs}}$/K
30 Nov 19	-	0.2
24 Dec 19	-	0.8
25 Dec 19	-	1.0
28 Dec 19	-	0.6
07 Jan 20	11.8	1.3
16 Jan 20	2.0	0.5
21 Jan 20	2.5	0.3
28 Jan 20	2.3	1.0
04 Feb 20	2.4	0.6
12 Feb 20	0.5	0.2

Details on the thermodynamic model

The definition of upwelling longwave radiation $F_{\mathrm{LW,up}}$ is:

$$F_{\mathrm{Lw,up}} = \sigma {T_{\mathrm{s}}}^4, \tag{S1}$$

with the Stefan-Boltzmann constant σ and the surface temperature T_{s}.

This is linearized by Taylor series expansion to:

$$\sigma {T_{\mathrm{s}}}^4 = \sigma[f(T_0) + (T_{\mathrm{s}} - T_0)f'(T_0)/1!] = \sigma[T_0^4 + (T_{\mathrm{s}} - T_0)4T_0^3] = a + bT_{\mathrm{s}}, \tag{S2}$$

with $a = -3\sigma {T_0}^4$, and $b = 4\sigma {T_0}^3$ as coefficients of linearization based on the background temperature T_0 which is at 240 K as best guess. The results are tested to be not sensitive to the variation of T_0 in a reasonable temperature range (below the freezing point).

The definition of conductive heat flux F_{cond} is:

$$F_{\mathrm{cond}} = \frac{(T_{\mathrm{s}} - T_{\mathrm{w}})}{\frac{h_{\mathrm{i}}}{k_{\mathrm{i}}} + \frac{h_{\mathrm{s}}}{k_{\mathrm{s}}}}. \tag{S3}$$

The definition of sensible heat flux F_{sens} is:

$$F_{\mathrm{sens}} = c(T_{\mathrm{s}} - T_{\mathrm{a}}) = \rho_{\mathrm{air}} c_{\mathrm{p}} C_{\mathrm{s}} (T_{\mathrm{s}} - T_{\mathrm{a}}), \tag{S4}$$

with the sensible transfer coefficient c, the air density ρ_{air}, the heat capacity c_{p}, the turbulent transfer coefficient C_{s}, and the 2 m air temperature T_{a}.

Table 4.3: Input parameter for model. These are the values for 21 January 2020.

Variable	Long name	Value	Comment
T_{a}*	2 m air temperature	243.5 K	on floe at recording time
u*	10 m wind speed	5.4 m s^{-1}	on floe at recording time
$F_{\mathrm{LW,down}}$*	Downwelling longwave radiation	193.6 W m^{-2}	on floe at recording time
$h_{\mathrm{i,level}}$	Level ice thickness	1.11±0.09 m	from transect
$h_{\mathrm{s,level}}$	Level snow depth	0.16±0.06 m	from transect
$h_{\mathrm{i,deformed}}$	Deformed ice thickness	3.74±1.91 m	from transect
$h_{\mathrm{s,deformed}}$	Deformed snow depth	0.29±0.13 m	from transect
k_{i}	Thermal conductivity of ice	2.0 W m^{-1} K^{-1}	after Untersteiner (1964)
k_{s}	Thermal conductivity of snow	0.3 W m^{-1} K^{-1}	common literature value
ρ_{a}	Air density	1.44 kg m^{-3}	for p=1013 hPa, T=245 K
T_{w}	Sea water temp. at freezing point	271.35 K	-
T_0	Background temp. for lineraization	240 K	best guess
σ	Stefan-Boltzmann constant	5.67×10^{-8} W m^{-2} K^{-4}	-
c_{p}	Specific heat capacity of air	1000 W s K^{-1} kg^{-1}	-
C_{s}	Sensible turbulent transfer coefficient	0.001 75	Yu and Rothrock (1996)

Snow and ice conditions

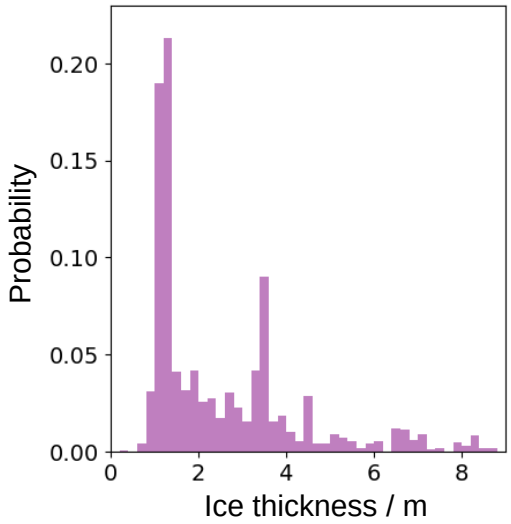

Figure 4.4: Histogram of the ice thickness retrieved from an ice thickness transect over the study area on 07 January 2020.

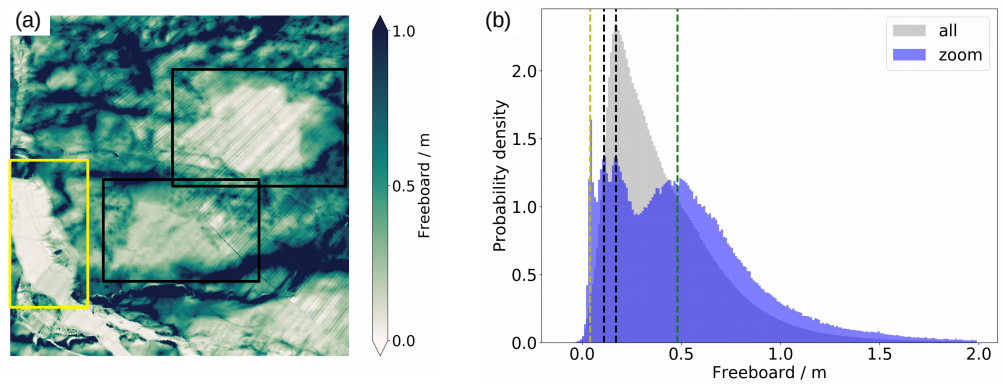

Figure 4.5: Freeboard map from ALS for a selection of the study area with a size of 300 m × 300 m. (a) Map for the area of the melt pond boxes 3, 4, and 5, and (b) histogram of the freeboard of the full study area (gray) and the area of (a) in blue with modes (vertical lines) of the warm anomalies (yellow/black dashed) as well as the surroundings (green dashed).

Chapter 5

Small-scale lead properties

This chapter is based on the following manuscript:

Thielke, L., G. Spreen, M. Huntemann, D. Murashkin (2023, in review for Elementa Sci. Anth.). Spatio-temporal variability of small-scale leads based on helicopter winter sea ice surface temperatures [Preprint]. *EarthArXiv*. https://doi.org/10.31223/X5R07W

Relevance

In this chapter, we address the third research question R3: *What are the geometrical properties of leads on horizontal scales of meters?*

Small-scale leads, on scales of meters, are strongly relevant for the Arctic heat budget, particularly in winter. TIR imaging detects leads well because they have a strong temperature contrast to the surrounding thicker ice. The leads, covered with open water or thin ice, are an area of strong heat exchange between the ocean and the atmosphere. Therefore, they are a crucial feature of the Arctic sea ice cover. With the 1 m resolution surface temperature maps (presented in Chapter 3), there is the possibility to classify small-scale leads (orders of meters) and to determine their geometrical properties. This would not be possible with operational TIR satellite observations as they have a horizontal resolution of about 1 km.

Contributions

I contributed to the conception and design of this study. I did the data analysis and investigation with the contribution of all authors. I wrote the first draft of the manuscript.

Abstract

Surface temperature is crucial in studying the Arctic climate, particularly during winter. We examine 1 m resolution surface temperature maps of 35 helicopter flights between 02 October 2019 and 23 April 2020, recorded during the Multidisciplinary drifting Observatory for the Study of Arctic Climate (MOSAiC). The seasonal cycle of the average surface temperature spans from 265.6 K on 02 October 2019 to 231.8 K on 28 January 2020. The surface temperature is affected by atmospheric changes and also varies across scales. Furthermore, we concentrate on leads in sea ice because they allow for greater heat exchange between ocean and atmosphere than thick, snow-covered ice. Leads, which appear considerably warmer than sea ice, are classified by a temperature threshold. The local scale (5–10 km) lead area fraction varies between 0% and 4% with a higher variability than on a regional scale (20–40 km), where leads cover a more stable fraction of 0-1% until mid-January when it increases to 4%. The variability in the lead area is caused by sea ice dynamics (opening and closing of leads), as well as thermodynamics with ice growth (lead closing). To understand better the ice rheology throughout the winter, we identify lead orientation distributions. We find that the orientation varies between different flights but the distribution mostly shows one prominent orientation peak. Thus, we are not able to determine predominant intersection angles, which would need two modes in the orientation distribution. The lead width distribution follows a power law with a negative exponent of 2.63, which agrees with literature values, proves the comparability to other datasets, and extends the existing relationship to the smaller scales, as observed here. The appearance of many more small leads compared to wider leads is important since they only occur on the sub-footprint scale of thermal infrared (TIR) satellite data. Sub-satellite-footprint lead statistics are essential for Arctic-climate investigations because the ocean-atmosphere heat exchange does not scale linearly with lead area fraction and is larger for smaller leads.

5.1 Introduction

This study presents the spatio-temporal evolution of the Arctic sea ice surface temperature and lead area fraction, as well as the lead width and intersection angle. In this analysis, we refer to fractures in the sea ice cover like cracks and leads (>50 m width according to the definition of the World Meteorological Organization (WMO), (WMO, 2014)), jointly as "leads". The helicopter-borne surface temperature measurements were taken as part of the Multidisciplinary drifting Observatory for the Study of Arctic Climate (MOSAiC) in the central Arctic (Shupe et al., 2020). The MOSAiC expedition (Sep 2019–Oct 2020) allowed us to collect in-situ measurements from the central Arctic over a whole seasonal cycle for different aspects of the Arctic system (Nicolaus et al., 2022; Rabe et al., 2022; Shupe et al., 2022). Our measurement program was part of the sea ice and remote sensing teams (Nicolaus et al., 2022), which conducted a large collection of data from sea ice physics, on-ice remote sensing, over albedo, to snow properties. The analysis is based on data from 35 helicopter survey flights between October 2019 to April 2020, recorded with an infrared camera over the same ice floe and surrounding regions along the Transpolar Drift.

The investigation of sea ice processes is crucial for studying climate warming, which is especially strong in the high latitudes (Arctic Amplification) (Serreze and Barry, 2011; Wendisch et al., 2017; Dai et al., 2019; IPCC, 2021). The warming is even stronger in winter than in summer, related to the feedbacks of infrared (IR) radiation in winter and ice-albedo during summer (Bintanja and Van Der Linden, 2013). Sea ice becomes significantly thinner (Meredith et al., 2019; IPCC, 2021) with an average reduction of 2 m from the period 1958-1976 (submarine record) to the current altimeter period with strongest thinning during the ICESat period (2003-2008) (Kwok, 2018). With the decline in annual sea ice minimum extent in late summer, also the multiyear ice area has strongly decreased (Kwok, 2018). The thinner ice makes the sea ice more susceptible to wind and ocean current forcing, resulting in higher ice drift speeds (Spreen et al., 2011; Kwok et al., 2013). Rampal et al. (2009) hypothesizes that thinner sea ice has less mechanical strength, allowing easier breaking of the sea ice. The changing sea ice conditions influence the heat exchange between ocean and atmosphere, which is important for the whole Earth's Climate System and not only the Arctic regions (Serreze et al., 2009; Meredith et al., 2019). Leads and thin ice are much warmer than the surrounding sea ice and snow and thus heat loss is more than a magnitude larger in leads compared to the surrounding ice (Maykut, 1982). Therefore, a better understanding of the interaction between ocean, sea ice, and atmosphere is essential. The high resolution lead data presented here have the potential for evaluation of the sub-footprint scale information of satellite remote sensing products.

Leads, with open water or thin ice cover, have high variability in time and space (Yu and Rothrock, 1996; Willmes and Heinemann, 2015). Therefore, it is important to monitor their conditions throughout the year. In Arctic pack ice during winter, a lead area fraction (open water and thin ice combined) of less than 10% can be expected (Yu and Rothrock, 1996), while in the Central Arctic lead area fractions are typically even lower (Wang et al., 2016). Willmes and Heinemann (2016) (2003–2015; satellite) and Wang et al. (2016) (1985–2014; model) could not find a trend in the lead area fraction, and Wang et al. (2016) found that the winds mainly determine the inter-annual variability in lead area fraction. However, a precise determination of the lead area fraction is crucial. Lüpkes et al. (2008) showed that a slight change in the high sea ice concentration (SIC) range, e.g., by the opening of leads, affects the near-surface air temperature. According to their study, a change of 1% in SIC could cause an air temperature change of up to 3.5 K. Small reductions in SIC, mostly induced by leads, have a (non-linear) more efficient effect on the heat exchange between the ocean and atmosphere than when a closed sea ice cover is present (Maykut, 1978). Therefore small changes in winter sea ice concentration, i.e., changes in lead area fraction are necessary to monitor. For example, if an increase of surface temperature on regional scale (e.g. satellite footprint) is (i) caused by many small leads the heat flux is stronger affected than if it is (ii) caused by a thinner but closed ice cover.

We first describe our helicopter measurement program and explain the principles of thermal sea ice observation. In the next part, we describe the spatio-temporal variability of our high resolution surface temperatures. Afterwards, we describe the lead classification based on the temperature difference. In the next section, we analyse the temporal variability of the surface temperature and lead area fraction on different spatial scales and present a case study of the November 2019 storm event. The last part focuses on the lead properties, i.e., width and orientation, derived after segmenting the classified leads.

5.2 Data

In this section, the used data set from thermal sea ice observations, the meteorological context, as well as the supporting data.

5.2.1 Thermal sea ice observation

With an infrared camera (InfraTec VarioCAM HD) installed, 35 helicopter flights were performed on a roughly weekly basis between 02 October 2019 and 23 April 2020 from RV *Polarstern* (Alfred-Wegener-Institut Helmholtz-Zentrum für Polar- und Meeresforschung, 2017) (Figure 5.1). The set of flights consists of four main flight patterns: (i) Central Observatory (CO) (local), (ii) L-Site triangles (regional), (iii) L-Site grids (other), and (iv)

event-related (other), like mapping particular leads. Detail about the surface temperature maps (Thielke et al., 2022c) and pre-processing are presented in Thielke et al. (2022e). To our knowledge regional scale sea ice infrared imaging has not yet been analysed and published before, such as done in the scope of this study.

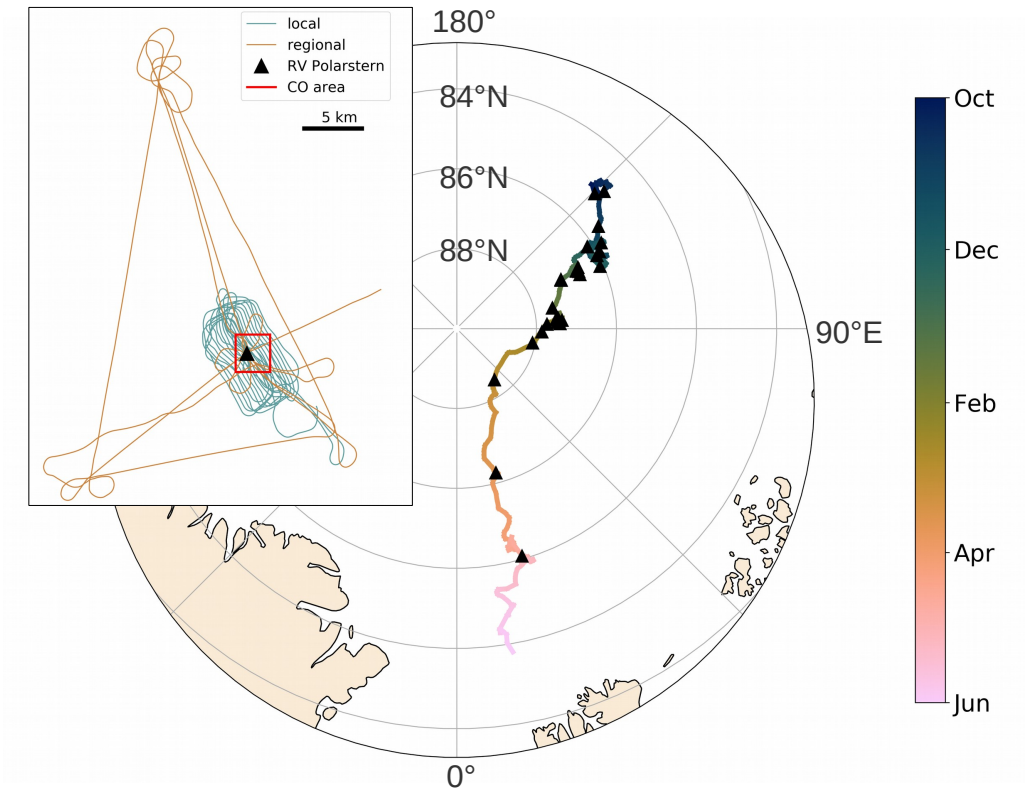

Figure 5.1: This figure shows the helicopter flight locations and flight patterns. The colored track shows the drift of RV *Polarstern* from October 2019 until June 2020. The black triangles represent the location of the 35 helicopter flights. Additionally, as inlay on the left, we show a typical local (turquoise) and regional (orange) flight pattern with *Polarstern* as the center (black triangle). The red box marks the CO area (Supplement Figure 5.10).

Our measurements with helicopter-borne thermal infrared (TIR) imaging provide temperatures of the sea ice surface with a high spatial resolution of 1 m which is substantially higher than TIR satellites, like Moderate Resolution Imaging Spectroradiometer (MODIS), that have a resolution of about 1 km. Nevertheless, satellites are the primary tool for the Arctic sea ice state observations (Spreen and Kern, 2017; Fox-Kemper et al., 2021). Compared to pan-Arctic coverage from satellites, we can provide with our helicopter data restricted area coverage from a local 5 km scale to a regional 40 km scale. Investigating the small-scale variability is important to better understand the representation of sea ice properties in models and satellite retrievals on a sub-grid scale (Vihma et al., 2014). Thus, this data is valuable for evaluating models and satellite retrievals (Ivanova et al., 2016).

The TIR temperature can distinguish open water and thin ice from thick ice, particularly for thin ice thickness of less than 1 m (Shokr and Sinha, 2015). Open water rarely exists in winter because the freezing starts directly after a lead opening. Therefore, we expect to capture mainly thin ice and only small open water areas with significantly warmer surface temperatures. Open water and thin ice areas influence the Arctic heat budget by allowing increased heat exchange between the ocean and the atmosphere. Above 1 m ice thickness, heat flux changes are minimal and have minor relevance for the Arctic heat budget (Maykut, 1982). Maykut (1982) found that in winter, the heat contribution from thin ice in leads is similar to the open water area and even larger than the dominating thick ice area.

The radiation in the TIR spectral region has a very small penetration depth on a submillimeters scale in snow, and ice (Shokr and Sinha, 2015, pages 272,294). As a result, the TIR brightness temperature provides a measurement of the upper surface of snow or sea ice. Thus, the recorded temperature is expected to be influenced by atmospheric changes through the radiation balance at the snow/ice-air interface. Clouds strongly influence the surface temperature (Vihma and Pirazzini, 2005), i.e., they reduce the radiative cooling (Wang et al., 2001). Our flights were performed only during calm and clear weather conditions. Thus, we can neglect a dependence on changing cloud cover. However, the changing air temperature still plays a role, which needs to be taken into account (Thielke et al., 2022e).

5.2.2 Meteorological context

How representative are our results from the MOSAiC winter in terms of surface temperature and lead area fraction in context with the meteorological condition? The meteorological conditions are discussed in Rinke et al. (2021) based on the ERA5 reanalysis data between 1979 and 2019. There were mostly typical meteorological conditions present during MOSAiC, although some unusual events happened during our observation period and before the expedition. Summer 2019, before the MOSAiC expedition started, was very warm and had unusually long low sea ice extent as well as thinner ice (Rinke et al., 2021; Krumpen et al., 2020). During the expedition, unusual conditions occurred during the following periods, all according to Rinke et al. (2021):

- Unusual cold at the beginning of November 2019 and March 2020
- Warming events in mid-November, beginning of December, mid-February, and mid-April
- Unusual positive Arctic Oscillation with associated fast sea ice drift in spring 2020 (Krumpen et al., 2021; Dethloff et al., 2022)

- Anomalous low pressure January to April 2020 associated with more frequent storm events during winter and spring (relatively low cyclone counts for October 2019 – January 2020)

5.2.3 Supporting data

We use atmospheric data from the 12 m meteorological mast on the MOSAiC ice floe, i.e., 2 m air temperature, measured with a Vaisala HMT 330, and 10 m wind speed, measured with a Metek uSonic-3 cage Cox et al. (2021). These supporting measurements were measured at the location of Met City in the CO (Details see Shupe et al. (2022)).

5.3 Surface temperature variability

This study focuses on the gridded time-fixed helicopter surface temperature maps (Thielke et al., 2022c), which will be referred to as surface temperature for simplicity. Based on the series of 35 helicopter flights with the TIR camera during the MOSAiC winter, we present and discuss the spatio-temporal surface temperature variability. We present and discuss the complete seasonal cycle of the MOSAiC ice floe and its surrounding for the whole winter 2019/2020. There are unprocessed data from nine more flights available (for detailed explanation see Thielke et al. (2022e)).

5.3.1 Temporal variability

Ice surface temperature varies even on short timescales, i.e., within the flight duration of 90 minutes. This effect, however, is largely corrected in our dataset. See Thielke et al. (2022e) for how the corrected and time-fixed surface temperature maps are calculated. Here, in the following, we discuss the surface temperature seasonal variability. The average surface temperature decreased from 02 October 2019 at 265.6 K until it reaches its minimum with 231.8 K on 28 January 2020 (Figure 5.2 A). Later in the winter season, the average surface temperature increased to 251.4 K until the latest flight on 23 April 2020, while at that time, the 2 m air temperature was already about 20 K higher and close to the freezing point. However, the temporal evolution of the surface temperature is comparable to that of the 2 m air temperature. This is consistent with our expectation that, due to the shallow penetration depth (micrometer range) of electromagnetic waves in the TIR region, air temperature will have a substantial influence on our surface temperature observations. Also, Vihma and Pirazzini (2005) highlight the importance of the surface temperature and coupling to the atmosphere. At the same time, the heterogeneity of the surface temperature in ice-covered regions can also influence the atmosphere. But as long as the surface is frozen, the surface temperatures stay well below the freezing point. The surface temperature can be cooler during clear sky conditions due to radiative cooling.

A prominent interruption in the cooling happened at the beginning of the winter in mid-November due to a substantial increase in the surface and air temperature caused by a storm event (Rinke et al., 2021). More warming events (Subsection 5.2.2) are reflected in the surface temperature record. From mid-February onward, the frequency of flights was reduced, so we cannot reflect all single atmospheric events. However, we can show the warming of the surface temperature towards spring.

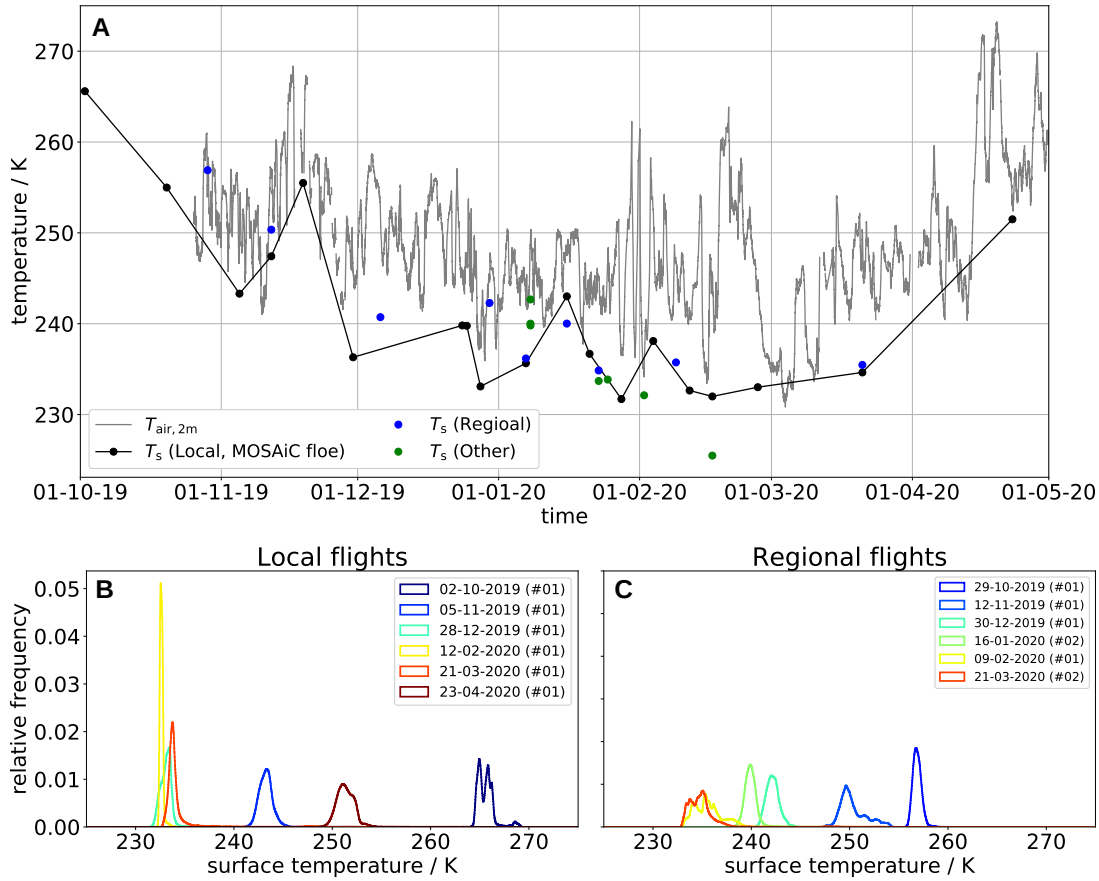

Figure 5.2: This figure shows the evolution of MOSAiC surface temperatures from 35 helicopter flights. (A) Temporal evolution of the average surface temperature throughout winter 2019/2020 from 02 October 2019 to 23 April 2020. Black indicates the local flights covering the Central Observatory (CO). They are connected to show the temporal evolution of the primary MOSAiC observation area. The regional flights, repeatedly visiting the L-Sites in the MOSAiC distributed network, are displayed in blue, whereas green shows additional flights not falling in one of these two categories. The grey line represents the 2 m air temperature measured at the floe in Met City. In the lower panel, a selection of surface temperature distributions is shown for different dates in the winter for (B) the local and (C) the regional flights. The colors continue from blue (begin of the winter) to red (end of the winter).

5.3.2 Spatial variability

In January 2020, there is a high density of flights, which allows us to illustrate the variability between different scales nicely or even on a short timescale for similar spatial surveys (Figure 5.2 A). On 07 and 16 January 2020, a local (black) and a regional (blue) flight were conducted on the same day (the regional flight is in both cases about 3 hours later). On 07 January, the average surface temperature of the different flights is similar, with an increase of only 0.6 K for the regional flight, which corresponds to an increase of 0.8 K in the 2 m air temperature. On 16 January 2020, the difference is larger with a decrease of 2.7 K while the 2 m air temperature only decreased by about 0.9 K. Thus, changes in the spatial surface temperature variability, either on the local or regional scale, has to explain the increasing temperature difference within nine days between the local and regional scale (flights had similar flight patterns). A likely candidate would have been changing lead fraction but actually a change of number of leads does not seem to be the reason for the higher temperature difference on 16 January: On 07 January there is actually a higher lead area fraction for the colder local flight (2.02% vs. 0.23% for the regional flight, see Table 5.1). While on 16 January 2020 the colder regional flight had a higher lead area fraction (1.37% vs. 0% on local scale; see Table 5.1). Thus, likely changes in other ice types with different thermal properties, snowfall, or snow redistribution should have caused these changes in spatial surface temperature variability.

The spread of the surface temperature varies from flight to flight. It is illustrated with the exemplary selection of six surface temperature distributions for local and regional scales throughout the winter season (Figure 5.2 B, C). Mostly, the distributions are wider for regional flights (right) than for local flights (left) because they include a larger variety of surface types due to the wider spatial extent. The major peak represents the predominant surface type, snow-covered thick ice, in all cases. The surface temperatures of this thick ice are more similar to the 2 m air temperature because of the reduced heat flux from the ocean through the thick ice and snow (Shokr and Sinha, 2015). The warm tail shows the presence of leads, but its peak is often too small (only visible in the log-scale), and the different thin ice thicknesses in leads of different ages widen the lead temperature distribution. In the local flights, we can find a transition from a wider distribution at the beginning of the winter season (blue) to a narrow distribution in mid-winter (yellow), and back to a wider distribution towards the end of the winter season (red). The more narrow distributions indicate the prevalence of the thick, consolidated ice due to cold and constant conditions. A wider distribution indicates the presence of several ice classes and spread towards warmer temperatures.

In the time series, we could already show the close connection to the atmospheric state, represented by the 2 m air temperature. Additionally, we look at the dependence of the

surface temperature standard deviation, as a measure of spatial variability, (leads were excluded to have a comparable basis of the thick ice) on the 10 m wind speed (Supplement Figure 5.11). We expect a lower surface temperature standard deviation for higher wind speeds caused by an increased exchange between the surface and atmosphere. We find a correlation of –0.38 between the surface temperature standard deviation and 10 m wind speed around the target time of the flight with the significance of a p-value of 0.04. The relationship with wind speed supports our assumptions that increasing wind speeds reduce surface temperature variability and can explain the greater sensible heat exchange due to faster air mass exchange. Because leads are not taken into account here, a potentially more dynamic ice pack that would result in more leads (and thus greater temperatures) can be ruled out. There is no relation between the average surface temperatures and the standard deviation. Although a low-temperature regime can create more compact and consolidated ice (uniform temperature), even under cold conditions, deformation can cause variability in ice classes with warmer surface temperatures, which increases the variation.

5.4 Lead classification

The leads are classified based on a one-dimensional, temperature-only approach, i.e., leads are characterized by a specific surface temperature range, defined by the temperature distribution of the corresponding flight. We apply a binary classification, discriminating between sea ice (snow-covered thicker ice) and leads, which are mostly covered with thin ice due to the fast freezing of the ocean surface under cold winter conditions. The classification is applied to the surface temperature grids. The pre-processing described in Thielke et al. (2022e) avoids the influence of changes in surface temperature during one flight. The thermal distinction for surface types with larger ice thickness is getting weaker due to low heat transfer through the ice (Maykut, 1978). Thus, the discrimination of leads from thick ice is easier due to large temperature differences, and we do not aim to discriminate the thick ice classes further (e.g., in first-year ice (FYI) and second-year ice (SYI)). We apply dynamic thresholds for different flights (Supplement Table 5.2 and Subsection 5.4.1) in order to establish the same classes defined with different surface temperature distributions in different flights. The dynamic threshold is required because the surface temperature is strongly connected to the ambient air temperature, which is strongly variable with time (see Subsection 5.3.1).

5.4.1 Iterative threshold selection

We apply the iterative threshold selection from Ridler and Calvard (1978) to the two-dimensional temperature arrays. The temperature distribution has its major mode towards the colder part of the distribution and a smaller secondary mode along the tail towards the warmest temperatures (caused, e.g., by leads). The initial threshold is the middle range of

the temperature distribution (average of the minimum and maximum value). Due to the long tail towards the warmer temperatures, it is ensured that the initial threshold is on the warmer side of the major mode so that the iteration can converge towards a minimum between the two modes. Starting from the initial threshold, the threshold is adjusted iteratively based on the new "lead" mask (defined by the threshold of each iteration) for the temperature array until it reaches the final temperature threshold. The updated threshold is calculated from the mean of the "lead" (all values larger than the threshold) and "sea ice" (all values smaller than the threshold) temperatures based on the current threshold. The iteration stop criterion is achieved when the temperature threshold change between one iteration to the next is within the tolerance of 0.02 K, which corresponds to the precision of the infrared (IR) camera.

The main steps are shown in the flowchart in Figure 5.3, and the Python3 code is shared in the Supplement (Section 5.8). For three flights (20191224_01, 20191225_01, 20200108_01), the threshold did not converge to a reasonable value; therefore, the tolerance had to be increased to 0.8 K. For the cases with this larger allowed tolerance in the difference, the obtained threshold still results in a reasonable lead classification, i.e., can be confirmed by the manual classification (see below in Subsection 5.4.2).

Classification example 20 October 2019

The threshold-based lead classification is shown for the flight on 20 October 2019 at the beginning of the winter season in Figure 5.4. We show steps 0 (initial threshold) to 2 for the temperature threshold iteration (A). With step 2, the result is already close to the final result (step 5) shown in (D). The surface temperature (B) is dominated by low temperatures (blue), associated with snow-covered thick ice. The warm surface temperatures (red domain) are referred to as leads. The binary classification map (D) resulting in "sea ice" (gray) or "leads" (red) is based on the iterative temperature threshold applied to the temperature distribution (C), showing the two classes as two main temperature regimes. The lead area fraction for this case on 20 October 2019 is the highest in our time series, with close to 10% for the full area covered by the helicopter flight.

5.4.2 Evaluation using manual thresholds

We use manual thresholds as a comparison for the reliability of the iterative method. The authors performed the manual threshold selection based on the minima in the distribution and visual approval of the classified map compared to the surface temperature map. The manual selection is a rather arbitrary and conservative choice but it can be used for the evaluation of the automatic, iterative classification method. The thresholds are determined for each flight individually because the surface temperature values and their distributions change from flight to flight. The manual selection was, in some cases, more conservative,

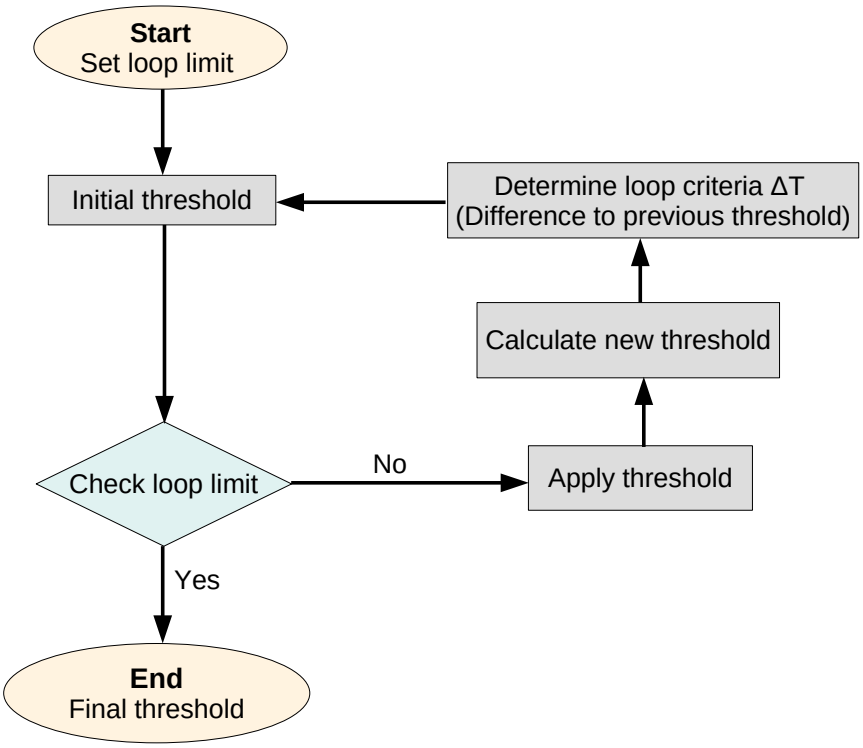

Figure 5.3: This figure shows the flowchart for the processes of the iterative threshold selection. Main processing steps for the iterative threshold selection to determine a temperature threshold for lead classification.

i.e., it has warmer thresholds but does not significantly influence the resulting lead area fractions (Supplement Table 5.2). Although the manual temperature threshold is 1.97 K higher than the one from the automatic and reproducible method (Subsection 5.4.1), its derived lead area fraction is only 0.1% lower than for the iterative method. Thus, the threshold difference does not significantly affect the lead area fraction because it is in the minimum of the surface temperature distribution. The small difference demonstrates that the automatic method aligns well with the manually defined thresholds and the resulting lead classification. We chose results from the automatic method for the following discussion because it is reproducible and can also be applied to further flights.

5.5 Winter lead area fraction

This section presents the analysis of the winter lead area fraction with a description of the lead formation during the November storm event and the spatial-temporal variability for the winter time series.

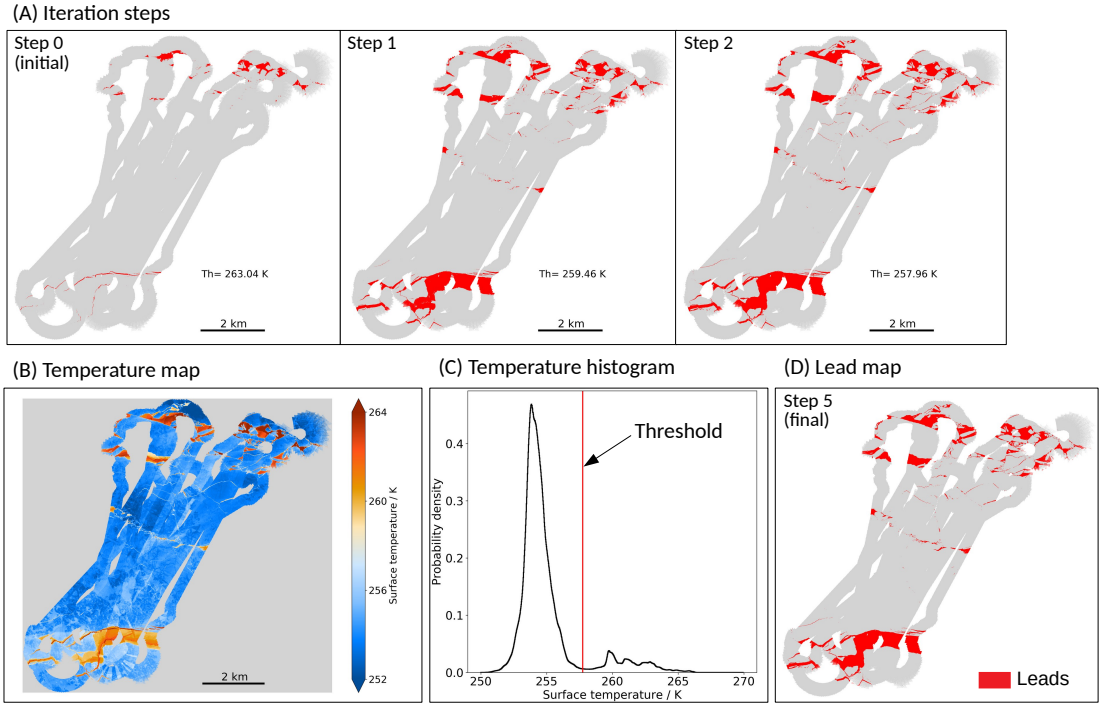

Figure 5.4: This figure shows the lead classification example for the flight on 20 October 2019. (A) Results from steps 0, 1, and 2 for the iterative threshold selection. (D) Final (step 5) binary lead classification based on (B) the gridded surface temperature maps. (C) The temperature distribution of (B). The red vertical line represents the found iterative temperature threshold to discriminate between "lead" and "no lead" surfaces.

5.5.1 Lead formation during the November storm event

Here, we discuss the storm event, which happened from 16 to 20 November 2019 (Rinke et al., 2021). This event had a major influence on the MOSAiC Central Observatory (CO) due to several leads appearing across the measurement sites. It had a significant relevance for several measurements (Nicolaus et al., 2022; Shupe et al., 2022) and was, e.g., influencing the snow transport as discussed in Nandan et al. (2022). We conducted one flight before (12 November 2019) and one flight after the storm (19 November 2019) and compare both flights directly in Figure 5.5. This storm event with high wind speeds was associated with warm air advection. It resulted in increased ice dynamics, which caused the break-up of the sea ice along various fracture lines, which are visible in Figure 5.5 B and D. The surface temperatures on 19 November 2019 after the storm are overall higher than before the storm event (mind the different temperature scales for (A)/(C) and (B)/(D)). Before the storm, there are a few narrow cracks in the outer areas of the flight pattern (Figure 5.5 (A)), but no prominent cracks in the vicinity of RV *Polarstern* (Figure 5.5 (C)). The surface temperature map of 19 November 2019 includes warm linear structures throughout the CO area and beyond (Figure 5.5 (B, D)), which causes an increase of lead

area fraction from 0.07% (Figure 5.5 (C)) to 1.73% (Figure 5.5 (D)) and therewith to a higher surface temperature variability.

5.5.2 Spatio-temporal variability

We discuss the spatio-temporal variability of the lead area fraction, which was calculated based on our lead classification (Section 5.4). The local lead area fraction (orange line in Figure 5.6) is constrained to the CO area of 3×3 km. In the CO area (Supplement Figure 5.10), always the same area around RV *Polarstern* is covered and makes the lead area fraction better comparable during the winter season as for the entire local flights. In most cases, the CO area lead area fraction is close to the one for the complete local flights (not shown); however, there is a large difference in lead area fraction on 20 October 2019 (1.3% for the CO area; 10.2% for the full local flight) because the majority of the detected leads are outside of the CO area. The data coverage of the CO area is sufficient for all flights with more than 50% and, except for the flights in November, even with more than 75% (Supplement Figure 5.12). The lead area fraction within the CO area shows high variability between 0% and 4%, but no trend can be seen in the temporal evolution (Figure 5.6, orange line). For the November storm event (Subsection 5.5.1), there is an increase in lead area fraction for the CO area from close to 0% on 12 November 2019 to 1.7% on 19 November 2019. We find for the regional scale, there is a steady low lead area fraction between 0% and 1% until mid-January. Towards the end of the winter season (21 March 2020), the lead area fraction increases to up to 4%. The increase in lead area fraction might be related to the increased number of storm events between January and April, compared to previous months (Subsection 5.2.2).

The higher lead area fraction observed in March in our data aligns with the temporal lead area evolution discussed for the regional scale in Krumpen et al. (2021). However, they observe a distinct higher lead area fraction of up to 20%, derived from MODIS TIR satellite data. The regional lead area fraction evolution also agrees well with the regional satellite Synthetic Aperture Radar (SAR) derived time series from Guo et al. (2022), which is in the similar range of 0-4% as ours and starts to increase only in March. Kortum et al. (2022) performed an ice classification based on SAR satellite data during winter on the same scale as our CO area. Our leads should be represented by the sum of open water and young ice classes of this study, where daily data are available (higher temporal resolution than our data). Their daily data generally show a comparable to our lead area fraction below 5% in mid-winter but exceed this value on a few days to up to 15% around 23 November 2019. Additionally, during March and April, their lead area fraction is for a longer time on a higher level of up to 10%. The high values at the beginning of the winter in Kortum et al. (2022) might be caused by the characteristics of the method based on SAR data. The same method from Kortum et al. (2022) was applied on the regional scale. The

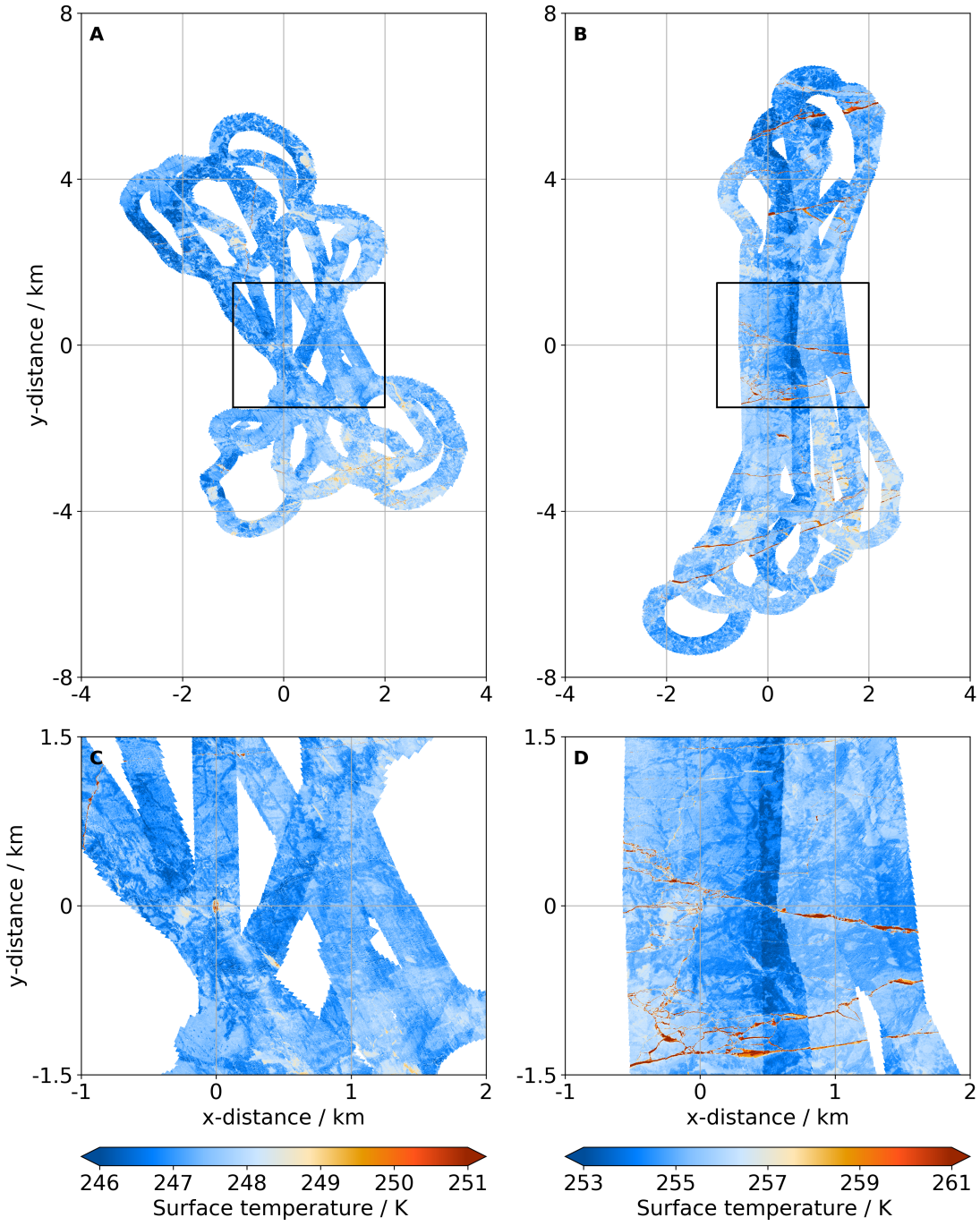

Figure 5.5: This figure shows the surface temperature maps before and after the November storm event. Comparison of two time-fixed surface temperature maps displayed in relative coordinates before the storm event (A, C) on 12 November 2019, and after the storm event (B, D) on 19 November 2019 with their respective CO area around RV *Polarstern* (0,0). Please note the different temperature ranges, adjusted to allow clearer visibility of the spatial variability of the temperature. For the flight on 19 November 2019, an increased area of warmer temperatures (reddish) is prominent.

regional lead area fraction has a peak in mid-November of 6%, stays below 4% and even lower during mid-winter, and increases in the second half of March to 7% (Karl Kortum, personal communication on 08 December 2022). While we do not capture their peak in November and the absolute values differ with a few percentage points, also the regional evolution aligns with our time series. Thus our results align reasonably well (considering different temporal and spatial sampling) with the two SAR-based studies, while for the MODIS TIR-based study only the temporal evolution agrees but the absolute values are different (much higher in the MODIS lead time series).

Within our data, we see scale-dependent differences in the lead area fraction with less variability on the regional scale than on the local CO scale but no trend in the local scale, while the regional lead area fraction increases throughout the winter (Figure 5.6). Nevertheless, the overall magnitude is similar. Thus the CO area is representative of the measurement sites in the CO of the MOSAiC expedition but the temporal development does not necessarily represent the lead area fraction on a larger scale. Nonetheless, the local data are helpful for a better understanding of the condition at and around the MOSAiC floe, particularly in connection to other in-situ measurements. Our lead area fractions (0-4%) are comparable to other previous studies of Marcq and Weiss (2012) with 1–2%, and Lindsay and Rothrock (1995) with 2–3%; both these winter lead area fractions were also derived in the central Arctic. Generally, the lead area fraction for the MOSAiC winter seems to align with the climatological mean and might be influenced by the changing location due to the MOSAiC drift (Krumpen et al., 2021). Yet, comparing different lead area fraction retrievals remains challenging because of different definitions of leads (e.g. open leads vs. leads covered by thin ice or even frost flowers) with other methods used on different scales (von Albedyll et al., 2022a).

Relation to wind speed

We are interested in the connection between lead area fraction and wind speed because wind events can cause increased ice dynamics and, therefore, possibly more leads. Thus, we compare our lead area fraction to the 10 m wind speed. We use the 7-day running mean for the wind speed to find prominent high wind regimes rather than short-term fluctuations because we can not represent these fluctuations with the limited temporal frequency of the helicopter flights.

We do not find significant correlation between wind speed and lead area fraction on the local and regional scale. However, we see sometimes a relation, such as for the increase of the lead area fraction (Figure 5.6) during the November storm event (Subsection 5.5.1). We have to note that our flights are only snapshots of a specific time with a weekly to biweekly frequency, while leads can open and close within hours. However, in most cases, they prevail for several days (if not closed by another ice dynamic event) until, eventually,

the ice thickness and snow accumulation within them gets too thick to be discernible from the surrounding ice in TIR imagery.

We highlight two cases in our time series: 1) the highest local lead area fraction within the CO area of 4% end of December occurs after a high wind regime that lasted several days, and 2) basically no presence of leads in mid-January during an increased wind speed regime while the regional fraction increases. Especially the high lead area fraction variability for the local CO area illustrates that local changes are rather random, not always representing large scale changes (see different temporal development between local and regional lead area fraction). Nevertheless, the local lead area fraction is valuable in combination with other interdisciplinary measurements obtained during MOSAiC and valuable for getting a better process understanding.

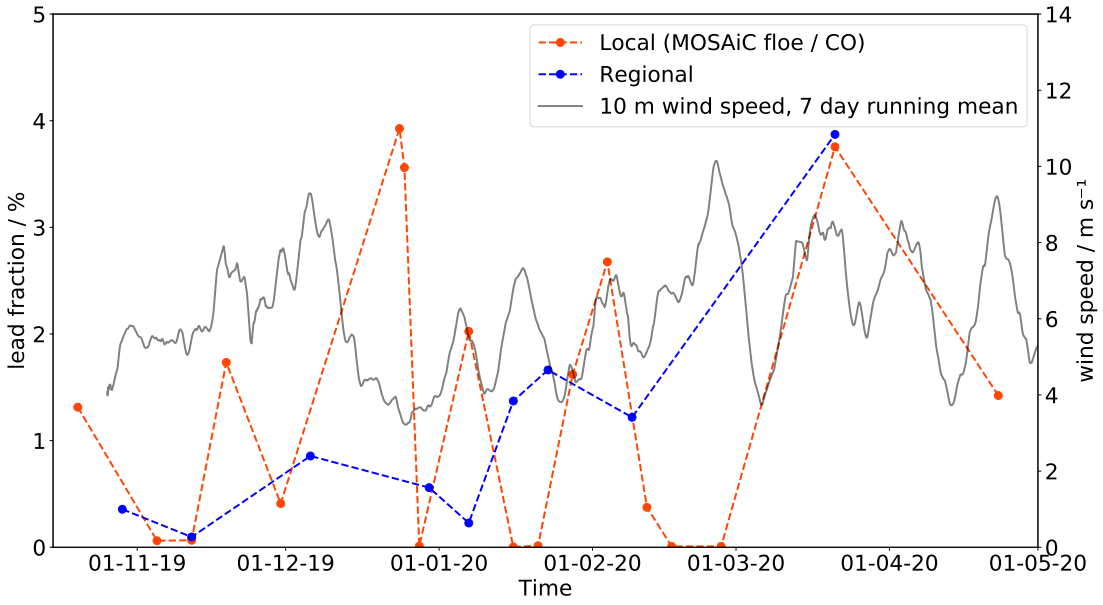

Figure 5.6: This figure shows the evolution of the lead area fraction on different scales. Temporal evolution of the lead area fraction throughout winter 2019/2020 from 02 October 2019 to 23 April 2020. The orange points show the lead area fraction for the CO area. The blue points illustrate the lead area fraction for the regional flights, visiting the L-Sites. The grey line shows the 10 m wind speed averaged to a 7-day running mean. Please note that there might be a minor influence by in and out coming support vessels, which could slightly increase the lead area fraction by breaking the ice.

Table 5.1: Lead area fraction values from Figure 5.6. Lead area fraction values for the local and regional scale in %. The same as the displayed values of the data shown in Figure 5.6.

Date	Local fraction / %	Regional fraction / %
2019-10-20	1.31	-
2019-10-29	-	0.36
2019-11-05	0.06	-
2019-11-12	0.07	0.10
2019-11-19	1.73	-
2019-11-30	0.41	-
2019-12-06	-	0.86
2019-12-24	3.93	-
2019-12-25	3.56	-
2019-12-28	0.01	-
2019-12-30	-	0.56
2020-01-07	2.02	0.23
2020-01-16	0.00	1.37
2020-01-21	0.01	-
2020-01-23	-	1.66
2020-01-28	1.62	-
2020-02-04	2.68	-
2020-02-09	-	1.22
2020-02-12	0.37	-
2020-02-17	0.01	-
2020-02-27	0.01	-
2020-03-21	3.76	3.87
2020-04-23	1.42	-

5.6 Lead properties

This section presents and discuss the lead segmentaion based on the lead classification as well as the properties of the lead orientation and the lead width.

5.6.1 Lead segmentation

We apply a segmentation algorithm to the lead map to define the properties of single leads, i.e, width and orientation. The segmentation is performed according to the watershed segmentation (Najman and Schmitt, 1994). Next, a set of object lead properties (width and orientation from enclosing ellipse, its area, orientation, and major axis) is derived based on (Burger and Burge, 2009) with 'scikit-image' library for Python.

In Figure 5.7, we illustrate the object properties for two example lead segments. The warmer temperatures on the left (yellow) are classified as lead, consistent with the red areas on the right that indicate the lead areas. We retrieve the lead properties width and orientation (calculated from ellipse parameters), assuming the lead properties are

representative, even if the ellipse does not cover the full lead due to the limited spatial coverage of our data or if the lead is interrupted. We therefore can only determine width but not length of the leads. The key lead parameters are the classified area (red) in the enclosing rectangle (dashed line in Figure 5.7), minor and major axis, as well as the orientation of the ellipse (pointing in the direction of the major axis). The zero line for the orientation is the north-south axis (all our surface temperature maps are oriented North along the y-axis). The ellipse defined for the lead segment is not representing the real length, but can be seen as a stable approximation for an object of arbitrary shape. Generally, the ellipses of close-by leads can overlap, which is required to calculate the lead properties individually, even though the two lead segments are not overlapping (Supplement Figure 5.13).

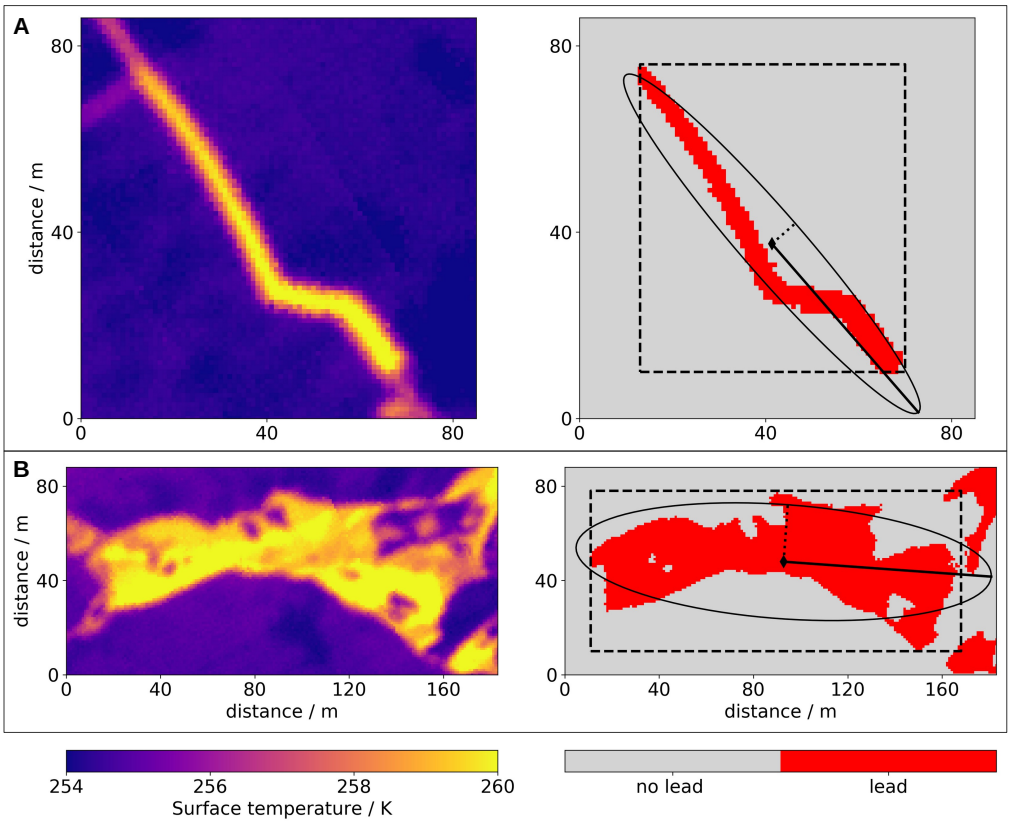

Figure 5.7: This figure shows the lead segmentation to derive lead width and orientation properties. Two lead segments from the lead classification result of the flight on 20 October 2019 with the temperature map on the left and the lead classification including the ellipse geometry on the right. The ellipse and their major axis (solid) and minor axis (dotted) are shown. The dashed rectangle marks the area from which the classified area in red is determined. (A) Shows a narrow lead with a mean lead width of 3 m and an orientation (of the major axis) of –41°. (B) Shows a wider and slightly scattered lead. It has a 26 m mean width and –86°as orientation.

We must deal with some artificial effects, such as the map's edge or shifts inside the map caused by small offsets in the geolocation of different helicopter overflights. Shifts or gaps could cause an artificial break of a lead into more segments, whereas it would have been only a single lead. Also, due to ice drift direction changes (i.e., shear), which can cause real breaks and gaps in the classified leads, the segments can represent a subset of a lead. The segments of the subsets of leads will result in an overestimation of the total number of leads. However, it is not expected to impact our results for lead width and orientation (we do not analyse the number of leads). Therefore, we assume that the segmentation is representative of our purpose of an overall statistical analysis of lead width and orientation. Width and orientation may also be critical parameters for evaluating the turbulent heat flux from leads (Tschudi et al., 2002). On the one hand, the efficiency of the heat transfer is dependent on the orientation relative to the wind direction (e.g., Tetzlaff et al., 2015). On the other hand, the heat transfer is more efficient for narrow leads, which makes the transfer dependent on the lead width distribution (Marcq and Weiss, 2012).

5.6.2 Lead orientations

A good understanding of lead orientation is crucial because they represent the ice dynamics of the sea ice (Lindsay and Rothrock, 1995). Ringeisen et al. (2019) emphasize the lack of knowledge of lead orientation at the floe scale because of missing high resolution observations. Here, the MOSAiC observations like ours can contribute new data. Better knowledge of small-scale leads is also crucial for a good representation of ice rheology in sea ice models (Hutter et al., 2018; Ringeisen et al., 2021). The orientation of leads shows the effect of ice dynamics in sea ice, influences it, and is connected to prevailing regional wind and ocean current (Lindsay and Rothrock, 1995). In the long term, leads have a non-random orientation during the Arctic winter, mainly influenced by coastlines and atmospheric and oceanic currents (e.g., Bröhan and Kaleschke, 2014). In general, lead features, including width and orientation, are similar across a large range of scales, including the smallest scales (Schulson, 2004).

We here look at the lead orientations of nine local flights (full coverage, i.e. not restricted to the CO area), which have in the CO area a lead area fraction of $\geq 1\%$. This ensures a sufficient presence of leads to perform a statistical analysis of lead orientations. We decided not to connect the single lead segments which might be split within one lead (Subsection 5.6.1) because we look at statistical distributions of lead properties and do not distinguish single leads. Furthermore, we bin our data in 5° steps.

Comparing the nine flights between 20 October 2019 and 23 April 2020, we see a high temporal variability in the lead orientation distribution (see examples in Figure 5.8), also shown for passive microwave based analysis in Bröhan and Kaleschke (2014). We find

prevailing orientations of –80°, –10°, 30°, or 60° (Supplement Table 5.3). In the following part, we focus on three examples from 07 January 2020, 28 January 2020, and 21 March 2020 (Figure 5.8). We identify modes of the lead orientation probability distributions of the orientation from –90 to 90°, binned in 5° steps (Supplement Figure 5.14). We constrain our data to elongated ellipse shapes with an axis ratio (major/minor) of at least two.

Additionally, we compare the leads of all widths with leads of a width of more than 3 m which is consistent with the valid range of the power law. With the constraint of the axis ratio, the data are reduced to 89% of the full dataset. With the minimum width of 3 m the data amount is reduced to 21% of the complete dataset. Starting with the case in March (Figure 5.8 C), we cannot find a major peak in the distribution of all lead width. With only wider leads ($\geq$ 3 m), the distribution of orientation angles is modified to a preferred direction at 35°, but still most orientations are present and not a clear prevailing orientation can be identified. Going backward in time to the end of January (Figure 5.8 B), we have one prominent orientation at –35° (all leads) which is even more emphasised for leads with the minimum width of 3 m (slightly shifted to –30°). There is a second minor peak at 40°, but this is very small and does not allow us to infer any intersections between two main orientations. For the case on 07 January 2020 (Figure 5.8 A) we identify one clear main direction of –10°. We see a variation in the primary lead orientation throughout the winter but no prevailing orientations on longer time scales.

For none of the nine investigated flight we can infer two main directions (bimodal distribution) from which we could infer an average intersection angle. Usual lead intersection angles from different studies, including satellite and laboratory measurements, would be 30–50° (Hutter et al., 2022), also shown for a SAR dataset from MOSAiC Ringeisen et al. (2022). There is a difference between using all data and the width restricted subset, but overall both show the same picture (Supplement Table 5.3). The variability might depend on the regional wind patterns that create direction-related fracture patterns. The investigation of the reasons for the variability in lead orientation is beyond the scope of this study, but is encouraged for future research. Different to many previous studies is that we are (a) far from land (which can introduce prevailing lead orientation by restricting ice drift in one direction) and (b) following the Lagrangian approach of the MOSAiC drift, which results in different locations of the Arctic Ocean to be monitored.

5.6.3 Lead width distribution

We discuss here the power law scaling of lead width (i.e. many more narrow leads than wide leads). Equation 5.1 gives the relation between lead width x and number of observed leads (as probability density) of a respective width assuming a power law relationship:

$$f(x) = ax^{-b}. \tag{5.1}$$

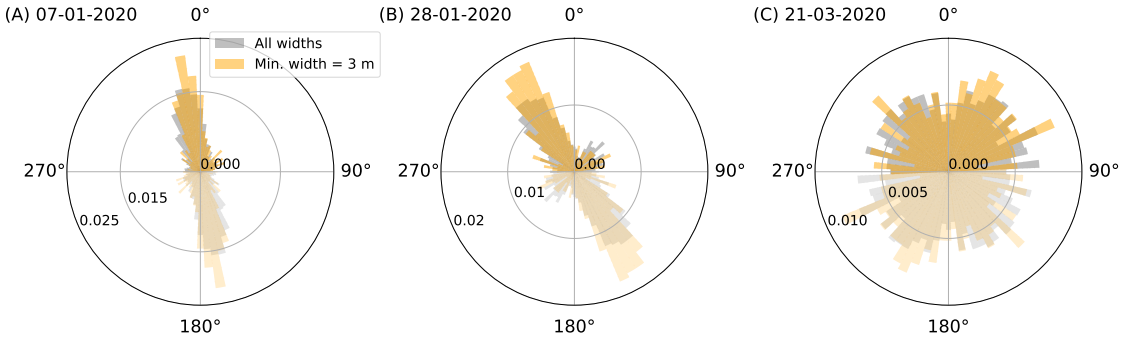

Figure 5.8: This figure shows the orientation angles of leads for three example cases. Probability density distribution for the orientation angles of the flight from (A) 07 January 2020, (B) 28 January 2020, and (C) 21 March 2020, as polar histogram. The radius indicated the probability density, which is different for all three cases. Only lead segments with an axis ratio (major/minor) ≥ 2 are included. We discriminate between two cases: leads of all widths included (gray) and only leads with a minimum width of 3 m included (orange). The lead orientation have only a range of 180°but are valid in both directions, they are mirrored to the opposite direction (slightly transparent). The total number of lead segments used for the histograms (270°to 90°only) are (all; $\geq$ 3 m): A=(1736; 500), B=(1326; 303); C=(1378; 464).

The parameter a is the scaling parameter (related to the number of measurements), but not further analysed here. The parameter x is the variable lead width, and b is the power law exponent, determining the (negative) slope. Thus, a larger power law exponent b results in a steeper (more negative) power law. The ratio of the classified segment area (shown in red in Figure 5.7) and the major axis length of the ellipse approximates the lead width. We detected in total 33855 lead segments in our classified maps for all 35 flights (but see explanation above why the number of segments should not be mistaken as the number of leads). The detected lead width varies between 1 m and 464 m. From the distribution of the lead widths, we perform a linear fit for Equation 5.1 (Figure 5.9 A) in the log-log space with logarithmic bins. We exclude leads smaller than 3 m width because they are too close to the spatial resolution of the dataset to be fully resolved in the segmentation. This can be seen from the deviation from the power law below 3 m in Figure 5.9. This is confirmed by the stabilisation of the power law exponent for a minimum lead width of 3 m and larger (Supplement Figure 5.15). However, for a minimum lead width between 9 m and 26 m we see an slight increase of the power law exponent. We do not know the reason for the increase but our hypothesis is that the value is less reliable because of the strong decrease of number of observations available for the power law fit. Our power law is calculated up to the lead width of 336 m (largest logarithmic bin). The resulting exponent of b=2.63 agrees with literature values at the upper end of the previously found exponent value range (2.0 to 2.6) (Wadhams, 1981; Wadhams et al.,

1985; Marcq and Weiss, 2012; Wernecke and Kaleschke, 2015; Qu et al., 2019) and proves the compatibility with other datasets. From the stability of b in Figure 5.15 (Supplement) we estimate the uncertainty of our b to be smaller than the range of the literature values of 2.0–2.6. The so far presented literature values of the power law exponents are summarized in Muchow et al. (2021).

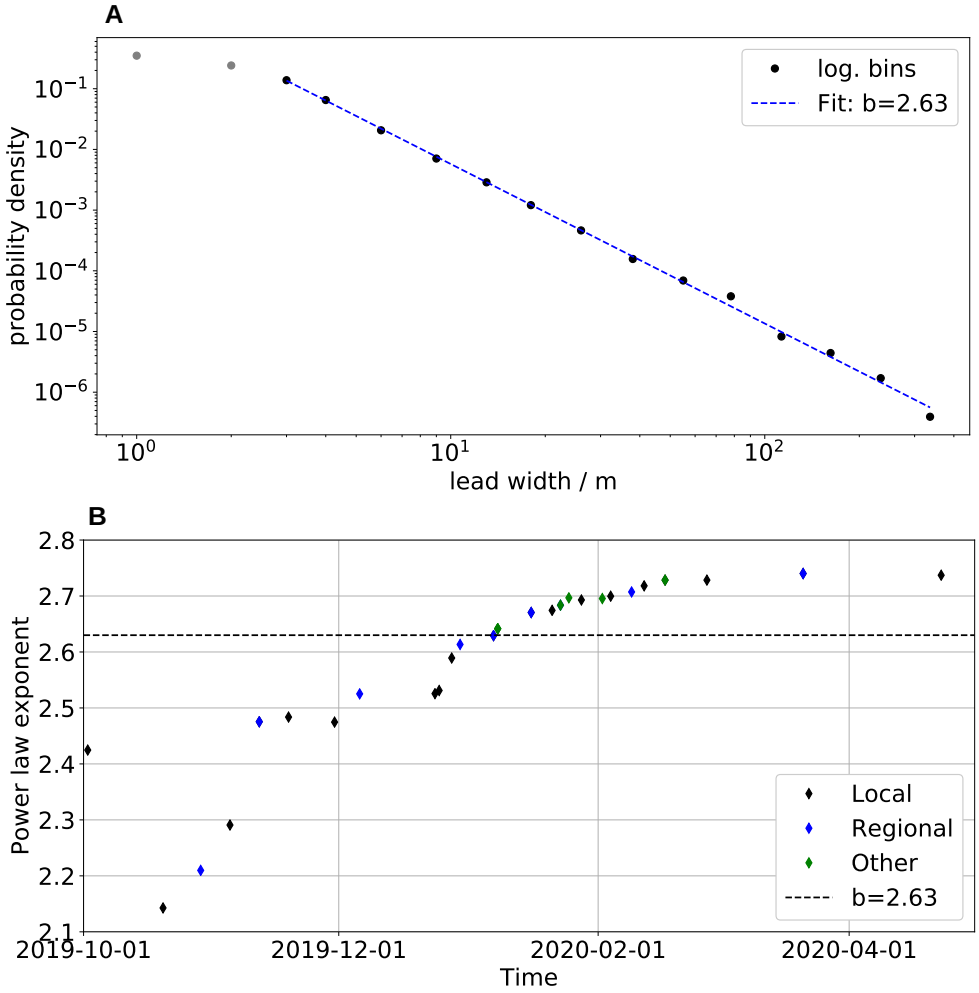

Figure 5.9: This figure shows the lead width distribution with the power law fit for all and single flights. (A) The logarithmic frequencies of the lead widths of all 35 flights combined, also binned logarithmic, are represented as black points. The blue dashed line shows the negative power law fit exponent b=2.63. The power law fit is constrained to the lead width $\geq$ 3 m. (B) Time series of the power law exponent for all 35 flights between 02 October 2019 and 23 April 2020; in black for local flight, in blue for regional flights, and in green for other flight types. The horizontal line marks the exponent of all flights (2.63) from (A).

Lindsay and Rothrock (1995) determines a smaller exponent of 1.6 ± 0.18 (less steep), which might differ because the power law is calculated to the lead width that is equal to the spatial resolution, while we see in our data that the power law is not valid anymore close to the spatial resolution and the slope between the bins has a smaller absolute value. In previous studies, the range of the power law exponent (dependent on the instrument and resolution) was determined starting between 20 m and 2 km lead width. Our study adds to the lower end of lead width with a range down to 3 m lead width and shows that the power law agrees with other methods and resolutions. As expressed by the power law, there are many more leads with small lead width, which were not resolved in previous studies. Also, our 3 m, the smallest resolvable lead width, likely is not the end of the lead width distribution. There are likely many cracks with a smaller width, which we do not resolve (but also can be important for, e.g., heat flux estimates). Our exponent is one of the largest (i.e., most negative) compared to the literature values. The other studies are also based on primarily winter data (Oct-Apr) but performed in different regions of the Arctic, which might influence the results due to different characteristics of the ice rheology. The power law distribution tells us that there are many more narrow leads than wider leads, which emphasizes the importance of small-scale features. The area contribution of the smallest leads are: (i) 4%, for lead width <3 m, (ii) 64%, for lead width between 3 and 100 m, and (iii) 32%, for lead width >100 m.

Additionally, we found a seasonal dependence of the power law exponent, with a tendency of an increasing power law exponent throughout the winter season (Figure 5.9 B). The seasonal increase in the power law exponent can also have a spatial component because of the drift into different regions during MOSAiC (Figure 5.1). The power law exponent drops from 2.42 to 2.14 at the start of the winter season in October (freeze-up time and consolidations of the ice north of the Laptev Sea). This is followed by a steady increase to 2.63 on 07 January 2020 (Central Arctic). Following that, there is a further increase and then stabilisation around 2.74 in March and April (North of Svalbard). Mind that we are not covering the full melting and summer season, which again might introduce a change in the exponent. For the power law exponent, there is: (i) no scale dependence (no variation between local and regional flight, also on the same day; compare black and blue dots), and (ii) no clear effect on the exponent by a rapid change in lead area fraction (Subsection 5.5.2) caused by ,e.g., the November storm event (Figure 5.9 B). An increasing exponent during winter time contrasts with the findings of Lindsay and Rothrock (1995) where the monthly average of the power law exponent for the central Arctic decreases from February to April and again decrease from October to December in the following season. We can only comment on several theories without providing a certain explanation why the power law exponent increases (relatively more narrow leads) throughout the winter. Three exponents in October and the beginning of November are lower (2.1 to 2.3), probably because during the freeze-up phase the ice floes were still in rather free drift, which could

more easily cause relatively wider leads (decrease of the exponent). The power law fit aligns for these three flights not as good as for the other flights, which is more prominent for smaller lead widths. In December and January, the exponent is increasing from 2.5 to 2.7, which may be related to a more consolidated and thicker ice pack far away from the coastlines (potential change of internal ice strength). This time was also characterized by less storms and lower wind speeds (Figure 5.6). The stabilization at the end of the winter could show the maximum power law exponent that can be reached during winter before it decreases towards the melt season with free drift conditions (which is not included in our dataset anymore).

The clear power law relationship for the lead width found here supports the validity of our lead property data and that representative statistical conclusions can be obtained from it. Our results indicate that we miss many leads in satellite remote sensing products with coarser spatial resolutions. This could already be extrapolated from the found power-law in previous studies, but is here shown for the first time down to a lead width of 3 m. Our widest leads are still narrower than the resolution of about 1 km of TIR satellites. Lead retrieval results vary (e.g., in frequency and how thick the ice in the lead can be) between different remote sensing approaches (von Albedyll et al., 2022a). Thus, direct and absolute comparison of lead retrievals can be difficult for different products and resolutions. Nevertheless, the same physical principles (like the power law correspondence) are valid for different scales and resolutions (Wernecke and Kaleschke, 2015). We recommend that any lead width study should check if the power law scaling conditions are fulfilled to increase confidence in the validity of the obtained results.

5.7 Conclusions

On a local (5–10 km) and regional (20–40 km) scale, we investigate the variation of the surface temperatures in time and space and derived lead properties. Along the MOSAiC drift during the winter season, we use high resolution surface temperature maps obtained from helicopter flights to examine small-scale lead properties. First, we investigated the surface temperatures and found: (i) its temporal variability is influenced by meteorological changes, such as warm air intrusions, often associated with high wind speeds, and (ii) its spatial variability over thick ice decreases as wind speed increases. For each flight, we retrieve classified lead maps and lead area fractions, based on a lead classification applied to the surface temperature maps using a dynamic temperature threshold. We see a high variability of the local lead area fraction and the influence of events, like the November 2019 storm. On a regional scale, there is a more stable lead area fraction evolution between 0% and 1% (until January), followed by an increase to 4% (March). This evolution agrees well with other MOSAiC studies on the regional scale. From the classified lead maps, we additionally determine lead width and orientation for all lead segments of every flight.

This reveals three main findings: 1) the lead width distribution follows a power law (Equation 5.1) with an exponent of b=2.63 (narrow leads dominate wide leads), which is consistent with previous research, 2) the power law exponent increases in the course of the winter, 3) small-scale leads typically have one primary orientation. However, that orientation changes between the flights and throughout the winter season and no overall prevailing orientation is found. The abundance of small-scale leads emphasises the necessity to understand their physical processes better, where our high spatial resolution data can help. However, those narrow leads are not individually included in the current TIR satellite data of about 1 km resolution (e.g., MODIS). We suggest a representation of the smallest leads on the satellite sub-footprint scale because the heat transfer is not linear with surface temperature. In fact, the heat exchange is larger for leads within thick sea ice compared to larger areas of uniformed thinner sea ice with the same average surface temperature. Such parameterizations could also improve model simulation for considering small-scale lead processes.

Beyond this study, we plan to perform a one-to-one comparison of the high-resolution helicopter-borne data with TIR satellite data, e.g., MODIS ice surface temperatures. The aim is to assess how well the lead's impact on the atmosphere is represented in the satellite retrieval. Additionally, comparisons with the deformation rate from buoy grids on different scales or inter-comparison with helicopter-borne topography data can be used to understand the MOSAiC lead characteristics better.

Data accessibility statement

- Helicopter-borne surface temperature maps, 1 m resolution: (Thielke et al., 2022c).
- Lead classification maps, 1 m resolution: (Thielke et al., 2022f)
- Atmospheric in-situ data: Cox et al. (2021) [updated version used]

Acknowledgments

This work was supported by the German Ministry for Education and Research (BMBF) as part of the International Multidisciplinary drifting Observatory for the Study of the Arctic Climate (grant MOSAiC20192020), and IceSense (grant 03F0866B). We acknowledge the support by the Deutsche Forschungsgemeinschaft (DFG) through the International Research Training Group IRTG 1904 ArcTrain (grant 221211316), the MOSAiCmicrowaveRS project (grant 420499875), and the Transregional Collaborative Research Center TRR 172 (grant 268020496) Arctic Amplification: Climate Relevant Atmospheric and

Surface Processes, and Feedback Mechanisms (AC)^3". We thank all persons who contributed to the expedition of the Research Vessel *Polarstern* during MOSAiC in 2019-2020 (AWI_PS122_00) (Nixdorf et al., 2021), and especially, HeliService and their pilots. Without them, the helicopter survey flights and the collection of the data would not have been possible. We thank Janna Rückert for the discussions about this manuscript.

5.8 Supplement

Code: Iterative threshold selection (python3)

```
def iterative_classification(Ts_arr,cr=0.02):
    """
    Input:
        - Ts_arr: surface temperatures (2d array)
        - cr: loop limit (float)
    Output:
        - thr: temperature threshold (float)
    """

    thr = 0.5*(np.nanmin(Ts_arr)+np.nanmax(Ts_arr)) # initial threshold
    dT=1

    while dT > cr:
        g = (Ts_arr>thr) # mask with threshold applied
        thr_new = 0.5*(np.nanmean(Ts_arr[g])+np.nanmean(Ts_arr[~g]))
        dT = np.abs(thr-thr_new)
        thr=thr_new

    return thr
```

Table 5.2: Temperature thresholds for the lead classification. List for all flights with the respective temperature thresholds used for the lead classification. One for the iterative method and, for comparison, the threshold derived with the manual approach. The flights can be identified by the expedition-specific Device Operation and Flight ID that includes the date information (YYYYMMDD_counter).

Device Operation	**Flight ID**	**Flight type**	**Iterative / K**	Manual / K (not used)
PS122-1_2-57	20191002_01	CO	266.83	267.42
PS122-1_2-167	20191020_01	CO	257.75	258.05
PS122-1_5-9	20191029_01	L-Site	259.58	261.98
PS122-1_6-11	20191105_01	CO	247.34	252.15
PS122-1_7-24	20191112_01	L-Site	256.13	260.17
PS122-1_7-25	20191112_02	CO	252.30	250.50
PS122-1_8-23	20191119_01	CO	259.60	258.81
PS122-1_9-98	20191130_01	CO	245.87	242.94
PS122-1_10-78	20191206_01	L-Site	250.82	254.41
PS122-2_17-98	20191224_01	CO	241.47	242.70
PS122-2_17-99	20191225_01	CO	241.63	243.06
PS122-2_17-101	20191228_01	CO	239.93	238.44
PS122-2_18-7	20191230_01	L-Site	251.50	250.64
PS122-2_19-44	20200107_01	CO	238.94	248.30
PS122-2_19-45	20200107_02	L-Site	245.94	251.76
PS122-2_19-46	20200108_01	L-Site grid	242.97	244.41
PS122-2_19-52	20200108_03	L-Site grid	249.28	251.10
PS122-2_19-53	20200108_04	L-Site grid	247.38	249.35
PS122-2_20-52	20200116_01	CO	246.53	247.86
PS122-2_20-53	20200116_02	L-Site	243.12	246.26
PS122-2_21-41	20200121_01	CO	240.15	242.87
PS122-2_21-77	20200123_01	L-Site	244.30	246.58
PS122-2_21-78	20200123_02	Lead-Event	244.50	244.64
PS122-2_21-122	20200125_01	Lead-Event	243.13	248.39
PS122-2_22-16	20200128_01	CO	237.23	239.48
PS122-2_22-97	20200202_01	L-Site (partly)	241.51	244.10
PS122-2_23-14	20200204_01	CO	245.48	247.50
PS122-2_23-109	20200209_01	L-Site	241.28	248.44
PS122-2_24-31	20200212_01	CO	234.55	234.97
PS122-2_25-7	20200217_01	L-Site (partly)	231.66	237.61
PS122-2_25-8	20200217_02	CO	239.11	234.26
PS122-3_29-49	20200227_01	CO	236.17	235.14
PS122-3_32-70	20200321_01	CO	241.78	244.63
PS122-3_32-71	20200321_02	L-Site	242.64	244.42
PS122-3_37-63	20200423_01	CO	256.09	259.52

Table 5.3: Main lead orientation angles per flight. List for nine selected flights with the main lead orientation angle (0=north-south line) for all data and the data restricted to the lead width ≥ 4 m. The flights are identified with their Flight ID.

Flight ID	Peak (all) / deg	Peak (≥ 3 m) / deg
20191020_01	−80/85	−80/90
20191119_01	−70	−75
20191224_01	60	65
20191225_01	60	60
20200107_01	−10	−10
20200128_01	−35	−30
20200204_01	35	30
20200321_01	None	(35)
20200423_01	None	−5

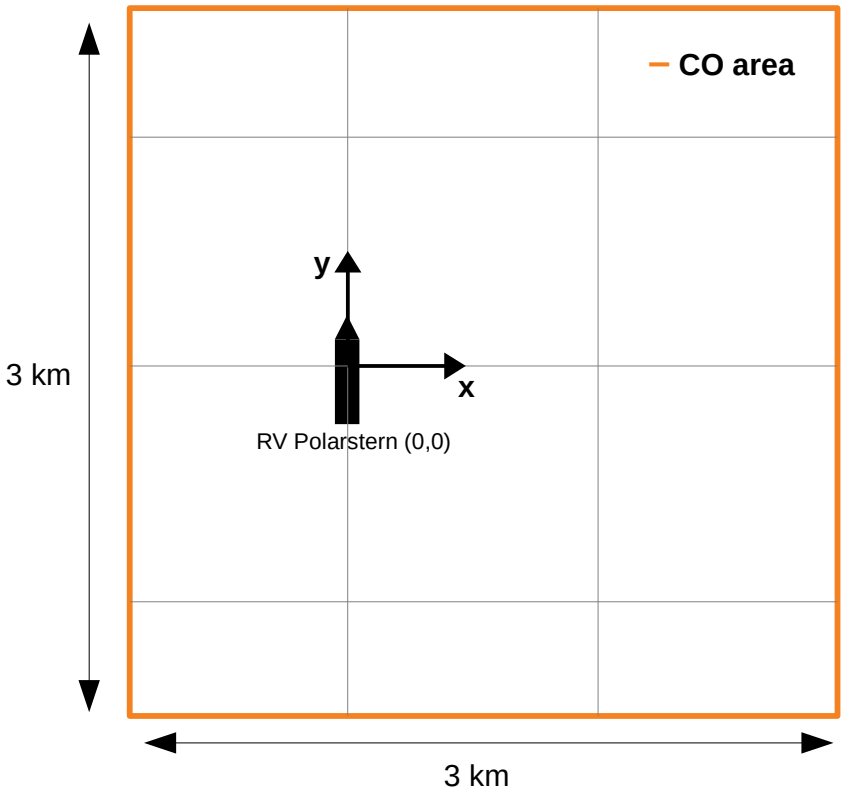

Figure 5.10: This figure shows the definition of CO area. This schematic shows the main CO area with an extent of 3x3 km and the orientation of RV *Polarstern* in the relative coordinates whereas the center of RV *Polarstern* is the point (0,0). In the CO area, most of the measurement sites were located. The edge points are: xmin,xmax,ymin,ymax=(-1000,2000,-1500,1500) m. The arrows indicate the orientation of the coordinate system for the relative coordinates.

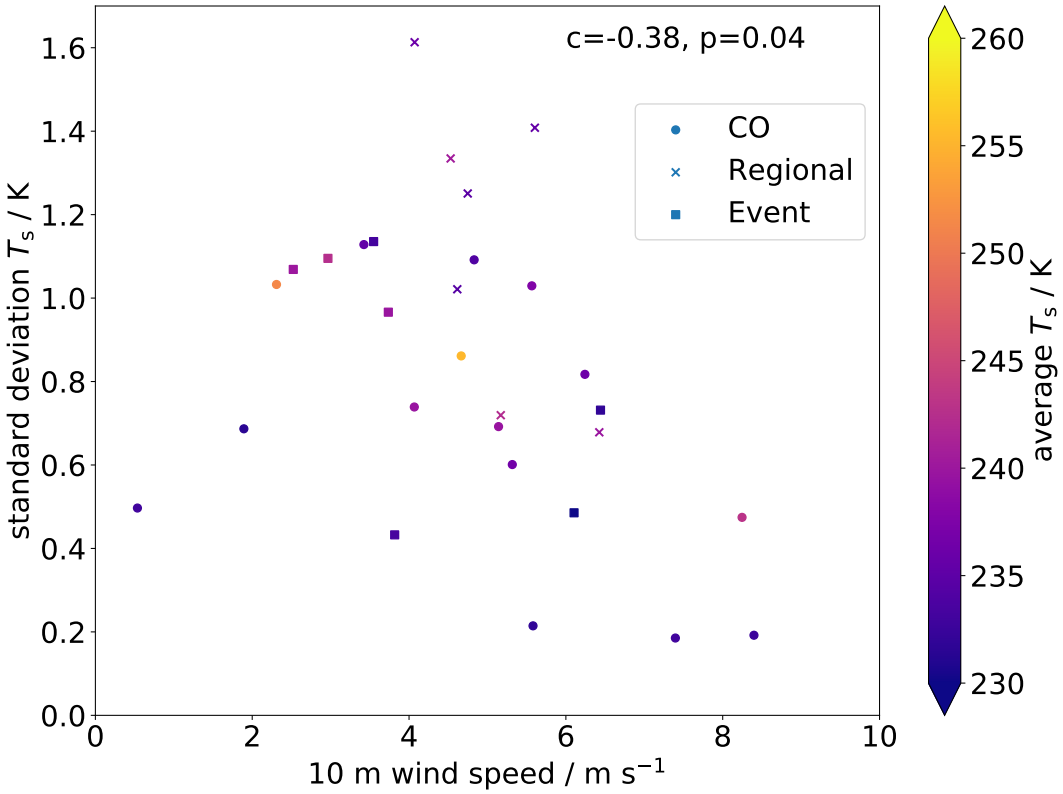

Figure 5.11: This figure shows the connection between the 10 m wind speed and surface temperature standard deviation. For every flight, the standard deviation of the surface temperature is set in connection to the 10 m wind speed as 10 minutes average around target time, shown as points. The correlation is -0.38, the significance 0.04 (p-value). The color of the points indicates the average surface temperature of the whole flight, presented in the colorbar. The different point shapes represent the flight types: CO (circle), L-Site/regional (cross), and events (square).

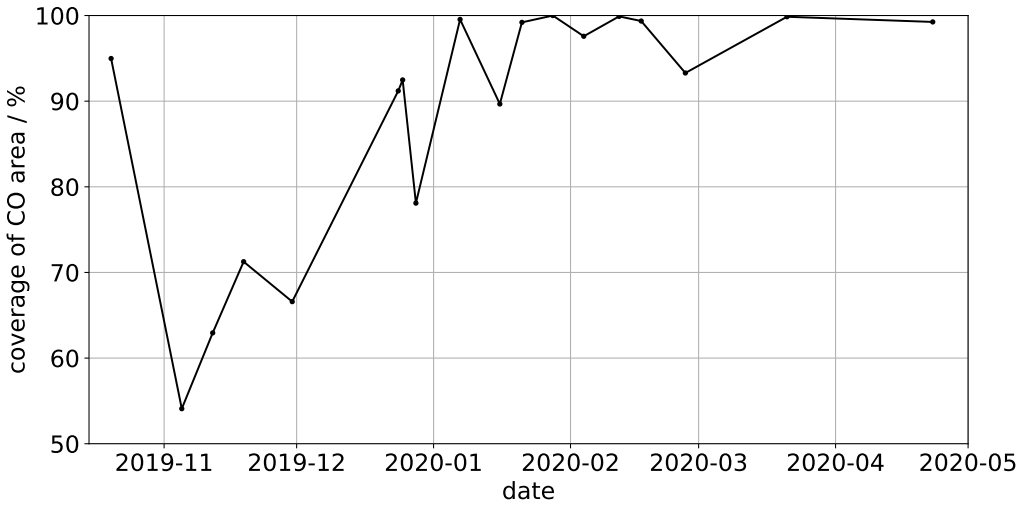

Figure 5.12: This figure shows the data coverage of the CO box for each flight. Time series of data points available in the CO box (as defined in Figure 5.10) for all local flights.

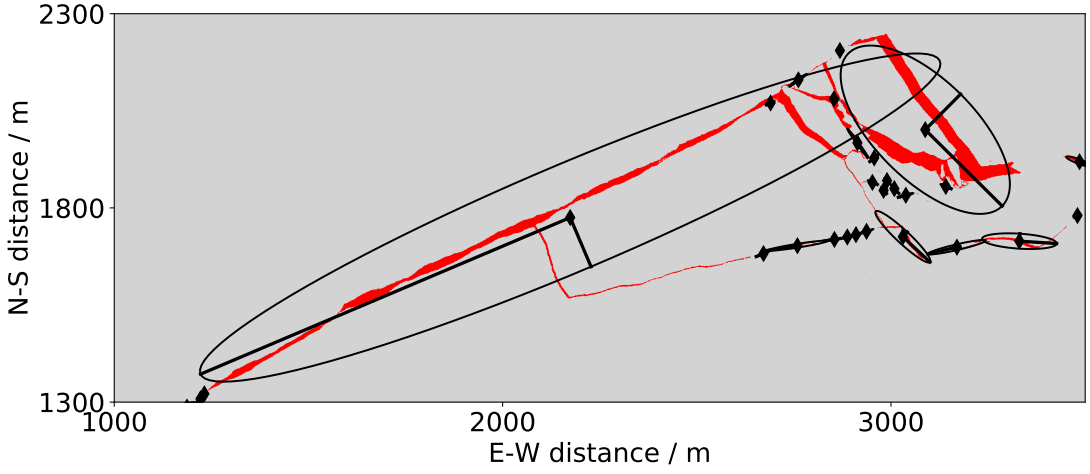

Figure 5.13: This figure shows an example of a set of segments. Selection of the lead classification map for 23 January 2020 in with the ellipse geometry for several segments which are automatically determined and might overlap.

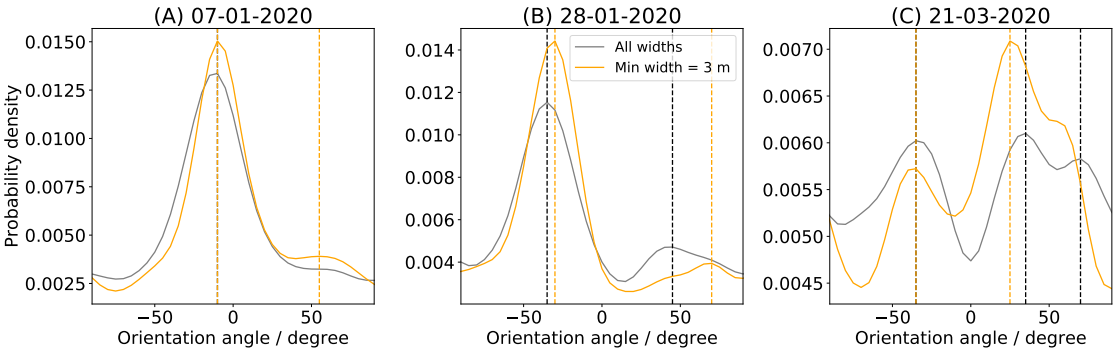

Figure 5.14: This figures shows the distribution and peaks of lead orientations in three flights. Probability density function and its peaks, according to the distributions of Figure 9 in the article.

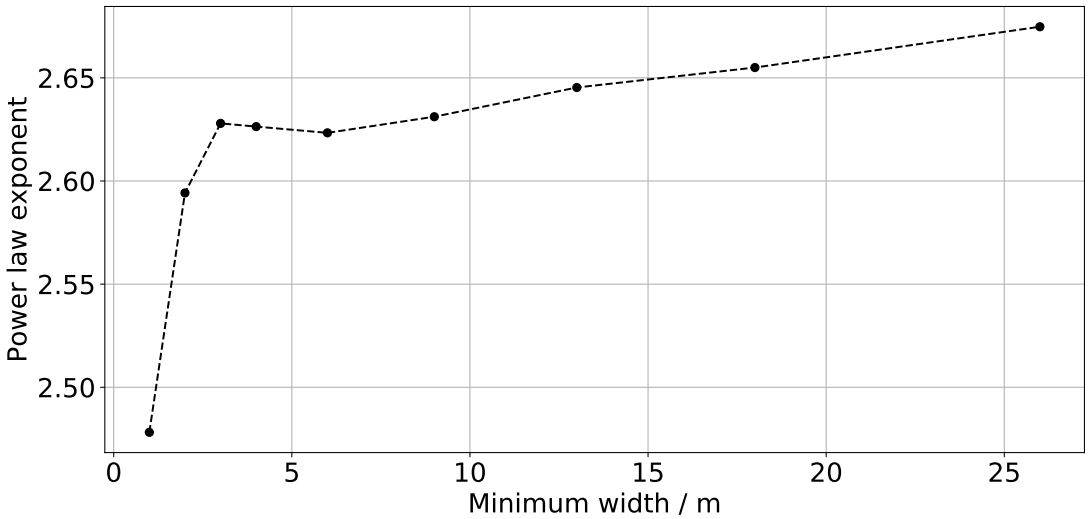

Figure 5.15: This figure shows the change of the power law exponent with minimum widths. Relation between power law exponent and applied minimum width for the linear fit in the log-log room of lead width against probability.

Chapter 6

Satellite sub-footprint scale variability

This chapter is based on the following manuscript draft:

Thielke, L., M. Huntemann, G. Spreen, C. J. Cox, V. Ludwig, M. D. Shupe (under preparation). Differences of sensible heat exchange over sea ice based on the satellite sub-footprint scale variability.

Relevance

In this chapter, we address the fourth research question R4: *Do satellite surface temperatures sufficiently represent the sub-footprint scale variability of the sensible heat exchange?*

Satellite products are common operational observations for the remote areas of Arctic sea ice. Thus, their retrievals are essential and should be evaluated for a more precise understanding of sea ice processes. Here, the focus is on the sub-footprint scale variability of surface temperatures. The high number of narrow leads, found in the previous Chapter 5, are not directly resolved within a thermal infrared (TIR) satellite footprint but change the heat exchange. This illustrates the importance of the spatial scales. The surface temperature is a crucial parameter for the Arctic heat budget, determining the changing sea ice mass balance. Therefore we use the 1 m resolution surface temperature maps from Chapter 3 to investigate the difference to the satellite surface temperature product with its coarser resolution of 1 km.

Contributions

I contributed to the conceptualization of this study and the methodology. I performed the formal analysis, investigated the data, and wrote the first draft of the manuscript.

Abstract

The sensible heat flux is a crucial component of the sea ice heat budget at the interface between the atmosphere and the surface of sea ice or snow. Most of the ocean-ice-atmosphere sensible heat flux in winter occurs in leads. This is due to the large temperature contrast between the ocean and the atmosphere, whereas typically sea ice and snow act as insulators. We use helicopter-borne surface temperature data at 1 m resolution to investigate the sub-footprint scale sensible heat flux variability for the satellite-based Moderate Resolution Imaging Spectroradiometer (MODIS) ice surface temperature product at 1 km resolution. The helicopter-borne data were recorded during the MOSAiC expedition in the winter 2019/2020. Here, we focus on five helicopter flights between 30 November 2019 and 23 April 2020, which overlap with MODIS data. For a consistent comparison, the MODIS data were temperature- and drift-corrected to match the recording time of the helicopter data. We compare the helicopter-borne data at 1 m with the same data re-gridded to 1 km resolution. We find an underestimated sensible heat flux in the 1 km data because the sub-footprint scale leads are not resolved while they have a large sensible heat flux. The resolution-caused differences increase linearly with the lead fraction of the given flight. With the findings we demonstrate the importance of the spatial scale for investigating the sensible heat exchange over sea ice. Next, we compare the 1 km helicopter-borne data with the MODIS ice surface temperatures and the derived sensible heat flux. The two products have no apparent similarities. The spatial variability is different, and there are no similar patterns of temperature and sensible heat flux. Hence, we recommend a further investigation by, for example, further validation and comparison with in-situ data.

6.1 Introduction

Leads are linear openings in the sea ice and are crucial for the winter heat budget within the Arctic ice pack. They allow for a more efficient heat exchange than the surrounding ice, in particular during winter, when there is a high temperature contrast between the ocean and the atmosphere (Maykut, 1978). Even small changes in sea ice concentration of 1% can cause an air temperature increase of 3.5 K (Lüpkes et al., 2008) and, therefore, affect the lower atmosphere's stability (Maykut, 1978). Helicopter-borne thermal infrared (TIR) imaging demonstrates a power law scaling for lead widths larger than 3 m, which shows that the number of narrow leads dominates over wider leads (Thielke et al., 2023). However, the narrow leads are not resolved in the TIR satellite data due to their limited spatial resolution of 1 km. Thus, small leads can not be directly considered for sensible heat flux calculations in satellite data (Figure 6.1). Additionally, narrow leads are more efficient per width in heat exchange than wider leads (Marcq and Weiss, 2012). The sensible heat flux is driven by the temperature difference between the air temperature and the surface temperature. Wider lead provide a larger area fraction of warm ocean surface which reduces the local temperature difference as the air is transported over the leads and thus reduce the sensible heat flux. Over narrow leads instead the advected air is colder and allows for an high sensible heat flux.

We hypothesize that the sensible heat exchange is underestimated when derived using satellite-based surface temperatures observations because the sub-footprint scale variability is reduced and the small-scale leads are not directly considered. To examine this process, we use the Moderate Resolution Imaging Spectroradiometer (MODIS) ice surface temperature product (Hall et al., 2004) because it is a commonly used product, e.g., to derive lead frequencies (Willmes and Heinemann, 2016), thin ice thickness (Preußer et al., 2016), or to create a merged sea ice concentration product (Ludwig et al., 2020). There is also new observational potential with new Arctic TIR satellite retrievals at 30 m spatial resolution (Qiu et al., 2023). The challenge of spatial resolution is present not only for remote sensing observations but also for modeling, which requires an adapted representation of leads for different approaches and resolutions (Michaelis and Lüpkes, 2022). In this study, we also consider smaller openings as leads (smaller than the usual definition of 50 m). Generally, leads can be covered with open water or thin ice.

We calculate the sensible heat flux from a simple bulk approach, including atmospheric in-situ observations from the Multidisciplinary drifting Observatory for the Study of Arctic Climate (MOSAiC) expedition (point measurements) and surface temperature maps from helicopter-borne TIR imaging. The MOSAiC expedition took place from September 2019 to October 2020, drifting with the Arctic sea ice along the Transpolar Drift (Nicolaus et al., 2022; Shupe et al., 2022; Rabe et al., 2022). We use surface temperature maps from

winter helicopter flights between November 2019 and April 2020 (Thielke et al., 2022e). The helicopter-borne surface temperatures are provided in 1 m resolution and re-gridded to the TIR satellite resolution of 1 km. We selected five flights for this study because they overlap with the MODIS data, allowing a one-to-one comparison. In this study, we perform the comparison in two steps. First, we investigate only the resolution effect by comparing the statistics of both 1 m and 1 km resolution observations from the helicopter. Second, we compare the 1 km data from the helicopter and MODIS satellite.

In Section 6.2, we describe the surface temperature data set from the helicopter and MODIS, as well as the in-situ atmospheric observations. Then, we present the methods for the drift and temperature corrections and the calculation of sensible heat flux in Section 6.3. In Section 6.4, we show and discuss the results for the comparison of the 1 m and 1 km helicopter-borne data to identify the effect of the different resolutions. In Section 6.5, we investigate the comparison of the 1 km helicopter and 1 km MODIS data. In the concluding Section 6.6, the findings of the comparisons are summarized, and the next steps are outlined.

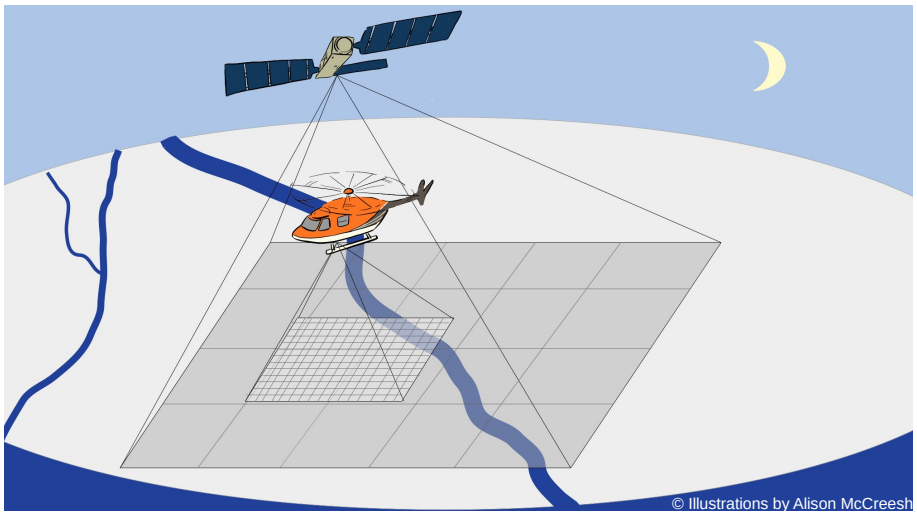

Figure 6.1: Schematic of helicopter-borne and satellite-based observations of sea ice at different resolutions. While the high-resolution helicopter-borne data can resolve the leads, a satellite footprint has several surface types within one footprint. [© Helicopter and Satellite Illustration Copyright Alison McCreesh.]

6.2 Data

In this section, the used datasets are presented. This comprises helicopter-borne surface temperature maps from the MOSAiC expedition, MODIS ice surface temperature swaths, and atmospheric in-situ observations during the MOSAiC expedition.

6.2.1 Helicopter-borne surface temperature

The helicopter-borne surface temperature maps with 1 m resolution (Thielke et al., 2022c) are based on images recorded with the TIR camera InfraTec VarioCam HD.

The helicopter surface temperature $T_{\mathrm{s,heli}}$ is derived with:

$$T_{\mathrm{s,heli}} = \frac{T_{\mathrm{b,heli}}}{e}, \tag{6.1}$$

with the brightness temperature $T_{\mathrm{b,heli}}$ and the emissivity e (assumed constant at 0.996 from Høyer et al. (2017)).

Note that the surface temperature does not represent the exact physical surface temperature as the emissivity is an approximation. Thus, this data product will be corrected with the in-situ skin temperature from the meteorological tower in the MOSAiC observatory (Subsection 6.2.4). While the helicopter flight time was about 90 minutes, we consider one fixed recording time (in the data named: target time) that corresponds to the middle of the flight. We use the time-fixed surface temperature, which is already corrected for temporal changes within the flight (details see Chapter 3). More information about the measurement setup can be found in Chapter 3.

6.2.2 MODIS ice surface temperature

MODIS is a widely used instrument with 36 spectral bands from the visible to mid-infrared wavelength (645 nm – 14.235 μm) while the spatial resolution decreases with increasing wavelength from 250 m to 1 km (Lubin and Massom, 2006). Further applications of the MODIS sensor are: monitoring glaciers, terrestrial vegetation, cloud and aerosol properties retrieval, synoptic meteorology, and sea or ice surface temperature (Lubin and Massom, 2006). MODIS is a push-broom sensor which covers the Earth every 1–2 days with a typical swath width of 2330 km (Lubin and Massom, 2006). The MODIS instrument is part of the National Aeronautics and Space Administration (NASA) Terra and Aqua satellites, launched in 1999 and 2002. We use the MODIS ice surface temperature product MYD29 (only Aqua) as 1 km swath data (Hall and Riggs, 2015; NSIDC, 2023a) in combination with the geolocation files (MYD03). There is a regular grid spacing of 1 km while the actual spatial resolution varies depending on the incidence angle and is 4.8×2.4 km at the swath edges (Masuoka et al., 1998). The bias of the ice surface temperature has been determined to be -2.1 K and the RMSE is 3.7 K (Hall et al., 2004).

For the MYD29 ice surface temperature retrieval, the bands 31 and 32 (11 and 12 μm) are used within a split-window technique and calculated according to:

$$T_s = a + bT_{11} + c(T_{11} - T_{12}) + d[(T_{11} - T_{12})(sec\theta - 1)], \tag{6.2}$$

with the measured brightness temperatures in the 11 and 12 μm channel T_{11} and T_{12},

sensor scan angle θ (determines path length of radiation in the atmosphere), and regression coefficients a, b, c, d (given on the products homepage NSIDC (2023a)). The data are provided by the NSIDC (NSIDC, 2022). The MYD29 swath data are provided as granules with 1 km horizontal resolution. The granule covers about 5 minutes and has a size of 2030×1354 km. Further details on the MYD29 product are presented in Hall et al. (2004) and can be looked up in the Algorithm Theoretical Basis Document (ATBD) (GSFC, 2001). We re-gridded the swath data to the NSIDC projection with 1 km resolution (NSIDC, 2023b).

TIR imaging only has an atmospheric pathway of about 300 m, while the satellite observations are made at an altitude of about 700 km. Therefore, we must pay more attention to the atmospheric influence of the satellite product. The product includes a conservative cloud mask which is applied by filtering the pixels with the flag *confident cloudy*. This is sufficient for our study because we look at single small-scale cases from the helicopter which were performed only during clear-sky conditions.

6.2.3 Days of interest

In this study, we focus on five cases with overlapping helicopter-borne and MODIS data. For some cases there were several swaths overlapping but we present only the swath with the smallest time difference. In Table 6.1, we show the recording times of each data set on the respective days. The smallest time difference of 1 hour and 24 minutes was on 27 February 2020; on 23 April 2020 we had a maximum time difference of 4 hours and 23 minutes. The larger the time difference, the larger the uncertainty due to ice drift and atmospheric changes, which should be considered when interpreting the results. Nevertheless, the ice drift was relatively small on 23 April 2020 compared to the time difference (Table 6.2). The furthest ice drift occurred for the case on 12 February 2020. We listed the location of RV *Polarstern* at the helicopter target time in Table 6.2, so there is a reference for other data sets.

Table 6.1: Time of recording in UTC on the investigated dates for the helicopter-borne data and the MODIS data.

Date	Time (Heli)	Time (MODIS)
30 November 2019	05:19:30	07:25:00
28 January 2020	07:21:30	10:25:00
12 February 2020	09:41:00	13:00:00
27 February 2020	12:31:30	13:55:00
23 April 2020	08:42:00	13:05:00

Table 6.2: Geolocation of RV *Polarstern* at the helicopter target time and the drift correction for the MODIS data for the difference to the helicopter recordings.

Date	latitude / deg north	longitude / deg east	Drift correction [x,y] / km
30 November 2019	86.0634	113.0630	-0.61, -0.84
28 January 2020	87.4523	95.8220	-0.25, 0.21
12 February 2020	87.8713	87.6950	-1.52, 1.59
27 February 2020	88.4087	36.6170	-0.58, -0.46
23 April 2020	84.0761	16.0507	-0.26, -0.52

6.2.4 Atmospheric in-situ observations

The atmospheric measurements were recorded at the 10 m meteorological tower in the MOSAiC Central Observatory (CO) (Cox et al., 2021). The values are retrieved for the recording time of the helicopter and MODIS. We use the skin temperature at helicopter time as ground truth for the surface temperature (Table 6.3). The atmospheric temperature and the wind speed at 10 m (Table 6.4) as well as the calculated air density (Table 6.5) are used for the calculation of the sensible heat flux (Subsection 6.3.3). We chose the 10 m instead of the 2 m reference level because there is less influence by the direct surrounding and, therefore, the measurements are more representative for the investigated area. We expect lower skin temperatures than air temperatures due to longwave radiative cooling since the helicopter flights were only performed during clear weather conditions.

We calculated the air density ρ with the ideal gas equation:

$$\rho = \frac{p}{R_\mathrm{s}\ T_\mathrm{a}}. \tag{6.3}$$

p is the air pressure at 2 m, R_s (287 J kg^{-1} K^{-1}) is the specific gas constant, and T_a is the air temperature at 10 m.

Table 6.3: Skin temperature from the meteorological observations for the helicopter $T_{\mathrm{skin,Heli}}$ and MODIS $T_{\mathrm{skin,MODIS}}$ time and their difference $\Delta T_{\mathrm{skin,MODIS-Heli}}$ on the investigated days.

Date	$T_{\mathrm{skin,Heli}}$ / K	$T_{\mathrm{skin,MODIS}}$ / K	$\Delta T_{\mathrm{skin,MODIS-Heli}}$ / K
30 November 2019	243.24	242.93	-0.31
28 January 2020	235.18	235.85	0.66
12 February 2020	239.95	240.68	0.73
27 February 2020	240.68	240.51	-0.18
23 April 2020	254.67	256.34	1.67

Table 6.4: Air temperature T_{air} and wind speed u, both at 10 m from the meteorological observations for the helicopter and MODIS time on the investigated days.

Date	$T_{\mathrm{a,Heli}}$ / K	$T_{\mathrm{a,MODIS}}$ / K	u_{Heli} / m s^{-1}	u_{MODIS} / m s^{-1}
30 November 2019	244.51	244.15	6.05	5.82
28 January 2020	237.71	238.39	1.86	3.17
12 February 2020	240.99	241.88	8.41	9.13
27 February 2020	241.10	240.99	7.37	7.66
23 April 2020	255.10	256.91	2.24	2.41

Table 6.5: Atmospheric pressure p from the meteorological observations and the calculated density ρ (with Equation 6.3) for the helicopter and MODIS time on the investigated days.

Date	p_{Heli} / hPa	p_{MODIS} / hPa	ρ_{Heli} / kg m^{-3}	ρ_{MODIS} / kg m^{-3}
30 November 2019	1017.40	1018.01	1.45	1.45
28 January 2020	1013.27	1012.71	1.49	1.48
12 February 2020	1013.55	1012.6	1.47	1.46
27 February 2020	1006.32	1006.72	1.45	1.46
23 April 2020	1024.82	1025.27	1.40	1.39

6.3 Methods

In this section, the methods, i.e., re-gridding of the data, temperature correction, and calculation of the sensible heat flux are presented. Also, the assumptions and uncertainties are listed.

6.3.1 Re-gridding of the data

We perform three steps to make the two different surface temperature data sets from the helicopter and MODIS comparable:

(i) We apply a drift correction to the MODIS data based on the drift of RV *Polarstern* between the recording time of the helicopter (reference) and MODIS data.

(ii) We remap the MODIS swath data to the NSIDC projection using a grid spacing of 1 km.

(iii) We use a drop-in-the-bucket (DITB) method to assign the values from the 1 m resolution helicopter data to the same 1 km NSIDC grid as for MODIS. The DITB method takes all values within the 1 km grid cell and calculates statistical values for each grid cell (mean, median, standard deviation).

6.3.2 Temperature correction

We want to eliminate differences between the two data sets that arise from the different retrieval methods and recording times. As described in Section 6.2, we have the following constraints for this study:

(i) The original helicopter-borne surface temperature measurements are based on a literature value for the emissivity; these measurements are offset corrected using surface observations.

(ii) The helicopter-borne data are corrected for the atmospheric influence within the flight by a fit function (Thielke et al., 2022e).

(iii) The MODIS ice surface temperatures have a temporal difference that can enclose changes in the surface temperature due to changes in the atmospheric conditions

We aim to achieve reasonable results when calculating the sensible heat flux with the helicopter surface temperature and the atmospheric parameters (Subsection 6.3.3). Thus, we performed an offset correction by the 10th percentile of the surface temperature against the in-situ skin temperature:

$$T_{\mathrm{s,corr}} = T_{\mathrm{s}} + [T_{\mathrm{skin,heli}} - P_{10}(T_{\mathrm{s}})]. \tag{6.4}$$

$T_{\mathrm{s,corr}}$ is the corrected surface temperature, T_{s} is the surface temperature of the helicopter or MODIS product, $T_{\mathrm{skin,heli}}$ is the in-situ skin temperature at the time of the helicopter flight, and $P_{10}(T_{\mathrm{s}})$ is the 10th percentile of the given surface temperature product (helicopter or MODIS). We choose the 10th percentile because it represents most prominent colder temperature of the thick ice and excludes the warm tail of the leads (not shown).

The calculated bias of the helicopter surface temperature is between 3.53 K on 23 April 2020 and 7.83 K on 27 February 2020 (Table 6.6). A bias of 7.5 K would be comparable to an emissivity correction of 0.03 at 250 K. Please note that there is an emissivity dependence on incidence angle and surface type (Hori et al., 2013), which we neglect here.

The potential atmospheric correction of the surface brightness temperature for the five flights is between -0.39 and -0.61 K (Cox, 2023). The adjustment, performed with the Rapid Radiative Transfer Model (RRTM) v3.3 (Mlawer et al., 1997; Iacono et al., 2000), includes (i) the effect of the atmospheric influence up to the flight altitude within the spectral range of the infrared (IR) camera and (ii) the downward longwave radiation reflected from the surface. This correction is not applied here, because it is assumed to be indirectly included in the here applied temperature correction.

Table 6.6: Bias of the surface temperature on the investigated days for the 1 m helicopter data $\Delta T_{\mathrm{s,heli,1m}}$, the 1 km helicopter data $\Delta T_{\mathrm{s,heli,1km}}$, and the MODIS $\Delta T_{\mathrm{s,MODIS}}$ data.

Date	$\Delta T_{\mathrm{s,heli,1m}}$ / K	$\Delta T_{\mathrm{s,heli,1km}}$ / K	$\Delta T_{\mathrm{s,MODIS}}$ / K
30 November 2019	7.50	7.18	1.83
28 January 2020	4.31	3.89	0.26
12 February 2020	7.45	7.36	1.25
27 February 2020	7.83	7.75	3.94
23 April 2020	4.06	3.53	-0.90

6.3.3 Sensible heat flux approximation

We calculate the surface sensible heat budget after the bulk formulation of Shokr and Sinha (2015):

$$F_{\mathrm{s}} = \rho \; c_{\mathrm{p}} \; u \; C \; (T_{\mathrm{s}} - T_{\mathrm{a}}). \tag{6.5}$$

ρ is the density of air, c_{p} is the heat capacity of air, u is the 10 m wind speed, C the bulk transfer coefficient, T_{s} the surface temperature, and T_{a} the 10 m air temperature. We define upward fluxes as positive (surface is warmer than atmosphere) and downward fluxes as negative (surface is colder than atmosphere).

The input values for the sensible heat flux are the surface temperature from the helicopter and MODIS and the atmospheric parameters for the helicopter flight time because the MODIS data are also corrected to match the helicopter flight conditions (Subsection 6.2.4). Nevertheless, conditions (T_{a}, u) different from those measured at the surface site at different times or locations of helicopter and satellite recordings could affect the sensible heat flux. Due to the temperature correction we only retrieve an approximated sensible heat flux. We would like to emphasize that the focus of this work is to compare different products and investigate the difference, but not aim to calculate the exact sensible heat flux value.

We use a simple approximation of the bulk transfer coefficient (as in Maykut (1978)), separated for thick ice (C=0.00175) and newly forming thin ice on leads (C=0.003). For the distinguished application of the bulk transfer coefficient, we use a flight-specific temperature threshold (Table 5.2) from the lead classification of the helicopter data (Thielke et al., 2022f, 2023). A more detailed formulation of the bulk transfer coefficient would require additional information, e.g., surface roughness and stability of the lower atmosphere. The consideration of these aspects is beyond the scope of this study.

6.3.4 Assumptions and uncertainties

In this part, we summarize the assumptions and uncertainties included in this study to be considered for the interpretation of the results:

- Surface temperature correction based on a point measurement of surface observations

- 10 m values of T_a and u are assumed to be representative of the full footprints of helicopter and satellite
- Emissivity assumption for the helicopter surface temperature
- Temporal changes during the helicopter flight and between the helicopter and MODIS data
- Different atmospheric effects (pathways) for helicopter and MODIS data
- Simplified bulk transfer coefficient for the sensible heat flux
- Small geolocation offset between helicopter and MODIS data due to a linear drift correction and the re-gridding of the data sets

6.4 Comparison of 1 m and 1 km helicopter data

In this section, we investigate the effect of the resolution change for the helicopter-borne data from 1 m to 1 km horizontal grid size because the MODIS product has a grid size of 1 km. To rule out any additional effects from the different products or the temporal difference, we first compare only the helicopter data at 1 m and 1 km resolution and then compare the 1 km helicopter data with the 1 km MODIS data in Section 6.5. In this section, the case on 28 January 2020 is described as an example, while the other cases are shown in Section 6.7 (Supplement). Lastly, the resulting differences of the sensible heat flux are compared for all cases.

6.4.1 Surface temperature differences

The surface temperature is a key variable for the Arctic heat budget as it is a required parameter for determining several heat fluxes (conductive, sensible, upwelling longwave radiative) (Lubin and Massom, 2006). The surface temperatures are presented in the left column of Figure 6.2. In Figure 6.2 (a) and (c), the helicopter-borne data at 1 m and 1 km resolution are shown, respectively. Thick ice, represented by lower temperatures, is blue, and leads, represented by higher temperature, are shown in yellow.

The strong temperature contrast between thick ice and leads allows for their clear distinction. Leads contribute higher surface temperatures and increase the spatial variability across the surface temperature maps as described above. We classify leads by a temperature threshold as described in Thielke et al. (2023). The resulting lead area fraction varies for the selected cases between 0.01% (27 February 2020) and 1.62% (28 January) (Table 6.7).

Based on the DITB method, we can provide different statistics within the grid cells, i.e., the mean (c), the median (g) and the standard deviation (h) of the grid cell. We see that for the 1 m data, the spatial variability is higher than the 1 km scale and no grid cell in the 1 km data is completely covered by a lead. Thus the temperature spread is strongly reduced for the 1 km data relative to the 1 m data. For the median values, the temperature is even lower than for the mean values as the minor fraction of leads is negligible in the median statistic. The presence of leads as warm anomalies is reflected in the higher standard deviation due to the stronger spatial variability of the 1 m data within the 1 km grid cell. We assume that the satellite signal at 1 km resolution is averaged and, thus, consider the mean per grid cell for the further analysis.

Table 6.7: Lead area fraction for the helicopter data on the investigated days as well as the resolution-caused sensible heat flux difference $\Delta F_{\mathrm{s,res}}$ between the 1 m and 1 km helicopter data. The 1 km sensible heat flux is always lower (less positive or more negative, see Table 6.8).

Date	Lead fraction / % (Heli)	$\Delta F_{\mathrm{s,res}}$ / W m^{-2}
30 November 2019	0.41	0.68
28 January 2020	1.62	0.66
12 February 2020	0.37	0.14
27 February 2020	0.01	0.04
23 April 2020	1.42	0.56

6.4.2 Sensible heat flux differences

The sensible heat flux describes the transfer of sensible heat at the interface between the atmosphere and snow or ice surface. As the sensible heat flux is a function of the surface temperature, we see the same characteristics as for the surface temperatures. The atmosphere is much colder than the ocean because the data were recorded during winter. The 1 m helicopter data (Figure 6.2 (b)) show a high spatial variability compared to the 1 km data (d). Due to the warmer surface temperatures of leads compared to the air temperature, there is a positive sensible heat flux over leads and a negative flux over thicker ice. The positive sensitive heat flux over leads is much larger in magnitude as leads are a large source of heat at the surface. The negative flux appears because the surface temperature is lower than the air temperature because of radiative cooling under the clear-sky conditions considered here.

To quantify the effect of the resolution, we take the mean and median over the whole domain for both resolutions and compare these integrated values (Table 6.8). Comparing the mean values, we see a reduction of the sensible heat flux (more negative or less positive) for the coarser resolution data at 1 km. This is reasonable because the warm anomalies of leads are not resolved. The sensible heat flux difference varies between 0.04 and 0.68 W m^{-2}

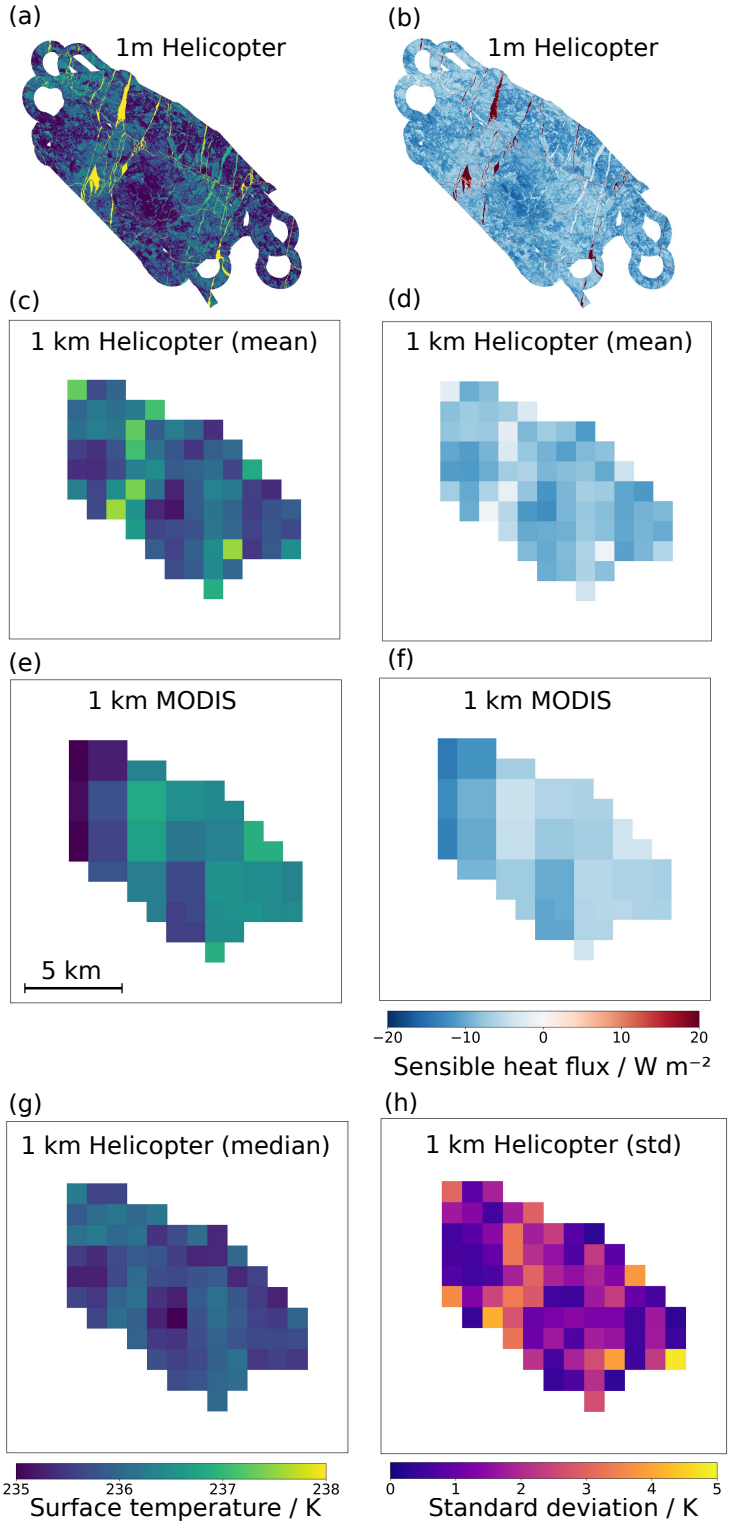

Figure 6.2: Surface temperature (left column) and sensible heat flux (right column) on 28 January 2020 for the helicopter data at 1 m (a and b), 1 km resolution (c and d), and MODIS data at 1 km resolution (e and f). Also, the 1 km helicopter median (g) and standard deviation (h) within the one grid cell is presented.

(27 February 2020 and 30 November 2019). The flight on 30 November 2019 is a special case because there is a still remaining temporal variation in the time-fixed surface temperature, which increases the spatial variability. On 28 January 2020, there is a similar large difference of 0.66 W m^{-2}.

Table 6.8: Mean and median for the sensible flux F_s for the 1 m helicopter data, the 1 km re-gridded helicopter data, and the 1 km re-gridded MODIS data on the investigated days. All values are in W m^{-2}.

Date	$F_{s,heli\_1m}$ (mean)	$F_{s,heli\_1m}$ (median)	$F_{s,heli\_1km}$ (mean)	$F_{s,heli\_1km}$ (median)	$F_{s,modis\_1km}$ (mean)	$F_{s,modis\_1km}$ (median)
30 November 2019	-10.60	-14.97	-11.28	-11.58	-9.30	-10.50
28 January 2020	-7.47	-9.62	-8.13	-8.58	-7.78	-6.79
12 February 2020	-19.24	-20.00	-19.38	-19.64	-15.74	-15.17
27 February 2020	-4.96	-5.36	-5.00	-4.75	-3.66	-3.98
23 April 2020	3.05	1.52	2.49	2.37	1.37	1.15

6.4.3 Contributions of leads

When comparing the sensible heat flux change with the lead area fraction (Table 6.7), we see the minimum of both parameters (close to zero) on 27 February. On 30 November 2019 and 12 February 2020, we have a similar lead fractions (0.41% and 0.37%), but the largest resolution-caused difference for the sensible heat flux on 30 November 2019. This probably results from the temporal variation of the surface temperature during this helicopter flight, increasing spatial variability. A small lead fraction change (sub-percent) of 0.37% causes additional 0.14 W m^{-2} of sensible heat flux (12 February 2020). Further, 1.42% and 1.62% lead area fraction cause sensible heat flux differences of 0.56 W m^{-2} and 0.66 W m^{-2}, respectively. We find a linear relationship between the lead fraction and the resolution-caused sensible heat flux difference (Figure 6.3), except for the outlier on 30 November 2019. This linear relationship is expected as the difference of the sensible heat flux occurs because the leads are not directly represented in the 1 km data but are more efficient in the heat exchange. As we look at the average over the whole domain, we can assume an average temperature for leads and thick ice; both needs to be classified due to the different transfer coefficient.

To describe the linear relation between the lead area fraction and the resolution-dependent sensible heat flux difference, we take the difference between the average sensible heat flux at 1 m resolution and 1 km resolution. We have the same values of the density of air (ρ), the heat capacity of air (c_p), and the 10 m wind speed (u) for both resolutions. Therefore, we assume that the sensible heat flux F_s is proportional to bulk transfer coefficient C and the temperature difference between the surface and the atmosphere.

The sensible heat flux of the 1 m resolution data is the sum of two parts: (1) the bulk transfer coefficient for thin ice (0.003) and the average lead surface temperature $\overline{T_{s,lead}}$ for

the lead fraction l, and (2) the remaining ice area with the bulk transfer coefficient for thick ice (0.00175) and the average ice surface temperature $\overline{T_{\mathrm{s,ice}}}$:

$$F_{\mathrm{s,1m}} \propto l \cdot 0.003 \cdot (\overline{T_{\mathrm{s,lead}}} - T_{\mathrm{a}}) + (1 - l) \cdot 0.00175 \cdot (\overline{T_{\mathrm{s,ice}}} - T_{\mathrm{a}}). \tag{6.6}$$

The sensible heat flux of the 1 km data is calculated only with the bulk transfer coefficient for thick ice, while the surface temperature is an average of the lead and ice surface temperature, weighted by the lead fraction:

$$F_{\mathrm{s,1km}} \propto 0.00175 \cdot [(l \cdot \overline{T_{\mathrm{s,lead}}} + (1 - l)\overline{T_{\mathrm{s,ice}}}) - T_{\mathrm{a}}]. \tag{6.7}$$

When subtracting $F_{\mathrm{s,1m}}$ and $F_{\mathrm{s,1km}}$ the resolution-dependent sensible heat flux difference ΔF_{s} is:

$$\Delta F_{\mathrm{s}} \propto l \cdot [0.003 \cdot (\overline{T_{\mathrm{s,lead}}} - T_{\mathrm{a}}) - 0.00175 \cdot (\overline{T_{\mathrm{s,lead}}} - T_{\mathrm{a}})]. \tag{6.8}$$

Thus, we can show that ΔF_{s} has a linear relation to the lead area fraction l while its slope is defined by the temperature difference (and the not considered parameter ρ, c_{p}, and u):

$$\Delta F_{\mathrm{s}} \propto 1.25 \times 10^{-3} \cdot l \cdot (\overline{T_{\mathrm{s,lead}}} - T_{\mathrm{a}}). \tag{6.9}$$

As the temperature difference between air and lead surface differs from flight to flight, the resulting sensible difference might vary slightly and change the slope of the linear relationship. The larger the difference between the lead surface temperature and the air temperature, the larger the sensible heat flux difference. In conclusion, the 1 km resolution data are lacking in comparison to the 1 m resolution data a higher heat input to the atmosphere due to a more positive heat fluxes over the leads.

6.5 Comparison of 1 km helicopter and MODIS data

Here, we compare the 1 km helicopter and the 1 km MODIS ice surface temperatures. Both products have the same spatial resolution and are drift corrected. Thus, we can compare their surface temperatures directly. The MODIS ice surface temperature is an operationally used product, while the helicopter surface temperature map is a new product and not validated with in-situ observations yet. We performed the temperature correction to achieve similar surface temperatures for the direct comparison on the same scale. Herrmannsdörfer et al. (2023) shows in the context of the MOSAiC measurements the significant errors of the MODIS ice surface temperature. Here, we focus on the differences between the products rather than the absolute values. In this section again, we focus on the case 28 January.

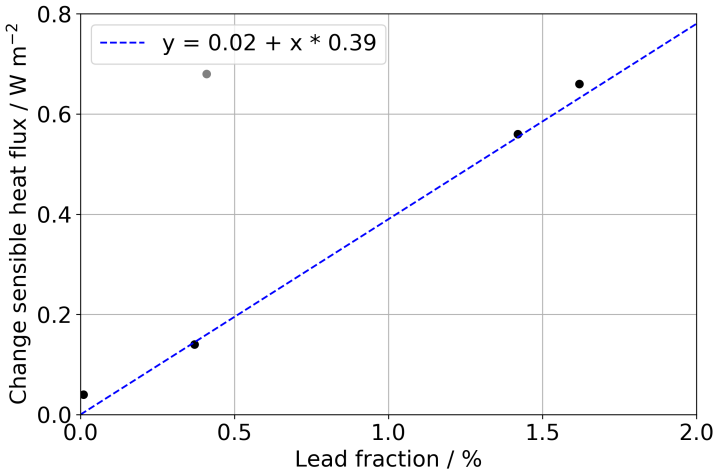

Figure 6.3: Lead fraction versus resolution-caused sensible heat flux difference ΔF_s (points). The gray point is the outlier from 30 November 2019. The blue dashed line is a linear fit of the four black points. Data point can be found in Table 6.7.

6.5.1 Surface temperature differences

The 1 km MODIS surface temperature on 28 January, restricted to the helicopter-covered area, is shown in Figure 6.2 (e). Generally, there is less spatial variability, but also, the temperature patterns are not aligned with the helicopter data, for either the mean or the median approach. There are block-like structures, which are already in the MODIS product and no artefact of our gridding. This results for some cases in an effective resolution of 2 km and additionally reduces the spatial variability. The time difference between the helicopter and the MODIS recording was about 3 hours on 28 January 2020. The potential temporal change is mitigated by the drift correction and temperature correction. Thus, the time difference is likely not the reason for the different spatial patterns of surface temperature. For all cases, no connection appears between the helicopter and MODIS ice surface temperature (Figure 6.8 in Section 6.7, Supplement). Among other potential reasons, an atmospheric influence could be possible because only a conservative cloud mask is applied. Consequently, a direct comparison between both products is at this state limited but might be improved by new analysis steps in future work (Subsection 6.6.1).

6.5.2 Sensible heat flux differences

Similar results as for the surface temperature apply to the sensible heat flux based on the findings of the surface temperature comparison (Subsection 6.5.1). The sensible heat flux for the 1 km helicopter-borne data (Figure 6.2 (d)) has a higher spatial variability than the MODIS-based sensible heat flux (Figure 6.2 (f)). The absolute values of the sensible heat flux should be interpreted with caution because the surface temperature correction

is an approximation. When comparing the mean values for the 1 km helicopter and the MODIS data, MODIS observes fewer extreme values on either side. This could indicate that MODIS represents rather averaged conditions (with less spatial variability), and the more extreme surface temperatures are smoothed out. Here, also the lower effective resolution could play a role. Due to the less diverse temperature distribution for the 1 km data (helicopter and MODIS), the median and mean are more similar than for the 1 m data, where the warm tail from the lead temperatures influences the mean value more. Examples of the surface temperature distribution of the 1 m resolution helicopter-borne data are shown in the previous Chapters in Figure 3.8, Figure 5.2, and Figure 5.4.

6.6 Discussion and Conclusions

This study analyzes the role of the sub-footprint scale variability of the sea ice surface temperature and sensible heat flux. We use helicopter-borne data from the MOSAiC expedition and MODIS ice surface temperatures to analyze five cases for which we have an overlap between the two data sets. We investigate the potential impacts of resolution-based and product-based temperature differences on the sensible heat flux for sea ice in the Central Arctic during winter. The results are discussed in a two-fold comparison: (i) the helicopter-borne data for the original resolution at 1 m resolution and the re-gridded at 1 km, and (ii) the helicopter-borne data and MODIS data both at 1 km resolution.

With the averaging of the helicopter-borne data to the 1 km resolution, the temperature range is decreased, and the leads are not directly represented. Thus, the sensible heat flux is underestimated for the 1 km data by 0.04–0.66 $\mathrm{W\,m^{-2}}$ (0.68 $\mathrm{W\,m^{-2}}$ on 30 November 2019 due to an artefact). We show a linear relationship between the lead fraction and the resolution-dependent sensible heat flux difference. Due to the limited number of four cases (one outlier due to temporal drift), we recommend augmenting the relation with more cases (Subsection 6.6.1). The resolution-dependent difference occurs due to the higher efficiency of sensible heat transfer for leads than of the snow-covered thicker ice (represented by the bulk transfer coefficient in Equation 6.5). These findings are constrained to the winter time due to the strong contrast between the air and sea temperatures. The difference of the sensible heat flux shows the importance of considering spatial scales for the investigation of the heat exchange over sea ice with a focus on small-scale leads.

The resolution-dependent difference can have several implications. The underestimated sensible heat flux in the 1 km data causes an underestimation of the heat input into the atmosphere. The relevance of additional 0.66 $\mathrm{W\,m^{-2}}$ needs to be investigated. Our result should be compared to other studies, e.g, Lüpkes et al. (2008). They found an increase of 3.5 K due to the reduction of sea ice concentration by 1%. Besides the atmospheric changes, there are also implications for the sea ice mass balance. The slightly higher

averaged surface temperatures (colder thick ice and warmer leads) for the 1 km data have a negligible effect on the total ice thickness. But due to the stronger heat release through leads, there is a higher ice production in leads which is not considered in the 1 km data. Thus, the ice growth might be underestimated in 1 km data, which can be related to the fractional coverage of leads over the 1 km domain under consideration of the atmospheric conditions (T_a, u).

The comparison with the MODIS ice surface temperature revealed a distinct difference to the re-gridded 1 km helicopter-borne surface temperatures. Due to the temperature correction, a comparison between the helicopter and MODIS observations is possible. However, there are limited similarities in the spatial patterns for all cases. The partly coarser effective resolution of the MODIS data should be examined for other cases and compared against the results of the 2 km average helicopter data. Furthermore, we recommend a more detailed comparison that takes into account additional factors that allow a quantification of the comparability of the two surface temperature products. This would help in conducting a more in-depth investigation of the sub-footprint scale variability for operational satellite products.

Nonetheless, the resolution-based differences from the helicopter-borne data reveal the relevance of small-scale variations for calculating the surface energy budget over sea ice. We recommend developing an approximation of the spatial variability, possibly based on lead fraction data, that can contribute to the calculation of the sensible heat flux. This could be also applicable to regional or global climate models with resolutions of 1 km or lower, which have parameterization for thermal sea ice processes occurring at smaller scales. The model improvement was one key purpose of the MOSAiC expedition.

6.6.1 Next steps

Based on the finding and the discrepancies presented here, we recommend the following steps forward:

- Validation of helicopter-borne surface temperature, including the emissivity, with other surface temperature measurements from the MOSAiC expedition.
- Use of the typical helicopter-borne surface temperature standard deviation within one satellite footprint as an approximation for the spatial variability
- Calculation of more detailed transfer coefficients (using surface roughness, stability) and consideration of the lead width dependent heat exchange (Marcq and Weiss, 2012).
- Include another satellite-based data set from a different sensor, i.e., VIIRS surface temperature at 750 m resolution (Tschudi et al., 2017).

- Comparison with the in-situ point measurements of the sensible heat flux (no spatial variability), to provide an absolute assessment of the ability to derive surface sensible heat fluxes from helicopter and satellite measurements.
- Inclusion of more helicopter flights (without MODIS overlap) to investigate further the linear relationship of the lead fraction and the resolution-dependent sensible heat flux difference.
- Comparison to the MODIS lead product (Willmes and Heinemann, 2015)
- Quantification of the effect of the leads by investigating the surface temperature differences between the 1 km data and the 1 m data with the two cases: (i) all data included (as done here) and (ii) surface temperatures with classified leads excluded.
- Parameterization of sub-footprint variability (e.g., assumption of a lead fraction based on the large scale lead fraction).

Data availability

- Helicopter-borne surface temperature: Thielke et al. (2022c)
- Helicopter-borne lead classification: Thielke et al. (2022f)
- MODIS ice surface temperature: Hall and Riggs (2015)
- Atmospheric data: Cox et al. (2021) [updated version used]

Acknowledgements

This work was supported by the German Ministry for Education and Research (BMBF) as part of the International Multidisciplinary drifting Observatory for the Study of the Arctic Climate (grant MOSAiC20192020), and IceSense (grant 03F0866B). We acknowledge the support by the Deutsche Forschungsgemeinschaft (DFG) through the International Research Training Group IRTG 1904 ArcTrain (grant 221211316), the MOSAiCmicrowaveRS project (grant 420499875), and the Transregional Collaborative Research Center TRR 172 (grant 268020496) Arctic Amplification: Climate Relevant Atmospheric and Surface Processes, and Feedback Mechanisms (AC)^3. We thank all persons who contributed to the expedition of the Research Vessel *Polarstern* during MOSAiC in 2019-2020 (AWI_PS122_00) (Nixdorf et al., 2021). MDS was supported by a Mercator Fellowship as part of (AC)3, the US National Science Foundation (OPP-1724551) and by NOAA Global Ocean Monitoring and Observing program (via NA22OAR430151). CJC was supported by NOAAs Global Ocean Monitoring and Observing Program (FundRef https://doi.org/10.13039/100018302).

6.7 Supplement

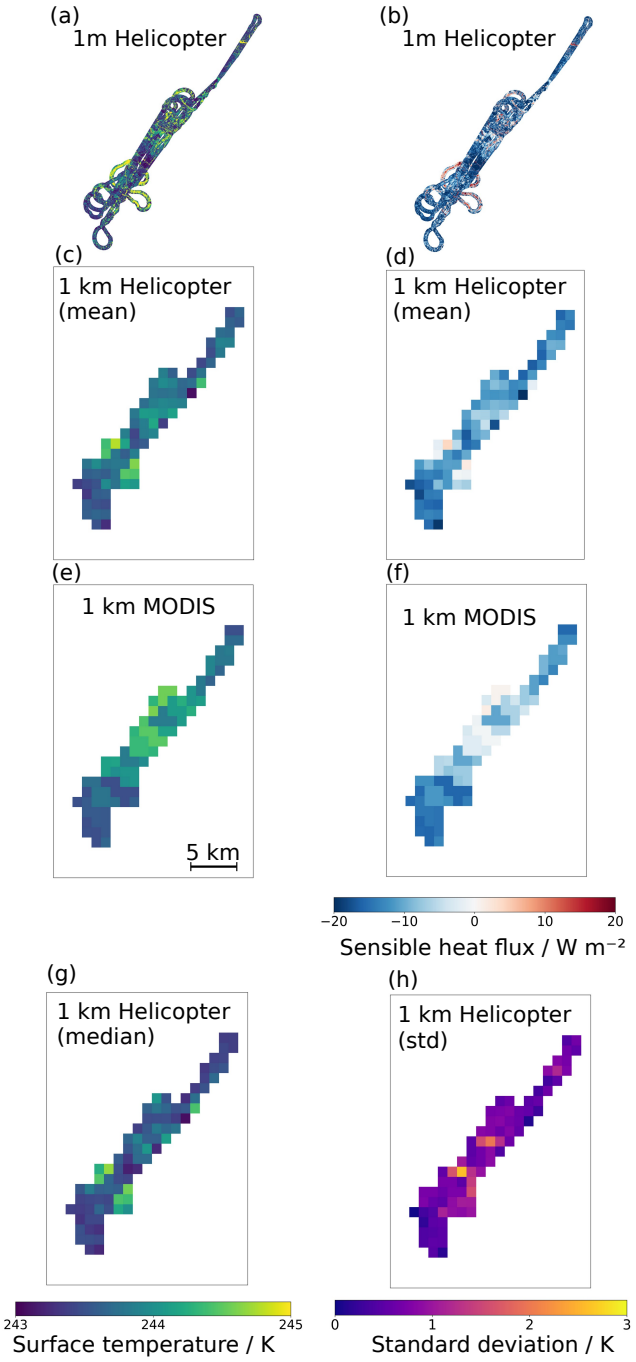

Figure 6.4: Surface temperature (left column) and sensible heat flux (right column) on 30 November 2019 for the helicopter data at 1 m (a and b), 1 km resolution (c and d), and MODIS data at 1 km resolution (e and f). Also, the 1 km helicopter median (g) and standard deviation (h) within the one grid cell is presented.

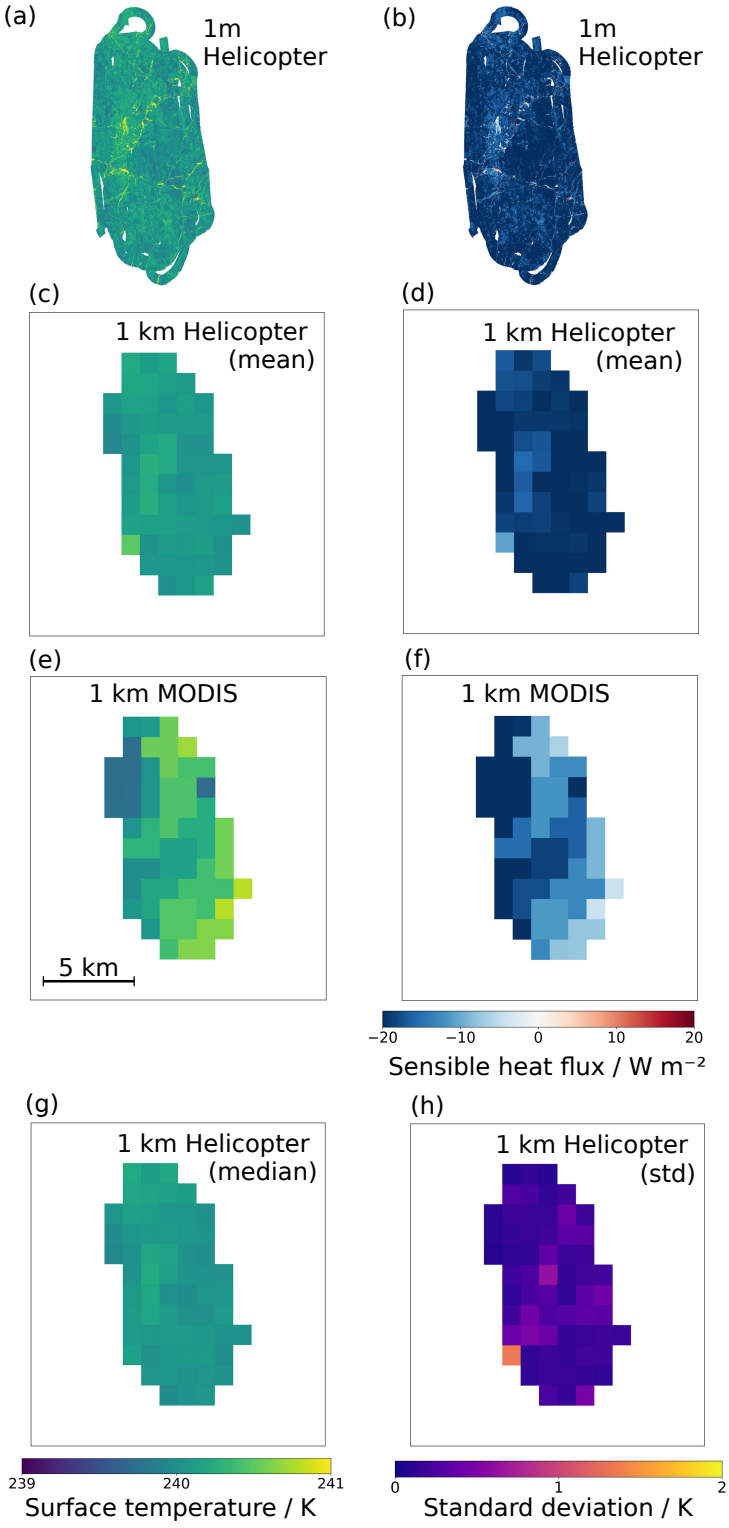

Figure 6.5: Surface temperature (left column) and sensible heat flux (right column) on 02 February 2020 for the helicopter data at 1 m (a and b), 1 km resolution (c and d), and MODIS data at 1 km resolution (e and f). Also, the 1 km helicopter median (g) and standard deviation (h) within the one grid cell is presented.

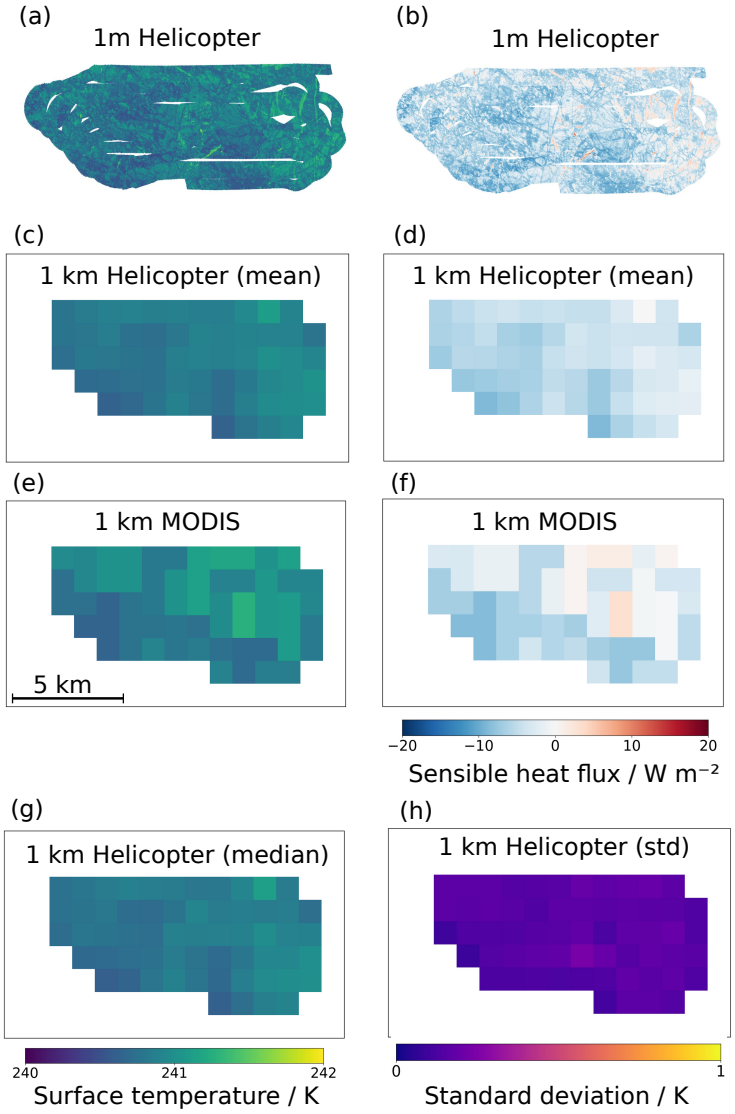

Figure 6.6: Surface temperature (left column) and sensible heat flux (right column) on 27 February 2020 for the helicopter data at 1 m (a and b), 1 km resolution (c and d), and MODIS data at 1 km resolution (e and f). Also, the 1 km helicopter median (g) and standard deviation (h) within the one grid cell is presented.

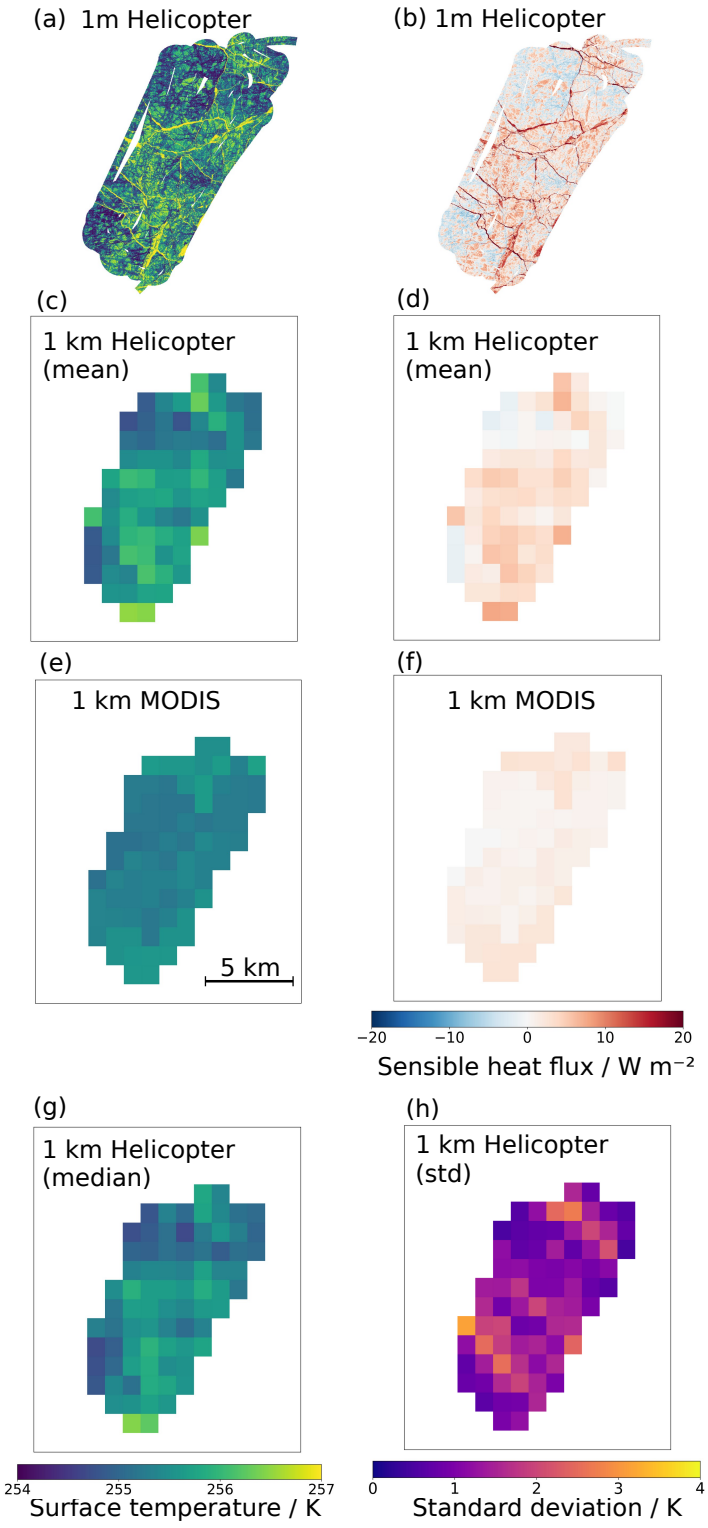

Figure 6.7: Surface temperature (left column) and sensible heat flux (right column) on 23 April 2020 for the helicopter data at 1 m (a and b), 1 km resolution (c and d), and MODIS data at 1 km resolution (e and f). Also, the 1 km helicopter median (g) and standard deviation (h) within the one grid cell is presented.

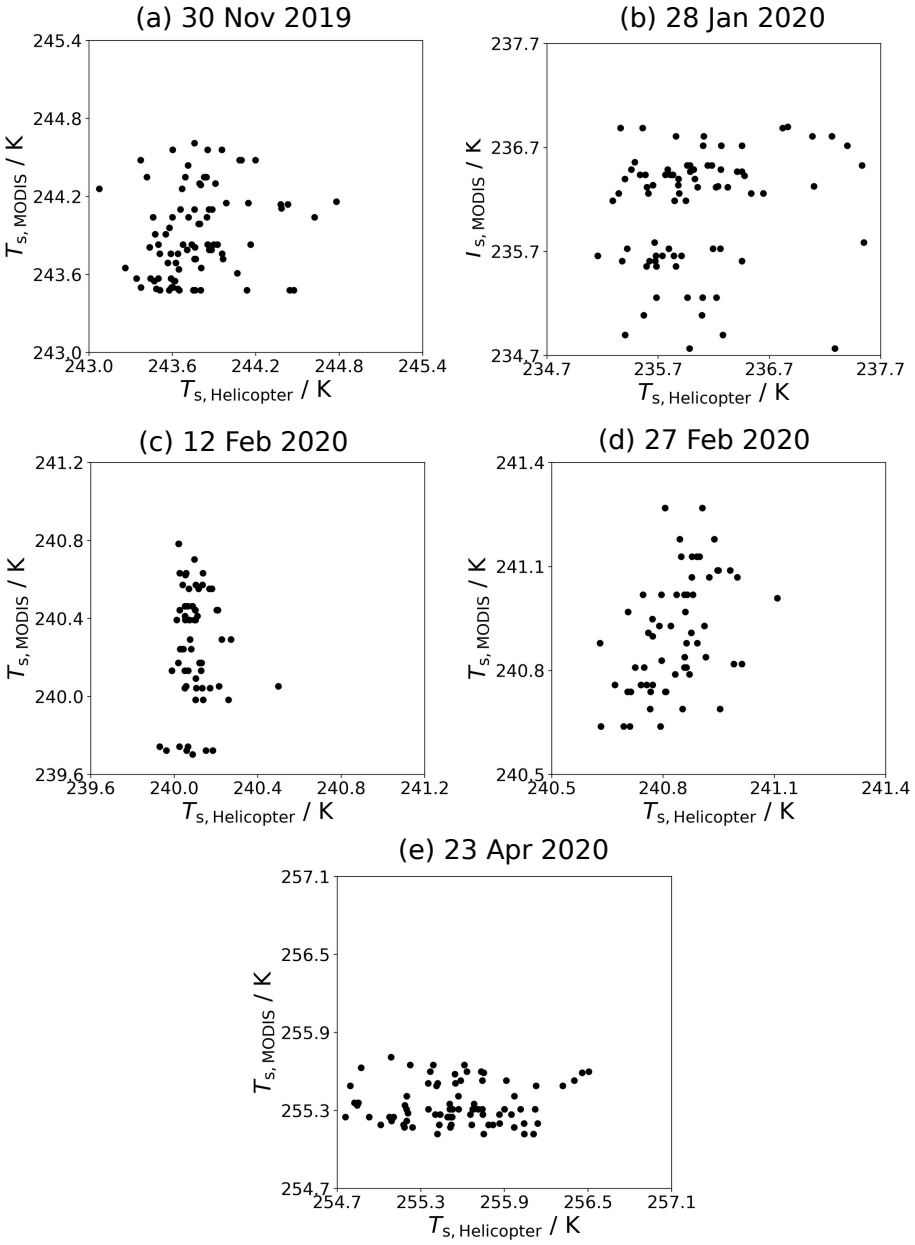

Figure 6.8: Scatter of the 1 km surface temperatures from the helicopter versus MODIS data for all five cases on (a) 30 November 2019, (b) 28 January 2020, (c) 12 February 2020, (d) 27 February 2020, and (e) 23 April 2020.

Chapter 7

Conclusions

7.1 Key findings

The findings presented in this thesis uncover new aspects of small-scale sea ice characteristics during winter 2019/2020 based on helicopter-borne thermal infrared (TIR) imaging in the central Arctic. The data were recorded during the MOSAiC expedition, which provides a large suite of measurements to support this analysis. In Section 1.2, I presented four research questions, which are the key scientific motivations of this thesis.

At first, the potential of the TIR imaging for the spatial analysis of sea ice during winter is addressed. With the resulting surface temperature maps, relevant conditions for melt ponds during winter are determined. Based on the full set of surface temperature maps, the geometrical properties of small-scale leads (area fraction, width, and orientation) are analyzed for horizontal scales of meters. Lastly, based on the found properties of small-scale leads, the satellite sub-footprint scale variability and its relevance for sensible heat exchange are investigated.

R1: What is the potential of thermal infrared (TIR) imaging for the spatial analysis of sea ice during winter?

The findings regarding this research question are presented in Chapter 3. The helicopter-borne TIR imaging shown in this thesis was performed on Arctic sea ice for the first time to this extent. TIR imaging uses the peak of the Earth's radiation at around 10 μm (Chapter 2). During the MOSAiC expedition, several thousands of images were recorded during 35 flights that covered sea ice in the central Arctic during winter between October 2019 and April 2020. More than 150000 images with 480×640 temperature values (pixel) were collected; more than 46×10^9 temperature values in total. Several processing steps had to be identified and applied to get an accessible and easy-to-handle dataset:

(i) Image correction: this includes gradient correction and an additional corner mask to remove areas of strong distortion,

(ii) Mapping: performing ice drift correction, georeferencing, gridding, and constraining the incidence angle to avoid large distortions,

(iii) Optimization: adjusting values recording time, roll, pitch, heading, effective focal length, and radial distortion coefficient,

(iv) Temperature correction: temporal drift changes corrected to a fixed reference target time.

After the processing, small artifacts, like minor geolocation shifts, remain but are no problem for statistical analysis, which is the main focus of this thesis. Combining the images into one map created a surface temperature dataset for each flight. The advanced data product is also advantageous because it contains the spatial context of the overflown sea ice. The flights on the local scale (5–10 km) can provide a coherent area coverage of the Central Observatory (CO) and its surroundings, while regional flights (20–40 km) provide statistics over a larger area with often single, not overlapping tracks.

One challenging factor is the change of atmospheric conditions (e.g., air temperature or wind speed) that changed the surface temperature within one helicopter flight. Therefore, the surface temperature changes were corrected to a reference time with a fit function. Also, clouds can alter the surface temperature but are difficult to monitor operationally during Arctic winter because visual observations of clouds are impossible during the polar night. The meteorological flight reports indicate the presence of sometimes high clouds and the possibility of fog or low clouds. However, because the flights were preferably conducted in clear skies, the cloud influence on the recorded data can be assumed to be minor.

With a flight altitude of 300 m, the processed maps can reach a horizontal resolution of 1 m. As a result small features on the sea ice surface can be resolved. Also, detailed temperature distributions on the local and regional scale can be analyzed. A strong temperature contrast allows the differentiation between thick ice and leads. Leads are often represented as a second minor peak in the warm part of the temperature distribution.

Single images with a close-to-nadir incidence angle have an even higher resolution and show very detailed information. To emphasize the questioned potential of TIR imaging: it is even possible to identify the paths of people or snow scooter tracks on snow-covered sea ice, or determine several temperature changes within a 100 m wide lead. More examples are motivated in the Introduction in Subsection 1.1.5.

All in all, the helicopter-borne TIR imaging requires several processing steps and supplementary data, like the geolocation information. The resulting surface temperature

maps are a valuable tool for the spatial analysis of the sea ice surface at high spatial resolutions of 1 m, compared to operationally used 1 km resolution satellite data. The surface temperature maps are the key dataset of this thesis. The data contribute to the following three research questions R2, R3, and R4.

R2: To which extent do winter surface temperatures reveal information about the characteristics of melt ponds?

This study builds on the outcome of the first research question: the surface temperature maps. In a case study with the surface temperature map from 21 January 2020 in Chapter 4, the preconditioning of melt ponds during winter is investigated. The same ice from the helicopter-borne visual observations in summer could be identified in the winter surface temperature maps. This is possible because the MOSAiC expedition drifted with the same ice across the Arctic Ocean from autumn 2019 until summer 2020. Warm surface temperature anomalies ranging from 0.3 to 2.5 K are identified and compared to complementary data. The helicopter-borne topographical observations during winter show that lower freeboard corresponds with the warm anomalies. A one-dimensional thermodynamic model can connect the observed temperature differences to the observed differences in ice thickness and snow depth (level versus deformed sea ice).

Moreover, a melt pond classification based on the warm anomalies was performed with a temperature threshold. A melt pond classification with a performance of 41% is achieved. The results illustrate that seasonal prediction of the summer melt pond locations and coverage from winter surface temperature anomalies is possible. Nevertheless, there is room for further investigation.

The three key findings are:

(i) Winter warm surface temperature anomalies are co-located with melt pond locations in the following summer,

(ii) Warm anomalies appear in refrozen leads, in refrozen melt ponds, and in surface depressions of deformed ice, due to thinner snow and ice,

(iii) There is a potential for predicting summer melt pond fraction from winter surface temperatures.

These findings are based on the case study with the data from 21 January 2020. A more extensive study for more dates can be done with the existing data but this is open future work. There is a potential to investigate data from different times during summer (different melt pond stages) and winter (changing properties and magnitudes of the warm anomalies). Looking at the evolution of two exemplary warm anomalies showed variations over time. Particularly the refrozen leads only appeared in mid-winter, and their warm

temperature anomalies decreased due to larger ice production and new snow cover. It is assumed that the topography-controlled warm anomalies in surface depressions could be refrozen melt ponds from the previous summer. Ideas for further improvement on the use of surface temperatures to understand melt pond characteristics are presented in Section 7.3.

R3: What are the geometrical properties of leads on horizontal scales of meters?

The large temperature contrast between the thin ice (or open water) and snow-covered thick ice allows for lead classification, as presented in Chapter 5. From the lead classification maps, the geometrical properties lead area fraction, width, and orientation are derived. Lead fractions of up to 4% considerably affect the surroundings by a stronger heat exchange during winter. The different evolution throughout the winter on local and regional scales shows the importance of understanding the different scales. The local conditions do not necessarily represent large-scale conditions but provide a valuable context for the MOSAiC observations in the Central Observatory (CO). For example, synoptic events, like the November storm during the MOSAiC expedition, can change the local conditions (increase in lead area fraction). The lead area fractions from helicopter-borne data are comparable to Synthetic Aperture Radar (SAR) classifications on similar scales.

Lead segmentation with an ellipse approximation for leads provides information on the width and orientation. The lead width distribution can be described by a power law with a negative exponent of 2.63. Following, there are exponentially more narrow leads than wider leads. The power law is valid down to a lead width of 3 m. The exponent found in this study agrees with literature values, while it is at the upper end of the reported values. This dataset from TIR imaging extends the knowledge of lead distribution to the meter scale, while previous studies were often limited to coarser resolutions (20 m to 1 km). There is an increase in the power law exponent (2.14–2.74) during the winter season, independent from the flight scale. The reason for the temporal increase needs to be further investigated.

Looking at the lead orientations within one flight, there is one predominant orientation but no similarity between different flights. There are no intersection angles determined so far, but the next possible steps are mentioned in Section 7.3.

These findings down to the meter scale are relevant to the Arctic observing system by understanding the spatial variability on the sub-footprint scale of TIR satellite products. Because the Arctic sea ice is too remote for regular and large-scale in-situ observations, operational satellite products are and will be commonly used. This topic is discussed with the following research question R4.

R4: Do satellite surface temperatures sufficiently represent the sub-footprint scale variability of the sensible heat exchange?

Building on the key findings of Chapter 5, helicopter-borne and satellite-based surface temperature products were compared in Chapter 6. The helicopter-borne data with 1 m horizontal resolution allows to study and quantify the spatial variability on the TIR satellite footprint of 1×1 km with 1000×1000 values.

The sensible heat exchange takes place at the interface between the atmosphere and the snow/ice or ocean surface. Therefore, the sensible heat flux directly depends on the surface temperature. A reduction of the resolution from 1 m to 1 km of the same helicopter data decreases, as expected, the spatial variability and spread of the surface temperature. In the 1 km resolution data the small-scale leads are not resolved while they are more efficient in the heat exchange. Hence, the sensible heat flux from the ocean to the atmosphere is underestimated. For the five cases of this study, the resolution-dependent difference of the sensible heat flux is linearly related to the lead area fraction of the respective flight. The underestimated heat flux can result in an underestimation of the heat input into the atmosphere. The missing heat input could contribute to a further warming. Also, leads are areas of large ice production that can influence the ice mass balance. These findings emphasize that the consideration of the spatial scales is crucial for investigating the heat exchange over sea ice.

When comparing the 1 km helicopter data with the 1 km MODIS ice surface temperatures, no alignment in the spatial patterns is found, even though a temperature and drift correction was done. The comparison of the corrected values shows differences in the surface temperature and sensible heat flux over the full domain. Thus, there is a potential for further investigation, described in Section 7.3.

7.2 Summary

This thesis presents helicopter-borne thermal infrared (TIR) imaging as a valuable method for studying Arctic sea ice during winter. The MOSAiC expedition offered the unique opportunity to observe the same sea ice over a full year. Many coherent observations provide valuable information that improve the understanding of the sea ice processes. Generally, there is a high potential for TIR imaging (Chapter 3) because it allows for a more detailed investigation of the spatial variability of sea ice with a resolution of 1 m. This method is advantageous during winter with large temperature contrasts between thick ice and leads (Chapter 5), and even the smaller temperature anomalies have potential for melt pond research (Chapter 4). The presented findings increase the understanding of melt ponds and leads, which are relevant contributions to the summer and winter heat budget of Arctic sea ice. It is essential to enlarge the process understanding, especially in a changing climate with Arctic Amplification. Leads and their increased heat exchange

(Subsection 1.1.1) and the challenges of different observations (Subsection 1.1.4) are the focus of the final Chapter 6. It addresses the emerging relevance of spatial scales for the sea ice heat budget (Subsection 1.1.2), which influences the sea ice mass balance and, thus, the future conditions of the Arctic sea ice.

All in all, Chapters 3, 4, 5, 6 are puzzle pieces (Section 1.1) which add to the big picture of winter sea ice characteristics in the central Arctic.

7.3 Outlook

From the key findings more questions and ideas arise that should be considered for future studies. There is a big potential in further analyzing the helicopter-borne surface temperatures. The validation of the helicopter-borne surface temperature values and a further investigation of the emissivity is required, aiming to develop a product that represents the exact physical surface temperatures for the whole flight. To achieve this, an improved correction of the temporal changes of the surface temperature within one flight can be helpful. The spatial variability of the surface temperatures, not necessarily focused on features like melt ponds and leads, can add important information:

(i) Provide further statistics on the sub-footprint scale variability,

(ii) Put local measurements in context by providing a reasonable range to the in-situ surface temperatures, which might be used as forcing for models.

As motivated in Subsection 1.1.5, additional cases for specific situations can be further investigated, e.g., the shadowing effect at the end of the winter season. Further action items for the analysis of the helicopter-borne data could be:

(i) Combining different flights, e.g., the set of three flights at the end of December, to monitor and quantify the changes for the same drifting sea ice area within a few days,

(ii) Processing flights that had technical issues or were conducted later in the year (not considered in the analysis for this thesis).

The analysis of these flights can add valuable information to the already existing time series, for example, by gaining a process understanding of the autumn-winter transition in September 2020. Moreover, it is possible to analyze additional data recorded during the ATWAICE (ATlantic WAter pathways to the ICE in the Nansen Basin and Fram Strait) expedition (Kanzow, 2023) in summer 2022. For the summer data, a melting surface has only small temperature contrast, which makes the surface classification more difficult.

Adding on the results for the preconditioning of melt ponds in Chapter 4, more cases, i.e., other helicopter flights during the winter season, should be analyzed. It would be

valuable to develop a systematic detection of the warm anomalies, which allows an automatic investigation of this phenomenon and improve the performance of the seasonal prediction of melt ponds.

In Chapter 5, the definition of lead intersection angles was challenging while encountering strong variability on the smallest scales. There may be opportunities for new approaches, such as connecting lead fragments with the same orientation or restricting the analysis to leads of a specific size or length.

As shortly presented in the Section 2.2, there is the possibility to derive thin ice thickness from the surface temperature maps using thermodynamic modeling. The relation can be applied to the surface temperature maps to create maps of thin ice thickness. From this, additional information on the thin ice thickness distribution can be determined, which is important for the sea ice mass balance and the heat exchange on the sub-footprint scale.

As mentioned in Subsection 6.6.1, there are several ways to continue the comparison between helicopter-borne and satellite-based surface temperatures, e.g., by incorporating a new dataset (e.g., VIIRS from Tschudi et al. (2017)) or investigating the different spatial patterns of the helicopter and MODIS data. Including more cases to analyze the resolution effect can show if the linear relation between the lead fraction and the sensible heat flux difference holds for more helicopter flights. This linear relation can be a valuable approach for implementing parameterizations. The additional sensible heat flux from the unresolved leads could then be estimated by the linear relationship based on the lead area fraction. For this, it has to be determined if the lead fraction can be scaled across different spatial scales. The power law from the lead width in Chapter 5 could support this estimation.

Following, the findings could be formulated as parameterizations for sub-footprint or sub-grid cell processes in satellite retrievals or models:

(i) The power law distribution of the lead width,

(ii) The linear relation of the lead area fraction and the resolution-dependent difference of sensible heat,

(iii) Classification of warm anomalies in winter, which define areas of potential melt pond formation during the following summer.

The subsequent analysis steps should make use of the huge set of observations from the MOSAiC expedition. The large variety of observations can provide valuable information on specific parameters and processes. For example, there is the possibility for a more detailed surface classification in combination with surface topography, especially because the TIR camera and the airborne laser scanner were flown in parallel. For example, the winter heat budget group (Section A.3) uses the interdisciplinary set of MOSAiC observations

to investigate the heat budget across the vertical column of the ocean, sea ice, and the atmosphere.

Appendix A

Contributions to further projects

In this part, I explain my further contributions, which resulted from the work on this dissertation. Most publications are related to my involvement in the MOSAiC expedition. The MOSAiC expedition was a unique opportunity to get involved and support different measurements and studies, which helped me better understand the broader context and the interdisciplinary aspects of Arctic sea ice. Thus, these contributions are relevant for my dissertation but not directly adding to the key research questions.

A.1 Measurements and datasets

During my participation in the last phase of the MOSAiC expedition, I performed various measurements. My work was mainly focused on the on-ice remote sensing measurements but also included support of helicopter-borne imaging, snow measurements, transects of snow depth and ice thickness, ice coring, and others. The on-ice remote sensing measurements included the setup, operation, and experiments with passive and active instruments, a GPS-based instrument, as well as visual and infrared cameras.

Relevance

It was a significant advantage for my dissertation that I gained experience in different observational methods, and learned about further measurements which can be linked to each other for a more complete understanding of the physical processes of Arctic sea ice. In the following, all datasets that I co-authored are listed. I contributed to all listed datasets by taking measurements in the field on behalf of the various projects during leg 5 of the MOSAiC expedition. All datasets are published on *PANGAEA*.

Dataset publications

- Spreen, G., **L. Thielke**, M. Huntemann, S. Hendricks, A. Jutila, R. Ricker (2021): Infrared camera raw data (ir_variocam_02) during helicopter flights from RV PO-

LARSTERN during MOSAiC expedition 2019/2020 [Dataset]. *PANGAEA*, https://doi.org/10.1594/PANGAEA.939361

- Spreen, G., M. Huntemann, R. Naderpour, M. Mahmud, A. Tavri, **L. Thielke** (2021): Optical IP Camera images (VIS_INFRALAN_01) at the remote sensing site on the ice floe during MOSAiC expedition 2019/2020 [Dataset]. *PANGAEA*, https://doi.org/10.1594/PANGAEA.939362
- Spreen, G., M. Huntemann, **L. Thielke**, R. Naderpour, M. Mahmud, A. Tavri (2022): Infrared camera raw data (ir_variocam_01) at the remote sensing site on the ice floe during MOSAiC expedition 2019/2020 [Dataset]. *PANGAEA*, https://doi.org/10.1594/PANGAEA.940717
- Gabarró, C., J. Martínez, J. Salvador, R. Jove, F. Hernández-Macià, G. Spreen, **L. Thielke**, L. von Albedyll (2022): Horizontal and Vertical polarization voltages (raw data) from the L-band BALAMIS ARIEL radiometer acquired during the MOSAiC expedition (Leg 4 and 5) [Dataset]. *PANGAEA*, https://doi.org/10.1594/PANGAEA.942958
- Rostosky, P., G. Spreen, T. Casal, C. Donlon, L. Kaleschke, J. Lemmetiynen, M. Mahmud, R. Naderpour, A. Tavri, **L. Thielke** (2023): Brightness temperature measured by HUTRAD radiometer at 6.8 and 10.65 GHz from March to September 2020 during the MOSAiC expedition [Dataset]. *PANGAEA*, https://doi.org/10.1594/PANGAEA.954608
- Rostosky, P., J. C. Stroeve, M. Huntemann, L. Kaleschke, R. Nanderpour, G. Spreen, **L. Thielke** (2023): Brightness temperature measured by UoM SBR radiometer at 19, 37 and 89 GHz from September 2019 to September 2020 during the MOSAiC expedition [Dataset]. *PANGAEA*, https://doi.pangaea.de/10.1594/PANGAEA.956108

A.2 Manuscripts

Here, I present a list of manuscripts that I was co-authoring, all related to my involvement in the work connected to the MOSAiC expedition. The following list shows the articles which are already published and those which are under preparation or not peer-reviewed. For each article, a short summary and my share is described.

Relevance

Through the work on these manuscripts, I got to know various research questions from different projects, learn about their methods and new results, and build valuable collaborations. For each manuscript a short summary and my share is described.

Peer-reviewed articles

- Nicolaus, M., D. K. Perovich, G. Spreen, M. A. Granskog, L. von Albedyll, M. Angelopoulos, P. Anhaus, S. Arndt, H. J. Belter, V. Bessonov, G. Birnbaum, J. Brauchle, R. Calmer, E. Cardellach, B. Cheng, D. Clemens-Sewall, R. Dadic, E. Damm, G. de Boer, O. Demir, K. Dethloff, D. V. Divine, A. A. Fong, S. Fons, M. M. Frey, N. Fuchs, C. Gabarró, S. Gerland, H. F. Goessling, R. Gradinger, J. Haapala, C. Haas, J. Hamilton, H.-R. Hannula, S. Hendricks, A. Herber, C. Heuzé, M. Hoppmann, K. V. Høyland, M. Huntemann, J. K. Hutchings, B. Hwang, P. Itkin, H.-W. Jacobi, M. Jaggi, A. Jutila, L. Kaleschke, C. Katlein, N. Kolabutin, D. Krampe, S. S. Kristensen, T. Krumpen, N. Kurtz, A. Lampert, B. A. Lange, R. Lei, B. Light, F. Linhardt, G. E. Liston, B. Loose, A. R. Macfarlane, M. Mahmud, I. O. Matero, S. Maus, A. Morgenstern, R. Naderpour, V. Nandan, A. Niubom, M. Oggier, N. Oppelt, F. Pätzold, C. Perron, T. Petrovsky, R. Pirazzini, C. Polashenski, B. Rabe, I. A. Raphael, J. Regnery, M. Rex, R. Ricker, K. Riemann-Campe, A. Rinke, J. Rohde, E. Salganik, R. K. Scharien, M. Schiller, M. Schneebeli, M. Semmling, E. Shimanchuk, M. D. Shupe, M. M. Smith, V. Smolyanitsky, V. Sokolov, T. Stanton, J. Stroeve, **L. Thielke**, A. Timofeeva, R. T. Tonboe, A. Tavri, M. Tsamados, D. N. Wagner, D. Watkins, M. Webster, M. Wendisch (2022). Overview of the MOSAiC expedition: Snow and sea ice. *Elementa: Science of the Anthropocene*, 10(1), 000046. https://doi.org/10.1525/elementa.2021.000046

This manuscript provides a comprehensive overview of the MOSAiC expedition measurement program regarding the physical properties and processes of snow and sea ice. There is a detailed description of the design and availability of the measurements, example results, and the implication of the first findings for the Arctic coupled system. I added the surface temperature data from the helicopter-borne thermal infrared (TIR) imaging, contributed to the description of the helicopter-borne measurements and the design of two figures, and revised the manuscript.

- Gabarró, C., P. Fabregat, F. Hernández-Macià, R. Jove, J. Salvador, G. Spreen, **L. Thielke**, R. Dadic, M. Huntemann, N. Kolabutin, D. Nomura, H.-R. Hannula, M. Schneebeli (2022). First results of the ARIEL L-band radiometer on the MOSAiC Arctic Expedition during the late summer and autumn period. *Elementa: Science of the Anthropocene*, 10(1). https://doi.org/10.1525/elementa.2022.00031

This study presents results from on-ice L-band radiometry during the MOSAiC expedition to investigate its sensitivity to thin ice thickness (<1 m) to improve microwave emission models. The measurements were sensitive to different types, like pack ice, leads, and melt ponds. The results of the microwave emission model (Burke model) could be reproduced, while the measurements show a sensitivity up to an ice thickness of 0.7 m when there is

low salinity in the ice. I contributed by performing the measurements during leg 5 and revising the manuscript.

- Stroeve, J., V. Nandan, R. Willatt, R. Dadic, P. Rostosky, M. Gallagher, R. Mallett, A. Barrett, S. Hendricks, R. Tonboe, M. McCrystall, M. Serreze, **L. Thielke**, G. Spreen, T. Newman, J. Yackel, R. Ricker, M. Tsamados, A. Macfarlane, H.-R. Hannula, M. Schneebeli (2022). Rain on snow (ROS) understudied in sea ice remote sensing: a multi-sensor analysis of ROS during MOSAiC (Multidisciplinary drifting Observatory for the Study of Arctic Climate). *The Cryosphere*, 16, 42234250. https://doi.org/10.5194/tc-16-4223-2022

This study investigates the effect of a rain on snow event on active and passive microwave remote sensing instruments deployed on the ice during the MOSAiC expedition. By increasing the liquid water content in the snow and the later refreezing, the rain on snow event impacts the satellite retrievals. The in-situ observations provide information for the detection of a rain on snow event. I contributed by performing the measurements and I revised the manuscript.

Dissertation chapter

- von Albedyll, L., S. Hendricks, R. Grodofzig, N. Hutter, D. Murashkin, L. Kaleschke, S .Willmes, **L. Thielke**, X. Tian-Kunze, G. Spreen, C. Haas (2022). Lead fractions from SAR-derived sea ice divergence during MOSAiC. Chapter 6 in *Sea ice deformation and sea ice thickness change*. https://doi.org/10.26092/elib/1868

This study compares a new lead fraction product based on divergence to existing lead fraction products. The new product is able to reproduce the temporal variability and identify the location of the leads. The comparison of the different products reveals a difference of 1–2 magnitudes in lead fraction caused by the different methods of retrieving different physical properties of the leads. I provided the lead fraction dataset from helicopter-borne TIR observation for comparison with other datasets. I contributed to the discussion and the revision the manuscript.

Under review

- Smith, M. M., H. Angot, E. J. Chamberlain, E. Droste, S. Karam , M. Muilwijk, A. L. Webb, S. Archer, I. Beck, B. W. Blomquist, J. Bowman, M. Boyer, D. Bozzato, M. Chierici, J. Creamean, A. D'Angelo, B. Delille, I. Fer, A. A. Fong, A. Fransson, N. Fuchs, J. Gardner, M. A. Granskog, C. J. M. Hoppe, M. Hoppema, M. Hoppmann, S. Muller, O. Müller, M. Nicolaus, D. Nomura, T. Petäjä, E. Salganik, J. Schmale, K. Schmidt, K. Schulz, M. D. Shupe, J. Stefels, **L. Thielke**, S. Tippenhauer, A. Ulfsbo,

M. van Leeuwe, M. Webster, M. Yoshimura, L. Zhan (2023). Critically important, yet forgotten: thin and transient meltwater layers and false bottoms. *Elementa: Science of the Anthropocene*, in review.

This manuscript emphasize the importance of a thin meltwater layer below the sea ice in the upper ocean during summer. Additionally, it presents novel findings from the MOSAiC expedition describing the physical, ecological, and chemical effects of the melting snow and sea ice. Examples are the formation of false bottoms, the reduction of gas exchange between the ocean and atmosphere, and implications on the ecosystem. I contributed content for the discussion and revised the manuscript. Additionally, I was involved in the organizational committee of the working group prior to the publication (e.g., coordinating potential contributions from the remote sensing community).

A.3 Winter heat budget group

The winter heat budget group is a project which I initiated and organize together with Martin Schneebeli from SLF Davos to aim to calculate a full sea ice heat budget for winter. About 60 scientists are part of this group; covering the ocean, sea ice and snow physics, and atmospheric science, including in-situ observation, airborne and satellite-borne observations, as well as experts from the modeling community. The motivation and theoretical background of the sea ice heat budget are given in Subsection 1.1.2 and Section 2.2.

The group writes an article on the winter heat budget for an exemplary week during the MOSAiC winter. As soon as the methods are in place, this calculation will be extended to a full winter time series that is more complex because it involves more temporal variability. To achieve these goals, the tasks of this group are:

- Combine datasets from different measurements and approaches
- Investigate the background conditions of the study area and period of investigation
- Quantify the uncertainties
- Determine values of the heat fluxes
- Calculate the balance at the ice/snow-atmosphere interface and ocean-ice interface
- Define the residual of the heat budget
- Discuss the influence of temporal variability
- Understand how representative a single heat budget is by investigating the spatial variability of the heat budget components

- Define winter heat fluxes that can be implemented in different types of models
- Compare results to previous measurement campaigns (e.g., SHEBA)

Relevance

Working with the winter heat budget group is an essential contribution to this dissertation because the discussion with experts in this field with different scientific backgrounds enables an increased understanding of all relevant physical processes for the group and myself. The group's aims allow for a more comprehensive view of the Arctic sea ice heat budget. It emphasizes the importance of the surface temperature, the main parameter of this work. Additionally, it provides a framework to use the helicopter-borne surface temperature maps to investigate the spatial variability of heat flux terms (e.g., sensible heat flux).

A.4 Responsible Science Initiative

Responsible Science Initiative (RISE) was founded by participants of the MOSAiC expedition in summer 2020 to find ways to reduce the environmental impact of polar research while maximizing the scientific output. I joined this group after the expedition and became a member of the initiative's committee. Recently, RISE was established as an APECS (Association of Polar Early Career Scientists) working group to create a larger network and provide a framework for new opportunities. The content presented here is based on the work of the RISE group, with substantial contributions from R. Calmer, A. R. Macfarlane, V. Mohaupt, D. Ruché, M. M. Smith, and myself.

As explained in Subsection 1.1.4, in-situ observations are crucial for studying the Arctic climate system. Thus, expeditions using a research vessel in the sea ice is an accepted approach without many alternatives. Scientists studying the changing climate should take all possible steps to protect the remote and fragile Arctic environment from human influence. Scientists might be concerned that the discussion of the environmental impact influences the perception of their research about the environment. With this group, we address this topic and motivate the scientific community to transition to a more environmentally sustainable science. The focus of this working group is on ship-based expeditions in the Arctic, based on the group members' experience. We collaborate with existing groups working on the same topic with a different focus, like Labos1.5 (https://labos1point5.org/). We build upon the exiting guidebooks in place, for example, from INTERACT to reduce the environmental impacts of Arctic fieldwork focused for work on land (Frendrup et al., 2021; Holste et al., 2022).

To figure out what is required, we had regular discussions on how to reduce the environmental impact of our scientific actions. We use the MOSAiC expedition as a case study to develop methods and recommendations for the impact assessment of future fieldwork. We developed a questionnaire that was sent to the MOSAiC community to assess different aspects of the environmental impact of the expedition. We are currently writing an impact report, including a summary of the expedition's environmental impact, a discussion of difficulties in assessing the impact, and providing guidelines to document and quantify the impact of future expeditions.

This working group aims to promote projects about the environmental impact of science, document and quantify the environmental impact of expeditions, collect ideas for research and development for more sustainable materials or methods, influences Arctic policies, and do outreach to the scientific community. For example, I led a "Sustainable science" workshop during the ICYMARE conference 2022 in Bremerhaven.

As a first result of our discussion and collaboration with Labos1.5, we wrote an article as a call for funding bodies to support the reduction of the environmental impact of fieldwork. I contributed to this work by revising the manuscript.

- Macfarlane, A. R., T. Ben-Ari, G. Blanc, D. Bozzato, R. Calmer, S. Haslett, S. Holste, E. Jardé, C. Rixen, D. Ruché, M. Schneebeli, M. M. Smith, **L. Thielke**, S. Vandevelde, H. C. Wheeler (2023). A call for funding bodies to influence the reduction of environmental impacts in remote scientific field work. *Submitted to Science.*

A.5 Sustainability statement

This statement is motivated by the work in the RISE, founded by members of the MOSAiC expedition.

With this statement, I would like to raise awareness of the environmental impact of scientific research based on fieldwork data. This thesis studies sea ice processes in a sensitive environment. Thus, it is necessary to take steps to reduce the environmental impact of our measurements and strive to get the most possible scientific output from the existing data. Beside this thesis, there is a lot of potential for scientific output from the helicopter-borne TIR imaging data, described in the outlook in Chapter 7, and these further projects should be explored before new data are recorded.

The data used in this thesis are collected during fieldwork over sea ice in the central Arctic. The expedition was performed by RV *Polarstern*. The main datasets of this project are based on helicopter-borne measurements. I declare for this thesis that there was a

human-made environmental impact by performing these measurements and collecting the used datasets. The impact of the key measurements of this thesis (helicopter-borne TIR imaging) consists of the following aspects:

- Partial share of the overall environmental impact of the expedition (ship emissions, light pollution, and others)
- Helicopter CO_2 emission (approximately 66 hours of helicopter flight time)
- Helicopter noise pollution

A.6 Outreach and science communication

It is crucial for scientists to communicate their experiences and findings in order to engage with a larger and broader community and ensure that the results are shared in an understandable way. During the work on my dissertation, I had the possibility to do several outreach activities in different ways. In the following, I highlight my scientific outreach for interested readers and describe my motivation to do different outreach activities, hopefully motivating other early career scientists to do science communication as well. An essential point for science communication is to engage with the audience, which can be scientists in other fields, fellow early career scientists, or people with a non-scientific background. For more information about science communication, I recommend, for example, the Nationales Institut fur Wissenschaftskommunikation (https://www.nawik.de/).

Articles

Blog articles:

- ArcTrain blog (2020): "Two ArcTrainees one big scientific question: A story about leads from the MOSAiC drift expedition". Written together with Luisa von Albedyll. [https://arctrain.de/two-arctrainees-one-big-scientific-question-a-story-about-leads-from-the-mosaic-drift-expedition/]
- ArcTrain blog (2021): "Experiences with online conferences from an Early Career Scientist perspective". Written together with Damien Ringeisen. [https://arctrain.de/experiences-with-online-conferences-from-an-early-career-scientist-perspective/]
- ArcTrain blog (2022): "Our research stay at the McGill University in Montreal". Written together with Yuqing Liu [https://arctrain.de/our-research-stay-at-the-mcgill-university-in-montreal/]
- EGU Cyroblog (2023): "Did you know about the dark secrets of sea ice?". [https://blogs.egu.eu/divisions/cr/2023/03/17/did-you-know-about-the-dark-secrets-of-arctic-sea-ice/]

With the blog articles, I could share experiences and results that I had during my dissertation work, including the MOSAiC expedition, online conferences during the pandemic restrictions, working at a partner institute, and presenting my scientific findings to a broader audience. My aim with the blog articles is to share easily accessible information from the perspective of an early career scientist for the interested audience with various backgrounds.

Web articles:

- Web article in up2date, University of Bremen Online Magazine (2020): "The Loneliest Place Has Become the Most Social Place" [https://up2date.uni-bremen.de/en/research/the-loneliest-place-has-become-the-most-social-place]
- Web article in up2date, University of Bremen Online Magazine (2021): "MOSAiC: Weeks in the Ice, Now the Analysis". In coorporation with Marcus Huntemann and Gunnar Spreen. [https://up2date.uni-bremen.de/en/research/nach-wochen-im-eis-folgt-nun-die-auswertung-kopie]

These web articles allowed me to share the actions after and before my participation in the MOSAiC expedition. This was an interesting approach because there was a lot of communication about the expedition. But to engage with the people, it is relevant to show them the different aspects of the preparation, e.g., Covid-related quarantine before going on the ship and having a lot of equipment ready. Further, it is essential to keep up communication after such a big expedition to keep the people updated and engaged. Hence, they know that the scientific work after the scientists return to the institute is also crucial.

Newspaper article:

- Local newspaper article about MOSAiC experience, Dewezet (2020): "Unterwegs auf der Polarstern, Eine Hamelnerin auf Expedition in der Arktis" [https://www.dewezet.de/region/hameln_artikel,-eine-hamelnerin-auf-expedition-in-der-arktis-_arid,2654840.html]

The article was published in a local newspaper in my hometown, where my relatives still live. This article engaged many people who know my relatives or me. If people are usually not involved in research and scientific expeditions, a personal relationship can be important to get the attention of the readers. I received a lot of feedback on this article and noticed a greater sensitivity to this topic. Thus, I have the impression that this kind of communication makes more people aware of the relevance of Arctic research and the changing climate in a broader sense.

School outreach

I participated in two different formats of school outreach to engage with pupils online while there was no possibility for an in-person event due to the Covid-pandemic. As a team of ArcTrain doctoral candidates, we offered online courses for school kids at the Digitale Drehtür about the Arctic. The courses included a presentation about the basic background information and group work afterward. Additionally, I presented my work as a scientist in the online format of the Kinderuni at the University of Bremen. This format enabled accessible communication for the pupils. It allowed me to break down my scientific work and my interest into the simplest terms which is important for communicating with different audiences. The pupils' many curious questions were inspiring and demonstrated their interest in the work of a scientist, the Arctic, and climate change.

Public talk

In 2022, I was invited to give a talk about the MOSAiC expedition. The talk was a part of the organized talk series "#LecturesForFuture Klimawandel in den (Weit)Blick nehmen" at University of Trier about topics related to climate change. My talk was entitled "Die MOSAiC Expedition: Ein Jahr im Arktischen Eis" [https://de.scientists4future.org/veranstaltungen/die-mosaic-expedition-ein-jahr-im-arktischen-eis/]. The audience had different backgrounds but with an already general interest in the relevance of the changing climate. The talk allowed me to present detailed insights into the work during the expedition and the scientific aims resulting from the collected data. The questions following the talk focused on long-term and large-scale effects of climate change rather than specific research approaches. Thus, the big picture and the implication of the Arctic research have a large relevance for a broad audience.

Presentation award

For my online presentation at the EGU General Assembly 2021 (international scientific conference), I received the "2021 Virtual Outstanding Student and PhD candidate Presentation (vOSPP) Award for the PICO entitled "Thermal sea ice classification during the MOSAiC expedition" (Thielke, L., M. Huntemann, G. Spreen, S. Hendricks, A. Juttila, R. Ricker) [https://www.egu.eu/awards-medals/ospp-award/2021/]. This PICO presentation was limited to one slide and only a few minutes, and, therefore, sensitive to the presented content. The success of this format showed me the possibility of reducing content and still engaging the scientific audience. It is crucial to present the key result of the study as a basis for the scientific understanding while leaving some potential questions open for a following discussion.

Bibliography

Adams, S., Willmes, S., Schröder, D., Heinemann, G., Bauer, M., and Krumpen, T. (2012). Improvement and sensitivity analysis of thermal thin-ice thickness retrievals. *IEEE Transactions on Geoscience and Remote Sensing*, 51(6):3306–3318. https://doi.org/10.1109/TGRS.2012.2219539.

Alam, A. and Curry, J. (1995). Lead-induced atmospheric circulations. *Journal of Geophysical Research*, 100:4643–4651. https://doi.org/10.1029/94JC02562.

Alfred-Wegener-Institut Helmholtz-Zentrum für Polar- und Meeresforschung (2017). Polar Research and Supply Vessel POLARSTERN operated by the Alfred-Wegener-Institute. *Journal of large-scale research facilities*, 3. https://dx.doi.org/10.17815/jlsrf-3-163.

Alhussein, M. and Haider, S. I. (2016). Simulation and analysis of uncooled microbolometer for serial readout architecture. *Journal of Sensors*, 2016. https://doi.org/10.1155/2016/9751056.

Andersen, O. B. and Knudsen, P. (2009). The DNSC08 mean sea surface and mean dynamic topography. *J. Geophys. Res.*, 114(C11). https://doi.org/10.1029/2008JC005179.

Anhaus, P., Katlein, C., Nicolaus, M., Hoppmann, M., and Haas, C. (2021). From bright windows to dark spots: Snow cover controls melt pond optical properties during refreezing. *Geophysical Research Letters*, 48(23):e2021GL095369. https://doi.org/10.1029/2021GL095369.

Arrigo, K. R. and van Dijken, G. L. (2015). Continued increases in Arctic Ocean primary production. *Progress in Oceanography*, 136:60–70. https://doi.org/10.1016/j.pocean.2015.05.002.

Assmy, P., Fernández-Méndez, M., Duarte, P., Meyer, A., Randelhoff, A., Mundy, C. J., Olsen, L. M., Kauko, H. M., Bailey, A., Chierici, M., Cohen, L., Doulgeris, A. P., Ehn, J. K., Fransson, A., Gerland, S., Hop, H., Hudson, S. R., Hughes, N., Itkin, P., Johnsen, G., King, J. A., Koch, B. P., Koenig, Z., Kwasniewski, S., Laney, S. R., Nicolaus, M., Pavlov, A. K., Polashenski, C. M., Provost, C., Rösel, A., Sandbu, M.,

Spreen, G., Smedsrud, L. H., Sundfjord, A., Taskjelle, T., Tatarek, A., Wiktor, J., Wagner, P. M., Wold, A., Steen, H., and Granskog, M. A. (2017). Leads in Arctic pack ice enable early phytoplankton blooms below snow-covered sea ice. *Scientific Reports*, 7:1–9. https://doi.org/10.1038/srep40850.

Barber, D. B., Redding, J. D., McLain, T. W., Beard, R. W., and Taylor, C. N. (2006). Vision-based target geo-location using a fixed-wing miniature air vehicle. *Journal of Intelligent and Robotic Systems*, 47(4):361–382. https://doi.org/10.1007/s10846-006-9088-7.

Bintanja, R. and Van Der Linden, E. C. (2013). The changing seasonal climate in the Arctic. *Scientific Reports*, 3:1–8. https://doi.org/10.1038/srep01556.

Bitz, C. M. and Lipscomb, W. H. (1999). An energy-conserving thermodynamic model of sea ice. *Journal of Geophysical Research: Oceans*, 104(C7):15669–15677. https://doi.org/10.1029/1999JC900100.

Bjornert, R. (1975). Field operations for the AIDJEX main experiment. *AIDJEX Bulletin*, (29):173–180.

Blackport, R., Screen, J. A., van der Wiel, K., and Bintanja, R. (2019). Minimal influence of reduced Arctic sea ice on coincident cold winters in mid-latitudes. *Nature Climate Change*, 9:697–704. https://doi.org/10.1038/s41558-019-0551-4.

Bröhan, D. and Kaleschke, L. (2014). A nine-year climatology of arctic sea ice lead orientation and frequency from AMSR-E. *Remote Sensing*, 6(2):1451–1475. https://doi.org/10.3390/rs6021451.

Burger, W. and Burge, M. J. (2009). *Undergraduate Topics in Computer Science. Principles of Digital Image Processing. Core Algorithms.* Springer-Verlag London. https://doi.org/10.1007/978-1-84800-195-4.

Cao, Y., Bian, L., and Zhao, J. (2019). Impacts of Changes in Sea Ice and Heat Flux on Arctic Warming. *Atmospheric and Climate Sciences*, 09:84–99. https://doi.org/10.4236/acs.2019.91006.

Cohen, J., Zhang, X., Francis, J., Jung, T., Kwok, R., Overland, J., Ballinger, T. J., Bhatt, U. S., Chen, H. W., Coumou, D., Feldstein, S., Gu, H., Handorf, D., Henderson, G., Ionita, M., Kretschmer, M., Laliberte, F., Lee, S., Linderholm, H. W., Maslowski, W., Peings, Y., Pfeiffer, K., Rigor, I., Semmler, T., Stroeve, J., Taylor, P. C., Vavrus, S., Vihma, T., Wang, S., Wendisch, M., Wu, Y., and Yoon, J. (2020). Divergent consensuses on Arctic amplification influence on midlatitude severe winter weather. *Nature Climate Change*, 10:20–29. https://doi.org/10.1038/s41558-019-0662-y.

Cox, C., Gallagher, M., Shupe, M., Persson, O., Solomon, A., Blomquist, B., Brooks, I., Costa, D., Gottas, D., Hutchings, J., Osborn, J., Morris, S., Preußer, A., and Uttal, T. (2021). 10-meter (m) meteorological flux tower measurements (Level 1 Raw), Multidisciplinary Drifting Observatory for the Study of Arctic Climate (MOSAiC), central Arctic, October 2019 - September 2020 [Dataset]. *Arctic Data Center*, https://doi.org/10.18739/A2VM42Z5F.

Cox, C. J. (2023). Atmospheric correction for surface brightness temperatures. *Personal communication*.

Curry, J. A. and Ebert, E. E. (1990). Sensitivity of the thickness of Arctic sea ice to the optical properties of clouds. *Annals of Glaciology*, 14:43–46. https://doi.org/10.3189/S0260305500008235.

Curry, J. A., Schramm, J. L., and Ebert, E. E. (1995). Sea Ice-Albedo Climate Feedback Mechanism. *Journal of Climate*, 8(2):240 – 247. https://doi.org/10.1175/1520-0442(1995)008<0240:SIACFM>2.0.CO;2.

Dai, A., Luo, D., Song, M., and Liu, J. (2019). Arctic amplification is caused by sea-ice loss under increasing CO_2. *Nature communications*, 10(1):1–13. https://doi.org/10.1038/s41467-018-07954-9.

Deser, C., Tomas, R., Alexander, M., and Lawrence, D. (2010). The seasonal atmospheric response to projected Arctic sea ice loss in the late twenty-first century. *Journal of Climate*, 23(2):333–351. https://doi.org/10.1175/2009JCLI3053.1.

Dethloff, K., Maslowski, W., Hendricks, S., Lee, Y. J., Goessling, H. F., Krumpen, T., Haas, C., Handorf, D., Ricker, R., Bessonov, V., Cassano, J. J., Kinney, J. C., Osinski, R., Rex, M., Rinke, A., Sokolova, J., and Sommerfeld, A. (2022). Arctic sea ice anomalies during the MOSAiC winter 2019/20. *The Cryosphere*, 16(3):981–1005. https://doi.org/10.5194/tc-16-981-2022.

Deutscher Wetterdienst (German Weather Service) (2021). Flight weather reports MOSAiC Leg 1, 2, and 3. *Personal communication*.

Divine, D. V., Pedersen, C. A., Karlsen, T. I., Aas, H. F., Granskog, M. A., Hudson, S. R., and Gerland, S. (2016). Photogrammetric retrieval and analysis of small scale sea ice topography during summer melt. *Cold Regions Science and Technology*, 129:77–84. https://doi.org/10.1016/j.coldregions.2016.06.006.

Eicken, H., Grenfell, T., Perovich, D., Richter-Menge, J., and Frey, K. (2004). Hydraulic controls of summer Arctic pack ice albedo. *Journal of Geophysical Research: Oceans*, 109(C8). https://doi.org/10.1029/2003JC001989.

Eicken, H., Krouse, H., Kadko, D., and Perovich, D. (2002). Tracer studies of pathways and rates of meltwater transport through Arctic summer sea ice. *Journal of Geophysical Research: Oceans*, 107(C10):SHE–22. https://doi.org/10.1029/2000JC000583.

Eicken, H., Tucker, W., and Perovich, D. (2001). Indirect measurements of the mass balance of summer Arctic sea ice with an electromagnetic induction technique. *Annals of Glaciology*, 33:194–200. https://doi.org/10.3189/172756401781818356.

Feldt, R. (2021). BlackBoxOptim.jl. https://github.com/robertfeldt/BlackBoxOptim.jl.

Fischler, M. A. and Bolles, R. C. (1981). Random Sample Consensus: A Paradigm for Model Fitting with Applications to Image Analysis and Automated Cartography. *Commun. ACM*, 24(6):381395. https://doi.org/10.1145/358669.358692.

Flocco, D., Feltham, D. L., Bailey, E., and Schroeder, D. (2015). The refreezing of melt ponds on Arctic sea ice. *Journal of Geophysical Research: Oceans*, 120(2):647–659. https://doi.org/10.1002/2014JC010140.

Flocco, D., Schroeder, D., Feltham, D. L., and Hunke, E. C. (2012). Impact of melt ponds on Arctic sea ice simulations from 1990 to 2007. *Journal of Geophysical Research: Oceans*, 117(C9). https://doi.org/10.1029/2012JC008195.

Fox-Kemper, B., Hewitt, H., Xiao, C., Aðalgeirsdóttir, G., Drijfhout, S., Edwards, T., Golledge, N., Hemer, M., Kopp, R., Krinner, G., Mix, A., Notz, D., Nowicki, S., Nurhati, I., Ruiz, L., Sallée, J.-B., Slangen, A., , and Yu, Y. (2021). Ocean, Cryosphere and Sea Level Change. In Climate Change 2021: The Physical Science Basis. Contribution of Working Group I to the Sixth Assessment Report of the Intergovernmental Panel on Climate Change [Masson-Delmotte, V., P. Zhai, A. Pirani, S.L. Connors, C. Péan, S. Berger, N. Caud, Y. Chen, L. Goldfarb, M.I. Gomis, M. Huang, K. Leitzell, E. Lonnoy, J.B.R. Matthews, T.K. Maycock, T. Waterfield, O. Yelekçi, R. Yu, and B. Zhou (eds.)]. https://doi.org/10.1017/9781009157896.011.

Francis, J. A. and Vavrus, S. J. (2012). Evidence linking Arctic amplification to extreme weather in mid-latitudes. *Geophysical Research Letters*, 39. https://doi.org/10.1029/2012GL051000.

Frendrup, L. L., Rasch, M., Topp-Jørgensen, E., and Arndal, M. F. (2021). INTERACT Reducing the Environmental Impacts of Arctic Fieldwork. https://doi.org/10.5281/zenodo.5139698.

Fuchs, N. (2023). PASTA-ice Github Repository https://github.com/nielsfuchs/pasta_ice (v2023.01) [Software]. *Zenodo*, https://doi.org/10.5281/zenodo.7548469.

Fuchs, N. and Birnbaum, G. (2022). Orthomosaics and surface type classifications of MOSAiC Leg 4 floe (2020-06-30, 2020-07-22) [Dataset]. *PANGAEA*, https://doi.org/10.1594/PANGAEA.949167.

Goosse, H., Kay, J. E., Armour, K. C., Bodas-Salcedo, A., Chepfer, H., Docquier, D., Jonko, A., Kushner, P. J., Lecomte, O., Massonnet, F., Park, H. S., Pithan, F., Svensson, G., and Vancoppenolle, M. (2018). Quantifying climate feedbacks in polar regions. *Nature Communications*, 9(1). https://doi.org/10.1038/s41467-018-04173-0.

GSFC (2001). MODIS Snow and Ice product ATBD. https://modis.gsfc.nasa.gov/data/atbd/atbd_mod10.pdf (last access: 03 April 2023).

Guo, W., Itkin, P., Singha, S., Paul Doulgeris, A., Johansson, M., and Spreen, G. (2022). Sea ice classification of TerraSAR-X ScanSAR images for the MOSAiC expedition incorporating per-class incidence angle dependency of image texture. *The Cryosphere Discussions*, 2022:1–29. https://doi.org/10.5194/tc-2022-86.

Haas, C. (2020). Links to master tracks in different resolutions of POLARSTERN cruise PS122/2, Arctic Ocean - Arctic Ocean, 2019-12-13 - 2020-02-24 (Version 2). *PANGAEA*, https://doi.org/10.1594/PANGAEA.924674.

Haine, T. W., Curry, B., Gerdes, R., Hansen, E., Karcher, M., Lee, C., Rudels, B., Spreen, G., de Steur, L., Stewart, K. D., and Woodgate, R. (2015). Arctic freshwater export: Status, mechanisms, and prospects. *Global and Planetary Change*, 125:13–35. https://doi.org/10.1016/j.gloplacha.2014.11.013.

Hall, D. K., Key, J. R., Casey, K. A., Riggs, G. A., and Cavalieri, D. J. (2004). Sea ice surface temperature product from MODIS. *IEEE Transactions on Geoscience and Remote Sensing*, 42:1076–1087. https://doi.org/10.1109/TGRS.2004.825587.

Hall, D. K. and Riggs, G. A. (2015). MODIS/Aqua Sea Ice Extent 5-Min L2 Swath 1km. Version 6 [Dataset]. Boulder, Colorado USA: NASA National Snow and Ice Data Center Distributed Active Archive Center. https://dx.doi.org/10.5067/MODIS/MYD29.006.

Hansen, J., Nazarenko, L., Ruedy, R., Sato, M., Willis, J., Genio, A. D., Koch, D., Lacis, A., Lo, K., Menon, S., Novakov, T., Perlwitz, J., Russell, G., Schmidt, G. A., and Tausnev, N. (2005). Earth's energy imbalance: Confirmation and implications. *Science*, 308(5727):1431–1435. https://doi.org/10.1126/science.1110252.

Hendricks, S., Itkin, P., Ricker, R., Webster, M., von Albedyll, L., Rohde, J., et al. (2022). GEM-2 quicklook total thickness measurements from the 2019-2020 MOSAiC expedition [Dataset]. *PANGAEA*, https://doi.org/10.1594/PANGAEA.943666.

Herrmannsdörfer, L., Müller, M., Shupe, M. D., and Rostosky, P. (2023). Surface temperature comparison of the Arctic winter MOSAiC observations, ERA5 reanalysis, and MODIS satellite retrieval. *Elementa: Science of the Anthropocene*, 11. https://doi.org/10.1525/elementa.2022.00085.

Hersbach, H., Bell, B., Berrisford, P., Biavati, G., Horányi, A., Sabater, J. M., Nicolas, J., Peubey, C., Radu, R., Rozum, I., Schepers, D., Simmons, A., Soci, C., Dee, D., and Thépaut, J.-N. (2023). ERA5 hourly data on single levels from 1940 to present [Dataset]. Copernicus Climate Change Service (C3S) Climate Data Store (CDS), https://doi.org/10.24381/cds.adbb2d47 (Accessed on 05-Apr-2023).

Holland, M. M., Bailey, D. A., Briegleb, B. P., Light, B., and Hunke, E. (2012). Improved sea ice shortwave radiation physics in CCSM4: The impact of melt ponds and aerosols on Arctic sea ice. *Journal of Climate*, 25(5):1413–1430. https://doi.org/10.1175/JCLI-D-11-00078.1.

Holland, M. M., Bitz, C. M., and Tremblay, B. (2006). Future abrupt reductions in the summer Arctic sea ice. *Geophysical Research Letters*, 33. https://doi.org/10.1029/2006GL028024.

Holste, S., Rasch, M., and Topp-Jørgensen, E. (2022). INTERACT Reducing CO2 Emissions in Arctic Science. https://doi.org/10.5281/zenodo.6683739.

Hori, M., Aoki, T., Tanikawa, T., Hachikubo, A., Sugiura, K., Kuchiki, K., and Niwano, M. (2013). Modeling angular-dependent spectral emissivity of snow and ice in the thermal infrared atmospheric window. *Applied Optics*, 52(30):7243–7255. https://doi.org/10.1364/AO.52.007243.

Hori, M., Aoki, T., Tanikawa, T., Motoyoshi, H., Hachikubo, A., Sugiura, K., Yasunari, T. J., Eide, H., Storvold, R., Nakajima, Y., and Takahashi, F. (2006). In-situ measured spectral directional emissivity of snow and ice in the 8-14 m atmospheric window. *Remote Sensing of Environment*, 100:486–502. https://doi.org/10.1016/j.rse.2005.11.001.

Høyer, J. L., Lang, A. M., Tonboe, R., Eastwood, S., Wimmer, W., and Dybkjær, G. (2017). Report from Field Inter-Comparison Experiment (FICE) for ice surface temperature. *Danish Meteorological Institute*.

Huang, W., Lu, P., Lei, R., Xie, H., and Li, Z. (2016). Melt pond distribution and geometry in high Arctic sea ice derived from aerial investigations. *Annals of Glaciology*, 57(73):105–118. https://doi.org/10.1017/aog.2016.30.

Huntemann, M., Heygster, G., Kaleschke, L., Krumpen, T., Mäkynen, M., and Drusch, M. (2014). Empirical sea ice thickness retrieval during the freeze-up period from SMOS

high incident angle observations. *Cryosphere*, 8:439–451. https://doi.org/10.5194/tc-8-439-2014.

Hutter, N., Bouchat, A., Dupont, F., Dukhovskoy, D., Koldunov, N., Lee, Y. J., Lemieux, J. F., Lique, C., Losch, M., Maslowski, W., Myers, P. G., Ólason, E., Rampal, P., Rasmussen, T., Talandier, C., Tremblay, B., and Wang, Q. (2022). Sea Ice Rheology Experiment (SIREx): 2. Evaluating Linear Kinematic Features in High-Resolution Sea Ice Simulations. *Journal of Geophysical Research: Oceans*, 127(4). https://doi.org/10.1029/2021JC017666.

Hutter, N., Hendricks, S., Jutila, A., Birnbaum, G., von Albedyll, L., Ricker, R., and Haas, C. (2022). Merged grids of sea-ice or snow freeboard from helicopter-borne laser scanner during the MOSAiC expedition flight 20200121_01, version 1 [Dataset]. *PANGAEA*, https://doi.pangaea.de/10.1594/PANGAEA.951010 (dataset in review).

Hutter, N., Losch, M., and Menemenlis, D. (2018). Scaling Properties of Arctic Sea Ice Deformation in a High-Resolution Viscous-Plastic Sea Ice Model and in Satellite Observations. *Journal of Geophysical Research: Oceans*, 123(1):672–687. https://doi.org/10.1002/2017JC013119.

Huwald, H., Tremblay, L. B., and Blatter, H. (2005). Reconciling different observational data sets from Surface Heat Budget of the Arctic Ocean (SHEBA) for model validation purposes. *Journal of Geophysical Research C: Oceans*, 110:1–17. https://doi.org/10.1029/2003JC002221.

Iacono, M. J., Mlawer, E. J., Clough, S. A., and Morcrette, J. J. (2000). Impact of an improved longwave radiation model, RRTM, on the energy budget and thermodynamic properties of the NCAR community climate model, CCM3. *Journal of Geophysical Research Atmospheres*, 105:14873–14890. https://doi.org/10.1029/2000JD900091.

Ingvaldsen, R. B., Assmann, K. M., Primicerio, R., Fossheim, M., Polyakov, I. V., and Dolgov, A. V. (2021). Physical manifestations and ecological implications of Arctic Atlantification. *Nature Reviews Earth and Environment*, 2:874–889. https://doi.org/10.1038/s43017-021-00228-x.

IPCC (2021). Climate Change 2021: The Physical Science Basis. Contribution of Working Group I to the Sixth Assessment Report of the Intergovernmental Panel on Climate Change [Masson-Delmotte, V., P. Zhai, A. Pirani, S.L. Connors, C. Péan, S. Berger, N. Caud, Y. Chen, L. Goldfarb, M.I. Gomis, M. Huang, K. Leitzell, E. Lonnoy, J.B.R. Matthews, T.K. Maycock, T. Waterfield, O. Yelekçi, R. Yu, and B. Zhou (eds.). https://doi.org/10.1017/9781009157896.

Itkin, P., Hendricks, S., Webster, M., von Albedyll, L., Arndt, S., Divine, D., Jaggi, M., Oggier, M., Raphael, I., Ricker, R., Rohde, J., Schneebeli, M., and Liston, G. E. (2023). Sea ice and snow characteristics from year-long transects at the MOSAiC Central Observatory. *Elementa: Science of the Anthropocene*, 11(1). https://doi.org/10.1525/elementa.2022.00048.

Itkin, P., Webster, M., Hendricks, S., Oggier, M., Jaggi, M., Ricker, R., Arndt, S., Divine, D. V., von Albedyll, L., Raphael, I., Rohde, J., and Liston, G. E. (2021). Magnaprobe snow and melt pond depth measurements from the 2019-2020 MOSAiC expedition [Dataset]. *PANGAEA*, https://doi.org/10.1594/PANGAEA.937781.

Ivanova, N., Rampal, P., and Bouillon, S. (2016). Error assessment of satellite-derived lead fraction in the Arctic. *Cryosphere*, 10(2):585–595. https://doi.org/10.5194/tc-10-585-2016.

Kanzow, T. (2020). Links to master tracks in different resolutions of POLARSTERN cruise PS122/3, Arctic Ocean - Longyearbyen, 2020-02-24 - 2020-06-04 (Version 2). *PANGAEA*, https://doi.org/10.1594/PANGAEA.924681.

Kanzow, T. (2023). The Expedition PS131 of the Research Vessel Polarstern to the Fram Strait in 2022. 770. https://doi.org/10.57738/BzPM_0770_2023.

Koetz, B., Bastiaanssen, W., Berger, M., Defourney, P., Del Bello, U., Drusch, M., Drinkwater, M., Duca, R., Fernandez, V., Ghent, D., Guzinski, R., Hoogeveen, J., Hook, S., Lagouarde, J.-P., Lemoine, G., Manolis, I., Martimort, P., Masek, J., Massart, M., Notarnicola, C., Sobrino, J., and Udelhoven, T. (2018). High Spatio- Temporal Resolution Land Surface Temperature Mission - a Copernicus Candidate Mission in Support of Agricultural Monitoring. In *IGARSS 2018-2018 IEEE International Geoscience and Remote Sensing Symposium*, pages 8160–8162. IEEE. https://doi.org/10.1109/IGARSS.2018.8517433.

Korhonen, M., Rudels, B., Marnela, M., Wisotzki, A., and Zhao, J. (2013). Time and space variability of freshwater content, heat content and seasonal ice melt in the Arctic Ocean from 1991 to 2011. *Ocean Science*, 9:1015–1055. https://doi.org/10.5194/os-9-1015-2013.

Kortum, K., Singha, S., and Spreen, G. (2022). Robust Multiseasonal Ice Classification From High-Resolution X-Band SAR. *IEEE Transactions on Geoscience and Remote Sensing*, 60:1–12. https://doi.org/10.1109/TGRS.2022.3144731.

Krumpen, T., Albedyll, L. V., Goessling, H. F., Hendricks, S., Juhls, B., Spreen, G., Willmes, S., Belter, H. J., Dethloff, K., Haas, C., Kaleschke, L., Katlein, C., Kunze, X. T., Ricker, R., Rostosky, P., Rueckert, J., and Sokolova, J. (2021). MOSAiC drift

expedition from October 2019 to July 2020: Sea ice conditions from space and comparison with previous years. *The Cryosphere*, 15(8):3897–3920. https://doi.org/10.5194/tc-15-3897-2021.

Krumpen, T., Birrien, F., Kauker, F., Rackow, T., von Albedyll, L., Angelopoulos, M., Bessonov, V., Damm, E., Dethloff, K., Haapala, J., Haas, C., Hendricks, S., Hoelemann, J., Hoppmann, M., Kaleschke, L., Karcher, M., Kolabutin, N., Lenz, J., Morgenstern, A., Nicolaus, M., Nixdorf, U., Petrovsky, T., Rabe, B., Rabenstein, L., Rex, M., Ricker, R., Rohde, J., Shimanchuk, E., Singha, S., Smolyanitsky, V., Sokolov, V., Stanton, T., Timofeeva, A., and Tsamados, M. (2020). The MOSAiC ice floe: sediment-laden survivor from the Siberian shelf. *The Cryosphere*, 14(7):2173–2187. https://doi.org/10.5194/tc-14-2173-2020.

Kwiatkowski, L., Torres, O., Bopp, L., Aumont, O., Chamberlain, M., Christian, J. R., Dunne, J. P., Gehlen, M., Ilyina, T., John, J. G., Lenton, A., Li, H., Lovenduski, N. S., Orr, J. C., Palmieri, J., Santana-Falcón, Y., Schwinger, J., Séférian, R., Stock, C. A., Tagliabue, A., Takano, Y., Tjiputra, J., Toyama, K., Tsujino, H., Watanabe, M., Yamamoto, A., Yool, A., and Ziehn, T. (2020). Twenty-first century ocean warming, acidification, deoxygenation, and upper-ocean nutrient and primary production decline from CMIP6 model projections. *Biogeosciences*, 17:3439–3470. https://doi.org/10.5194/bg-17-3439-2020.

Kwok, R. (2018). Arctic sea ice thickness, volume, and multiyear ice coverage: Losses and coupled variability (1958-2018). *Environmental Research Letters*, 13(10). https://doi.org/10.1088/1748-9326/aae3ec.

Kwok, R., Spreen, G., and Pang, S. (2013). Arctic sea ice circulation and drift speed: Decadal trends and ocean currents. *Journal of Geophysical Research: Oceans*, 118(5):2408–2425. https://doi.org/10.1002/jgrc.20191.

Kwok, R. and Untersteiner, N. (2011). The thinning of Arctic sea ice. *Phys. Today*, 64(4):36–41.

Laidre, K. L. and Regehr, E. V. (2017). Arctic marine mammals and sea ice. In *Sea ice / edited by David N. Thomas*, chapter 21. John Wiley & Sons.

Landrum, L. L. and Holland, M. M. (2022). Influences of changing sea ice and snow thicknesses on simulated Arctic winter heat fluxes. *Cryosphere*, 16:1483–1495. https://doi.org/10.5194/tc-16-1483-2022.

Landy, J., Ehn, J., Shields, M., and Barber, D. (2014). Surface and melt pond evolution on landfast first-year sea ice in the Canadian Arctic Archipelago. *Journal of Geophysical Research: Oceans*, 119(5):3054–3075. https://doi.org/10.1002/2013JC009617.

LeadEx Group (1993). The LEADEX experiment. *Eos, Transactions American Geophysical Union*, 74(35):393–397. https://doi.org/10.1029/93EO00341.

Li, X., Krueger, S. K., Strong, C., Mace, G. G., and Benson, S. (2020). Midwinter Arctic leads form and dissipate low clouds. *Nature Communications*, 11(1). https://doi.org/10.1038/s41467-019-14074-5.

Light, B., Grenfell, T. C., and Perovich, D. K. (2008). Transmission and absorption of solar radiation by Arctic sea ice during the melt season. *Journal of Geophysical Research: Oceans*, 113(C3). https://doi.org/10.1029/2006JC003977.

Light, B., Smith, M. M., Perovich, D. K., Webster, M. A., Holland, M. M., Linhardt, F., Raphael, I. A., Clemens-Sewall, D., Macfarlane, A. R., Anhaus, P., and Bailey, D. A. (2022). Arctic sea ice albedo: Spectral composition, spatial heterogeneity, and temporal evolution observed during the MOSAiC drift. *Elementa: Science of the Anthropocene*, 10(1):000103. https://doi.org/10.1525/elementa.2021.000103.

Lindsay, R. and Rothrock, D. (1995). Arctic sea ice leads from advanced very high resolution radiometer images. *Journal of Geophysical Research: Oceans*, 100(C3):4533–4544. https://doi.org/10.1029/94JC02393.

Lubin, D. and Massom, R. (2006). *Polar Remote Sensing: Volume I: Atmosphere and Oceans*. Springer Science & Business Media.

Ludwig, V., Spreen, G., Haas, C., Istomina, L., Kauker, F., and Murashkin, D. (2019). The 2018 North Greenland polynya observed by a newly introduced merged optical and passive microwave sea-ice concentration dataset. *Cryosphere*, 13:2051–2073. https://doi.org/10.5194/tc-13-2051-2019.

Ludwig, V., Spreen, G., and Pedersen, L. T. (2020). Evaluation of a new merged sea-ice concentration dataset at 1 km resolution from thermal infrared and passive microwave satellite data in the arctic. *Remote Sensing*, 12:1–28. https://doi.org/10.3390/rs12193183.

Lüpkes, C., Vihma, T., Bimbaum, G., and Wacker, U. (2008). Influence of leads in sea ice on the temperature of the atmospheric boundary layer during polar night. *Geophysical Research Letters*, 35. https://doi.org/10.1029/2007GL032461.

Marcq, S. and Weiss, J. (2012). Influence of sea ice lead-width distribution on turbulent heat transfer between the ocean and the atmosphere. *Cryosphere*, 6(1):143–156. https://doi.org/10.5194/tc-6-143-2012.

Masuoka, E., Fleig, A., Wolfe, R., and Patt, F. (1998). Key characteristics of MODIS data products. *IEEE Transactions on Geoscience and Remote Sensing*, 36(4):1313–1323. https://doi.org/10.1109/36.701081.

Maykut, G. A. (1978). Energy exchange over young sea ice in the central Arctic. *Journal of Geophysical Research: Oceans*, 83(C7):3646–3658. https://doi.org/10.1029/JC083iC07p03646.

Maykut, G. A. (1982). Large-Scale Heat Exchange and Ice Production in the Central Arctic. *Journal of Geophysical Research*, 87(C10):7971–7984. https://doi.org/10.1029/JC087iC10p07971.

Maykut, G. A. and Untersteiner, N. (1971). Some results from a time-dependent thermodynamic model of sea ice. *Journal of Geophysical Research*, 76(6):1550–1575. https://doi.org/10.1029/jc076i006p01550.

Meredith, M., Sommerkorn, M., Cassotta, S., Derksen, C., Ekaykin, A., Hollowed, A., Kofinas, G., Mackintosh, A., Melbourne-Thomas, J., Muelbert, M., Ottersen, G., Pritchard, H., and Schuur, E. (2019). Polar Regions. In: IPCC Special Report on the Ocean and Cryosphere in a Changing Climate [H.-O. Pörtner, D.C. Roberts, V. Masson-Delmotte, P. Zhai, M. Tignor, E. Poloczanska, K. Mintenbeck, A. Alegría, M. Nicolai, A. Okem, J. Petzold, B. Rama, N.M. Weyer (eds.)]. *Cambridge University Press, Cambridge, UK and New York, NY, USA*, pages 203–320. https://doi.org/10.1017/9781009157964.005.

Michaelis, J. and Lüpkes, C. (2022). The Impact of Lead Patterns on Mean Profiles of Wind, Temperature, and Turbulent Fluxes in the Atmospheric Boundary Layer over Sea Ice. *Atmosphere*, 13. https://doi.org/10.3390/atmos13010148.

Mlawer, E. J., Taubman, S. J., Brown, P. D., Iacono, M. J., and Clough, S. A. (1997). Radiative transfer for inhomogeneous atmospheres: RRTM, a validated correlated-k model for the longwave. *Journal of Geophysical Research Atmospheres*, 102:16663–16682. https://doi.org/10.1029/97jd00237.

Muchow, M., Schmitt, A. U., and Kaleschke, L. (2021). A lead-width distribution for Antarctic sea ice: a case study for the Weddell Sea with high-resolution Sentinel-2 images. *The Cryosphere*, 15(9):4527–4537. https://doi.org/10.5194/tc-15-4527-2021.

Najman, L. and Schmitt, M. (1994). Watershed of a continuous function. *Signal Processing*, 38(1):99–112. https://doi.org/10.1016/0165-1684(94)90059-0.

Nandan, V., Willatt, R., Mallett, R., Stroeve, J., Geldsetzer, T., Scharien, R., Tonboe, R., Landy, J., Clemens-Sewall, D., Jutila, A., Wagner, D. N., Krampe, D., Huntemann, M., Yackel, J., Mahmud, M., Jensen, D., Newman, T., Hendricks, S., Spreen, G., Macfarlane, A., Schneebeli, M., Mead, J., Ricker, R., Gallagher, M., Duguay, C., Raphael, I., Polashenski, C., Tsamados, M., Matero, I., and Hoppman, M. (2022). Wind Transport

of Snow Impacts Ka- and Ku-band Radar Signatures on Arctic Sea Ice. *The Cryosphere Discussions*, 2022:1–38. https://doi.org/10.5194/tc-2022-116.

Nicolaus, M., Katlein, C., Maslanik, J., and Hendricks, S. (2012). Changes in Arctic sea ice result in increasing light transmittance and absorption. *Geophysical Research Letters*, 39(24). https://doi.org/10.1029/2012GL053738.

Nicolaus, M., Perovich, D. K., Spreen, G., Granskog, M. A., von Albedyll, L., Angelopoulos, M., Anhaus, P., Arndt, S., Belter, H. J., Bessonov, V., Birnbaum, G., Brauchle, J., Calmer, R., Cardellach, E., Cheng, B., Clemens-Sewall, D., Dadic, R., Damm, E., de Boer, G., Demir, O., Dethloff, K., Divine, D. V., Fong, A. A., Fons, S., Frey, M. M., Fuchs, N., Gabarró, C., Gerland, S., Goessling, H. F., Gradinger, R., Haapala, J., Haas, C., Hamilton, J., Hannula, H. R., Hendricks, S., Herber, A., Heuzé, C., Hoppmann, M., Høyland, K. V., Huntemann, M., Hutchings, J. K., Hwang, B., Itkin, P., Jacobi, H. W., Jaggi, M., Jutila, A., Kaleschke, L., Katlein, C., Kolabutin, N., Krampe, D., Kristensen, S. S., Krumpen, T., Kurtz, N., Lampert, A., Lange, B. A., Lei, R., Light, B., Linhardt, F., Liston, G. E., Loose, B., Macfarlane, A. R., Mahmud, M., Matero, I. O., Maus, S., Morgenstern, A., Naderpour, R., Nandan, V., Niubom, A., Oggier, M., Oppelt, N., Pätzold, F., Perron, C., Petrovsky, T., Pirazzini, R., Polashenski, C., Rabe, B., Raphael, I. A., Regnery, J., Rex, M., Ricker, R., Riemann-Campe, K., Rinke, A., Rohde, J., Salganik, E., Scharien, R. K., Schiller, M., Schneebeli, M., Semmling, M., Shimanchuk, E., Shupe, M. D., Smith, M. M., Smolyanitsky, V., Sokolov, V., Stanton, T., Stroeve, J., Thielke, L., Timofeeva, A., Tonboe, R. T., Tavri, A., Tsamados, M., Wagner, D. N., Watkins, D., Webster, M., and Wendisch, M. (2022). Overview of the MOSAiC expedition: Snow and sea ice. *Elementa: Science of the Anthropocene*, 10(1):000046. https://doi.org/10.1525/elementa.2021.000046.

Niehaus, H., Spreen, G., Birnbaum, G., Istomina, L., Jäkel, E., Linhardt, F., Neckel, N., Fuchs, N., Nicolaus, M., Sperzel, T., Tao, R., Webster, M., and Wright, N. (2023). Sea Ice Melt Pond Fraction Derived From Sentinel2 Data: Along the MOSAiC Drift and ArcticWide. *Geophysical Research Letters*, 50. https://doi.org/10.1029/2022GL102102.

Nixdorf, U., Dethloff, K., Rex, M., Shupe, M., Sommerfeld, A., Perovich, D. K., Nicolaus, M., Heuzé, C., Rabe, B., Loose, B., Damm, E., Gradinger, R., Fong, A., Maslowski, W., Rinke, A., Kwok, R., Spreen, G., Wendisch, M., Herber, A., Hirsekorn, M., Mohaupt, V., Frickenhaus, S., Immerz, A., Weiss-Tuider, K., König, B., Mengedoht, D., Regnery, J., Gerchow, P., Ransby, D., Krumpen, T., Morgenstern, A., Haas, C., Kanzow, T., Rack, F. R., Saitzev, V., Sokolov, V., Makarov, A., Schwarze, S., Wunderlich, T., Wurr, K., and Boetius, A. (2021). MOSAiC Extended Acknowledgement. *Zenodo*, https://doi.org/10.5281/zenodo.5541624.

Notz, D. and Community, S. (2020). Arctic sea ice in CMIP6. *Geophysical Research Letters*, 47(10):e2019GL086749. https://doi.org/10.1029/2019GL086749.

NSIDC (2022). MODIS ice-surface temperature download. https://n5eil01u.ecs.nsidc.org/MOSA/MYD29.006/ (last access: 03 April 2022).

NSIDC (2023a). MODIS ice-surface temperature product homepage. https://nsidc.org/data/MYD29 (last access: 03 April 2023).

NSIDC (2023b). NSIDC projection grid. https://nsidc.org/data/polar-stereo/ps_grids.html (last access: 03 April 2023).

Oziel, L., Baudena, A., Ardyna, M., Massicotte, P., Randelhoff, A., Sallée, J. B., Ingvaldsen, R. B., Devred, E., and Babin, M. (2020). Faster Atlantic currents drive poleward expansion of temperate phytoplankton in the Arctic Ocean. *Nature Communications*, 11. https://doi.org/10.1038/s41467-020-15485-5.

Paturel, Y., Lacambre, J.-B., Patin, F., and Moynagh, C. (2015). Inertial navigation at high latitude: Trials and test results. In *OCEANS 2015-MTS/IEEE Washington*, pages 1–5. IEEE. https://doi.org/10.23919/OCEANS.2015.7401904.

Perovich, D., Andreas, E., Curry, J., Eiken, H., Fairall, C., Grenfell, T., Guest, P., Intrieri, J., Kadko, D., Lindsay, R., et al. (1999). SHEBA: The surface heat budget of the Arctic Ocean. *EOS, Transactions, American Geophysical Union*, 80(41):481–486.

Perovich, D. K., Richter-Menge, J. A., Jones, K. F., Light, B., Elder, B. C., Polashenski, C., Laroche, D., Markus, T., and Lindsay, R. (2011). Arctic sea-ice melt in 2008 and the role of solar heating. *Annals of Glaciology*, 52:355–359. https://doi.org/10.3189/172756411795931714.

Petrich, C., Eicken, H., Polashenski, C. M., Sturm, M., Harbeck, J. P., Perovich, D. K., and Finnegan, D. C. (2012). Snow dunes: A controlling factor of melt pond distribution on Arctic sea ice. *Journal of Geophysical Research: Oceans*, 117(C9). https://doi.org/10.1029/2012JC008192.

Pirazzini, R., Hannula, H.-R., Shupe, M. D., Uttal, T., Cox, C. J., Costa, D., Persson, P. O. G., and Brasseur, Z. (2022). Upward and downward broadband shortwave and longwave irradiance and downward diffuse and direct solar partitioning during the MOSAiC expedition [Dataset]. *PANGAEA*, https://doi.org/10.1594/PANGAEA.952359.

Pistone, K., Eisenman, I., and Ramanathan, V. (2019). Radiative Heating of an Ice-Free Arctic Ocean. *Geophysical Research Letters*, 46:7474–7480. https://doi.org/10.1029/2019GL082914.

Polashenski, C., Perovich, D., and Courville, Z. (2012). The mechanisms of sea ice melt pond formation and evolution. *Journal of Geophysical Research: Oceans*, 117(C1). https://doi.org/10.1029/2011JC007231.

Polyakov, I. V., Pnyushkov, A. V., Alkire, M. B., Ashik, I. M., Baumann, T. M., Carmack, E. C., Goszczko, I., Guthrie, J., Ivanov, V. V., Kanzow, T., Krishfield, R., Kwok, R., Sundfjord, A., Morison, J., Rember, R., and Yulin, A. (2017). Greater role for Atlantic inflows on sea-ice loss in the Eurasian Basin of the Arctic Ocean. *Science*, 356(6335):285–291. https://doi.org/10.1126/science.aai8204.

Polyakov, I. V., Rippeth, T. P., Fer, I., Alkire, M. B., Baumann, T. M., Carmack, E. C., Ingvaldsen, R., Ivanov, V. V., Janout, M., Lind, S., Padman, L., Pnyushkov, A. V., and Rember, R. (2020). Weakening of cold halocline layer exposes sea ice to oceanic heat in the eastern arctic ocean. *Journal of Climate*, 33:8107–8123. https://doi.org/10.1175/JCLI-D-19-0976.1.

Popović, P., Cael, B., Silber, M., and Abbot, D. S. (2018). Simple rules govern the patterns of Arctic sea ice melt ponds. *Physical review letters*, 120(14):148701. https://doi.org/10.1103/PhysRevLett.120.148701.

Preußer, A., Heinemann, G., Willmes, S., and Paul, S. (2016). Circumpolar polynya regions and ice production in the Arctic: Results from MODIS thermal infrared imagery from 2002/2003 to 2014/2015 with a regional focus on the Laptev Sea. *Cryosphere*, 10:3021–3042. https://doi.org/10.5194/tc-10-3021-2016.

Previdi, M., Smith, K. L., and Polvani, L. M. (2021). Arctic amplification of climate change: A review of underlying mechanisms. *Environmental Research Letters*, 16. https://doi.org/10.1088/1748-9326/ac1c29.

Pörtner, H.-O., Roberts, D., Adams, H., Adelekan, I., Adler, C., Adrian, R., Aldunce, P., Ali, E., Begum, R. A., Bednar-Friedl, B., Kerr, R. B., Biesbroek, R., Birkmann, J., Bowen, K., Caretta, M., Carnicer, J., Castellanos, E., Cheong, T., Chow, W., Cissé, G., Clayton, S., Constable, A., Cooley, S., Costello, M., Craig, M., Cramer, W., Dawson, R., Dodman, D., Efitre, J., Garschagen, M., Gilmore, E., Glavovic, B., Gutzler, D., Haasnoot, M., Harper, S., Hasegawa, T., Hayward, B., Hicke, J., Hirabayashi, Y., Huang, C., Kalaba, K., Kiessling, W., Kitoh, A., Lasco, R., Lawrence, J., Lemos, M., Lempert, R., Lennard, C., Ley, D., Lissner, T., Liu, Q., Liwenga, E., Lluch-Cota, S., Löschke, S., Lucatello, S., Luo, Y., Mackey, B., Mintenbeck, K., Mirzabaev, A., Möller, V., Vale, M. M., Morecroft, M., Mortsch, L., Mukherji, A., Mustonen, T., Mycoo, M., Nalau, J., New, M., Okem, A., Ometto, J., ONeill, B., Pandey, R., Parmesan, C., Pelling, M., Pinho, P., Pinnegar, J., Poloczanska, E., Prakash, A., Preston, B., Racault, M.-F., Reckien, D., Revi, A., Rose, S., Schipper, E., Schmidt, D., Schoeman, D., Shaw, R.,

Simpson, N., Singh, C., Solecki, W., Stringer, L., Totin, E., Trisos, C., Trisurat, Y., van Aalst, M., Viner, D., Wairiu, M., Warren, R., Wester, P., Wrathall, D., , and Ibrahim, Z. Z. (2022). Technical Summary. [H.-O. Pörtner, D.C. Roberts, E.S. Poloczanska, K. Mintenbeck, M. Tignor, A. Alegría, M. Craig, S. Langsdorf, S. Löschke, V. Möller, A. Okem (eds.)]. In: Climate Change 2022: Impacts, Adaptation and Vulnerability. Contribution of Working Group II to the Sixth Assessment Report of the Intergovernmental Panel on Climate Change [H.-O. Pörtner, D.C. Roberts, M. Tignor, E.S. Poloczanska, K. Mintenbeck, A. Alegría, M. Craig, S. Langsdorf, S. Löschke, V. Möller, A. Okem, B. Rama (eds.)]. *Cambridge University Press, Cambridge, UK and New York, NY, USA*, pages 37–118. https://doi.org/10.1017/9781009325844.002.

Qiu, Y., Li, X.-M., and Guo, H. (2023). Spaceborne thermal infrared observations of Arctic sea ice leads at 30 m resolution [Preprint]. *EGUsphere*, pages 1–33. https://doi.org/10.5194/egusphere-2022-1506.

Qu, M., Pang, X., Zhao, X., Zhang, J., Ji, Q., and Fan, P. (2019). Estimation of turbulent heat flux over leads using satellite thermal images. *The Cryosphere*, 13(6):1565–1582. https://doi.org/10.5194/tc-13-1565-2019.

Rabe, B., Heuzé, C., Regnery, J., Aksenov, Y., Allerholt, J., Athanase, M., Bai, Y., Basque, C., Bauch, D., Baumann, T. M., Chen, D., Cole, S. T., Craw, L., Davies, A., Damm, E., Dethloff, K., Divine, D. V., Doglioni, F., Ebert, F., Fang, Y. C., Fer, I., Fong, A. A., Gradinger, R., Granskog, M. A., Graupner, R., Haas, C., He, H., He, Y., Hoppmann, M., Janout, M., Kadko, D., Kanzow, T., Karam, S., Kawaguchi, Y., Koenig, Z., Kong, B., Krishfield, R. A., Krumpen, T., Kuhlmey, D., Kuznetsov, I., Lan, M., Laukert, G., Lei, R., Li, T., Torres-Valdés, S., Lin, L., Lin, L., Liu, H., Liu, N., Loose, B., Ma, X., McKay, R., Mallet, M., Mallett, R. D., Maslowski, W., Mertens, C., Mohrholz, V., Muilwijk, M., Nicolaus, M., OBrien, J. K., Perovich, D., Ren, J., Rex, M., Ribeiro, N., Rinke, A., Schaffer, J., Schuffenhauer, I., Schulz, K., Shupe, M. D., Shaw, W., Sokolov, V., Sommerfeld, A., Spreen, G., Stanton, T., Stephens, M., Su, J., Sukhikh, N., Sundfjord, A., Thomisch, K., Tippenhauer, S., Toole, J. M., Vredenborg, M., Walter, M., Wang, H., Wang, L., Wang, Y., Wendisch, M., Zhao, J., Zhou, M., and Zhu, J. (2022). Overview of the MOSAiC expedition: Physical oceanography. *Elementa: Science of the Anthropocene*, 10(1):00062. https://doi.org/10.1525/elementa.2021.00062.

Rampal, P., Weiss, J., and Marsan, D. (2009). Positive trend in the mean speed and deformation rate of Arctic sea ice, 1979-2007. *Journal of Geophysical Research: Oceans*, 114(5). https://doi.org/10.1029/2008JC005066.

Rantanen, M., Karpechko, A. Y., Lipponen, A., Nordling, K., Hyvärinen, O., Ruosteenoja, K., Vihma, T., and Laaksonen, A. (2022). The Arctic has warmed nearly four times

faster than the globe since 1979. *Communications Earth & Environment*, 3(1):168. https://doi.org/10.1038/s43247-022-00498-3.

Rex, M. (2020). Links to master tracks in different resolutions of POLARSTERN cruise PS122/1, Tromsø - Arctic Ocean, 2019-09-20 - 2019-12-13 (Version 2). *PANGAEA*, https://doi.org/10.1594/PANGAEA.924668.

Ridler, T. and Calvard, S. (1978). Picture thresholding using an iterative selection method. *IEEE trans syst Man Cybern*, 8(8):630–632. https://doi.org/10.1109/TSMC.1978.4310039.

Ringeisen, D., Hutter, N., and von Albedyll, L. (2022). Deformation lines in Arctic sea ice: intersection angles distribution and mechanical properties. *EGUsphere*, pages 1–22. https://doi.org/10.5194/egusphere-2022-1481.

Ringeisen, D., Losch, M., Bruno Tremblay, L., and Hutter, N. (2019). Simulating intersection angles between conjugate faults in sea ice with different viscous-plastic rheologies. *Cryosphere*, 13(4):1167–1186. https://doi.org/10.5194/tc-13-1167-2019.

Ringeisen, D., Tremblay, L. B., and Losch, M. (2021). Non-normal flow rules affect fracture angles in sea ice viscous-plastic rheologies. *Cryosphere*, 15(6):2873–2888. https://doi.org/10.5194/tc-15-2873-2021.

Rinke, A., Cassano, J. J., Cassano, E. N., Jaiser, R., and Handorf, D. (2021). Meteorological conditions during the MOSAiC expedition. *Elementa: Science of the Anthropocene*, 9(1). https://doi.org/10.1525/elementa.2021.00023.

Ross, Z. E., Trugman, D. T., Hauksson, E., and Shearer, P. M. (2019). Searching for hidden earthquakes in Southern California. *Science*, 364(6442):767–771. https://doi.org/10.1126/science.aaw6888.

Rudels, B. (2009). Arctic Ocean Circulation. In Steele, J. H., editor, *Encyclopedia of Ocean Sciences (Second Edition)*, pages 211–225. Academic Press, second edition edition. https://doi.org/10.1016/B978-012374473-9.00601-9.

Rudels, B., Jones, E. P., Anderson, L. G., and Kattner, G. (1994). On the Intermediate Depth Waters of the Arctic Ocean. *Washington DC American Geophysical Union Geophysical Monograph Series*, 85:33–46. https://doi.org/10.1029/gm085p0033.

Rückert, J. E., Rostosky, P., Huntemann, M., Clemens-Sewall, D., Ebell, K., Kaleschke, L., Lemmetyinen, J., Macfarlane, A. R., Naderpour, R., Stroeve, J., Walbröl, A., and Spreen, G. (2023). Sea ice concentration satellite retrievals influenced by surface changes due to warm air intrusions: A case study from the MOSAiC expedition [Preprint]. *EarthArXiv (submitted to Elementa: Sci. Anth.)*. https://doi.org/10.31223/X5VW85.

Schmithüsen, H., Raeke, A., and Kieser, J. (2021a). Meteorological observations during POLARSTERN cruise PS122/1 [Dataset]. *PANGAEA*, https://doi.org/10.1594/PANGAEA.935263. Downloaded from https://dship.awi.de/.

Schmithüsen, H., Rohleder, C., and Hausen, R. (2021b). Meteorological observations during POLARSTERN cruise PS122/3 [Dataset]. *PANGAEA*, https://doi.org/10.1594/PANGAEA.935265. Downloaded from https://dship.awi.de/.

Schmithüsen, H., Schröter, S., and Wenzel, J. (2021c). Meteorological observations during POLARSTERN cruise PS122/2 [Dataset]. *PANGAEA*, https://doi.org/10.1594/PANGAEA.935264. Downloaded from https://dship.awi.de/.

Schulson, E. M. (2004). Compressive shear faults within arctic sea ice: Fracture on scales large and small. *Journal of Geophysical Research C: Oceans*, 109(7). https://doi.org/10.1029/2003JC002108.

Scott, F. and Feltham, D. (2010). A model of the three-dimensional evolution of Arctic melt ponds on first-year and multiyear sea ice. *Journal of Geophysical Research: Oceans*, 115(C12). https://doi.org/10.1029/2010JC006156.

SENSOR (2021a). Device Information: Applanix AP60-Air. *AWI Sensor Web*, https://hdl.handle.net/10013/sensor.a9fee346-91e7-4eed-9f2f-89f1368e53a0.

SENSOR (2021b). Device Information: Infratec VarioCAM HD head 680. *AWI Sensor Web*, https://hdl.handle.net/10013/sensor.0542bbfb-172a-496f-9bce-b21c59cd02c9.

SENSOR (2021c). Device Information: iXBlue HYDRINS 1. *AWI Sensor Web*, https://hdl.handle.net/10013/sensor.9ec5232e-9b30-492f-9741-63f056691cad.

Serreze, M. C., Barrett, A. P., Stroeve, J. C., Kindig, D. N., and Holland, M. M. (2009). The emergence of surface-based Arctic amplification. *Cryosphere*, 3(1):11–19. https://doi.org/10.5194/tc-3-11-2009.

Serreze, M. C. and Barry, R. G. (2011). Processes and impacts of Arctic amplification: A research synthesis. *Global and Planetary Change*, 77(1):85–96. https://doi.org/10.1016/j.gloplacha.2011.03.004.

Shokr, M. and Sinha, N. (2015). *Sea ice: physics and remote sensing*. John Wiley & Sons.

Shupe, M. D., Rex, M., Blomquist, B., Persson, P. O. G., Schmale, J., Uttal, T., Althausen, D., Angot, H., Archer, S., Bariteau, L., Beck, I., Bilberry, J., Bucci, S., Buck, C., Boyer, M., Brasseur, Z., Brooks, I. M., Calmer, R., Cassano, J., Castro, V., Chu, D., Costa, D., Cox, C. J., Creamean, J., Crewell, S., Dahlke, S., Damm, E., de Boer, G., Deckelmann, H., Dethloff, K., Dütsch, M., Ebell, K., Ehrlich, A., Ellis, J., Engelmann,

R., Fong, A. A., Frey, M. M., Gallagher, M. R., Ganzeveld, L., Gradinger, R., Graeser, J., Greenamyer, V., Griesche, H., Griffiths, S., Hamilton, J., Heinemann, G., Helmig, D., Herber, A., Heuzé, C., Hofer, J., Houchens, T., Howard, D., Inoue, J., Jacobi, H.-W., Jaiser, R., Jokinen, T., Jourdan, O., Jozef, G., King, W., Kirchgaessner, A., Klingebiel, M., Krassovski, M., Krumpen, T., Lampert, A., Landing, W., Laurila, T., Lawrence, D., Lonardi, M., Loose, B., Lüpkes, C., Maahn, M., Macke, A., Maslowski, W., Marsay, C., Maturilli, M., Mech, M., Morris, S., Moser, M., Nicolaus, M., Ortega, P., Osborn, J., Pätzold, F., Perovich, D. K., Petäjä, T., Pilz, C., Pirazzini, R., Posman, K., Powers, H., Pratt, K. A., Preußer, A., Quéléver, L., Radenz, M., Rabe, B., Rinke, A., Sachs, T., Schulz, A., Siebert, H., Silva, T., Solomon, A., Sommerfeld, A., Spreen, G., Stephens, M., Stohl, A., Svensson, G., Uin, J., Viegas, J., Voigt, C., von der Gathen, P., Wehner, B., Welker, J. M., Wendisch, M., Werner, M., Xie, Z., and Yue, F. (2022). Overview of the MOSAiC expedition: Atmosphere. *Elementa: Science of the Anthropocene*, 10(1):00060. https://doi.org/10.1525/elementa.2021.00060.

Shupe, M. D., Rex, M., Dethloff, K., Damm, E., Fong, A., Gradinger, R., Heuzé, C., Loose, B., Makarov, A., Maslowski, W., et al. (2020). Arctic Report Card 2020: The MOSAiC Expedition: A Year Drifting with the Arctic Sea Ice. *NOAA*. https://doi.org/10.25923/9g3v-xh92.

Spreen, G., Kaleschke, L., and Heygster, G. (2008). Sea ice remote sensing using AMSR-E 89-GHz channels. *Journal of Geophysical Research: Oceans*, 113. https://doi.org/10.1029/2005JC003384.

Spreen, G. and Kern, S. (2017). Methods of satellite remote sensing of sea ice. In *Sea ice / edited by David N. Thomas*, chapter 9. John Wiley & Sons.

Spreen, G., Kwok, R., and Menemenlis, D. (2011). Trends in Arctic sea ice drift and role of wind forcing: 1992-2009. *Geophysical Research Letters*, 38(19):1–6. https://doi.org/10.1029/2011GL048970.

Steele, M., Ermold, W., and Zhang, J. (2008). Arctic Ocean surface warming trends over the past 100 years. *Geophysical Research Letters*, 35. https://doi.org/10.1029/2007GL031651.

Stroeve, J., Nandan, V., Willatt, R., Dadic, R., Rostosky, P., Gallagher, M., Mallett, R., Barrett, A., Hendricks, S., Tonboe, R., McCrystall, M., Serreze, M., Thielke, L., Spreen, G., Newman, T., Yackel, J., Ricker, R., Tsamados, M., Macfarlane, A., Hannula, H.-R., and Schneebeli, M. (2022). Rain on snow (ROS) understudied in sea ice remote sensing: a multi-sensor analysis of ROS during MOSAiC (Multidisciplinary drifting Observatory for the Study of Arctic Climate). *The Cryosphere*, 16(10):4223–4250. https://doi.org/10.5194/tc-16-4223-2022.

Stroeve, J. and Notz, D. (2018). Changing state of Arctic sea ice across all seasons. *Environmental Research Letters*, 13. https://doi.org/10.1088/1748-9326/aade56.

Stroeve, J. C., Markus, T., Boisvert, L., Miller, J., and Barrett, A. (2014). Changes in Arctic melt season and implications for sea ice loss. *Geophysical Research Letters*, 41:1216–1225. https://doi.org/10.1002/2013GL058951.

Stroeve, J. C., Serreze, M. C., Holland, M. M., Kay, J. E., Malanik, J., and Barrett, A. P. (2012). The Arctic's rapidly shrinking sea ice cover: A research synthesis. *Climatic Change*, 110:1005–1027. https://doi.org/10.1007/s10584-011-0101-1.

Studinger, M., Koenig, L., Martin, S., and Sonntag, J. (2010). Operation IceBridge: Using instrumented aircraft to bridge the observational GAP between icesat and ICESAT-2. In *2010 IEEE International Geoscience and Remote Sensing Symposium*, pages 1918–1919. Institute of Electrical and Electronics Engineers Inc. https://doi.org/10.1109/IGARSS.2010.5650555.

Sumata, H., de Steur, L., Divine, D. V., Granskog, M. A., and Gerland, S. (2023). Regime shift in Arctic Ocean sea ice thickness. *Nature*, 615:443–449. https://doi.org/10.1038/s41586-022-05686-x.

Terhaar, J., Kwiatkowski, L., and Bopp, L. (2020). Emergent constraint on Arctic Ocean acidification in the twenty-first century. *Nature*, 582:379–383. https://doi.org/10.1038/s41586-020-2360-3.

Tetzlaff, A., Lüpkes, C., and Hartmann, J. (2015). Aircraft-based observations of atmospheric boundary-layer modification over Arctic leads. *Quarterly Journal of the Royal Meteorological Society*, 141(692):2839–2856. https://doi.org/10.1002/qj.2568.

Thielke, L. and Huntemann, M. (2022). Python code for helicopter-borne surface temperature images and maps (2.1). *Zenodo*, https://doi.org/10.5281/zenodo.5956954.

Thielke, L., Huntemann, M., Hendricks, S., Jutial, A., Ricker, R., and Spreen, G. (2022a). Data Manual V1.1: Helicopter-borne thermal infrared surface temperature during the MOSAiC expedition. *Zenodo*, https://doi.org/10.5281/zenodo.5940546.

Thielke, L., Huntemann, M., Hendricks, S., Jutila, A., Ricker, R., and Spreen, G. (2022b). Helicopter-borne thermal infrared sea ice surface temperature maps with 1 m resolution during the MOSAiC expedition, NetCDF format, version 2 [Dataset]. *PANGAEA*, https://doi.org/10.1594/PANGAEA.940846.

Thielke, L., Huntemann, M., Hendricks, S., Jutila, A., Ricker, R., and Spreen, G. (2022c). Helicopter-borne thermal infrared sea ice surface temperature maps with 1 m resolution during the MOSAiC expedition, NetCDF format, version 3 [Dataset]. *PANGAEA*, https://doi.org/10.1594/PANGAEA.950683.

Thielke, L., Huntemann, M., Hendricks, S., Jutila, A., Ricker, R., and Spreen, G. (2022d). Helicopter-borne thermal infrared sea ice surface temperatures during the MOSAiC expedition [Dataset]. *PANGAEA*, https://doi.org/10.1594/PANGAEA.941017.

Thielke, L., Huntemann, M., Hendricks, S., Jutila, A., Ricker, R., and Spreen, G. (2022e). Sea ice surface temperatures from helicopter-borne thermal infrared imaging during the MOSAiC expedition. *Scientific Data*, 9(1):1–16. https://doi.org/10.1038/s41597-022-01461-9.

Thielke, L., Huntemann, M., and Spreen, G. (2022f). Lead classification maps from helicopter-borne surface temperatures with 1 m resolution during the MOSAiC expedition [Dataset]. *PANGAEA*, https://doi.org/10.1594/PANGAEA.951568.

Thielke, L., Spreen, G., Huntemann, M., and Murashkin, D. (2023). Spatio-temporal variability of small-scale leads based on helicopter winter sea ice surface temperatures [Preprint]. *EarthArXiv (in review for Elementa: Sci. Anth.)*. https://doi.org/10.31223/X5R07W.

Thorndike, A. S., Rothrock, D. A., Maykut, G. A., and Colony, R. (1975). The thickness distribution of sea ice. *Journal of Geophysical Research*, 80:4501–4513. https://doi.org/10.1029/jc080i033p04501.

Timmermans, M. L. and Marshall, J. (2020). Understanding Arctic Ocean Circulation: A Review of Ocean Dynamics in a Changing Climate. *Journal of Geophysical Research: Oceans*, 125. https://doi.org/10.1029/2018JC014378.

Tschudi, M., Riggs, G., Hall, D. K., , and Román, M. O. (2017). VIIRS/NPP Ice Surface Temperature 6-Min L2 Swath 750m, Version 1 [Dataset]. Boulder, Colorado USA. NASA National Snow and Ice Data Center Distributed Active Archive Center. https://doi.org/10.5067/VIIRS/VNP30.001.

Tschudi, M. A., Curry, J. A., and Maslanik, J. A. (2002). Characterization of springtime leads in the Beaufort/Chukchi seas from airborne and satellite observations during FIRE/SHEBA. *Journal of Geophysical Research: Oceans*, 107(10). https://doi.org/10.1029/2000jc000541.

Untersteiner, N. (1964). Calculations of temperature regime and heat budget of sea ice in the central Arctic. *Journal of Geophysical Research*, 69(22):4755–4766. https://doi.org/10.1029/JZ069i022p04755.

Uttal, T., Curry, J. A., Mcphee, M. G., Perovich, D. K., Moritz, R. E., Maslanik, J. A., Guest, P. S., Stern, H. L., Moore, J. A., Turenne, R., Heiberg, A., Serreze, M. C., Wylie, D. P., Persson, O. G., Paulson, C. A., Halle, C., Morison, J. H., Wheeler, P. A.,

Makshtas, A., Welch, H., Shupe, M. D., Intrieri, J. M., Stamnes, K., Lindsey, R. W., Pinkel, R., Pegau, W. S., Stanton, T. P., and Grenfeld, T. C. (2002). Surface heat budget of the Arctic Ocean. *Bulletin of the American Meteorological Society*, 83(2):255–276. https://doi.org/10.1175/1520-0477(2002)083<0255:SHBOTA>2.3.CO;2.

Valkonen, E., Cassano, J., and Cassano, E. (2021). Arctic Cyclones and Their Interactions With the Declining Sea Ice: A Recent Climatology. *Journal of Geophysical Research: Atmospheres*, 126. https://doi.org/10.1029/2020JD034366.

Vavrus, S. (2004). The impact of cloud feedbacks on Arctic climate under greenhouse forcing. *Journal of Climate*, 17(3):603–615. https://doi.org/10.1175/1520-0442(2004)017<0603:TIOCFO>2.0.CO;2.

Vihma, T. (2014). Effects of Arctic Sea Ice Decline on Weather and Climate: A Review. *Surveys in Geophysics*, 35(5):1175–1214. https://doi.org/10.1007/s10712-014-9284-0.

Vihma, T. and Pirazzini, R. (2005). On the factors controlling the snow surface and 2-m air temperatures over the Arctic sea ice in winter. *Boundary-Layer Meteorology*, 117(1):73–90. https://doi.org/10.1007/s10546-004-5938-7.

Vihma, T., Pirazzini, R., Fer, I., Renfrew, I. A., Sedlar, J., Tjernström, M., Lüpkes, C., Nygård, T., Notz, D., Weiss, J., Marsan, D., Cheng, B., Birnbaum, G., Gerland, S., Chechin, D., and Gascard, J. C. (2014). Advances in understanding and parameterization of small-scale physical processes in the marine Arctic climate system: a review. *Atmospheric Chemistry and Physics*, 14(17):9403–9450. https://doi.org/10.5194/acp-14-9403-2014.

von Albedyll, L., Hendricks, S., Grodofzig, R., Hutter, N., Murashkin, D., Kaleschke, L., Willmes, S., Thielke, L., Tian-Kunze, X., Spreen, G., and Haas, C. (2022a). Lead fractions from SAR-derived sea ice divergence during MOSAiC [Chapter 6 in Dissertation: Sea ice deformation and sea ice thickness change].

von Albedyll, L., Hendricks, S., Grodofzig, R., Krumpen, T., Arndt, S., Belter, H. J., Birnbaum, G., Cheng, B., Hoppmann, M., Hutchings, J., Itkin, P., Lei, R., Nicolaus, M., Ricker, R., Rohde, J., Suhrhoff, M., Timofeeva, A., Watkins, D., Webster, M., and Haas, C. (2022b). Thermodynamic and dynamic contributions to seasonal Arctic sea ice thickness distributions from airborne observations. *Elementa: Science of the Anthropocene*, 10. https://doi.org/10.1525/elementa.2021.00074.

Wadhams, P. (1981). Sea-ice topography of the Arctic Ocean in the region 70 W to 25 E. *Philosophical Transactions of the Royal Society of London. Series A, Mathematical and Physical Sciences*, 302(1464):45–85. https://doi.org/10.1098/rsta.1981.0157.

Wadhams, P., McLaren, A. S., and Weintraub, R. (1985). Ice thickness distribution in Davis Strait in February from submarine sonar profiles. *Journal of Geophysical Research: Oceans*, 90(C1):1069–1077. https://doi.org/10.1029/JC090iC01p01069.

Wang, Q., Danilov, S., Jung, T., Kaleschke, L., and Wernecke, A. (2016). Sea ice leads in the Arctic Ocean: Model assessment, interannual variability and trends. *Geophysical Research Letters*, 43(13):7019–7027. https://doi.org/10.1002/2016GL068696.

Wang, S., Wang, Q., Jordan, R. E., and Persson, P. O. (2001). Interactions among longwave radiation of clouds, turbulence, and snow surface temperature in the Arctic: A model sensitivity study. *Journal of Geophysical Research Atmospheres*, 106(D14):15323–15333. https://doi.org/10.1029/2000JD900358.

Wang, X. and Key, J. R. (2003). Recent trends in Arctic surface, cloud, and radiation properties from space. *Science*, 299(5613):1725–1728. https://doi.org/10.1126/science.1078065.

Webster, M. A., Holland, M., Wright, N. C., Hendricks, S., Hutter, N., Itkin, P., Light, B., Linhardt, F., Perovich, D. K., Raphael, I. A., Smith, M. M., von Albedyll, L., and Zhang, J. (2022). Spatiotemporal evolution of melt ponds on Arctic sea ice: MOSAiC observations and model results. *Elementa: Science of the Anthropocene*, 10(1):000072. https://doi.org/10.1525/elementa.2021.000072.

Wendisch, M., Brückner, M., Burrows, J., Crewell, S., Dethloff, K., Ebell, K., Lüpkes, C., Macke, A., Notholt, J., Quaas, J., Rinke, A., and Tegen, I. (2017). Understanding causes and effects of rapid warming in the Arctic. *Eos*, 98. https://dx.doi.org/10.1029/2017EO064803.

Wendisch, M., Brückner, M., Crewell, S., Ehrlich, A., Notholt, J., Lüpkes, C., Macke, A., Burrows, J. P., Rinke, A., Quaas, J., Maturilli, M., Schemann, V., Shupe, M. D., Akansu, E. F., Barrientos-Velasco, C., Bärfuss, K., Blechschmidt, A.-M., Block, K., Bougoudis, I., Bozem, H., Böckmann, C., Bracher, A., Bresson, H., Bretschneider, L., Buschmann, M., Chechin, D. G., Chylik, J., Dahlke, S., Deneke, H., Dethloff, K., Donth, T., Dorn, W., Dupuy, R., Ebell, K., Egerer, U., Engelmann, R., Eppers, O., Gerdes, R., Gierens, R., Gorodetskaya, I. V., Gottschalk, M., Griesche, H., Gryanik, V. M., Handorf, D., Harm-Altstädter, B., Hartmann, J., Hartmann, M., Heinold, B., Herber, A., Herrmann, H., Heygster, G., Höschel, I., Hofmann, Z., Hölemann, J., Hünerbein, A., Jafariserajehlou, S., Jäkel, E., Jacobi, C., Janout, M., Jansen, F., Jourdan, O., Jurányi, Z., Kalesse-Los, H., Kanzow, T., Käthner, R., Kliesch, L. L., Klingebiel, M., Knudsen, E. M., Kovács, T., Körtke, W., Krampe, D., Kretzschmar, J., Kreyling, D., Kulla, B., Kunkel, D., Lampert, A., Lauer, M., Lelli, L., von Lerber, A., Linke, O., Löhnert, U., Lonardi, M., Losa, S. N., Losch, M., Maahn, M., Mech, M., Mei, L., Mertes, S., Metzner,

E., Mewes, D., Michaelis, J., Mioche, G., Moser, M., Nakoudi, K., Neggers, R., Neuber, R., Nomokonova, T., Oelker, J., Papakonstantinou-Presvelou, I., Pätzold, F., Pefanis, V., Pohl, C., van Pinxteren, M., Radovan, A., Rhein, M., Rex, M., Richter, A., Risse, N., Ritter, C., Rostosky, P., Rozanov, V. V., Donoso, E. R., Garfias, P. S., Salzmann, M., Schacht, J., Schäfer, M., Schneider, J., Schnierstein, N., Seifert, P., Seo, S., Siebert, H., Soppa, M. A., Spreen, G., Stachlewska, I. S., Stapf, J., Stratmann, F., Tegen, I., Viceto, C., Voigt, C., Vountas, M., Walbröl, A., Walter, M., Wehner, B., Wex, H., Willmes, S., Zanatta, M., and Zeppenfeld, S. (2023). Atmospheric and Surface Processes, and Feedback Mechanisms Determining Arctic Amplification: A Review of First Results and Prospects of the $(AC)^3$ Project. *Bulletin of the American Meteorological Society*, 104(1):E208 – E242. https://doi.org/10.1175/BAMS-D-21-0218.1.

Wernecke, A. and Kaleschke, L. (2015). Lead detection in Arctic sea ice from CryoSat-2: Quality assessment, lead area fraction and width distribution. *Cryosphere*, 9(5):1955–1968. https://doi.org/10.5194/tc-9-1955-2015.

Wever, N., Rossmann, L., MaaSS, N., Leonard, K. C., Kaleschke, L., Nicolaus, M., and Lehning, M. (2020). Version 1 of a sea ice module for the physics-based, detailed, multi-layer SNOWPACK model. *Geoscientific Model Development*, 13:99–119. https://doi.org/10.5194/gmd-13-99-2020.

Willmes, S. and Heinemann, G. (2015). Pan-arctic lead detection from MODIS thermal infrared imagery. *Annals of Glaciology*, 56(69):29–37. https://doi.org/10.3189/2015AoG69A615.

Willmes, S. and Heinemann, G. (2016). Sea-ice wintertime lead frequencies and regional characteristics in the Arctic, 2003-2015. *Remote Sensing*, 8(1):2003–2015. https://doi.org/10.3390/rs8010004.

Willmes, S., Heinemann, G., and Schnaase, F. (2023). Patterns of wintertime Arctic sea ice leads and their relation to winds and ocean currents. *The Cryosphere Discussions*, pages 1–23. https://doi.org/10.5194/tc-2023-22.

WMO (2014). Sea-ice Nomenclature. https://library.wmo.int/index.php?lvl=notice_display&id=6772 (last access: 03 April 2023).

Yu, Y. and Rothrock, D. A. (1996). Thin ice thickness from satellite thermal imagery. *Journal of Geophysical Research C: Oceans*, 101(C11):25753–25766. https://doi.org/10.1029/96JC02242.

Zakhvatkina, N., Smirnov, V., and Bychkova, I. (2019). Satellite SAR data-based sea ice classification: An overview. *Geosciences*, 9. https://doi.org/10.3390/geosciences9040152.

Acknowledgements

I would like to express my sincere gratitude to my supervisors, Dr. Gunnar Spreen and Dr. Marcus Huntemann, for their valuable support and excellent guidance throughout my dissertation. Their constructive feedback and insightful suggestions have been conducive in enhancing the quality of my research and the development of my thesis. I am grateful for their mentorship throughout my doctoral studies.

I would also like to extend my many thanks to the working group 'Remote Sensing of Polar Regions,' especially Alexander, Christian, Hannah, Janna, and Philip. Their regular feedback, interesting discussions during coffee breaks, and insightful ideas shared during group meetings and meetings among doctoral candidates have been immensely beneficial. I am thankful to everyone in the group for the positive and constructive work environment.

As a doctoral candidate, the ArcTrain Community, led by Prof. Dr. Michal Kucera, has been my academic home and a wonderful network. ArcTrain provided excellent training in terms of workshops and supported many unique opportunities for me, including retreats, international annual meetings, several conferences, and my research stay in Montreal, Canada. I appreciate the third cohort for accompanying me on this journey and thank the second cohort for introducing us to the life as a doctoral candidate within ArcTrain. I especially want to thank my ArcTrain fellows Charles, Damien, Franziska, Jenny, Johanna, Kevin, Luisa, Valentin, and Yuqing.

I am grateful to my former colleagues and friends Arantxa, Catalin, Dmitrii, and Christine, who played an important role in supporting me when I started my new position as doctoral candidate. I particularly appreciate the support of my former office mates Raul and Junshen for their patience in answering my numerous questions, and Valentin, who introduced me to the new world as a doctoral candidate at the University of Bremen and directly introduced me to the ArcTrain community.

I am grateful to Prof. Dr. Bruno Tremblay and his group for hosting and supporting my research stay at McGill in Montreal, Canada, even during the pandemic. I also thank my friend Adina, who shared her wonderful home with me and contributed to my successful research stay.

My thesis committee, comprising Dr. Marcus Huntemann, Dr. Martin Losch, Dr. Martin Schneebeli, Dr. Gunnar Spreen and Prof. Dr. Bruno Tremblay, provided excellent guidance throughout my dissertation. I am thankful that every member took time for my committee meetings. Every meeting was very supportive and motivating. I additionally thank Dr. Martin Schneebeli for his mentorship in organizing the winter heat budget group and hosting me for a short research stay in Davos, Switzerland.

I also would like to express my appreciation to GLOMAR for providing a platform for the development of new skills for my doctorate by offering support for any concerns as a doctoral candidate and organizing workshops.

I appreciate the opportunity to join the MOSAiC expedition. The crew, scientists, and organizers of the expedition were essential for a professional and personal successful, and memorable expedition in the central Arctic. I particularly appreciate the Leg 5 team and, therein, the ICE team for their inspiration and support during my time on RV Polarstern and beyond. The expedition and MOSAiC community had an essential contribution to my scientific development. It is a great network from which I learned a lot.

I appreciate the contribution of my co-authors to the manuscripts on which the Chapters 3, 4, 5, and 6 are based on. I am grateful to the anonymous reviewers for their constructive feedback, which improved the quality of the scientific output in Chapter 3 and Chapter 4. Thank you to Alexander, Christian, Franziska, Hannah, Janna, Philip, Stefan, Valentin, and Yuqing for proofreading parts of this thesis. I would like to express my appreciation to Malte Gerken and Peter Grupe for their technical support, which was crucial to the smooth running of my doctoral work.

I would like to highlight the importance of my dear friends Sophie, Sandra, Sonja, and many more, who shared my fascination with the Arctic and supported me throughout the years of my dissertation and beyond. Most importantly, I am deeply grateful to my family, especially my parents and grandparents, for their love, unconditional support, and encouragement throughout my whole life. Thank you for everything you have done for me. This work would have not been possible without you. I express my deepest gratitude to my partner, Stefan, for his positivity and constant support, which is essential for me to achieve my goals.